

**POLITECHNIKA KRAKOWSKA im. T. Kościuszki**



Faculty of Environmental  
Engineering and Power  
Engineering



**Department of Energy**

***Development of a new cooling system for  
photovoltaic modules with a sun-tracking system***

---

Doctoral Dissertation

Mgr inż. Mehmet Ali Yildirim

Supervisor:

**Dr hab. inż. Artur Cebula, prof. PK**

Assistant Supervisor:

**Dr hab. inż. Piotr Cisek**

Cracow 2024

## Streszczenie

Integracja odnawialnych źródeł energii w produkcji energii stała się koniecznością, ponieważ świat zmierza w kierunku bardziej ekologicznej przyszłości. Rosnące zapotrzebowanie na zrównoważoną i wydajną energię skłania naukowców do opracowywania hybrydowych systemów energetycznych. Systemy fotowoltaiczne/termiczne (PV/T) przyciągnęły ogromną uwagę badaczy ze względu na ich zalety w porównaniu z samodzielnymi systemami fotowoltaicznymi i słoneczno-termicznymi (ST), ponieważ systemy PV/T są hybrydowymi systemami energetycznymi, które jednocześnie przekształcają energię słoneczną w energię elektryczną i ciepłą. Biorąc pod uwagę obecne progi maksymalnej sprawności cieplnej osiąganey przez moduły PV/T proponowane w literaturze i dostępne na rynku moduły PV/T, zwykle wahające się między 30% a 85%, niniejsza rozprawa doktorska miała na celu opracowanie wysoce wydajnego, łatwego w produkcji, zaawansowanego i kompaktowego systemu chłodzenia dla modułów PV. Badania koncentrowały się na zaprojektowaniu nowego modułu PV/T, którego celem było przekroczenie 90% sprawności cieplnej przy jednoczesnym zachowaniu maksymalnej sprawności konwersji elektrycznej modułu PV.

Metodologia badań obejmowała zaprojektowanie i opracowanie wysoce wydajnego systemu chłodzenia, który może zmaksymalizować chłodzenie modułu fotowoltaicznego i zbierać ciepło odpadowe. Do ostatecznego zaprojektowania systemu chłodzenia wykorzystano najnowocześniejsze narzędzia symulacyjne. Wyprodukowany system chłodzenia został przebadany w warunkach laboratoryjnych i zewnętrznych w celu przeanalizowania wydajności cieplnej i sprawności konwersji elektrycznej zaprojektowanego modułu PV/T.

Wyprodukowany system chłodzenia został najpierw przetestowany w laboratorium. Zbadano wydajność cieplną i charakterystykę wymiany ciepła w różnych warunkach. Zaprojektowany system PV/T osiągnął sprawność cieplną na poziomie  $96,47 \pm 1,40\%$ , a system chłodzenia był w stanie obniżyć temperaturę warstwy ogniów PV o  $40,72 \text{ }^\circ\text{C}$ .

Eksperymenty zewnętrzne przeprowadzono w celu przeanalizowania wydajności systemu PV/T we wrześniu i październiku. Maksymalne chłodzenie modułu PV zaobserwowano 12 września 2023 r., a temperatura tylnej powierzchni chłodzonych i niechłodzonych modułów PV wynosiła odpowiednio  $16,56 \text{ }^\circ\text{C}$  i  $70,98 \text{ }^\circ\text{C}$ . Maksymalna sprawność cieplna wynosząca  $98,03 \pm 1,57\%$  osiągnięta w ciągu dnia była najwyższą sprawnością cieplną zaobserwowaną podczas dwumiesięcznego eksperymentu. Sprawność konwersji elektrycznej modułu PV wyniosła  $19,12 \pm 1,14\%$ . Wdrożony system chłodzenia pozwolił na wygenerowanie  $38,86\%$  więcej energii elektrycznej na koniec dnia testowego. Eksperymenty na zewnątrz wykazały, że zaprojektowany moduł PV/T przekroczył przewidywaną docelową sprawność cieplną  $90\%$  i utrzymał maksymalną sprawność konwersji elektrycznej.

## Abstract

The integration of renewable energy sources in energy production has become imperative as the world transitions towards a greener future. The growing demand for sustainable and efficient energy leads researchers to develop hybrid energy systems. Photovoltaic/thermal systems (PV/T) drew huge attention from researchers due to their benefits compared to stand-alone photovoltaic and solar-thermal (ST) systems, as PV/T systems are hybrid energy systems that simultaneously convert solar energy into electrical and thermal energy. Acknowledging the current thresholds of maximum thermal efficiency achieved by the PV/T modules proposed in the literature and commercially available PV/T modules, typically hovering between 30% and 85%, this dissertation focused on inventing a highly efficient, easy-to-produce, advanced, and compact cooling system for PV modules. The research focused on designing a novel PV/T module aimed at exceeding 90% thermal efficiency while maintaining the maximum electrical conversion efficiency of the PV module.

The research methodology involved designing and developing a highly efficient cooling system that can maximize the cooling of the PV module and harvest the waste heat. Cutting-edge simulation tools were used to achieve the final design of the cooling system. The manufactured cooling system was studied in laboratory and outdoor environments to analyze the thermal performance and electrical conversion efficiency of the designed PV/T module.

The manufactured cooling system was first tested in the laboratory. The thermal efficiency and heat transfer characteristics under various conditions were investigated. The designed PV/T system reached a thermal efficiency of  $96.47 \pm 1.40\%$ , and the cooling system was able to reduce the PV cell layer temperature by  $40.72\text{ }^\circ\text{C}$ .

The outdoor experiments were conducted to analyze the performance of the PV/T system in September and October. The maximum cooling of the PV module was observed on the 12<sup>th</sup> of September, 2023, where the back surface temperatures of cooled and non-cooled PV modules were  $16.56\text{ }^\circ\text{C}$  and  $70.98\text{ }^\circ\text{C}$ , respectively. The maximum thermal efficiency of  $98.03 \pm 1.57\%$  achieved during the day was the highest thermal efficiency observed during the experiment period of two months. The electrical conversion efficiency of the PV module was  $19.12 \pm 1.14\%$ . The implemented cooling system allowed for generating 38.86% more electrical energy at the end of the test day. The outdoor experiments showed that the designed PV/T module surpassed the projected 90% thermal efficiency target and maintained the maximum electrical conversion efficiency.

## Acknowledgment

There is a well-known proverb that says, “It takes a village to raise a child,” and I heartily believe that a PhD also requires the support of the village. Therefore, I would like to express my deepest gratitude to the people who supported me and played significant roles in my PhD journey.

First and foremost, I would like to thank my supervisors, dr hab. inż. Artur Tadeusz Cebula, prof. PK and dr hab. inż. Piotr Cisek. Your exceptional academic expertise, constant support, guidance, and encouragement have been invaluable throughout the entire process. I extend my heartfelt appreciation to prof. dr hab. inż. Paweł Ocioń and prof. dr hab. inż. Wiesław Zima for generously sharing their extensive academic knowledge. I would also like to express my gratitude to Mr. Marek Czamara, who was my supervisor in the company. His invaluable knowledge of renewable energy systems shaped and enhanced my skills and knowledge in the industry.

In addition to my supervisors, I am indebted to my colleagues in the university and company, whose support has been a continuous source of motivation. A special appreciation goes to my colleagues, Piotr Czamara and Rafał Giza, for their great help in conducting experiments at the company. I would like to extend my appreciation to Michał Franczak, Agnieszka Drzyzga, and Hubert Krok for small talks during our breaks that helped me to focus and bring new ideas.

I would like to express my thankfulness to my mum, dad, and brother for their constant support, motivation, and patience while waiting for the moment of success.

My better half, Klaudia, you have been my biggest cheerleader throughout this journey, and I cannot thank you enough for your love and support.

I am incredibly grateful to the Ministry of Science and Higher Education of Poland for accepting me in the Implementation Doctorate Program to allow me to start and pursue my PhD and get experience in the industry.

# Contents

|  |           |
|--|-----------|
| <b>Nomenclature</b> .....  | <b>ix</b> |
| <b>Chapter 1 - Introduction</b> .....  | <b>1</b>  |
| <b>Chapter 2 - Research aim and scope</b> .....                              | <b>6</b>  |
| <b>Chapter 3 - Review of the literature</b> .....                            | <b>8</b>  |
| 3.1 Influence of operating temperature on the performance of PV modules..... | 8         |
| 3.2 PV/T systems .....   | 10        |
| 3.2.1 Air-based PV/T systems.....  | 10        |
| 3.2.2 Water-based PV/T systems.....  | 12        |
| 3.2.3 PV/T systems with heat pipes .....                                     | 15        |
| 3.2.4 Thermoelectric generator (TEG) combined PV/T systems.....              | 17        |
| 3.2.5 Phase change material (PCM) based PV/T systems .....                   | 18        |
| 3.2.6 Nanofluid-based PV/T systems .....                                     | 20        |
| 3.3 Summary .....  | 21        |
| <b>Chapter 4 - Research methodology</b> .....                                | <b>23</b> |
| <b>Chapter 5 - Thermal model of PV module</b> .....                          | <b>26</b> |
| 5.1 Physical model .....   | 26        |
| 5.2 Optical and radiation model .....  | 27        |
| 5.3 Heat sources .....   | 28        |
| 5.4 Heat conduction equation .....   | 29        |
| 5.5 Boundary conditions .....  | 30        |
| 5.6 Energy balance and finite difference methods .....                       | 32        |
| 5.6.1 Energy balance on bottom and top surface nodes.....                    | 33        |
| 5.6.2 Energy balance on the interior nodes .....                             | 34        |
| 5.6.3 Energy balance on interior interface nodes .....                       | 34        |
| 5.7 Model validation.....  | 35        |
| 5.8 Summary.....   | 38        |

|  |            |
|--|------------|
| <b>Chapter 6 - Design of the cooling system and numerical studies</b> .....    | <b>39</b>  |
| 6.1 Numerical analysis of the initial PV/T design .....                        | 42         |
| 6.2 The enhanced design of the cooling system .....                            | 47         |
| 6.3 Numerical analysis of the final PV/T design .....                          | 48         |
| 6.4 The manufacturing process of the cooling system .....                      | 52         |
| 6.5 Summary .....  | 53         |
| <b>Chapter 7 - The laboratory tests of the designed cooling system</b> .....   | <b>54</b>  |
| 7.1 Thermal tests of the cooling system.....                                   | 54         |
| 7.2 CFD model validation of the cooling system .....                           | 57         |
| 7.3 Thermal tests of the cooling system coupled with the PV module .....       | 61         |
| 7.4 CFD model validation of the cooling system coupled with the PV module..... | 63         |
| 7.5 Uncertainty analysis .....   | 65         |
| 7.6 Summary .....  | 65         |
| <b>Chapter 8 - Outdoor experiments of the designed PV/T module</b> .....       | <b>67</b>  |
| 8.1 The test rig preparation.....  | 67         |
| 8.2 Outdoor experiments .....  | 72         |
| 8.2.1 Outdoor experiments with active chiller .....                            | 72         |
| 8.2.2 Outdoor experiments without an active chiller .....                      | 82         |
| 8.3 Cooling uniformity.....  | 93         |
| 8.4 Pressure drop in the test rig.....   | 94         |
| 8.5 The energy analysis .....  | 95         |
| 8.5.1 Numerical model of the PV/T module .....                                 | 98         |
| 8.5.2 Yearly energy generation .....   | 100        |
| 8.6 The uncertainty analysis .....   | 102        |
| 8.7 Summary .....  | 102        |
| <b>Chapter 9 - Discussion</b> .....  | <b>104</b> |

|  |            |
|--|------------|
| 9.1 Comparison between the proposed PV/T systems in the literature and the designed PV/T system..... | 104        |
| 9.2 Summary.....   | 110        |
| <b>Chapter 10 - The economic analysis of the designed PV/T system .....</b>                          | <b>111</b> |
| 10.1 The cost analysis of the designed PV/T module .....   | 111        |
| 10.2 Economic analysis.....  | 112        |
| 10.3 Case study system definition .....  | 116        |
| 10.3.1 DHW system developed in TRNSYS.....   | 118        |
| 10.3.2 Payback period analysis.....  | 123        |
| 10.4 Summary.....  | 126        |
| <b>Chapter 11 - Conclusions.....</b>   | <b>127</b> |
| <b>Bibliography.....</b>   | <b>131</b> |
| <b>Appendices .....</b>  | <b>139</b> |
| <b>Appendix A.....</b>   | <b>139</b> |
| A.1 Top part.....  | 139        |
| A.2 Left part.....   | 140        |
| A.3 Right part .....   | 140        |
| A.4 Inlet part.....  | 141        |
| A.5 Outlet part .....  | 141        |
| A.6 Bottom part .....  | 142        |
| <b>Appendix B.....</b>   | <b>143</b> |
| B.1 Test results – 15/09/2023 and 16/09/2023 .....   | 143        |
| B.2 Test results – 17/09/2023 and 18/09/2023 .....   | 143        |
| B.3 Test results – 20/09/2023 and 21/09/2023 .....   | 144        |
| B.4 Test results – 22/09/2023 and 02/10/2023 .....   | 144        |
| B.5 Test results – 27/09/2023 and 28/09/2023 .....   | 145        |
| B.6 Test results – 03/10/2023 and 04/10/2023 .....   | 146        |

|   |            |
|---|------------|
| B.7 Test results – 05/10/2023 and 06/10/2023 .....  | 146        |
| B.8 Test results – 07/10/2023 and 11/10/2023 .....  | 147        |
| B.9 Test results – 12/10/2023 and 13/10/2023 .....  | 147        |
| B.10 Test results – 19/10/2023 and 20/10/2023 ..... | 148        |
| B.11 Test results – 21/10/2023 and 24/10/2023 ..... | 148        |
| B.12 Test results – 28/10/2023 and 29/10/2023 ..... | 149        |
| <b>List of Figures .....</b>                        | <b>150</b> |
| <b>List of Tables.....</b>                          | <b>154</b> |



## Nomenclature

### List of Abbreviations

|        |                                    |
|--------|------------------------------------|
| ARC    | Antireflection coating             |
| CFD    | Computational fluid dynamics       |
| DHW    | Domestic hot water                 |
| FD     | Finite difference                  |
| GHG    | Greenhouse gas emissions           |
| LCOE   | Levelized cost of electricity      |
| LCOH   | Levelized cost of heat             |
| LEC    | Levelized energy cost              |
| NOCT   | Nominal operating cell temperature |
| NZEB   | Nearly zero-energy building        |
| OM     | Operation and maintenance          |
| PCM    | Phase change material              |
| PV     | Photovoltaic                       |
| PV/T   | Photovoltaic/thermal modules       |
| RES    | Renewable energy sources           |
| SDHW   | Solar domestic hot water system    |
| ST     | Solar-thermal                      |
| STC    | Standard test conditions           |
| TEG    | Thermoelectric generator           |
| TMY    | Typical meteorological year        |
| TRNSYS | Transient system simulation tool   |
| UDF    | User-defined function              |

### List of Symbols

|               |   |
|---------------|---|
| $A_c$         | The surface area of the PV cell (m <sup>2</sup> )                         |
| $A_{effc}$    | Effective cooling area (m <sup>2</sup> )                                  |
| $A_p$         | The total front surface area of the photovoltaic module (m <sup>2</sup> ) |
| $A_{pv}$      | Total area of the photovoltaic cells (m <sup>2</sup> )                    |
| $c$           | Specific heat capacity (J/kg.K)   |
| $c_{air}$     | Specific heat capacity of the air (J/kg.K)                                |
| $c_{gl}$      | Specific heat capacity of the glass (J/kg.K)                              |
| $c_{eva}$     | Specific heat capacity of the EVA (J/kg.K)                                |
| $c_{pvcells}$ | Specific heat capacity of the PV cells (J/kg.K)                           |

|                    |   |
|--------------------|---|
| $c_f$              | Specific heat capacity of the working fluid in the cooling system (J/kg.K)      |
| $c_R$              | Correction factor for the assumption of the time of presence of occupants       |
| $D_m$              | Number of days in a month   |
| $E_b$              | The energy balance error (%)  |
| $E_T$              | The sum of electrical and thermal energy generation (kWh/y)                     |
| $\dot{E}_g$        | Energy generated within the control volume (W)                                  |
| $\dot{E}_{in}$     | Amount of energy entering the control volume (W)                                |
| $\dot{E}_{st}$     | Energy stored in the control volume (W)   |
| $F_{surface-sink}$ | View factor   |
| $FF$               | Fill factor   |
| $g$                | Gravitational acceleration (m/s <sup>2</sup> )                                  |
| $g_x$              | Gravitational acceleration in x-direction (m/s <sup>2</sup> )                   |
| $g_y$              | Gravitational acceleration in y-direction (m/s <sup>2</sup> )                   |
| $g_z$              | Gravitational acceleration in z-direction (m/s <sup>2</sup> )                   |
| $G$                | Solar irradiation level (W/m <sup>2</sup> )                                     |
| $G_b$              | Beam component of total global horizontal irradiation (W/m <sup>2</sup> )       |
| $G_d$              | Diffuse component total global horizontal irradiation (W/m <sup>2</sup> )       |
| $G_{HOR}$          | Total global horizontal irradiation (W/m <sup>2</sup> )                         |
| $G_{on}$           | Extraterrestrial irradiation (W/m <sup>2</sup> )                                |
| $G_{available}$    | Available solar energy (kWh/m <sup>2</sup> )                                    |
| $Gr$               | Grashof number  |
| $G_{sur}$          | Solar irradiation falling onto the surface of PV modules (W/m <sup>2</sup> )    |
| $H$                | Average heat flux on the surface (W/m <sup>2</sup> )                            |
| $h_{conv}$         | Combined convective heat transfer coefficient (W/m <sup>2</sup> .K)             |
| $h_{conv,forced}$  | Forced convective heat transfer coefficient (W/m <sup>2</sup> .K)               |
| $h_{conv,free}$    | Natural convective heat transfer coefficient (W/m <sup>2</sup> .K)              |
| $h_{rad}$          | Linearized radiative heat transfer coefficient (W/m <sup>2</sup> .K)            |
| $h_{rad,N-ground}$ | Radiative heat transfer coefficient from node N to ground (W/m <sup>2</sup> .K) |
| $h_{rad,N-sky}$    | Radiative heat transfer coefficient from node N to sky (W/m <sup>2</sup> .K)    |
| $I$                | The current output of the PV module (A)   |
| $i$                | Inflation rate (%)  |
| $I_{MP}$           | The maximum current generated by PV cell (A)                                    |
| $I_{SC}$           | Short-circuit current (A)   |
| $k$                | Thermal conductivity (W/m.K)  |
| $k_{air}$          | Thermal conductivity of air (W/m.K)   |

|                    |   |
|--------------------|---|
| $K_C$              | The sum of the capital cost (€)   |
| $k_{eva}$          | Thermal conductivity of EVA (W/m.K)   |
| $k_{gl}$           | Thermal conductivity of glass (W/m.K)   |
| $K_{OM}$           | Present value of the annualized costs of operation and maintenance (€)        |
| $k_{pvcells}$      | Thermal conductivity of PV cells (W/m.K)                                      |
| $k_T$              | Hourly clearness index  |
| $K_{\tau\alpha,b}$ | Incidence angle modifier at the beam incidence angle (deg)                    |
| $K_{\tau\alpha,d}$ | Incidence angle modifier for diffuse radiation (deg)                          |
| $K_{\tau\alpha,g}$ | Incidence angle modifier for ground-reflected radiation (deg)                 |
| $l_{ch}$           | Characteristic length of the photovoltaic module (m)                          |
| $M$                | Air mass modifier   |
| $m_f$              | The mass flow rate of the working fluid in the cooling system (kg/s)          |
| $\dot{m}$          | Mass flow rate (kg/s)   |
| $Nu_{free}$        | Nusselt number  |
| $N_p$              | Number of people  |
| $NPV_Y$            | Net present value (€)   |
| $p$                | Pressure (Pa)   |
| $P$                | Power output (W)  |
| $P_{aux}$          | The monthly electrical energy consumption of the auxiliary heater (kWh/month) |
| $P_{annual}$       | Annual electrical energy production (kWh/y)                                   |
| $P_{cooled}$       | The power output of the cooled PV module (W)                                  |
| $P_{drop}$         | Pressure drop in the PV/T system (kPa)  |
| $P_{net}$          | The monthly total net electrical energy generation (kWh/month)                |
| $P_{non-cooled}$   | The power output of the non-cooled PV module (W)                              |
| $P_{pump}$         | Power consumption of the pump (kWh)   |
| $P_{PV/T}$         | Electrical energy generated by the PV/T module (kWh)                          |
| $Pr$               | Prandtl number  |
| $q$                | Volumetric flow rate in the PV/T module inlet (l/min)                         |
| $Q_{annual}$       | Annual thermal energy production (MWh/y)                                      |
| $Q_{aux}$          | Monthly thermal energy generated by the auxiliary heater (kJ/month)           |
| $Q_{check}$        | Monthly difference in thermal gains and losses (kJ/month)                     |
| $Q_{conv}$         | Convective heat loss (W)  |
| $Q_{DHW}$          | Monthly thermal energy consumed by DHW system (kJ/month)                      |
| $Q_{DHW,monthly}$  | Monthly usable energy for DHW (kWh/month)                                     |

|                      |  |
|----------------------|--|
| $Q_{DHW,yearly}$     | Yearly usable energy for DHW (kWh/y)   |
| $Q_{max}$            | Maximum thermal power output of PV/T modules                                 |
| $Q_{monthly\_gains}$ | The monthly energy gain in the DHW system (kJ/month)                         |
| $Q_{thermal}$        | Thermal energy generation of the PV/T module (kWh/m <sup>2</sup> )           |
| $Q_u$                | Useful thermal energy gain of the cooling system (W)                         |
| $\dot{q}_f$          | The inlet volumetric flow rate (L/h)   |
| $\dot{Q}_g$          | Internal heat generation (W/m <sup>3</sup> )                                 |
| $\dot{Q}_{gl}$       | Internal heat generation in the glass layer (W/m <sup>3</sup> )              |
| $Q_{pipe}$           | Monthly energy lost to the environment from the pipe (kJ/month)              |
| $Q_{pump}$           | Monthly heat transferred to the fluid by pump operation (kJ/month)           |
| $Q_{pump\_loss}$     | Monthly heat transferred from pump to environment (kJ/month)                 |
| $\dot{Q}_{pv}$       | Internal heat generation in the photovoltaic cells layer (W/m <sup>3</sup> ) |
| $Q_{PV/T}$           | Monthly thermal energy generated by the PV/T modules (kJ/month)              |
| $Q_{PV/Ts}$          | Total monthly thermal energy generated by the PV/T modules (kWh/month)       |
| $r$                  | Discount rate for renewable energy systems (%)                               |
| $Ra$                 | Rayleigh number  |
| $R_b$                | The angle of beam radiation on the horizontal and tilted surfaces (deg)      |
| $S$                  | Total absorbed solar irradiation (W/m <sup>2</sup> )                         |
| $T_{amb}$            | Ambient temperature (°C)   |
| $T_{avg-outlet}$     | The monthly average outlet temperature of the PV/T module (°C)               |
| $T_{avg\_fluidom}$   | The average temperature of the fluid domain (°C)                             |
| $T_{avg\_solidom}$   | Average temperature of the solid domain (°C)                                 |
| $T_{bcooled}$        | The back surface temperature of the cooled PV module (°C)                    |
| $T_{bncooled}$       | The back surface temperature of the non-cooled PV module (°C)                |
| $T_{bufferbot}$      | The bottom side temperature of the buffer tank (°C)                          |
| $T_{buffertop}$      | Top side temperature of the buffer tank (°C)                                 |
| $T_c$                | The temperature of the water before heating for DHW (°C)                     |
| $T_{DHW}$            | Design temperature of DHW in the tap (°C)                                    |
| $T_{f,in}$           | The inlet temperature of the working fluid (°C)                              |
| $T_{f,out}$          | Outlet temperature of the working fluid (°C)                                 |
| $T_{in}$             | Inlet temperature (°C)   |
| $T_{npvcells}$       | Average temperature of the PV cells for the non-cooled PV module (°C)        |
| $T_{out}$            | Outlet temperature (°C)  |
| $T_{outlet\_cfd}$    | Outlet temperature obtained from the CFD analysis (°C)                       |

|                            |  |
|----------------------------|--|
| $T_{outlet\_cf\_previous}$ | Outlet temperature from the CFD analysis of the previous design (°C)           |
| $T_{outlet\_exp}$          | Outlet temperature obtained in the experiment (°C)                             |
| $T_{pvcells\_cooled}$      | Average temperature of the PV cells for the cooled PV module (°C)              |
| $T_{red}$                  | Temperature reduction on the back surface of the PV module (°C)                |
| $T_{rear\_cooled}$         | The average temperature of the rear side of the cooled PV module (°C)          |
| $T_{rear\_non-cooled}$     | The average temperature of the rear side of the non-cooled PV module (°C)      |
| $T_{ref}$                  | Reference temperature for PV module (°C)                                       |
| $T_{sink}$                 | Temperature of the sink, ground/sky (K)  |
| $T_{surf}$                 | Surface temperature, °C  |
| $T_0$                      | The optimal operating temperature for PV cells (°C)                            |
| $u$                        | Velocity component at a point x, y, z (m/s)                                    |
| $U_G$                      | Uncertainty in the independent variable, solar irradiation (W/m <sup>2</sup> ) |
| $U_H$                      | Uncertainty in the independent variable, heat flux (W/m <sup>2</sup> )         |
| $U_I$                      | Uncertainty in the independent variable, current (A)                           |
| $U_{net}$                  | Uncertainty in the results of electrical conversion efficiency (%)             |
| $U_{nth}$                  | Uncertainty in the results of thermal efficiency (%)                           |
| $U_{T_{in}}$               | Uncertainty in the independent variable, inlet temperature (°C)                |
| $U_{T_{out}}$              | Uncertainty in the independent variable, outlet temperature (°C)               |
| $U_V$                      | Uncertainty in the independent variable, voltage (V)                           |
| $U_{\dot{m}}$              | Uncertainty in the independent variable, mass flow rate (L/min)                |
| $v$                        | Velocity component at a point x, y, z (m/s)                                    |
| $V$                        | Voltage output of the PV module (V)  |
| $\nu_{air}$                | Kinematic viscosity of the air (m <sup>2</sup> /s)                             |
| $V_{DHW}$                  | Daily DHW usage per person (dm <sup>3</sup> /person/day)                       |
| $V_{gl}$                   | Front glass volume of the photovoltaic module (m <sup>3</sup> )                |
| $V_{in}$                   | Inlet velocity of the working fluid (m/s)                                      |
| $V_{MP}$                   | The maximum voltage generated by PV cell (V)                                   |
| $V_{OC}$                   | Open-circuit voltage (V)   |
| $V_{PV}$                   | The total volume of the photovoltaic cells (m <sup>3</sup> )                   |
| $v_w$                      | Wind speed (m/s)   |
| $w$                        | Velocity component at a point x, y, z (m/s)                                    |

## Greek symbols

|               |   |
|---------------|---|
| $\alpha$      | Thermal diffusivity (m <sup>2</sup> /s) |
| $\alpha_{gl}$ | Absorptivity of glass                   |

|                         |   |
|-------------------------|---|
| $\beta$                 | Surface tilt angle (deg)  |
| $\beta_{air}$           | Coefficient of thermal expansion of air (K <sup>-1</sup> )        |
| $\varepsilon_{surface}$ | The emissivity of the front and back glass                        |
| $\zeta_{ref}$           | Temperature coefficient of the solar cells (K <sup>-1</sup> )     |
| $\eta_{el}$             | Electrical conversion efficiency                                  |
| $\eta_{PV}$             | Electrical conversion efficiency of the photovoltaic cells        |
| $\eta_{pv-cooled}$      | Electrical conversion efficiency of the cooled PV module          |
| $\eta_{pv-non-cooled}$  | Electrical conversion efficiency of the non-cooled PV module      |
| $\eta_{PV,ref}$         | Reference electrical conversion efficiency of photovoltaic module |
| $\eta_{th}$             | Thermal efficiency  |
| $\mu_{air}$             | The viscosity of the air (kg/m.s)                                 |
| $\rho$                  | Density (kg/m <sup>3</sup> )                                      |
| $\rho_{eva}$            | Density of the EVA (kg/m <sup>3</sup> )                           |
| $\rho_g$                | Ground reflectance  |
| $\rho_{gl}$             | The density of the glass (kg/m <sup>3</sup> )                     |
| $\rho_{pvcells}$        | Density of the PV cells (kg/m <sup>3</sup> )                      |
| $(\tau\alpha)_n$        | Transmittance at normal incidence                                 |

### Physical constants

|          |   |
|----------|---|
| $\sigma$ | Stefan-Boltzmann constant (5.6704x10 <sup>-8</sup> W/m <sup>2</sup> .K <sup>4</sup> ) |
|----------|---|

## Chapter 1 - Introduction

The rise in energy prices and the desire to reduce the environmental impact of pollution emitted into the atmosphere encourage researchers and scientists to find solutions to cover the energy demand. The share of renewable energy in energy consumption in the EU was still as low as 22.1% in 2020 [1]. The use of renewable energy has many potential benefits, including a reduction in greenhouse gas emissions (GHGs), the diversification of energy supplies, and a reduced dependency on fossil fuel markets. EU directives require the member states to increase the share of renewable energy sources (RES) in the total energy mix – Directive 2009/28/EC, with a new emission reduction target of 50% by 2030 compared with 2021. The energy demand of the buildings is essential for the European Union's energy efficiency policy, as they account for 40% of total energy consumption. Under Directive 2010/31/EU of the European Parliament and of the Council of 19 May 2010 on the energy performance of buildings, by 31 December 2020, all new buildings should be zero-energy buildings [2]. The nearly zero or very low amount of energy required should be covered to a very significant extent by energy from renewable sources, including energy from renewable sources produced on-site or nearby, taking into account the following:

- decentralized energy supply systems based on energy from renewable sources;
- simultaneous generation in one process of thermal energy and electrical and/or mechanical energy;
- district or block heating or cooling, mainly where it is based entirely or partially on energy from renewable sources;

In 2016, the European Commission [3] recommended 2016/1318 on guidelines for the promotion of nearly zero-energy buildings and best practices to ensure that, by 2020, all new buildings are nearly zero-energy. The document explains the definition of such a building included in the EU Directive 2010/31. The nearly zero-energy building (NZEB) concept reflects that renewable energy and efficiency measures work together. When placed on-building, renewable energy will reduce net delivered energy. In many cases, on-site renewable energy will not be sufficient to bring energy needs close to zero without further energy efficiency measures or a significant decrease in primary energy factors for off-site renewable energy sources. Therefore, higher and more demanding requirements for highly efficient NZEB will also drive increased use of on-building renewables, resulting in the adaptation of primary energy factors for off-site energy carriers, considering their renewable energy content. The framework definition of NZEB in the Directive does not differentiate between new and existing buildings. 'Refurbishment into NZEB' means a refurbishment of a magnitude that allows the

energy performance requirements of an NZEB level to be met. This does not prevent having different timelines and financial support for existing buildings in recognition of the more extended period required for NZEB levels to be cost-optimal in the case of existing buildings. In its recommendations, the European Commission draws attention to the fact that there cannot be a single level of ambition for NZEB across the EU. Flexibility is needed to account for the impact of climatic conditions on heating and cooling needs and the cost-effectiveness of energy efficiency packages and renewable energy source measures.

Numerous negative consequences arise because of the global population and the environmental impacts of GHGs. The change in climate and low air quality are the two most visible effects of GHG. Residential buildings in the world consume a significant fraction of energy. CO<sub>2</sub> emissions from residential buildings reached 10 Gigatons in 2019, representing 28% of global energy-related emissions [4]. In the EU, the building sector consumes 40% of the total energy. Space heating and cooling and domestic hot water preparation represent 55% of the total energy consumption [5]. The EU has taken several initiatives to ensure a clean and fair energy transition across all economic areas.

The Clean Energy for All Europeans package, introduced in 2016, was described as the most ambitious set of proposals in the field of energy. One of the areas that the package covered was to take global leadership in using renewable energy sources, which in practice means achieving a target of 32% renewables by 2030. The second area concerned energy efficiency and aimed to achieve at least 32.5% efficiency in energy use. In particular, the focus is on improving the energy performance of buildings, which account for 40% of final energy consumption and 36% of greenhouse gas emissions in Europe [6]. More than half (55.5%) of the European Union's energy, particularly crude oil and natural gas, was imported in 2021 [7]. EU regulations aimed to reduce energy imports and increase the use of local renewable energy sources. Saving energy by increasing energy efficiency and producing energy from RES is one of the easiest ways to increase energy independence. In 2020, the EU published another new strategy for action called the European Green Deal. The main objective of the plan was to transform the EU into a modern and efficient economy by ensuring:

- by 2050, becoming climate-neutral;
- decoupling economic growth from resource use.

The discussed measures require investment in improving energy efficiency and increasing the share of renewable energy sources. Renewable energy resources become viable solutions at this point as they are primarily pollutant-free and harmless to nature. Thanks to technological progress, harvesting clean energy from renewable energy sources has been developing dynamically.



## Current status of the solar energy systems

Renewable energy sources provided 14.21% of the total world primary energy supply and 19.29% of the EU27 (27 countries) energy supply in 2022. The primary energy consumption of EU27 in 2022 was by source: 6,148.37 TWh – oil, 3,433.64 TWh – gas, 1,938.50 TWh – coal, 1,522.53 TWh – nuclear, 1,096.26 TWh – wind, 721.81 TWh – hydropower, 540.30 TWh – solar, 208.64 TWh – biofuels, 551.05 TWh – other renewables [8]. The share of energy sources in consumption of EU27 energy in 2022 is shown in Figure 1-1.

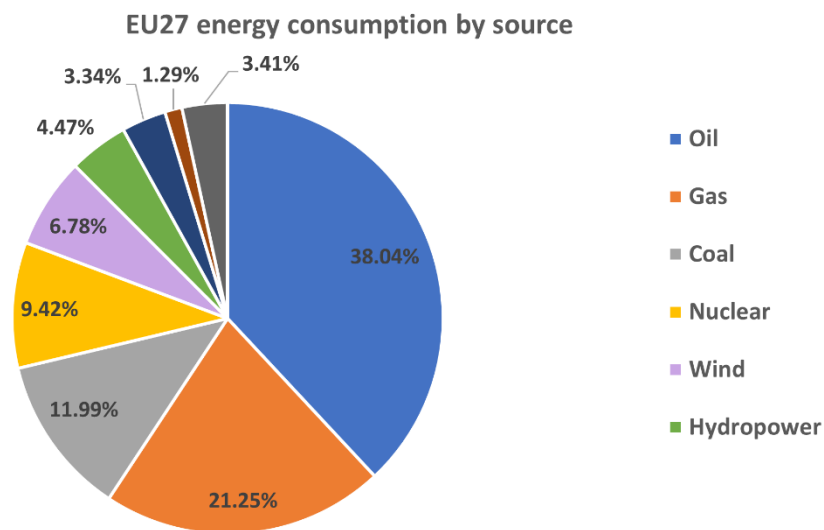


**Figure 1-1. EU27 energy consumption by source**

Solar energy was 3.34% of the total energy consumption in 2022. Compared to 2021, energy consumption by the source of solar energy constituted 2.64% of the total energy consumption. Due to the fast annual growth rate compared to other renewable sources, the solar fraction of the total energy consumption increased the most in 2022.

Solar energy is most often used by photovoltaic (PV) cells that convert direct sunlight radiation to electricity. Over the past 15 years, the cumulative annual growth rate of photovoltaic production has been over 40%, making the photovoltaic industry the fastest-growing industry in the world. The global annual installed capacity of new photovoltaic installations increased from 29.5 GWp in 2012 to 107 GWp in 2018. China (44 GWp) accounted for the largest share of this result, followed by India (9 GWp) and the United States (8 GWp). The total installed photovoltaic capacity worldwide at the end of 2018 was 489 GWp [9]. Between 2010 and 2021, the PV capacity grew 21 times, with 862 GW cumulative installed PV capacity worldwide by the end of 2021. The global cumulative installed PV capacity amounted to 1.05 GW, with roughly 191 GW of new solar PV capacity installed in 2022.

Poland's cumulative yearly photovoltaic (PV) installation capacity is shown in Figure 1-2.

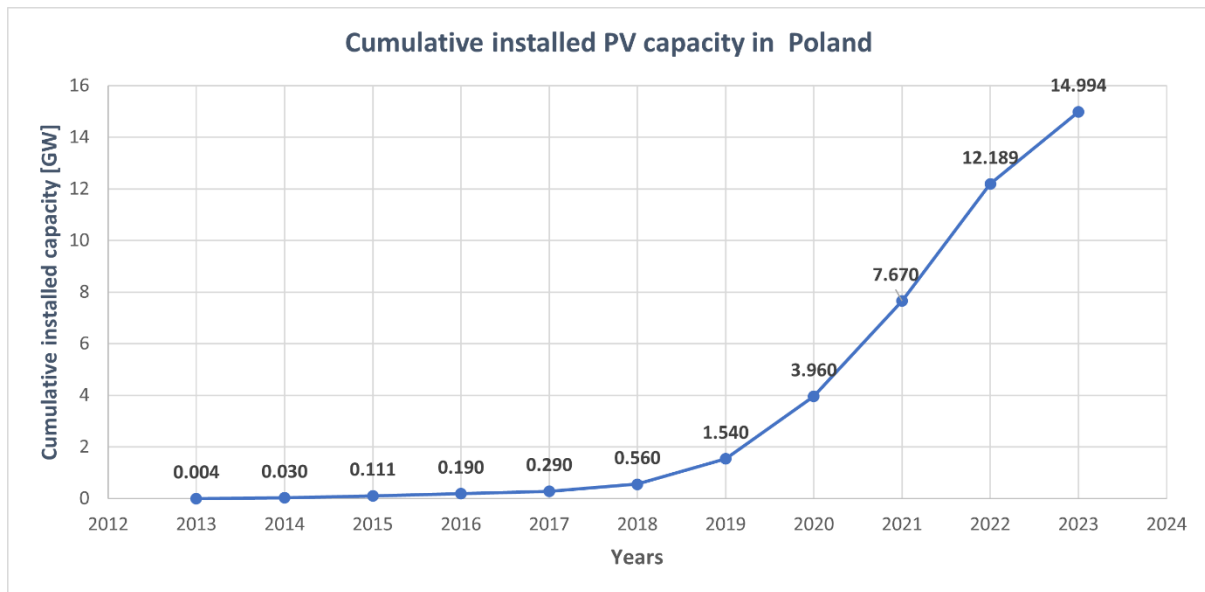


**Figure 1-2 PV installation capacity of Poland during the years [10]**

The increased interest in photovoltaic technology in recent years was mainly due to decreased prices of PV modules. The average installed cost of a PV system was 823.44 €/kW in 2022, 82.90% lower than in 2010 and 4.47% lower than in 2021 [11], as illustrated in Figure 1-3.

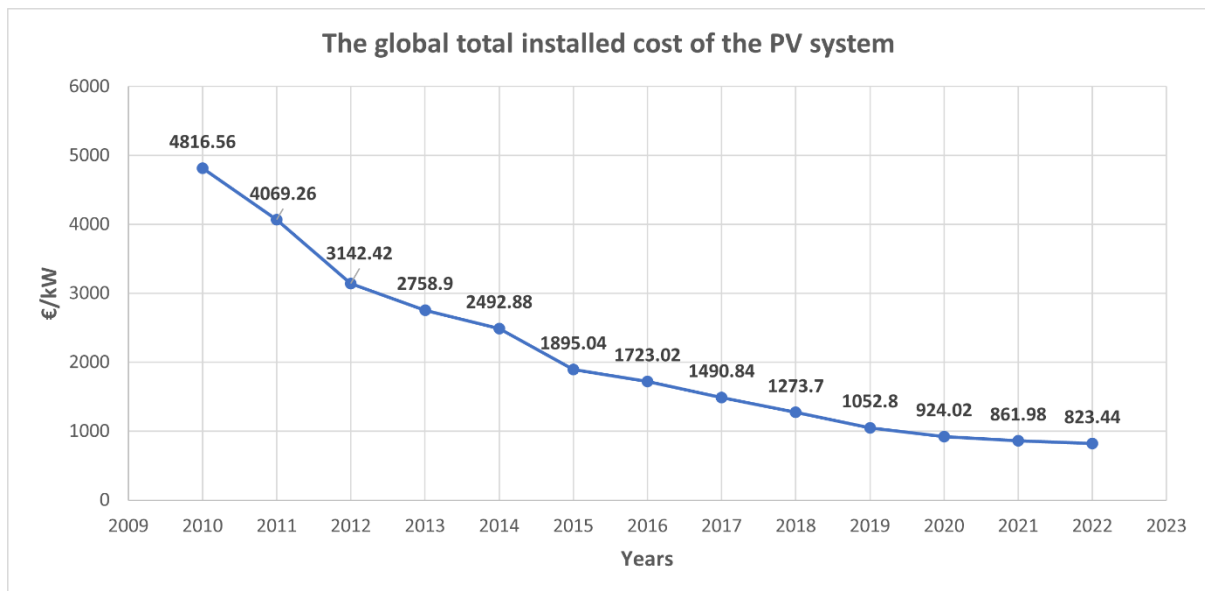


**Figure 1-3 The global total installed cost of the PV system**

The levelized cost of electricity (LCOE) obtained from photovoltaics in 2010 was 0.418 €/kilowatt hour (kWh), while in 2022, it decreased to 0.046 €/kWh, indicating an 88.99% decline, as shown in Figure 1-4.

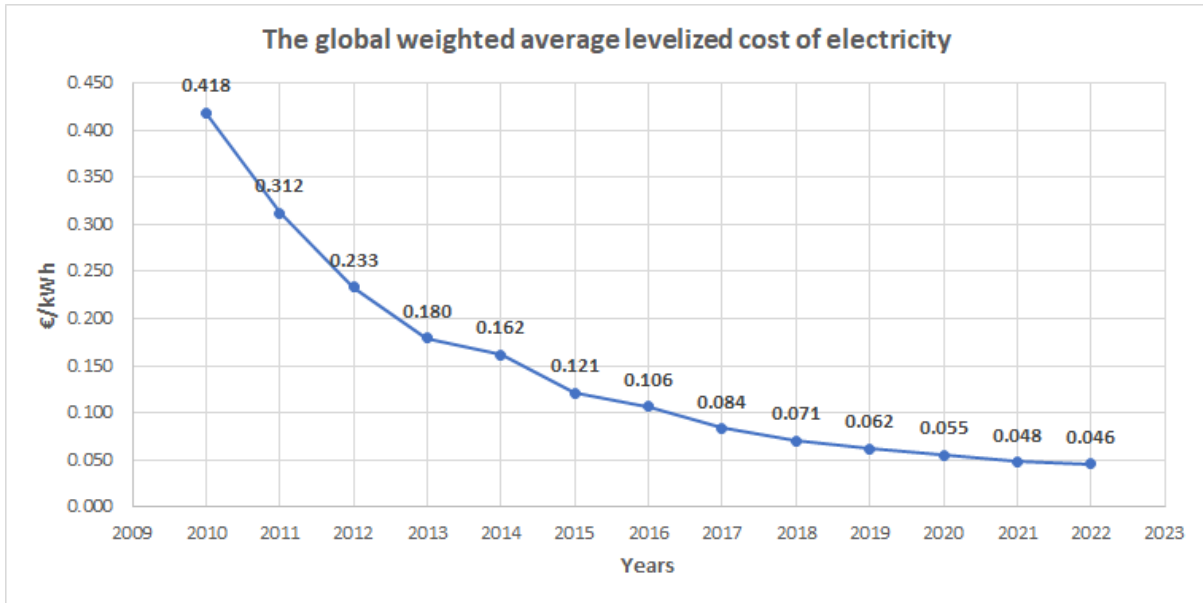


**Figure 1-4 The global weighted average levelized cost of electricity**

In 2009, the Ministry of Economy of Poland published a document entitled “Energy Policy of Poland until 2030” describing Poland’s energy policy directions. The record indicated that one of the directions is the development of the use of RES [12]. However, attention was given to biomass, followed by wind, hydroelectric, geothermal, and, at the very end, solar energy due to technology lag in solar energy and PV systems. In 2020, The Ministry of Climate submitted an updated version of the energy policy of Poland underlining a minimum share of 32% of RES in electricity production through photovoltaics and wind [13].

The recent actions taken by the Polish government, the development of the technology in RES, the adverse effects of GHG and RES subsidies, the “my electricity” subsidy in 2019, and the launch of auction systems led to the rapid growth of PV in Poland over the years. Other effects of the rapid growth of interest in PV systems were due to the continuous improvement and development of PV technology.

On the 2<sup>nd</sup> of February 2021, the Ministry of Climate and Environment of Poland adopted Poland’s energy policy until 2040 [14]. One of the key energy transition topics was adopting zero-emission energy systems. The expectation is that in 20 years, reaching an almost new electricity system and, by 2040, withdrawing a large amount of coal-fired capacity from the national energy system. The policy also stated that there will be a significant increase in installed capacity in PVs. Approximately 5-7 GW increase of installed capacity by 2030 and 10-16 GW by 2040.

## Chapter 2 - Research aim and scope

Acknowledging the current thresholds of maximum thermal efficiency achieved by the PV/T modules proposed in the literature and commercially available PV/T modules, typically hovering between 30% and 85%, this doctoral research stated and aimed to break new ground. Through designing an innovative cooling system and taking advantage of water as a working fluid, the designed PV/T module aspires to outperform existing PV/T systems. The thesis hypothesized that the designed PV/T module will exceed 90% thermal efficiency. The envisioned outcomes aimed to introduce a transformative and groundbreaking solution for PV/T technology. The core idea was to invent a highly efficient, compact, cost-effective water-based PV/T system that redefines industry expectations. While achieving the water-based PV/T system, the scope of the research has been:

- Numerical modeling of a PV module to analyze the thermal behavior of PV module and temperature effects on electrical conversion efficiency and power output.
- Designing a highly efficient cooling system for PV/T modules by considering the thermal behavior of PV modules and recent developments in PV/T technology.
- Conducting laboratory and outdoor experiments on the manufactured prototype to assess the effectiveness of the designed PV/T system by evaluating the performance metrics such as electrical and thermal efficiency;
- Carrying out a comparative study between the developed PV/T module in this dissertation and existing state-of-the-art PV/T systems proposed in the literature.
- Conducting a techno-economic analysis in a comparative manner with available PV/T systems in the market to determine the viability and potential for commercial implementation.

In order to invent a highly efficient, compact, cost-effective water-based PV/T system within the scope of the study, the objectives of this dissertation have been as follows:

- Identifying the adverse effects of the temperature on PV modules and conducting a comprehensive literature review on PV/T systems to analyze the design considerations and limitations of the proposed PV/T systems.
- Developing a numerical thermal model of a PV module to analyze the influence of temperature effects on electrical power output and efficiency of PV modules. Use of the numerical model to estimate the electrical power output and efficiency of the designed PV/T module before manufacturing and conducting outdoor experiments.
- Designing a cooling system and conducting 3-D numerical analysis. Manufacturing the cooling system and conducting thermal tests in the laboratory.

- Carrying out outdoor experiments and conducting an energy analysis to estimate the yearly electrical and thermal energy generation of the designed PV/T module.
- Realization of a comprehensive comparative analysis of the designed PV/T system with the existing systems in the literature.
- A comparative techno-economic assessment to analyze the economic performance of the designed PV/T module, along with available PV/T modules in the market.
- Designing and implementing a case study based on domestic hot water demand coverage of a single-family house using the designed PV/T module.

### **Structure of the thesis**

The introduction section starts with bringing the latest policies and regulations of the EU on green energy transition based on renewable energy systems. The chapter discusses the concept of NZEB and the future goals of the EU on energy transition. The current status of solar energy systems and the share of solar energy in renewable energy generation in the EU are detailed. The cost of PV energy per kW over the years, the cumulative installed capacity of PV systems in Poland, and the policies of the Ministry of Climate and Environment of Poland are presented at the end of chapter one. The aim and scope of the dissertation are explained in detail, along with the objectives to achieve the aim of the research in chapter two. Chapter three briefly provides the influence of temperature on the electrical conversion efficiency and power output of PV modules. The chapter extends with the state-of-the-art PV/T technologies in the literature. The drawbacks of the proposed PV/T technologies are highlighted in this chapter. The research methodology employed while designing a highly efficient cooling system and developing a PV/T module is explained in chapter four. The thermal modeling of a PV module to determine the effects of temperature on PV modules is realized and presented in chapter five. The steps taken for designing a cooling system for PV modules, procedures of numerical studies on initial and final designs, along the manufacturing process of the final design are presented in chapter six. The laboratory tests conducted on the cooling system and PV/T module are presented in chapter seven. The outdoor experiments, along with the analysis of cooling uniformity, pressure drop, and yearly energy generation of the designed PV/T module, are presented in chapter eight. A comparative study of existing literature with the designed PV/T module is presented in chapter nine. A techno-economic analysis of the designed PV/T module is presented comparatively with PV/T modules available in the Polish market in chapter ten. A case study is conducted to cover the domestic hot water demand of a single-family house with the PV/T module and a conventional gas boiler system. The conclusions related to the objectives and scope of the dissertation are presented in chapter eleven.

## Chapter 3 - Review of the literature

This chapter presents the influence of temperature on the electrical power output and lifetime of PV cells. The chapter continues with a critical review of relevant research work on PV/T systems and provides an in-depth understanding of the various proposed systems in the literature. The performance of the various PV/T systems was reviewed to determine key points in designing a cooling system for PV modules. The extensive literature review provided in this chapter endeavors to convey a better understanding of current state-of-the-art PV/T technologies.

### 3.1 Influence of operating temperature on the performance of PV modules

The PV cells operate best at low temperatures as other semiconductor devices. Higher operating temperatures shift the properties of semiconductors, subsequently resulting in a slight increase in current; however, more considerable decreases in voltage in PV cells. Almost 80% of the absorbed solar radiation is turned into heat in PV cells, causing higher operating temperatures and consequently decreasing electrical conversion efficiency and power output. The electrical conversion efficiency ( $\eta_{el}$ ) is the percentage of power converted from solar irradiation to electricity by PV cells. The efficiency of the PV cell is determined as given in Eq. 1.

$$\eta_{el} = \frac{V_{OC}I_{SC}FF}{GA_c}, \quad (1)$$

where  $V_{OC}$ ,  $I_{SC}$ , and  $FF$  are the open-circuit voltage, short-circuit current, and fill factor of the solar cell, respectively.  $G$  stands for the solar irradiation level falling on the cell and  $A_c$  is the surface area of the cell. The fill factor determines the maximum power from a PV cell and can be calculated using Eq. 2.

$$FF = \frac{V_{MP}I_{MP}}{V_{OC}I_{SC}}, \quad (2)$$

The power output of photovoltaic cells is greatly influenced by the rise in operating temperature. The PV modules operate mainly above the ambient temperature owing to the thermal energy of solar irradiation from the sun. Mounting configuration, solar irradiation, wind speed, and ambient temperature are the factors that affect the operating temperature.

The operating temperature of the PV module affects the most the open-circuit voltage. The open-circuit voltage is adversely affected by the increase in temperature of PV cells. In contrast, the short-circuit current slightly increases with the higher operating temperature of the PV module. The change in short-circuit current with temperature is smaller than the change

in open-circuit voltage, as shown in Figure 3-1, causing the drop in power output of the PV cells.

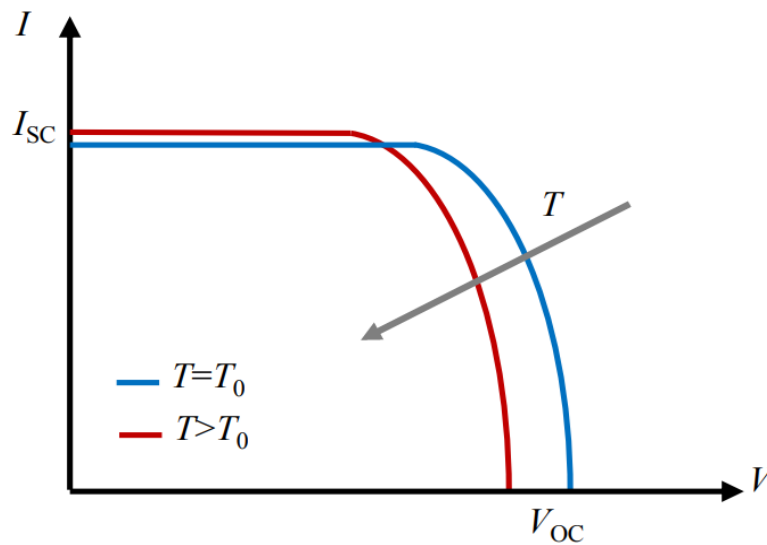


**Figure 3-1. The temperature effect on open-circuit voltage and short-circuit current**

In Figure 3-1, the  $T_0$  temperature is 25 °C; when the temperature of PV cells rises over the  $T_0$  temperature, a slight increase in  $I_{sc}$  and a drastic drop in  $V_{oc}$  can be seen. Every one degree increase over 25°C in PV cell temperature causes a drop in the power output of the PV modules. The temperature coefficient of power of PV modules ranges between 0.11% and 0.63% based on the type of PV cells used [15].

In addition to the adverse effects of temperature on electrical conversion efficiency and power output, the high operating temperature of the PV modules causes degradation in PV cells. Koehl et al. [16] conducted accelerated damp-heat testing on commercially available PV modules. Experimental tests were conducted by exposing PV modules to 75 °C, 85 °C and 90°C. The degradation in a chosen PV cell due to thermal stress was observed during the experiments, as shown in Figure 3-2.

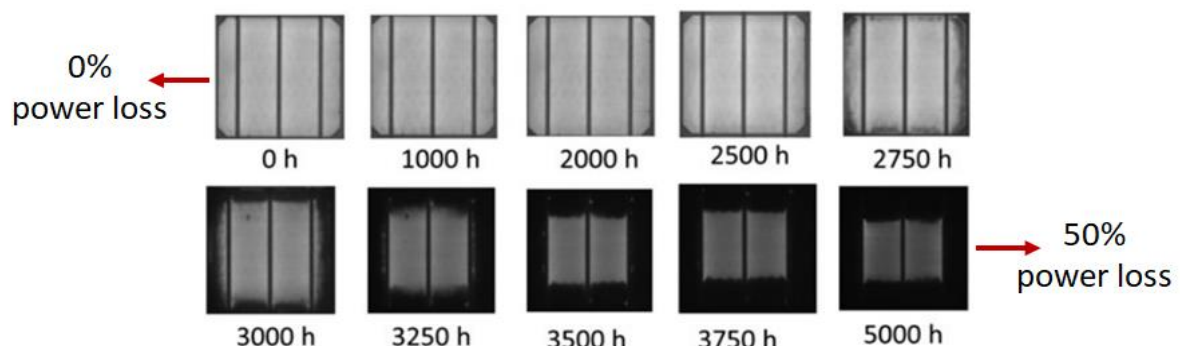


**Figure 3-2. Electroluminescence pictures of a PV cell at different times during damp-heat testing at 85 °C [16]**

In the study, the time of failure of PV modules was chosen as the 20% power loss. Testing at 85 °C was realized for 5000 h, and results showed that more than 20% of power losses occurred before 4000 h. One of the PV modules tested lost 90% of its initial power at the end of the test. The results showed that for this PV module, the PV cells lost 50% of their capacity. The damp-heat testings at 75 °C and 90 °C led to similar results, as shown in Figure 3-2. However, the test durations were 3250 h and 8500 h for the tests conducted at 90 °C and 75 °C, respectively. The failure time (20% power loss) was 5000 h for most PV modules at 75 °C.

The negative effects of temperature on electrical power output and degradation of PV modules showed that cooling PV modules could eliminate the adverse effects of temperature by reducing the operating temperature. Cooling of the PV modules is realized by combining a PV module with a cooling system to reduce the operating temperature for harvesting the maximum available electrical energy from the PV cells. The heat dissipated by the PV module can be extracted during the cooling procedure according to the design type of the photovoltaic/thermal system.

### **3.2 PV/T systems**

Photovoltaic/thermal systems drew huge attention from researchers and academics due to their ability to convert solar energy into electrical and thermal energy simultaneously. The dual energy generation capability using a single PV module minimizes the issue of space availability compared to stand-alone PV modules and solar thermal collectors. Numerous PV/T system designs and working fluids have been proposed in the literature to harvest the waste heat from PV modules and minimize the adverse effects of temperature, starting from the 1970s. [17]. The state-of-the-art PV/T systems reviewed in this section are as follows:

- Air-based PV/T systems,
- Water-based PV/T systems,
- PV/T systems with heat pipes,
- Thermoelectric generator combined PV/T systems,
- Phase change material based PV/T systems,
- Nanofluid-based PV/T systems.

#### **3.2.1 Air-based PV/T systems**

In air-based PV/T systems, the air is used as heat transfer fluid from the PV module. The cooling is achieved using a single or double pass with active or passive mode. The passive cooling mode uses natural convection and heat conduction to remove the excess heat from the PV module, whereas, in active cooling mode, a fan or blower is used to force the air to



flow in the thermal collector of the PV/T system. Air-preheating, drying, space heating, and ventilation are the main application areas of air-based PV/T systems.

In air-based PV/T systems, Cetina-Quiñones et al. [18] conducted a two-phase study on an air-based photovoltaic thermal (PV/T) system; a numerical and parametric analysis was conducted in the first phase. Different exergetic, energetic, and environmental analyses were realized in the second phase. In the numerical analysis, various shapes of fins were studied to cool down the PV module. The authors concluded that wavy fins were proved to be best on the basis of outlet air and PV module temperatures. The overall thermal efficiency of 33.02% was achieved. Saygin et al. [19] designed a modified air-based PV/T system. The designed system was investigated experimentally in Istanbul, Turkey. In this system, the air flows over and below the PV module in opposite directions to remove the excess heat, as shown in Figure 3-3. The distance of the PV module inside the collector was varied from 3 cm to 7 cm to the collector to analyze the performance of the system. A fan was used to circulate the air in the system. Different cooling system configurations were tested, and results showed that the highest thermal efficiency of 56.41% was obtained when the distance between the PV module and the cooling system was 3 cm.

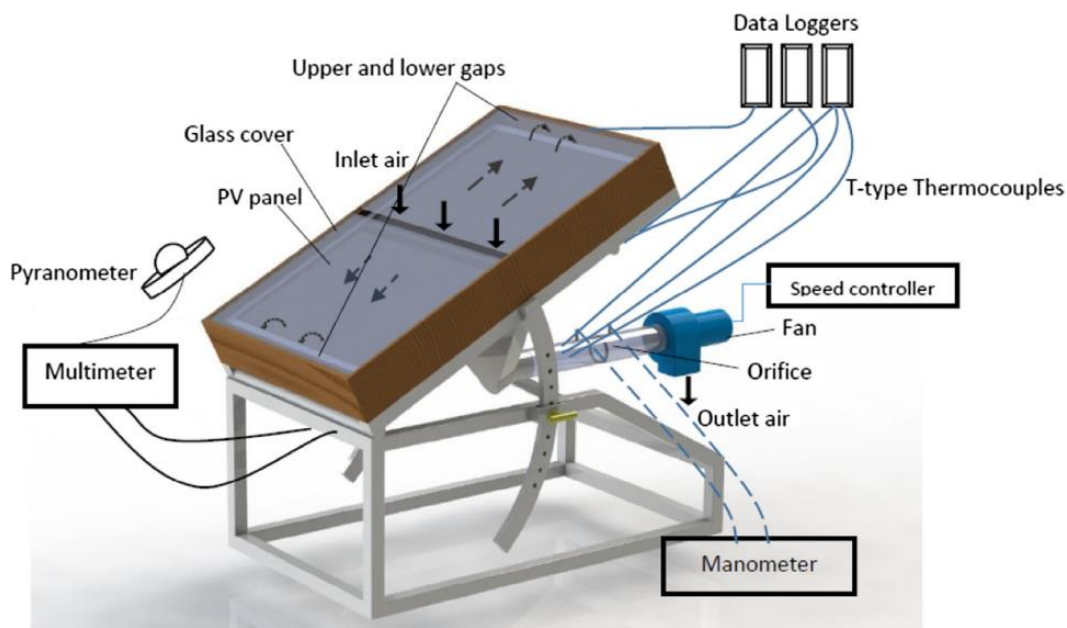


**Figure 3-3. Schematic diagram of an air-based PV/T system [19]**

Sarhaddi et al. [20] developed a numerical model of an air-based PV/T collector to estimate the thermal and electrical parameters, including PV cell temperature, rear side temperature, and outlet air temperature of a typical PV/T air collector. The results show that the thermal and electrical efficiency of the investigated air-based PV/T system was 17.18% and 10.01%, respectively. Ozakin and Kaya [21] investigated an air-cooled PV/T system. An air channel

was prepared to circulate the forced air under the PV module. An experiment stand was prepared for the tests, and a theoretical model was developed using commercial software. The thermal efficiency of the air channel system was found to be between 33% and 35%. Teo et al. [22] presented a study of a cooling PV panel where fins attached to a duct that is placed under the panel, and a direct current and alternative current blower were used to enhance heat transfer. The results showed that the temperature of the non-cooled panel was as high as 68 °C, and the electrical efficiency dropped to 8.6%. An operating temperature of the module at 38 °C was achieved by taking advantage of using a blower and maintaining the electrical conversion efficiency of 12.5%. In the experiment, an airflow rate of 0.055 kg/s was used and found to be sufficient to absorb the maximum amount of heat from the PV panel.

The literature review on air-based PV/T systems showed that the general framework efficiency (electrical plus thermal) ranged from 20% to 60% due to the low heat capacity of the working fluid. These values were rarely surpassed in proposed air-based PV/T systems. The low heat capacity of air led to the removal of a limited amount of heat from the PV module. The increased flow rate of air to enhance thermal efficiency in these systems resulted in higher electricity consumption due to the increased fan operation.

### **3.2.2 Water-based PV/T systems**

Water is one of the most commonly used working fluids in PV/T systems due to its availability, low price, high heat transfer coefficient, and specific heat capacity. Water-based PV/T systems are one of the active cooling types. A pump is often used to circulate the water through the cooling system to cool down the PV module. The waste heat recovered from the PV/T system is utilized in many applications, such as heat pumps and space heating. Other areas where thermal energy is utilized are swimming pool heating, low-temperature thermal desalination, and domestic hot water heating.

In water-based PV/T systems, Hussein [23] conducted research on a water-based PV/T system in Oman. In the experiment, two 100 W PV modules were used, and a water-based cooling system was placed on one PV panel. A rectangular absorber shape with a direct flow configuration was designed and placed on the rear side of the PV module. The electrical performance of the water-based PV/T and conventional PV modules was compared. The author found that the average power of the PV/T system was 6% higher than the conventional one. Shalaby et al. [24] investigated the influence of back surface cooling on the electrical efficiency of PV modules experimentally. Two identical 250 W PV modules were tested simultaneously, while one had the rear surface cooling system attached. The cooling system was created using fifteen PVC tubes of half circular cross sections of 0.0381 m diameter. The test results showed that the power generation of the cooled PV module was improved by 14%.

Gomaa et al. [25] designed a water-based cross-fined cooling system for PV systems and numerically analyzed the system using commercial software. Two different configurations, thin and thick cross-fined constructions, 3 mm and 15 mm, respectively, were studied. A 300 W PV module was modeled, and the cooling system was attached to the rear side. Different solar irradiation levels and flow rates were investigated. The numerical analysis showed that when the PV/T system was subjected to intense solar irradiation, such as  $1,000 \text{ W/m}^2$ , optimal cooling was possible for both thin and thick cooling systems with a flow rate of 3 liters per minute (L/min). Ocloń et al. [26] proposed a PV/T system consisting of sheet and U-tube type segments and a water-glycol mixture as a working fluid. Numerical and experimental analyses were conducted using a 280 W PV module. The effects of the number of segments and different mass flow rates were investigated. The results showed that the cooling system with six segments (12 U-tubes) was optimal for the proposed PV/T system. Zhang et al. [27] investigated a spray-cooling integrated PV/T system with different nozzle heights, installation angles, water pressure, and ambient conditions. The optimal configuration of the systems led to a  $12.31 \text{ }^\circ\text{C}$  reduction in PV cell temperature and an increment of 1.10% of electrical conversion efficiency under  $800 \text{ W/m}^2$  solar radiation and an ambient temperature of  $35 \text{ }^\circ\text{C}$ .

Salman et al. [28] proposed a water-based thermal collector to enhance the performance of PV modules. The paper studied the effects of solar radiation, porosity, and mass flow rate on the average temperature of the proposed PV/T system numerically and experimentally using water as the working fluid. The results showed that the cooling system with a porosity of 0.53 and flow rate of  $0.0166 \text{ kg/s}$  exhibited the optimum behavior while reducing the surface temperature of the PV module by  $10 \text{ }^\circ\text{C}$ .

Erdogan et al. [29] studied a water film cooling design implemented on the upper surface of a PV module to minimize the negative effects of temperature experimentally. Two PV modules with a maximum power output of 270 W were used to demonstrate the effectiveness of the cooling system. The experiments were conducted for three days between 11.30 a.m. and 2.30 p.m. A 9.51% average power output increase and 13.69% enhancement of electrical conversion efficiency were achieved.

Nižetić et al. [30] proposed an alternative cooling system using ten water nozzles placed on the rear side and ten nozzles on the upper side of the PV module, as shown in Figure 3-4. The cooling system was tested in outdoor conditions of the Mediterranean climate in June between 11 a.m. and 2 p.m. The solar irradiation level ranged from  $810 \text{ W/m}^2$  to  $850 \text{ W/m}^2$ , and the surrounding air temperature varied between  $27 \text{ }^\circ\text{C}$  and  $30 \text{ }^\circ\text{C}$ . The effects of flow rate on the temperature of the PV module were analyzed. The electrical power output and

conversion efficiency were enhanced by 16.3% and 14.1%, respectively, compared to the non-cooled PV module.

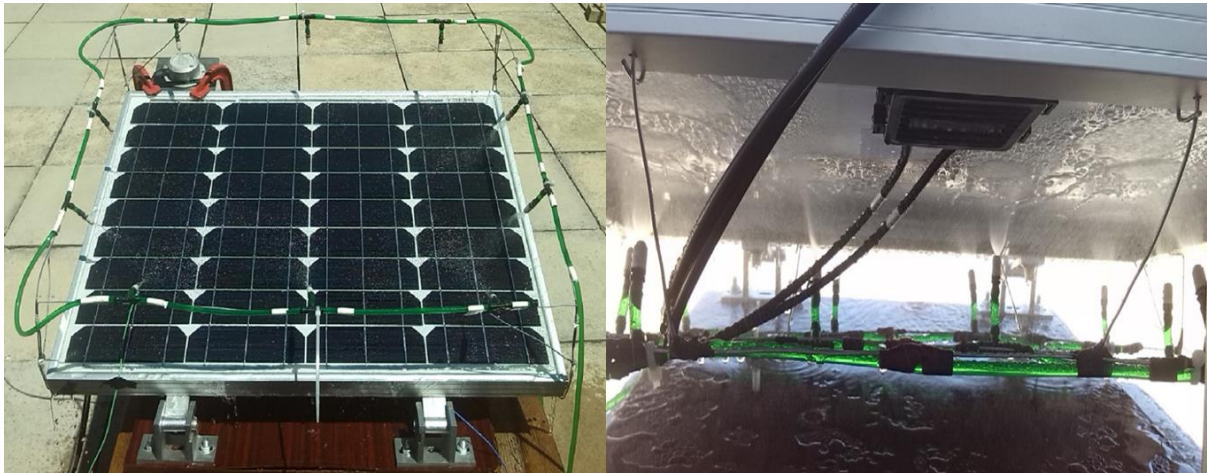


**Figure 3-4. Water-based PV/T system [30]**

Herrando et al. [31] numerically analyzed an uncovered water-based PV/T system with a roll-bonded thermal collector. The fluid flow and energy analysis were conducted on a developed detailed computational fluid dynamic (CFD) model. The acquired numerical results were compared to experimental test results obtained from the PV/T system manufacturer. The maximum electrical conversion efficiency of 14.5% was achieved. The comparison of the thermal efficiency between the CFD model and experimental results showed a maximum of 6.5% error. Abdullah et al. [32] designed a dual oscillating absorber copper pipe flow combined with a PV module, creating a water-based PV/T system. The developed system was studied theoretically, and data collected from simulation results were validated with indoor experiments. The system's electrical, thermal, and combined efficiency was measured under different solar radiation levels and mass flow rates. The maximum electrical efficiency of 8.23% and thermal efficiency of 58.64% were achieved with a volumetric flow rate of 5 L/min under the solar irradiation level of  $1,000 \text{ W/m}^2$ .

The water-based PV/T systems in the literature are considered the most efficient type of PV/T technology. Due to significant attention received from water-based PV/T systems, numerous materials and geometries were proposed. The designed PV/T systems primarily consist of a sheet-and-tube absorber placed on the rear side of the PV module. The working fluid was circulated via forced convection through the pipes. Various flow designs such as serpentine, web-flow, parallel pipes, and spiral shapes were proposed; however, the most used configuration was the parallel pipes. The literature review showed that copper was the most widely used material due to its high thermal conductivity. The thermal efficiency of the water-based PV/T systems in the literature varied between 30% to 85%.

### 3.2.3 PV/T systems with heat pipes

Heat pipes are widely used, highly efficient heat transfer devices that enable heat transportation. Heat pipes are also called thermal superconductors due to their high thermal conductivity and ability to transfer heat even in small temperature gradients. One of the advantages of heat pipes is that they do not consume energy. No moving part exists in heat pipes, allowing them preferable heat transfer devices. A typical heat pipe structure is an evacuated tube partially filled with a working fluid. Inside the heat pipe, the working fluid exists in liquid and vapor phases. One side of the heat pipe is an evaporator, which absorbs heat and evaporates the working fluid. Then, the working fluid, in the form of vapor, condenses and releases heat at the condenser side of the heat pipe. The phase transition allows for high heat transfer.

In PV modules coupled with heat pipes for cooling, Gang et al. [33] proposed a PV/T system with heat pipes and investigated the thermal efficiency and electrical conversion efficiency of the PV cells experimentally. The experimental data was used to validate the dynamic numerical model of the system. The effects of various parameters on cooling efficiency, such as flow rate, tube spaces of heat pipes, and the number of heat pipes, were analyzed. During the experiments, an average electrical conversion efficiency of 10.2% and thermal efficiency of 45.7% were achieved under  $590 \text{ W/m}^2$ . The results showed that when the tube space of heat pipes was reduced, the thermal and electrical energy generation was enhanced. Zhang et al. [34] conducted a numerical, experimental, and design sensitivity analysis for a heat pipe PV/T system. The paper investigated wickless gravity-assisted four heat pipes coupled with a PV module. An aluminum plate was placed at the rear side of the PV module, and the evaporator section of the heat pipe was welded to the plate, whereas the condenser part of the heat pipe was inserted in the water header. Water was circulated through the condenser side of the heat pipes, as shown in Figure 3-5. A deviation of 4.5% occurred between the experimental results and the transient numerical model of the system. Various parameters affecting thermal and electrical energy efficiency were investigated based on the validated numerical model. The results indicated that the electrical and thermal energy efficiencies increased with the increase of water mass flow rate and the diameter of the condenser section of the heat pipe. The numerical results concluded that a maximum thermal efficiency of 47.96% and a maximum electrical conversion efficiency of 10.13% could be achieved using the proposed PV/T system.

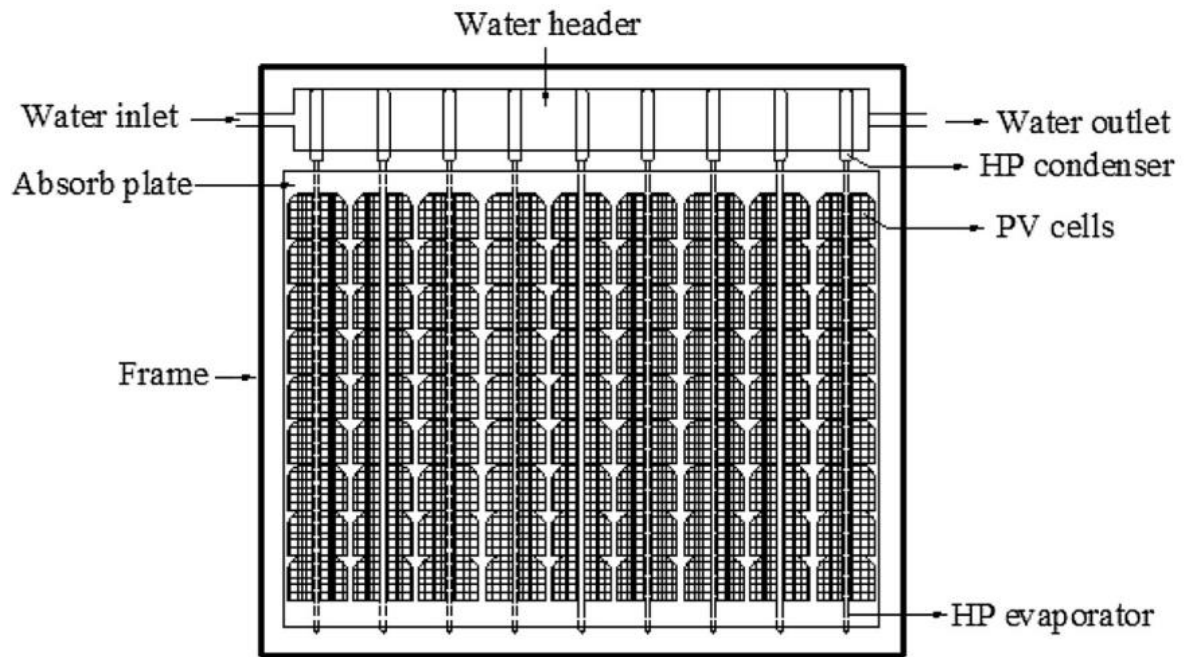


**Figure 3-5. The front view of the heat pipe employed PV/T system [34]**

Hou et al. [35] proposed a PV/T system with a micro heat pipe array. An experimental and numerical study was conducted. A seasonal experiments approach was used, and the data was collected annually. The results showed that the thermal efficiency of the proposed system could reach up to 40%, whereas the electrical conversion efficiency was approximately stable at 13%. Moradgholi et al. [36] employed a heat pipe structure at the rear side of the PV module and constituted a PV/T system. Methanol was used as a working fluid in twelve heat pipes, which have a length of 35 cm and a diameter of 8 mm. The water was used to cool the working fluid in the condenser side of the heat pipes. The set of experiments was conducted during spring and early summer. The results showed that the PV module temperature could be reduced up to 15 °C while 15.3% and 44.38% higher efficiency (including thermal efficiency) were achieved during spring and summer, respectively, compared to the stand-alone photovoltaic system. Modjinou et al. [37] designed a PV/T system with micro-channel heat pipes and crystalline silicon PV modules. The acetone was used as a working fluid in heat pipes. The study was conducted experimentally, and a numerical model was created using MATLAB software to predict the transient behavior of the proposed PV/T system. A maximum thermal efficiency of 54.0% and a maximum electrical conversion efficiency of 7.6% were achieved.

Microchannel flat heat pipes and cylindrical heat pipes were the most used types in PV/T systems. The literature review showed that this type of PV/T technology is still undeveloped due to less attention received and low thermal efficiency. In most cases, the establishment of heat-pipe combined PV/T systems was not clearly explained. The non-uniform cooling of the

PV module was another drawback of this technology. The reviewed studies showed that the thermal efficiency did not exceed 60% in this PV/T technology.

### **3.2.4 Thermoelectric generator (TEG) combined PV/T systems**

Thermoelectric generators are devices that directly convert a temperature gradient into electrical energy through a phenomenon called the Peltier effect. The temperature difference between the hot and cold junctions formed by alloys allows for generating potential between junctions. The use of TEGs in PV/T systems increases energy yield by 1-10%, depending on configuration and TEG material.

In TEG-combined PV/T systems, Lin et al. [38] conducted a performance analysis of a PV/T system consisting of a PV module, a TEG module, and a heat sink. In the model, the hot side of the TEG was connected to the rear side of the PV module, and the cold side was connected to the heat sink to create a temperature gradient. The numerical results showed that the maximum efficiency of the PV/T system could reach up to 13%. The created model allows one to conduct a theoretical study on the performance characteristics of a TEG-combined PV/T system. Babu and Ponnambalam [39] developed a hybrid PV system using thermoelectric generators (TEGs). The excess heat produced by the PV module was utilized to generate electricity using TEGs. A numerical analysis was conducted on flat plate PV-TEG configuration, and the results showed that the energy production was improved by 5% and the overall efficiency was enhanced by 6%. Fini et al. [40] proposed a PV/T system consisting of TEGs and water-cooled heat exchangers. The designed system was studied numerically and validated by conducting experimental research. The average system temperature was measured as 44.2 °C at maximum irradiation and compared to the conventional system, which was at 57.1 °C. Maleki et al. [41] established a test stand including a hybrid TEG-PCM-based PV/T system with metallic heat transfer enhancers to compare it to a TEG-based PV/T system experimentally. In the proposed system, TEGs were used to generate electricity by taking advantage of the temperature gradient, and PCM was used to minimize the adverse effects of temperature on the PV module. The results showed that the average electrical efficiency of the system was 8.1% higher than the PV/T-TEG system. Gopinath and Marimuthu [42] experimentally investigated the different heat dissipators in TEG-combined PV/T system under various solar irradiation levels. In the experiments, 40 in-series TEGs are attached at the rear side of a 12 W polycrystalline PV module, as shown in Figure 3-6. Under three irradiation levels, 516 W/m<sup>2</sup>, 704 W/m<sup>2</sup>, and 823 W/m<sup>2</sup>, colloidal graphite, and aluminum were tested as cold-side heat sinks. The use of graphite sheets improved the TEG voltage 0.75 times and increased the temperature gradient between hot and cold sides up to 3.92 °C

compared to TEG alone under  $823 \text{ W/m}^2$ . In contrast, using aluminum as a heat sink enhanced the TEG voltage 1.78 times and increased the temperature difference up to  $5.96 \text{ }^\circ\text{C}$ .



**Figure 3-6. TEG combined PV/T system [42]**

The main drawback of the TEG combined PV/T system was the economic feasibility due to the material cost of TEGs. Most studies focused on small-scale (from 10 W to 50 W PV modules) experiments. The non-stable temperature of PV/T modules affecting the temperature gradient, causing impacts on the efficiency of TEGs, was another drawback of this technology.

### **3.2.5 Phase change material (PCM) based PV/T systems**

Phase change materials are used to eliminate the adverse effects of temperature on PV modules and improve performance. Many researchers suggest taking advantage of phase change by absorbing or releasing heat, as the PCMs have high latent heat storage capabilities. The PCM-based PV/T systems can further be enhanced by water or air cooling. The PCM-based PV/T systems are designed considering the design temperature range, specific heat capacity, thermal conductivity, and chemical properties of the PCM material.

Nizetic et al. [43] investigated and tested experimentally various PV/T systems incorporating with PCMs in an extensive review paper. The analyzed PV/T-PCM systems showed that the electrical efficiency was generally less than 20%, whereas the enhancement in thermal efficiency was between 40% and 70%. The authors suggested further investigation to discover variable economic solutions as the PCM materials have high unit costs. Zheng and Zhou [44] conducted research using PCM for a PV/T system numerically. In addition to the PCM, a



cooling system integrated at the rear side of the PV module, a porous material with high solar transmittance and low thermal conductivity, silica aerogel, was integrated into the top surface of the PV module in order to minimize heat losses. The authors proposed a structural design of the PV/T system along with guidelines on performance improvement. The results showed that the enhancement in overall energy efficiency was 40.2% and 42.4% for the summer and winter seasons, respectively. Xu et al. [45] investigated fatty acid PCM-based PV/T system in Shanghai. The cooling system consisted of a plexiglass container with a 60 mm depth filled with PCM, a copper plate with nine fins to increase heat transfer area, serpentine tubes for water flow, and thermocouples to monitor the temperature in the system, as shown in Figure 3-7. Five configurations were tested under real outdoor conditions to obtain the optimum solution. Three out of five configurations were thermally regulated during the experiments. The results showed that the overall energy efficiency of thermally regulated configurations was 5.4% and 22.2% higher than those that were not thermally regulated.

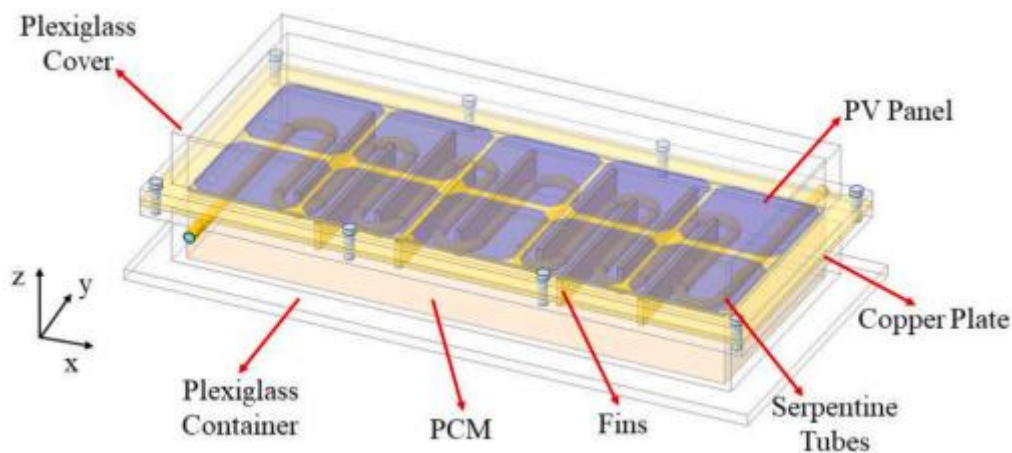


**Figure 3-7. PCM-based PV/T system [45]**

Zohra et al. [46] proposed a hybrid solar system to enhance electrical conversion efficiency by absorbing heat from PV modules. In this system, the issue of thermal stability was solved by using two different PCMs, RT35 and RT42. The results of the numerical analysis of the proposed PCM-based PV/T system showed that the electrical power output of the system was improved by 54.5% compared to the conventional PV system. The electrical conversion efficiency of the system was enhanced by 42.5% with two PCMs. Hossain et al. [47] designed a serpentine-shaped flow design with copper tubes mounted onto an aluminum sheet. The absorber was filled with different PCMs (lauric acid and paraffin). The water was used to regulate the heat transfer from PV to PCM. The system's thermal efficiency ranged between 75% and 85%. The maximal increase in electrical conversion efficiency was found to be 11%.

The design showed a high improvement in thermal efficiency; however, the improvement in electrical conversion efficiency was not as high as that of thermal.

The literature review showed that when the PV/T system is combined only with PCMs, the operating temperatures can not go below the ambient temperature. The PCM-based PV/T systems are coupled with air-based or water-based PV/T systems to transfer the stored heat within PCMs. The primary challenges faced by the PCM-integrated PV/T systems were the high cost and low thermal conductivity of PCMs, along with the selection of PCM, which depended on many parameters, such as solar intensity, ambient temperature, and wind velocity.

### **3.2.6 Nanofluid-based PV/T systems**

The nanofluids are one of the working fluids in PV/T systems and consist of dispersed mixtures of fluid and nanometer-sized particles, so-called nanoparticles. Most used nanoparticles are metal oxides and carbides, enhancing the thermal conductivity, heat capacity, and convective heat transfer coefficient through Brownian motion compared to the base fluid.

Various studies have been conducted in the literature on using nanofluids in PV/T systems. Hooshmandzade et al. [48] experimentally investigated the influence of single and hybrid nanofluids composed of water and  $\text{SiO}_2\text{-Al}_2\text{O}_3$  nanoparticles as a coolant for the PV/T system. Indoor and outdoor experiments were conducted using various volumes of nanofluids. The highest thermal and electrical efficiency results were obtained using the hybrid nanofluid, achieving 65.05% and 13.17% efficiencies for outdoor tests and 56.08% and 11.47% for indoor tests. Karaaslan and Menlik [49] numerically studied the effects of mono and hybrid nanofluids for sheet and tube PV/T systems. The performance of  $\text{CuO+Fe/water}$  and  $\text{CuO/water}$  (50:50) nanofluids as a working fluid was compared to water under different inlet boundary conditions. During the numerical analysis, the heat flux and inlet temperature were considered to be constant. The authors achieved the maximum electrical efficiency of 11.36%, 11.51%, and 11.60% for pure water,  $\text{CuO/water}$ , and  $\text{CuO + Fe/water}$  nanofluid, respectively. Sangeetha et al. [50] investigated the effects of three different nanoparticles, namely  $\text{TiO}_2$ , MWCNT, and  $\text{Al}_2\text{O}_3$ , with a constant volume ratio of 0.3% on PV/T systems. The impacts of nanofluids on PV module temperature and thermal efficiency of the PV/T system were analyzed. The water-based, nanofluid-enhanced cooling system was tested using a PV module with a peak power of 110 W. The highest thermal efficiency, electricity generation, and electrical conversion efficiency of the PV/T system were achieved using MWCNT nanoparticles. Naghdbishi et al. [51] prepared a system consisting of copper tubes mounted on a copper plate. The copper plate and tubes were covered with Merck 107158 PCM material. The base fluid, water/ethylene glycol mixture, was enhanced with MWCNT nanoparticles to

improve thermal conductivity. The system's electrical efficiency improved by 4.2%, whereas the thermal efficiency improved by 23.5%. Margoum et al. [52] numerically investigated the thermal and electrical efficiency performance of a conventional sheet-and-tube PV/T system using three different working fluids: pure water, Al<sub>2</sub>O<sub>3</sub>/water nanofluid, and Cu/water nanofluid. Copper and aluminum oxide nanoparticles with 2% volume were dispersed in water to prepare the working fluids in the PV/T system. The mathematical model of the system was created in MATLAB software based on the energy balance equation. The results indicated that when the mass flow rate of the working fluid was 0.04 kg/s, Cu/water nanofluid decreased the temperature of the PV module by 2.36 °C, whereas Al<sub>2</sub>O<sub>3</sub>/water nanofluid reduced by 1.89 °C. The thermal efficiency of the PV/T system was enhanced by 26% with Cu/water nanofluid and by 10.33% with Al<sub>2</sub>O<sub>3</sub>/water nanofluid.

The literature review showed that adding nanomaterials to the base fluids (water, ethylene glycol, or others) improved the thermal properties of the working fluid. Various types of nanoparticles were studied; however, the main issues with the nanofluids were the long-term thermal stability due to agglomeration of the nanoparticles, toxic characteristics, and high-cost implementation.

### **3.3 Summary**

The literature review on air-based PV/T systems showed that the general framework efficiency was low due to the low specific heat capacity of the working fluid. The low heat capacity of air led to the removal of a limited amount of heat from the PV module. The increased flow rate of air to enhance thermal efficiency in these systems resulted in higher electricity consumption due to the increased fan operation.

Previous research confirmed that most studies focused on conventional water-based PV/T systems. These systems added an absorber plate at the rear side of the PV module and a pipe network in various configurations, causing limited heat transfer and low thermal and electrical efficiency. In addition to conventional PV/T systems, the investigations on increasing the efficiency of PV/T systems targeted the working fluid by adding nanomaterials to enhance thermal conductivity and heat-carrying capacity rather than geometry optimization. Another type of PV/T technology reviewed was heat pipe combined PV/T systems. The literature review showed that this type of PV/T technology is still undeveloped due to less attention received by research activities and complex system design. The reviewed studies showed that the thermal efficiency did not exceed 60% in this PV/T technology.

Most studies on TEG-combined PV/T systems showed that TEG-based PV/T technology is still under development due to the complex integration of PV/T systems with TEGs. The non-

stable temperature of PV/T modules affecting the temperature gradient, causing impacts on the efficiency of TEGs and cost of thermoelectric materials, were the other drawbacks of this technology. The PCM-based PV/T systems were limited to cooling PV module temperature until the ambient temperature. This issue was solved by combining PCMs with water-based or air-based PV/T systems. The main issue of the PCM-based PV/T systems was the low thermal conductivity characteristic of PCMs. Nanoparticles gained popularity due to their effects on thermal conductivity and heat capacity. The high cost of implementation and the toxic nature of the nanoparticles were the main drawbacks to using nanoparticles in working fluid for PV/T systems.

Despite the significant attention received by PV/T technology and research activities, commercially available PV/T modules are scarce due to complex system designs and insufficient knowledge of PV/T technology.

## Chapter 4 - Research methodology

This chapter presents the research methods employed in this dissertation. A numerical and experimental research approach was used to develop a highly efficient cooling system for PV/T systems. A 1-D numerical transient thermal model of a PV module was developed in MATLAB software [53] to obtain the temperature distribution on each layer of the PV module. The developed numerical thermal model was validated using normal operating cell conditions (NOCT). The developed numerical model allowed for obtaining the PV cell layer temperature and consequently led to the estimation of electrical conversion efficiency and power output of the PV module from the 1-D thermal model. The numerical model was then used in the design process of the PV/T system. In the initial and final design stage of the PV/T system, the temperature of the PV cell layer obtained from the 3-D CFD model was fed to the 1-D thermal model to estimate the electrical conversion efficiency and power output.

The initial design of the cooling system was prepared based on knowledge obtained through the literature review and a 1-D thermal model. A commercial software, Ansys SpaceClaim 3D CAD modeling software [54], was then used to develop the 3-D initial design geometry. The designed cooling system was combined with a PV module and investigated by employing various inlet mass flow rates and temperatures under NOCT. The thermal efficiency of the system, temperature distribution on the PV cell layer, and uniformity of the cooling system were studied. Based on the results, the design was further improved to increase the thermal efficiency. The same boundary conditions were applied under NOCT to the 3-D CFD model of the final design of the PV/T system to compare the improvements. The achieved thermal efficiency and the uniform cooling of the PV module led to the preparation of the technical drawings of the cooling system for the manufacturing process. The prototype was prepared for the thermal tests in a laboratory.

The laboratory test rig was prepared to conduct the preliminary thermal tests of the designed PV/T system. The test rig consisted of three heating radiators, each with three modes of heating powers, P1-800 W, P2-1,600 W, and P3-2,500 W, placed 0.5 m above the cooling system. The test rig had a flow meter, pump, water storage tank, and K-type sheathed thermocouples in the inlet and outlet section. A self-calibrating digital heat flux sensor was used to measure the heat flux on the surface of the cooling and PV/T systems. Different inlet mass flow rates and temperatures were tested under P3-2,500 heating mode to analyze the thermal output and efficiency of the prototype cooling system. Upon completion of the experiments on the cooling prototype system, the 3-D CFD model of the cooling system was validated using the data obtained during the tests. The validation of the numerical model led to coupling the cooling system with a PV module to establish the PV/T module. Thermal

grease was used to adhere the PV module to the cooling system to eliminate air bubbles affecting effective heat transfer. Various inlet mass flow rates and temperatures were investigated under different heat flux conditions. The thermal output and efficiency of the PV/T system and the rear side temperature of the PV module were investigated. The rear side temperature of the PV module was compared when the cooling was active and non-active. The rear-side temperature of the PV module was then fed to the 1-D numerical model to estimate the PV cell layer temperature. The estimated PV cell layer temperature was used to calculate the electrical conversion efficiency and power output of the PV/T system. The cooling impact was determined by comparing the results of electrical conversion efficiency and power output of the PV module when it was cooled and non-cooled. The 3-D numerical model of the cooling system was combined with the PV module in the software and validated with the data obtained during the experiments. The validated numerical model allowed for analysis of the temperature distribution on the PV cell layer. An uncertainty analysis of thermal efficiency was performed with measured quantities to determine the reliability of the experiments.

The results obtained during the laboratory experiments confirmed that the prototype of the designed PV/T system was ready for outdoor tests. In order to conduct outdoor experiments, a test rig was prepared with the designed PV/T module and a non-cooled PV module. The test rig preparation was started by placing four PT-1000 temperature sensors on the rear side of the non-cooled PV module, and three PT-1000 temperature sensors were put on the rear side of the PV/T module. Three K-type sheathed thermocouples were inserted between the cooling system and the PV module to measure the rear side temperature of the PV module. When the temperature sensors were placed in proper locations, the test rig preparation was continued with the construction of a single-axis sun-tracking system. The system was placed near the roof of a building, where solar irradiation was not interrupted by any disturbance. The system was donated with a sun-tracking solar irradiation sensor, pyranometer, control system, and grid-tie microinverters. A pyranometer was placed between the non-cooled and cooled PV modules to measure the solar irradiation falling on the PV modules. High-performance PLC controllers and analog input modules were used to control and monitor the system and collect data from the sensors.

The designed test rig consisted of two loops where water was used in the PV/T cooling loop, and water/glycol mixture was used in the chiller loop. The PV/T loop comprised a pump, expansion vessel, heat meter, and hydraulic elements. The buffer tank contained an immersed coil heat exchanger. The tank was filled with water and used in the PV/T cooling loop. The water/glycol mixture was circulated through the heat exchanger coils inside the buffer tank. The coil of the immersed heat exchanger was connected to a heat exchanger, which was placed between the chiller and the buffer tank. The evaporator side of the chiller was

connected to the heat exchanger to cool down the water inside the buffer tank. The condenser side was connected to another heat exchanger, which was connected to an underground heat storage unit to reject the heat. Another heat meter was placed between the buffer tank and the heat exchanger to measure how much heat was rejected from the buffer tank.

The real outdoor tests were started after the test rig preparation. The outdoor tests were conducted for two months to analyze the performance of the PV/T system in September and October. Based on the collected data, an energy analysis of the PV/T system, including electrical conversion efficiency, thermal efficiency, electrical and thermal power outputs, was investigated. The cooling uniformity of the cooling system was analyzed, and the pressure drop tests were conducted with various flow rates in the test rig. An equation was derived to estimate the pressure drop. An uncertainty analysis was performed for the collected data during outdoor experiments. The reliability of the measured quantities obtained during the experiments was determined.

In order to assess the effectiveness of the designed PV/T system, a comparative study of existing literature with the proposed PV/T system was realized. A comparative framework was employed to highlight the key performance metrics. The comparative analysis consisted of analyzing the type of the PV/T system, mass flow rate, test conditions, type of study, and electrical and thermal efficiency.

An economic analysis of the proposed PV/T module was realized through market research. The energy generation and cost of PV/T modules available in the Polish market were compared to the designed PV/T module. A cost-benefit analysis was performed based on the actual domestic hot water demand of a single-family house. A comparative framework was deployed in the cost-benefit analysis by taking into account the designed PV/T module and a conventional gas boiler system. The standardized metrics, such as the levelized cost of electricity, levelized cost of heat, and levelized cost of energy, were used to assess and compare the lifetime costs of the proposed PV/T module. A payback analysis was conducted on the designed PV/T module by comparing it to a conventional gas boiler system to assess the cost recovery and financial viability.

## Chapter 5 - Thermal model of PV module

The first step while developing a thermal model of a photovoltaic panel is to consider the physical model, which provides each layer's material, thermal properties, and thickness. The optical and radiation model is needed to evaluate the total absorbed and reflected radiation by the layers of a photovoltaic module. The total radiation and coherent boundary conditions were used to achieve temperature distribution. In the developed 1-D transient thermal numerical model, the following assumptions were made:

- no contact resistance exists between the layers of the PV module;
- the surface of the PV module is not disturbed by shading, dust, or snow;
- the material and thermal properties are assumed to be isotropic and independent of temperature;
- each layer's transmittance and absorptance are independent of the wavelength of the incident solar irradiation.

### 5.1 Physical model

A commercial 325 W PV panel consists of 120 monocrystalline solar cells in series. The solar cells have a dimension of 158.75 × 79.375 mm. The overall length and width of the module are 1,696 × 1,002 mm. The layers of the PV module considered in thermal modeling are given in Table 5-1. The material and thermal properties of the layers considered are detailed in Table 5-1. The EVA Bottom and EVA Top layers have the same material and thermal properties and enclose the PV cells. The top-most and bottom-most layers are glass, with the same material and thermal properties. The model used to investigate the thermal behavior of the PV module does not contain thinner layers, such as the ARC layer, which has a thickness in the nanoscale, typically between 100-125 nm [56].

The material and thermal properties of layers are given in Table 5-1.

**Table 5-1. Material properties of the layers**

| Layer            | Thickness (mm) | Thermal Conductivity (W/m.K) | Specific Heat Capacity (J/kg.K) | Density (kg/m <sup>3</sup> ) |
|------------------|----------------|------------------------------|---------------------------------|------------------------------|
| Front side glass | 2.0            | 1.8                          | 790                             | 2,500                        |
| Top side EVA     | 0.2            | 0.4                          | 1,675                           | 1,090                        |
| PV cells         | 0.4            | 148.0                        | 677                             | 2,330                        |
| Bottom side EVA  | 0.2            | 0.4                          | 1,675                           | 1,090                        |
| Back side glass  | 2.0            | 1.8                          | 790                             | 2,500                        |

The layers of the PV module and the heat transfer mechanism considered to develop the thermal model of the PV module are illustrated in Figure 5-1.



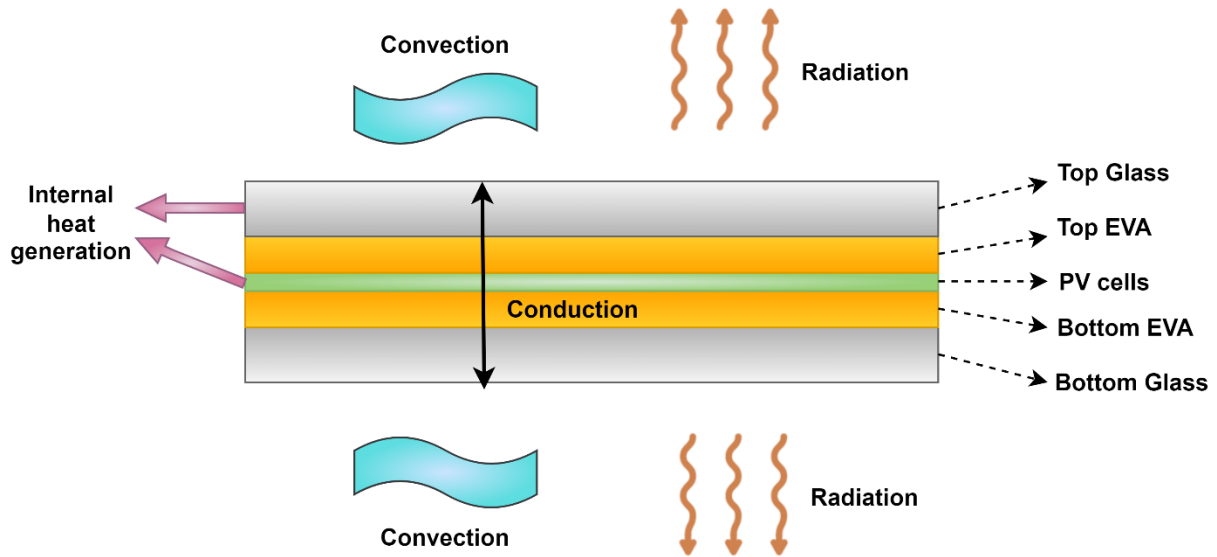


**Figure 5-1. Considered PV panel layers**

The PV module properties under standard test conditions (STC) provided by the manufacturer are given in Table 5-2.

**Table 5-2. PV module properties under STC**

| Properties                                       | Value  | Unit |
|--|--------|------|
| Nominal power output                             | 325.00 | W    |
| Maximum power voltage                            | 33.60  | V    |
| Maximum power current                            | 9.68   | A    |
| Open circuit voltage                             | 40.30  | V    |
| Short circuit current                            | 10.25  | A    |
| Module efficiency                                | 19.12  | %    |
| NOCT   | 44±3   | °C   |
| Temperature coefficient of power output          | -0.42  | %/°C |
| Temperature coefficient of open circuit voltage  | -0.29  | %/°C |
| Temperature coefficient of short circuit current | 0.05   | %/°C |

## 5.2 Optical and radiation model

A portion of incident solar irradiation falling on the solar panel is lost due to reflection and absorption in PV panel layers. The losses caused by reflection and absorption can be estimated employing the optical model, whereas the absorbed irradiation by PV cells is estimated using radiation models. The measured irradiation data is available in the form of total global horizontal irradiation ( $G_{HOR}$ ) with the unit  $W/m^2$ . The total global horizontal irradiation is also split into the beam and diffuse components. Duffie and Beckman [57] proposed two different correlations: the Erbs et al. [58] correlation and the Orgill and Hollands correlation to estimate the beam and diffuse components of the total global horizontal irradiation. The Orgill and Hollands [59] correlation was used and expressed in Eq. 3:

$$\frac{G_d}{G_b + G_d} = \begin{cases} 1 - 0.249k_T, & 0 \leq k_T < 0.35, \\ 1.557 - 1.84k_T, & 0.35 < k_T < 0.75, \\ 0.177, & k_T > 0.75, \end{cases} \quad (3)$$

where  $G_b$  and  $G_d$  are the beam component and diffuse component.  $k_T$  is the hourly clearness index. From the definition of  $k_T$ , Eq. 4 can be used to find the value of  $k_T$ :

$$k_T = \frac{G_b + G_d}{G_{on}}, \quad (4)$$

where  $G_{on}$  is extraterrestrial irradiation. Combining Eqs. 3 and 4, and using an iterative method, the values of  $G_b$ ,  $G_d$  and  $k_T$  can be estimated. The solar radiation absorbed by the PV cells,  $S$  was estimated using Eq. 5:

$$S = (\tau\alpha)_n M G_b R_b K_{\tau\alpha,b} + G_d K_{\tau\alpha,d} \left( \frac{1 + \cos\beta}{2} \right) + (G_b + G_d) \rho_g K_{\tau\alpha,g} \left( \frac{1 - \cos\beta}{2} \right), \quad (5)$$

where  $(\tau\alpha)_n$  is the transmittance at normal incidence, and  $R_b$  is the angle of incidence of beam radiation on the horizontal and tilted surfaces.  $M$  is the air mass modifier.  $K_{\tau\alpha,b}$ ,  $K_{\tau\alpha,d}$ , and  $K_{\tau\alpha,g}$  stand for the incidence angle modifier at the beam incidence angle, the incidence angle modifier at the effective incidence angle for diffuse radiation, and the incidence angle modifier at the effective incidence angle for ground-reflected radiation, respectively.  $\beta$  and  $\rho_g$  are the tilted surface angle and ground reflectance.

The air mass modifier,  $M$  is calculated using Eq. 6.

$$M = \sum_0^4 a_i (AM)^i, \quad (6)$$

where  $AM$  is the air mass and  $a_i$  are constants for different PV materials. Fanney et al. [60] reported that the values of  $a_0, \dots, a_4$  are 0.935823, 0.054289,  $-0.008677$ , 0.000527, and  $-0.000011$  for monocrystalline silicon cells.

In order to achieve the complete thermal model to find the temperature distribution of the module, the total absorbed solar irradiation was found.

### 5.3 Heat sources

A part of the total absorbed solar irradiation is not converted to electric current. The non-converted part generates heat within the solar panel. The front glass layer has an influential absorptivity ( $\alpha_{gl} = 0.05$ ), and the PV cell layer absorbs the incident irradiation. The internal heat generation as a result of absorption in the front glass was calculated in Eq. 7:

$$\dot{Q}_{gl} = \frac{\alpha_{gl} G_{HOR} A_P}{V_{gl}}, \quad (7)$$

where  $A_P$  stands for the entire area of the photovoltaic panel, 1.6994 m<sup>2</sup> and  $V_{gl}$  indicates the front glass volume, 0.0034 m<sup>3</sup>. The non-converted portion of the total absorbed solar energy is dissipated as heat in the PV cells' layer. The internal heat generation in the PV cell layer was found using Eq. 8:

$$\dot{Q}_{PV} = \frac{(1 - \eta_{PV}) A_{PV} S}{V_{PV}}, \quad (8)$$

where  $A_{PV}$  and  $V_{PV}$  express the total area of photovoltaic cells, 1.51 m<sup>2</sup>, and the total volume of PV cells, 0.0006 m<sup>3</sup>, respectively. Oliveti et al. [61] calculated  $\eta_{PV}$  the electrical efficiency of the solar panel using Eq. 9:

$$\eta_{PV} = \eta_{PV,ref} \left( 1 - \zeta_{ref} (T_{PV,cells} - T_{ref}) \right), \quad (9)$$

where  $\eta_{PV,ref}$  is the electrical efficiency referenced by the manufacturer, which equals 0.1912 at standard test conditions and 0.1779 at NOCT.  $\zeta_{ref}$  indicates the temperature coefficient of the solar cells and is set at 0.0042 °K<sup>-1</sup>.  $T_{PV,cells}$  and  $T_{ref}$  stand for the temperature of PV cells and the reference temperature, 25 °C.

#### 5.4 Heat conduction equation

The heat equation is a partial differential equation used to model how the heat diffuses through the solar panel's layers. For a solid domain in 3-D form, the heat equation is given in Eq. 10:

$$\rho c \frac{\partial T(x, y, z, t)}{\partial t} = k \left( \frac{\partial^2 T(x, y, z, t)}{\partial x^2} + \frac{\partial^2 T(x, y, z, t)}{\partial y^2} + \frac{\partial^2 T(x, y, z, t)}{\partial z^2} \right) + \dot{Q}_g(t), \quad (10)$$

where  $\rho$ ,  $c$ , and  $k$  are the density, the specific heat capacity, and the thermal conductivity, respectively.  $T$  is the temperature at point  $(x, y, z)$  at time  $t$ , and  $\dot{Q}_g$  is the internal heat generation. In this study,  $\rho$ ,  $c$ , and  $k$  are assumed to be constant for each layer given in Table 5-1. The 1-D thermal model was developed using the heat equation. The heat conduction equation can be reduced to Eq. 11:

$$\rho c \frac{\partial T(x, t)}{\partial t} = k \left( \frac{\partial^2 T(x, t)}{\partial x^2} \right) + \dot{Q}_g(t), \quad (11)$$

where  $x$  is the direction along with the thickness.

## 5.5 Boundary conditions

Eq. 11 was solved by applying the suitable boundary conditions on the top and bottom glass layers. The boundary conditions are illustrated in Figure 5-1. The convective and radiative heat transfer mechanisms occur between the environment and the front side glass and back side glass of the panel. The natural ( $h_{conv,free}$ ) and forced ( $h_{conv,forced}$ ) convection mechanism should be considered given in Eq. 12 [62]:

$$h_{conv} = h_{conv,free} + h_{conv,forced}. \quad (12)$$

The heat transfer coefficient for the natural convection can be calculated using Eq. 13 [62].

$$h_{conv,free} = \frac{Nu_{free}k_{air}}{l_{ch}}, \quad (13)$$

where  $Nu_{free}$  is the Nusselt number,  $k_{air}$  is the thermal conductivity of the air and  $l_{ch}$  is the characteristic length of the PV panel. Lloyd et al. [63] proposed the Eq. 14 to calculate the Nusselt number for free convection:

$$Nu_{free} = \begin{cases} 0.76Ra^{\frac{1}{4}}, & 10^4 < Ra < 10^7, \\ 0.15Ra^{\frac{1}{3}}, & 10^7 \leq Ra < 3 \times 10^{10}, \end{cases} \quad (14)$$

where  $Ra$  is Rayleigh number is given in Eq. 15 [62]:

$$Ra = Gr.Pr, \quad (15)$$

where  $Gr$  and  $Pr$  are the Grashof number and the Prandtl number [62].

$$Pr = \frac{c_{air}\mu_{air}}{k_{air}}, \quad (16)$$

$$Gr = \frac{g\beta_{air}(T_{surf} - T_{amb})l_{ch}^3}{\nu_{air}}, \quad (17)$$

where  $c_{air}$ ,  $\mu_{air}$  and  $k_{air}$  stand for the specific heat capacity of the air, the viscosity of the air, and the thermal conductivity of the air, respectively. In Eq. 17,  $g$  and  $\beta_{air}$  is the gravitational acceleration and the coefficient of thermal expansion of air.  $T_{surf}$  indicates the surface temperature (the front glass or rear glass) and  $\nu_{air}$  is the kinematic viscosity of the air. The mentioned properties are determined at the film ( $T_{film}$ ) temperature, which is calculated in Eq. 18 [62]:

$$T_{film} = \frac{T_{surf} + T_{amb}}{2}. \quad (18)$$

Kaplani and Kaplanis [64] determined the  $l_{ch}$  using the Eq. 19:

$$l_{ch} = 4 \frac{A_{panel}}{P_{panel}}, \quad (19)$$

where  $A_{panel}$  and  $P_{panel}$  stand for the total area of the PV panel and the perimeter of the PV, respectively. Ernani [65] calculated the heat transfer coefficient for forced airflow over flat surfaces as in Eq. 20:

$$h_{conv,forced} = 3.83 v_w^{0.5} l_{ch}^{-0.5}, \quad (20)$$

where  $v_w$  indicates the wind speed in  $m/s$ . The combined heat transfer coefficient  $h_{conv}$  can be obtained, and the convective heat loss  $Q_{conv}$  can be calculated using the Eq. 21:

$$Q_{conv} = h_{conv} A_{panel} (T_{surface} - T_{amb}), \quad (21)$$

where  $T_{surface}$  and  $T_{amb}$  are the surface and ambient temperatures.

The radiative heat losses from the front and back surfaces of the solar panel were estimated using a linearized heat transfer coefficient ( $h_{rad}$ ). The radiative heat transfer occurs in the following cases:

- Front side glass – sky
- Back side glass – sky
- Front side glass – ground
- Back side glass – ground

Shahzada et al. [66] proposed Eq. 22 to calculate the linearized radiative heat transfer coefficient,  $h_{rad}$ .

$$h_{rad} = \frac{\sigma (T_{surface}^2 - T_{sink}^2) (T_{surface} + T_{sink})}{\frac{1 - \varepsilon_{surface}}{\varepsilon_{surface}} + \frac{1}{F_{surface-sink}}}, \quad (22)$$

where  $\sigma$  is the Stefan-Boltzmann constant,  $T_{sink}$  is either the sky or ground temperature,  $T_{surface}$  is the solar panel's front or back surface temperature.  $\varepsilon_{surface}$  is the emissivity of the front and back glass, 0.85.  $F_{surface-sink}$  stands for the view factors which are defined from Eq. 23 to Eq. 26:

$$F_{frontglass-sky} = \frac{1}{2} (1 + \cos \theta), \quad (23)$$

$$F_{frontglass-ground} = \frac{1}{2} (1 - \cos \theta), \quad (24)$$

$$F_{backglass-sky} = \frac{1}{2} (1 + \cos(\pi - \theta)), \quad (25)$$

$$F_{backglass-ground} = \frac{1}{2}(1 - \cos(\pi - \theta)). \quad (26)$$

Jones and Underwood [67] proposed the Eq. 27 to calculate the sky temperature:

$$T_{sky} = T_{amb} - 20. \quad (27)$$

The ground temperature was assumed to be equal to the ambient temperature.

## 5.6 Energy balance and finite difference methods

The thermal model was solved using the energy balance method while using the finite difference (FD) method to discretize the heat equation. The finite difference scheme was applied, dividing the domain into smaller segments called nodes. The 1-D grid formation is shown in Figure 5-2. The 1-D grid was formed along the thickness of the PV module. The domain was subdivided into  $N$  sections of equal thickness,  $\Delta x$  on the x-direction.  $\Delta x$  was the distance between the adjacent nodes and was calculated by dividing the total thickness of the layers considered by the number of sections,  $N$ .

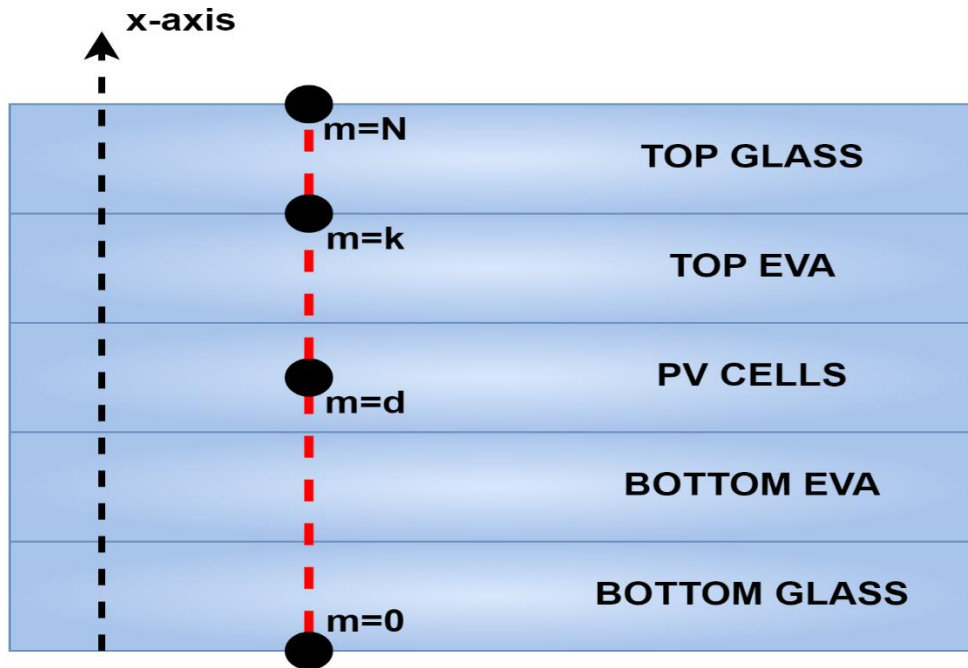


Figure 5-2. Grid formation

The heat equation in Eq. 11 was discretized to the following form using the FD formulation in Eqs. 28 and 29:

$$\frac{\partial T(x, t)}{\partial t} \approx \frac{T(x, t + \Delta t) - T(x, t)}{\Delta t} = \frac{T_m^{i+1} - T_m^i}{\Delta t}, \quad (28)$$

$$\frac{\partial^2 T(x, t)}{\partial x^2} \approx \frac{T_{m+1}^{i+1} - 2T_m^{i+1} + T_{m-1}^{i+1}}{\Delta x^2}, \quad (29)$$

where superscript  $i + 1$  and  $i$  stand for the new time  $t + \Delta t$  and previous time  $t$ , respectively. The subscript,  $m$  indicates the node of interest. Once the 1-D grid formation was prepared, the discretized heat equation was constructed by taking into account the energy balance in the rate form in Eq. 30:

$$\dot{E}_{in} + \dot{E}_g = \dot{E}_{st}, \quad (30)$$

where energy is entering  $\dot{E}_{in}$ , the energy is generated  $\dot{E}_g$ , and energy is stored  $\dot{E}_{st}$ . The different layers have various material properties, and control volumes store different amounts of energy.

### 5.6.1 Energy balance on bottom and top surface nodes

The bottom and top surface nodes exchange thermal energy by conduction with the interior nodes while exchanging thermal energy with the environment via radiation and convection. Thus, the equations at the bottom and top surface nodes were similar. As an example, node number  $N$  was studied. The node of interest had one neighbor, which is the bottom node  $N - 1$ . The node of interest exchanges thermal energy via conduction with adjacent node  $N - 1$  and exchanges thermal energy with the atmosphere via convection and radiation. The bottom node,  $N - 1$ , was  $\Delta x$  meters apart from the node of interest. Applying the energy balance on the node  $N$ , Eqs. 31, 32, and 33 can be obtained for  $\dot{E}_{in}$ ,  $\dot{E}_g$ , and  $\dot{E}_{st}$ , respectively. Similar equations were used for the bottom surface node.

$$\begin{aligned} \dot{E}_{in} = & k_{gl} \left( \frac{T_{N-1}^{i+1} - T_N^{i+1}}{\Delta x} \right) + h_{conv} (T_{amb} - T_N^{i+1}) + \\ & h_{rad,N-ground} (T_{ground} - T_N^{i+1}) + h_{rad,N-sky} (T_{sky} - T_N^{i+1}), \end{aligned} \quad (31)$$

$$\dot{E}_g = \dot{Q}_{gl} \frac{\Delta x}{2}, \quad (32)$$

$$\dot{E}_{st} = \rho_{gl} c_{gl} \frac{\Delta x}{2} \left( \frac{T_N^{i+1} - T_N^i}{\Delta t} \right), \quad (33)$$

where  $k_{gl}$ ,  $\rho_{gl}$  and  $c_{gl}$  are the thermal conductivity, density, and specific heat capacity of the glass, respectively.  $h_{rad,N-ground}$  and  $h_{rad,N-sky}$  stand for the linearized radiative heat transfer coefficient for node  $N$  to ground and node  $N$  to the sky. The upper script on temperature terms was the time steps, as the energy balance equations were solved in implicit form. The implicit

form was chosen as it is unconditionally stable and allows for freedom to control the execution time.

### 5.6.2 Energy balance on the interior nodes

The interior nodes lie inside each layer mentioned in Table 5-1. In order to demonstrate the equations for an interior node, the node  $d$ , an interior node of PV cell layer, was taken as an example. The node had two neighbor nodes: on the top side, node  $d + 1$ , and on the bottom side, node  $d - 1$ . Nodes on the top and bottom sides of  $d$  were  $\Delta x$  meters away from the node of interest. Applying the energy balance on the node  $d$ ,  $\dot{E}_{in}$ ,  $\dot{E}_g$ , and  $\dot{E}_{st}$ , equations can be derived.

$$\dot{E}_{in} = k_{pvcells} \left( \frac{T_{d+1}^{i+1} - T_d^{i+1}}{\Delta x} \right) + k_{pvcells} \left( \frac{T_{d-1}^{i+1} - T_d^{i+1}}{\Delta x} \right), \quad (34)$$

$$\dot{E}_g = \dot{Q}_{PV} \Delta x, \quad (35)$$

$$\dot{E}_{st} = \rho_{pvcells} c_{pvcells} \Delta x \left( \frac{T_d^{i+1} - T_d^i}{\Delta t} \right), \quad (36)$$

where  $k_{pvcells}$ ,  $\rho_{pvcells}$ , and  $c_{pvcells}$  are the thermal conductivity, density, and specific heat capacity of the PV cell layers.

### 5.6.3 Energy balance on interior interface nodes

The energy balance was applied on one of the interior interface nodes,  $k$ , shown in Figure 5-2, to demonstrate the equations implemented in the software to achieve a temperature distribution solution of PV module layers. The interface node had two neighbors: one node on the top side,  $k + 1$  and one node on the bottom  $k - 1$ . The node on the top side,  $k + 1$ , was inside the top glass layer and  $\Delta x$  meters away from the node  $k$ , whereas the node on the bottom side,  $k - 1$ , was inside the EVA layer and  $\Delta x$  meters away from the node  $k$ . Eqs. 37, 38, and 39 were derived for the interior interface nodes.

$$\dot{E}_{in} = k_{gl} \left( \frac{T_{k+1}^{i+1} - T_k^{i+1}}{\Delta x} \right) + k_{eva} \left( \frac{T_{k-1}^{i+1} - T_k^{i+1}}{\Delta x} \right) \quad (37)$$

$$\dot{E}_g = \dot{Q}_{gl} \frac{\Delta x}{2}, \quad (38)$$

$$\dot{E}_{st} = (\rho_{gl} c_{gl} + \rho_{eva} c_{eva}) \frac{\Delta x}{2} \left( \frac{T_k^{i+1} - T_k^i}{\Delta t} \right), \quad (39)$$



where  $k_{eva}$ ,  $\rho_{eva}$ , and  $c_{eva}$  are the thermal conductivity, density, and specific heat capacity of the EVA layer.

The total  $N$  equations were derived from the energy balance method as there were  $N$  unknown temperatures. As the equations were algebraic, it led to a system of linear equations.

$$[A]\{T\} = \{B\} \quad (40)$$

In Eq. 40,  $[A]$  is a matrix size of  $(N, N)$ , comprising the coefficients adjacent to the unknown temperature variables.  $\{T\}$  stands for the unknown temperatures with a size  $(N, 1)$  and  $\{B\}$  indicates the known quantities in a size of  $(N, 1)$ . One way to solve the system of linear equations is  $\{T\} = inv([A])\{B\}$ . The matrix  $[A]$  had the prominent feature of being a sparse tridiagonal matrix, meaning most of its elements are zero.

## 5.7 Model validation

The developed 1-D numerical transient thermal model of the PV module was validated using NOCT conditions. The validated model led to the study of the effect of temperature on electrical conversion efficiency and power output of the PV module.

### Nominal operating cell temperature (NOCT) validation

NOCT is one of the testing standards and was used to validate the numerical thermal model of the PV module. The NOCT is defined as the temperature reached by open-circuited PV cells in a PV module with a tilt angle of  $45^\circ$  under  $800 \text{ W/m}^2$  of incident solar irradiation,  $20^\circ\text{C}$  ambient temperature, wind speed of  $1 \text{ m/s}$  and air mass of  $1.5$  [68]. The datasheet information of the PV module under NOCT conditions is given in Table 5-3.

**Table 5-3. PV module datasheet under NOCT conditions**

| Property   | Value      | Unit |
|--|------------|------|
| Maximum power output                             | 241.90     | W    |
| Maximum power voltage                            | 31.10      | V    |
| Maximum power current                            | 7.79       | A    |
| Open-circuit voltage                             | 37.50      | V    |
| Short-circuit current                            | 8.28       | A    |
| Temperature coefficient of maximum power         | -0.42      | %/°C |
| Temperature coefficient of open-circuit voltage  | -0.29      | %/°C |
| Temperature coefficient of short-circuit current | 0.05       | %/°C |
| NOCT   | $44 \pm 3$ | °C   |
| Module efficiency                                | 17.79      | %    |

The boundary conditions, solar irradiation, ambient temperature, tilt angle, wind speed, and air mass were fed to the 1-D numerical thermal model of the PV module to estimate the PV cell layer temperature.

The developed 1-D numerical thermal model of the PV module was subjected to NOCT conditions. The temperature of the PV cell layer was estimated to be 44.30 °C by the developed numerical model, whereas the NOCT value indicated by the manufacturer was 44±3. The temperature difference between the datasheet NOCT value and model estimated NOCT value was 0.30 °C, indicating a good agreement.

The temperature distribution of the PV module through the thickness (x-direction) under NOCT conditions is shown in Figure 5-3.

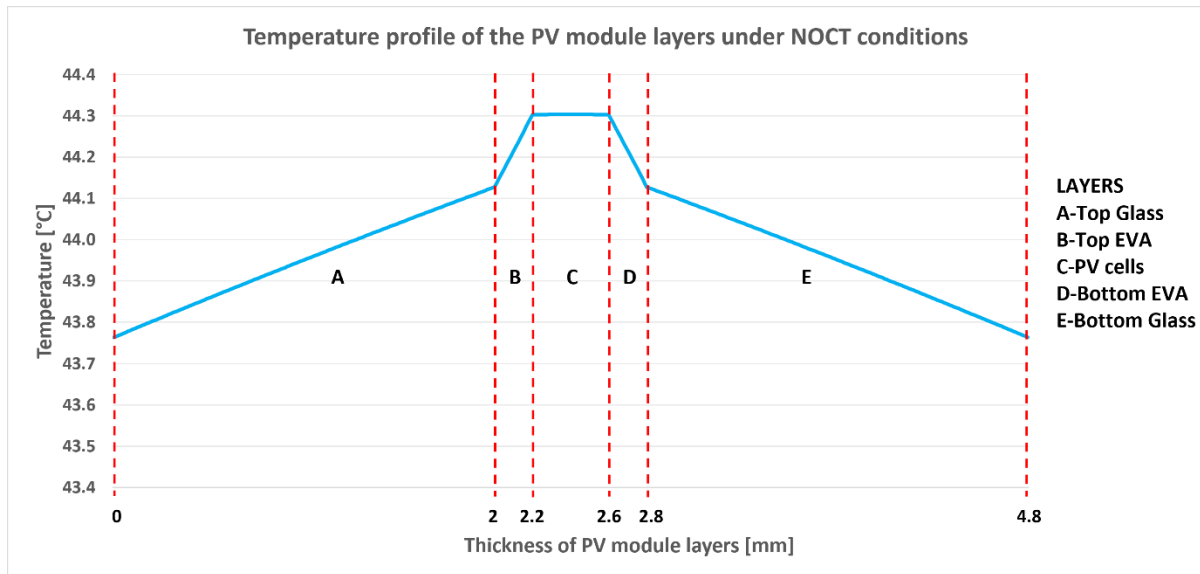


**Figure 5-3. The temperature profile of the PV module under NOCT conditions**

The developed model estimated the maximum power output of the PV module and was found to be 241.55 W. A difference of 0.14% occurred between the datasheet maximum power output and the model estimated maximum power output. As expected, the highest temperature occurred in the PV cell layer.

Based on the NOCT-validated 1-D numerical thermal model, the effect of temperature on the PV module was investigated. Various solar irradiation levels and ambient temperature were defined in the model to analyze the PV cell layer temperature.

Different solar irradiation levels ranging from 600 W/m<sup>2</sup> to 1000 W/m<sup>2</sup> at 25 °C ambient temperature were applied to the NOCT-validated 1-D transient numerical thermal model of the PV module to analyze the temperature of the PV cell layer. The PV cell layer temperature was initially assumed to be 25 °C for all conditions.

The temperature of the PV cell layer is shown in Figure 5-4.

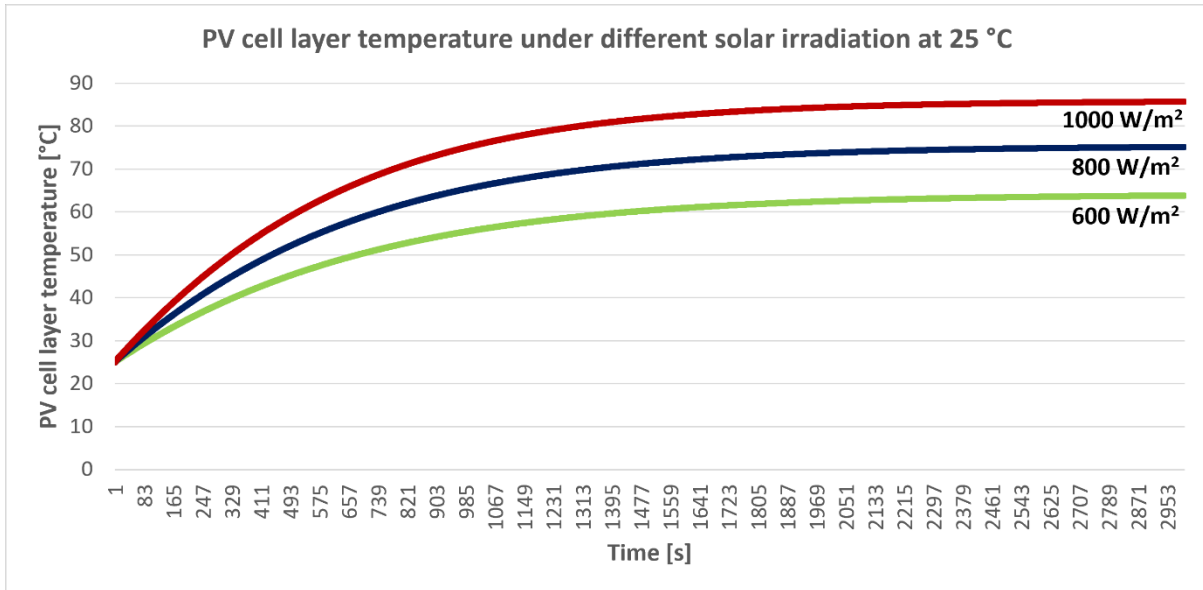


**Figure 5-4. PV cell layer temperature under different solar irradiation levels**

The temperature of the PV cell layer reached 64.13 °C, 75.40 °C and 85.89 °C under 600 W/m<sup>2</sup>, 800 W/m<sup>2</sup> and 1000 W/m<sup>2</sup> at 25 °C ambient temperature. The electrical conversion efficiency based on PV cell layer temperatures was calculated using Eq. 9. The electrical efficiency of the PV module drops to 14.23%, 15.07%, and 15.98% under 1000 W/m<sup>2</sup>, 800 W/m<sup>2</sup> and 600 W/m<sup>2</sup> from the optimal efficiency of 19.12% leading to 83.1 W, 55.02 W, and 32.04 W of power output drop.

The effect of ambient temperature under 1000 W/m<sup>2</sup> was investigated by varying the ambient temperature between 15 °C and 35 °C. The result of the analysis is shown in Figure 5-5.

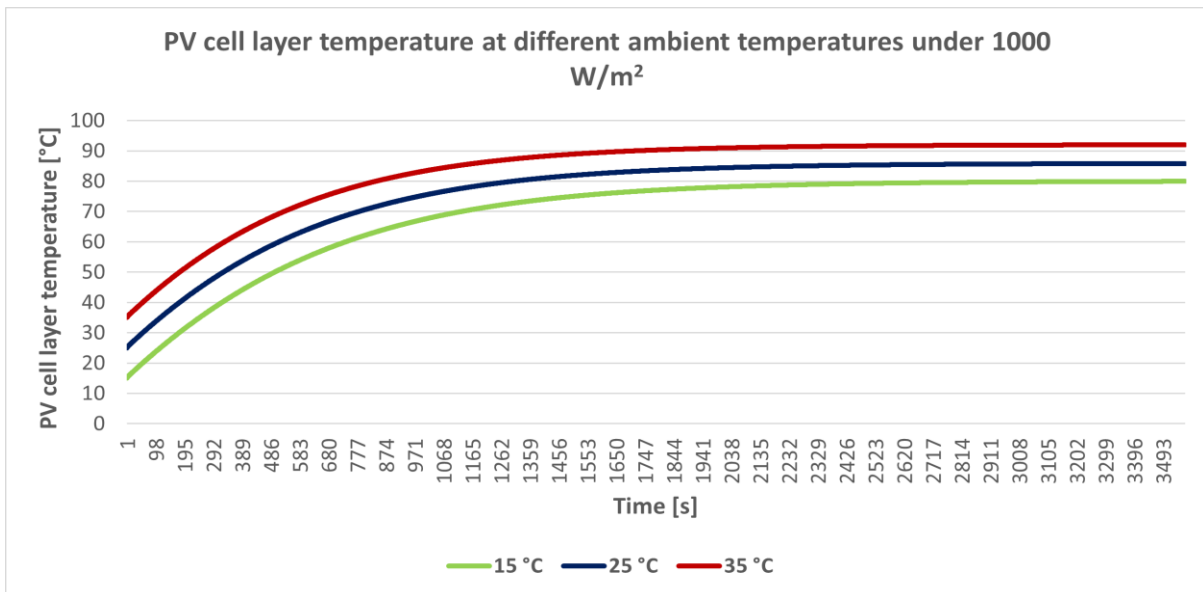


**Figure 5-5. PV cell layer temperature at different ambient temperatures under 1000 W/m<sup>2</sup>**

The temperature of the PV cell layer reaches up to 80.04 °C, 85.89 °C and 92.03 °C at 15 °C, 25 °C and 35 °C of the ambient temperature under 1000 W/m<sup>2</sup>. The increase in PV cell layer temperature led to a 28.15% electrical conversion efficiency drop of the PV cells and a 91.55 W power output drop at 35 °C ambient temperature.

## **5.8 Summary**

In this chapter, the 1-D transient numerical thermal model of a PV module was developed by determining the physical model of the module and the optical and radiation modeling in MATLAB software. The energy balance method and the finite difference numerical scheme were used to solve the heat transfer problem. The developed model was validated using NOCT conditions. A difference of 0.14% occurred between the datasheet maximum power output and the model estimated maximum power output.

Based on the validated thermal model of the PV module, the effect of temperature on electrical conversion efficiency and power output was studied by varying the solar irradiation and ambient temperature. The temperature of the PV cell layer reached 85.89 °C under 1000 W/m<sup>2</sup> at 25 °C ambient temperature. The electrical conversion efficiency of the PV module drops to 14.23% from the optimal efficiency of 19.12%, leading to a drop of 83.1 W in power output.

The temperature of the PV cell layer reaches up to 92.03 °C at 35 °C of the ambient temperature under 1000 W/m<sup>2</sup>. The increase in PV cell layer temperature leads to a 28.15% electrical conversion efficiency drop of the PV cells and a 91.55 W power output drop at 35 °C ambient temperature.

The adverse impacts of the temperature on the electrical power output and conversion efficiency of the PV cells showed the importance of cooling PV modules.

## Chapter 6 - Design of the cooling system and numerical studies

The thermal behavior analysis of the PV module concluded that the increase in operating temperature of the PV modules led to a drastic fall in electrical conversion efficiency and power output. The high temperatures that were reached indicate the importance of the heat transfer area, the material used in the cooling system, and the working fluid used to remove the heat from the PV modules. These considerations need to be taken into account to bring the operating temperature of the PV module to the optimal temperature, 25 °C.

In addition to conclusions obtained from the thermal modeling of the PV module, the literature review on air-based PV/T systems showed these systems lacked effective heat transfer due to the low specific heat capacity of the air, showing the importance of the working fluid selection. Most studies on water-based PV/T systems showed that adding an absorber plate at the rear side of the PV module and a pipe network in various configurations caused limited heat transfer. The heat transfer area had a crucial impact on the cooling effectiveness and thermal efficiency. Due to its high thermal conductivity, the proposed PV/T systems in the literature mostly used copper as the base material when manufacturing the sheet-and-tube systems. However, these studies did not consider the cost analysis while choosing the material. When selecting the material, there is usually a trade-off between the thermal properties and the cost of the material. In the literature, studies did not focus on the uniformity of the cooling. The uniformity of cooling is an important consideration that has to be taken into account due to the lifetime of the PV cells and thermal stresses.

The aim was to develop a highly efficient design that uses environmentally friendly, cost-effective, available, and thermally stable working fluid. Based on the studied 1-D numerical thermal model and extensive literature review, a process for designing a highly efficient cooling system was as follows:

- selection of cooling method;
- geometry of the design;
- material selection and cost;
- working fluid selection;

The liquid-based cooling method was chosen for designing the cooling system as the literature review showed that the thermal and electrical efficiency of the liquid-based PV/T systems was greater compared to air-based, TEG-combined, and PCM-based PV/T systems due to the high heat transfer capability of liquids. Once the type of system was decided, the geometry design was started. During the initial geometry design, the idea was to maximize the heat transfer area and use the heat transfer area available on the rear side of the PV module. The

manufactured PV modules generally have 15 to 25 mm of space on the rear side. The design was planned to be compact to fix the cooling system under the PV module without mechanical work, excluding adhesives, to avoid air bubbles.

The PV module used for the PV/T system had a length of 1,696 mm and a width of 1,002 mm. Based on the dimensions of the PV module, the initially designed cooling system had the dimensions of 1,670 x 965 x 10 mm, with a total surface area of 6.58 m<sup>2</sup> and a surface area of 1.59 m<sup>2</sup> in contact with the rear side of the PV module as shown in Figure 6-1. The bottom plate and top plate thickness of the cooling system was 2 mm, leaving a 6 mm thickness for the fluid flow inside the system. The system consisted of three channels separated by long aluminum rods with a total surface area of 0.019 m<sup>2</sup> contact with the working fluid to ensure uniform cooling, shown as A in Figure 6-1. Each channel had one inlet and outlet with an inner diameter of 5 mm and outer diameter of 5.5 mm, openings for electrical connections of the PV module, shown as B in Figure 6-1. Short, straight rods (a total surface area of 0.09 m<sup>2</sup> in contact with the working fluid), together with circular fins (a total surface area of 0.023 m<sup>2</sup> in contact with the working fluid) shown as C and D in Figure 6-1, was placed close to the inlet section in the first half of the cooling system to reinforce the strength to overcome any pressure-related issues and increase heat transfer to the working fluid. Similarly, in the second half of the cooling system, three rods for each channel, along with pins, were used to strengthen the cooling system and enhance the heat transfer.

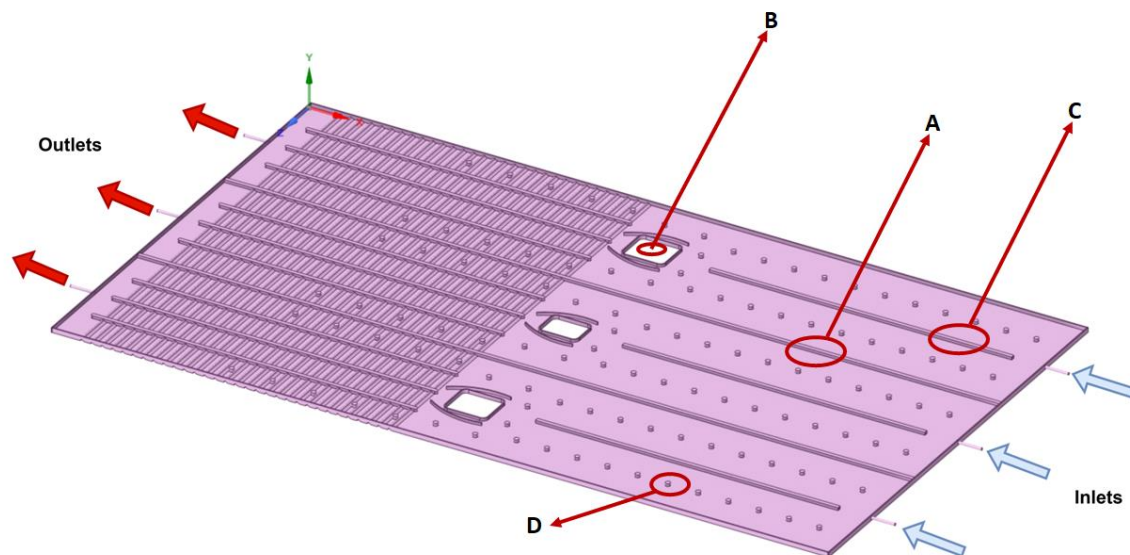


**Figure 6-1. The initial design of the cooling system**

Crescent-shaped flow routers were placed on the left and right sides of the openings to eliminate overheating under the opening areas. A dorsal-shaped design was applied under the cooling box to enhance the convection heat transfer with the outdoor air. The dorsal shape

applied to the second half of the design and the crescent-shaped flow routers are shown in Figure 6-2.

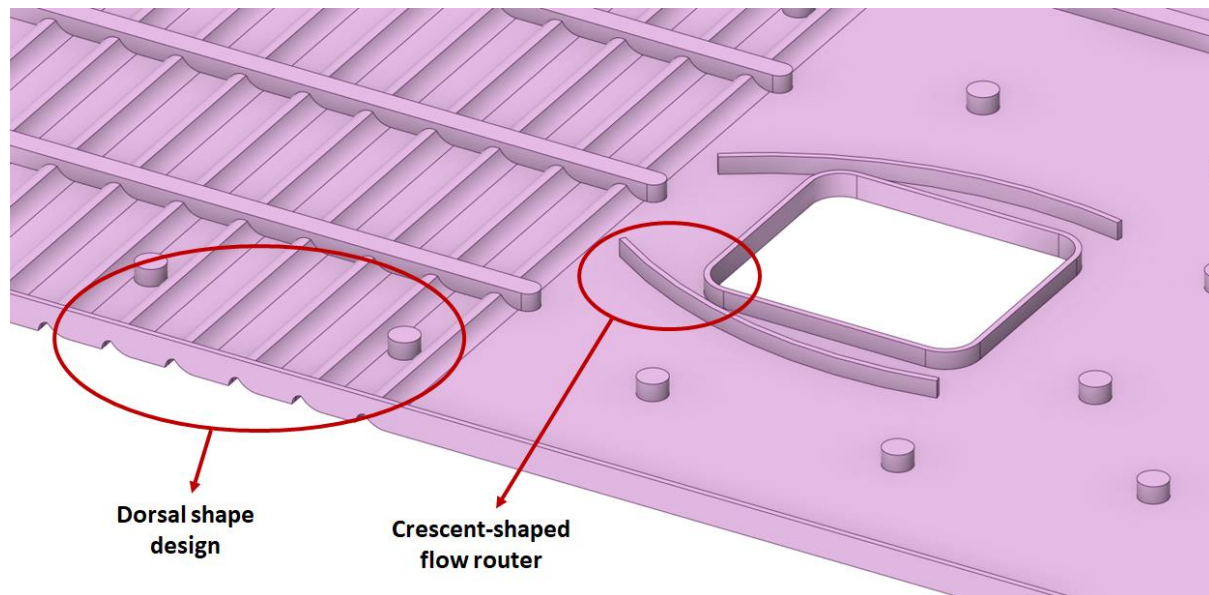


**Figure 6-2. The dorsal-shaped design**

The idea of using the dorsal-shaped design was to increase the heat transfer to dissipate the excess heat in the cooling system to the environment. Another aspect of using such a design was that the working fluids could reach high temperatures after the first half of the design due to their specific heat capacity, causing a drop in cooling efficiency. Such design allowed for enhanced heat transfer with the environment and better cooling. The dimensions of the designed dorsal-shaped geometry are shown in Figure 6-3.

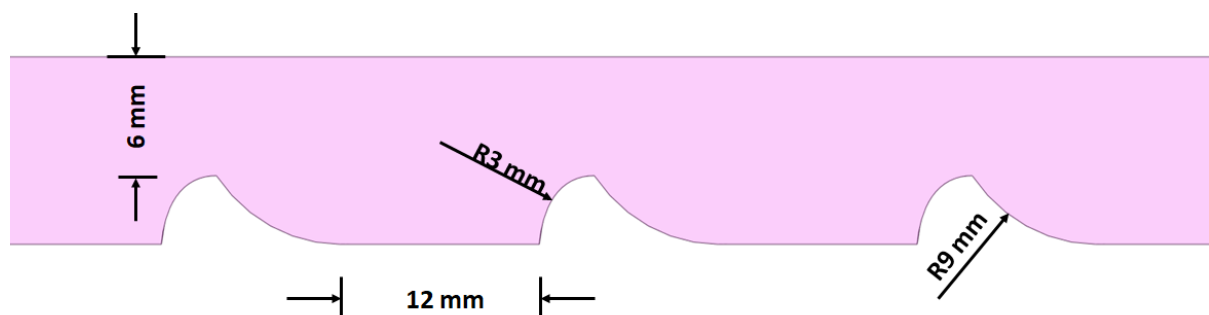


**Figure 6-3. Dimensions of the dorsal-shaped geometry**

Material selection is one of the most essential processes. Thermal conductivity is a crucial parameter when choosing the material as it highly contributes heat transfer from the PV module to the working fluid. In PV/T systems, copper and aluminum were the most used and suitable materials due to their high thermal conductivity. In the current design, aluminum was chosen as the base material due to its low density and low cost. The low-density characteristic

of aluminum allows for a 3.3 times lighter weight of design compared to copper. The material and thermal properties of the used aluminum alloy 6061 are given in Table 6-1.

**Table 6-1. The material and thermal properties of the base material**

| Properties             | Values   | Units             |
|------------------------|----------|-------------------|
| Density                | 2,700.00 | kg/m <sup>3</sup> |
| Specific Heat Capacity | 896.00   | J/kg.K            |
| Thermal Conductivity   | 166.00   | W/m.K             |
| Reflectivity           | 0.61     | -                 |
| Absorptivity           | 0.14     | -                 |
| Emissivity             | 0.25     | -                 |
| Tensile strength       | 310.00   | MPa               |

Additionally, aluminum offers better returns on investment than copper due to affordability, and its price tends to fluctuate less, making it a safer investment in solar applications.

The selection of the working fluid for the PV/T systems is another important aspect of designing an efficient and reliable system. The chosen fluid needs to be able to manage both electrical and thermal expectations, as there is always a trade-off due to the desired temperature of the working fluid and the operating temperature of the PV module. The thermal conductivity, convective heat transfer coefficient, availability, environmental impact, and cost are the parameters that affect the working fluid decision-making process. The climate also has an influence on selecting the correct working fluid, as in moderate climates, freezing can cause potential issues. Water and water/propylene glycol (%40) mixture are chosen as the cooling system was designed in Poland, where the climate is moderate. The availability, cost, environmental impact, and adequate heat transfer properties were the parameters that made these two working fluids preferable.

### 6.1 Numerical analysis of the initial PV/T design

The mathematical modeling was based on 3-D, steady, laminar, and incompressible flow. The Navier-Stokes's equations governed the fluid flow and convective heat transfer [69]. Eq. 41 is the continuity equation.

$$\frac{\partial u}{\partial x} + \frac{\partial v}{\partial y} + \frac{\partial w}{\partial z} = 0 \quad (41)$$

In Eq. 41,  $u$ ,  $v$ , and  $w$  are the components of velocity at the point  $(x, y, z)$ .

Eqs. 42, 43, and 44 represent the momentum equations in  $x$ ,  $y$ , and  $z$  directions, respectively.

$$\left( u \frac{\partial u}{\partial x} + v \frac{\partial u}{\partial y} + w \frac{\partial u}{\partial z} \right) = -\frac{1}{\rho} \frac{\partial p}{\partial x} + \nu \left( \frac{\partial^2 u}{\partial x^2} + \frac{\partial^2 u}{\partial y^2} + \frac{\partial^2 u}{\partial z^2} \right) + g_x \quad (42)$$



$$\left(u \frac{\partial v}{\partial x} + v \frac{\partial v}{\partial y} + w \frac{\partial v}{\partial z}\right) = -\frac{1}{\rho} \frac{\partial p}{\partial y} + \vartheta \left(\frac{\partial^2 v}{\partial x^2} + \frac{\partial^2 v}{\partial y^2} + \frac{\partial^2 v}{\partial z^2}\right) + g_y \quad (43)$$

$$\left(u \frac{\partial w}{\partial x} + v \frac{\partial w}{\partial y} + w \frac{\partial w}{\partial z}\right) = -\frac{1}{\rho} \frac{\partial p}{\partial z} + \vartheta \left(\frac{\partial^2 w}{\partial x^2} + \frac{\partial^2 w}{\partial y^2} + \frac{\partial^2 w}{\partial z^2}\right) + g_z \quad (44)$$

In Eqs. 42, 43, and 44,  $\rho$  and  $p$  are the density and pressure.  $\vartheta$  stands for the kinematic viscosity.  $g_x$ ,  $g_y$  and  $g_z$  are the gravitational acceleration in  $x$ ,  $y$ , and  $z$  directions, respectively.

Eq. 45 represents the energy equation.

$$\left(u \frac{\partial T}{\partial x} + v \frac{\partial T}{\partial y} + w \frac{\partial T}{\partial z}\right) = \alpha \left(\frac{\partial^2 T}{\partial x^2} + \frac{\partial^2 T}{\partial y^2} + \frac{\partial^2 T}{\partial z^2}\right) \quad (45)$$

In Eq. 5,  $T$  represents the temperature field, and  $\alpha$  stands for the thermal diffusivity.

A 3-D CFD model of the initial geometry design was developed in Ansys SpaceClaim 3-D CAD modeling. The designed initial cooling system consisted of three divided sections, each with an inlet and outlet. The middle section was chosen to be studied to obtain a high-resolution mesh to achieve accurate results and reduce computational time. The fluid domain was extracted from the solid domain to be analyzed. The developed fluid domain was discretized using Fluent meshing. The Poly-Hexcore elements were used to generate a high-quality and efficient mesh. The hexcore mesh filled the bulk region volume with perfect cubes of the same size, preventing orthogonal corrections and providing equal resolution in all directions. The polyhedral elements to fill the transition zone were used. The implemented process led to more accurate results while reducing the computational time and using less RAM.

When the pre-processing was completed, the solver settings were defined in the software. The gravity was inserted as  $9.81 \text{ m/s}^2$  in the  $-y$  direction. The energy equation model was activated to couple the fluid flow with energy analysis. The laminar flow type was chosen as the velocity of the fluid was relatively slow, indicating a low Reynolds Number. The water/propylene glycol mixture (40%) was used as the working fluid. The mixture properties are given in Table 6-2.

**Table 6-2. Water/propylene glycol mixture properties**

| Properties             | Values   | Units             |
|------------------------|----------|-------------------|
| Density                | 1,024.33 | kg/m <sup>3</sup> |
| Specific Heat Capacity | 3,823.50 | J/kg.K            |
| Viscosity              | 0.0027   | kg/m.s            |
| Thermal Conductivity   | 0.433    | W/m.K             |

The boundary conditions were defined based on the NOCT conditions. The shell conduction feature was used to model the PV module section above the cooling system. The shell

conduction becomes useful, particularly in modeling thin walls, as in the case of PV module layers. The shell conduction feature allows for creating one or more layers of virtual cells without the need to mesh the wall thickness in the preprocessor. The PV layers in Table 5-1 were used while managing the shell conduction walls. The shell conduction feature requires heat generation in each layer defined. The 1-D numerical thermal model was used to calculate the heat generation in the glass and PV cell layer using Eqs 7 and 8. The convective and radiative heat transfer coefficients were calculated using Eqs. 12 and 22. The ambient temperature was 20 °C as indicated in NOCT conditions. In addition to the explained boundary conditions, the pressure-outlet boundary condition was set at the outlet, whereas uniform flow at constant temperature was defined at the inlet. The boundary conditions given in Table 6-3 were applied in the software to analyze the behavior of the initial cooling system design.

**Table 6-3. The boundary conditions**

| Case | $\dot{q}_f$ (L/h) | $V_{in}$ (m/s) | $\dot{m}_f$ (kg/s) | $T_{f,in}$ (°C) |
|------|-------------------|----------------|--------------------|-----------------|
| 1    | 90                | 1.24           | 0.03               | 15              |
|      | 180               | 2.49           | 0.05               |                 |
|      | 270               | 3.73           | 0.08               |                 |
|      | 360               | 4.97           | 0.10               |                 |
|      | 450               | 6.21           | 0.13               |                 |
| 2    | 90                | 1.24           | 0.03               | 20              |
|      | 180               | 2.49           | 0.05               |                 |
|      | 270               | 3.73           | 0.08               |                 |
|      | 360               | 4.97           | 0.10               |                 |
|      | 450               | 6.21           | 0.13               |                 |
| 3    | 90                | 1.24           | 0.03               | 25              |
|      | 180               | 2.49           | 0.05               |                 |
|      | 270               | 3.73           | 0.08               |                 |
|      | 360               | 4.97           | 0.10               |                 |
|      | 450               | 6.21           | 0.13               |                 |

In Table 6-3,  $\dot{q}_f$  and  $V_{in}$  are the volumetric flow rate and the inlet velocity of the working fluid.  $\dot{m}_f$  and  $T_{f,in}$  stand for the inlet mass flow rate and temperature. The average temperature of the PV cell layer temperature and the outlet temperature of the cooling system were analyzed under NOCT conditions. The useful thermal energy generation and thermal efficiency of the cooling system were calculated using Eqs. 46 and 47.

$$Q_u = \dot{m}_f c_f (T_{f,out} - T_{f,in}), \quad (46)$$

where  $Q_u$  and  $T_{f,out}$  are the useful thermal energy gain and the outlet temperature of the working fluid.  $c_f$  stands for the specific heat capacity of the working fluid. The thermal efficiency is calculated using Eq. 47.

$$\eta_{th} = \frac{Q_u}{HA_{effc}}, \quad (47)$$

$\eta_{th}$  indicates the thermal efficiency of the cooling system,  $H$  and  $A_{effc}$  stand for the average heat flux on the surface of the system and effective cooling area, respectively.

The average temperature of the PV cell layer, outlet temperature, thermal energy generated, and thermal efficiency for each case are given in Table 6-4.

**Table 6-4. Numerical model results of initial cooling system design under NOCT conditions**

| Case | $\dot{m}_f$ (kg/s) | $T_{f,in}$ (°C) | $T_{f,out}$ (°C) | $T_{pvcells}$ (°C) | Qu (W)   | $\eta_{thermal}$ (%) |
|------|--------------------|-----------------|------------------|--------------------|----------|----------------------|
| 1    | 0.03               | 15              | 24.88            | 26.18              | 944.61   | 73.27                |
|      | 0.05               |                 | 20.25            | 21.50              | 1,003.95 | 77.87                |
|      | 0.08               |                 | 18.58            | 20.32              | 1,026.21 | 79.60                |
|      | 0.10               |                 | 17.71            | 19.73              | 1,034.72 | 80.26                |
|      | 0.13               |                 | 17.16            | 18.79              | 1,032.15 | 80.06                |
| 2    | 0.03               | 20              | 29.01            | 29.95              | 860.84   | 66.77                |
|      | 0.05               |                 | 24.77            | 26.28              | 911.05   | 70.67                |
|      | 0.08               |                 | 23.25            | 24.13              | 931.95   | 72.29                |
|      | 0.10               |                 | 22.46            | 23.57              | 939.18   | 72.85                |
|      | 0.13               |                 | 21.96            | 23.14              | 935.75   | 72.58                |
| 3    | 0.03               | 25              | 33.12            | 33.68              | 776.11   | 60.20                |
|      | 0.05               |                 | 29.29            | 31.14              | 819.62   | 63.57                |
|      | 0.08               |                 | 27.92            | 30.13              | 837.07   | 64.93                |
|      | 0.10               |                 | 27.22            | 29.59              | 849.57   | 65.90                |
|      | 0.13               |                 | 26.76            | 29.11              | 842.45   | 65.34                |

$T_{pvcells}$  is the average temperature of the PV cell layer. The average temperature of each PV cell layer decreased when the inlet flow rate increased up to 0.13 kg/s or the inlet temperature decreased. Increasing the mass flow rate from 0.03 kg/s to 0.10 kg/s and decreasing the inlet temperature from 25 °C to 15 °C led to a 21.79% improvement in thermal efficiency and keeping the PV cell layer temperature at 19.53 °C. The datasheet information of the PV module in Table 5-3 indicated that the NOCT temperature is 44±3 °C. The initial design of the cooling system was able to reduce the temperature of the PV cell layer by 25.21 °C when the inlet mass flow rate and temperature were 0.13 kg/s and 15 °C, respectively. The maximum thermal efficiency of 80.26% was achieved with the inlet mass flow rate of 0.10 kg/s and the inlet temperature of 15 °C. The increase in inlet temperature led to a drop in the thermal efficiency of the cooling system. The maximum thermal efficiency improvement was observed in all cases when the mass flow rate was increased from 0.03 kg/s to 0.05 kg/s. In cases 1, 2, and 3, the improvements were 6.28%, 5.83%, and 5.61%, respectively.

The post-processing procedure was carried out to visualize the temperature distribution of the PV cell layer for cases where the maximum thermal efficiency was observed, as shown in Figure 6-4.

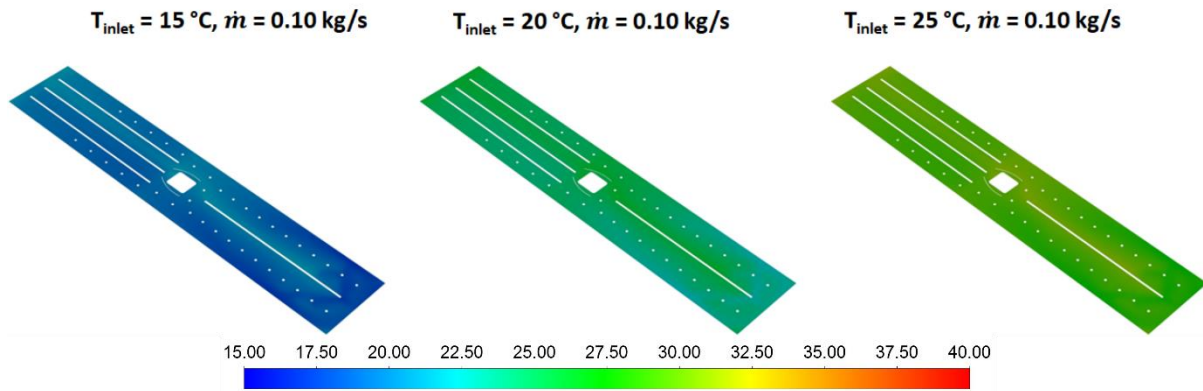


**Figure 6-4. The PV cell layer temperature distribution of cases for the initial design**

The maximum thermal efficiency of 80.26%, 72.85%, and 65.90% was achieved with the inlet temperature of 15 °C, 20 °C, and 25 °C at a constant flow rate of 0.10 kg/s, respectively. The post-processing results showed that the average PV cell layer temperature was 19.53 °C, 23.57 °C, and 29.59 °C for the cases studied. The initial design was also able to maintain a uniform temperature distribution for all cases, as seen in Figure 6-4.

The 1-D numerical thermal model was used to estimate the electrical conversion efficiency and power output of the PV module, as given in Table 6-5.

**Table 6-5. The electrical conversion efficiency and power output of initial design at NOCT conditions**

| Case | $T_{pvcells\_cooled}$ (°C) | $T_{npvcells}$ (°C) | $P_{cooled}$ (W) | $P_{non-cooled}$ (W) | $\eta_{pv\_cooled}$ (%) | $\eta_{pv\_non-cooled}$ (%) |
|------|----------------------------|---------------------|------------------|----------------------|-------------------------|-----------------------------|
| 1    | 26.18                      | 44.00               | 258.65           | 241.90               | 19.02                   | 17.79                       |
|      | 21.50                      | 44.00               | 259.94           | 241.90               | 19.12                   | 17.79                       |
|      | 20.32                      | 44.00               | 259.94           | 241.90               | 19.12                   | 17.79                       |
|      | 19.53                      | 44.00               | 259.94           | 241.90               | 19.12                   | 17.79                       |
|      | 18.79                      | 44.00               | 259.94           | 241.90               | 19.12                   | 17.79                       |
| 2    | 29.95                      | 44.00               | 254.53           | 241.90               | 18.72                   | 17.79                       |
|      | 26.28                      | 44.00               | 258.54           | 241.90               | 19.02                   | 17.79                       |
|      | 24.13                      | 44.00               | 259.94           | 241.90               | 19.12                   | 17.79                       |
|      | 23.57                      | 44.00               | 259.94           | 241.90               | 19.12                   | 17.79                       |
|      | 23.14                      | 44.00               | 259.94           | 241.90               | 19.12                   | 17.79                       |
| 3    | 33.68                      | 44.00               | 250.47           | 241.90               | 18.42                   | 17.79                       |
|      | 31.14                      | 44.00               | 253.24           | 241.90               | 18.63                   | 17.79                       |
|      | 30.13                      | 44.00               | 254.34           | 241.90               | 18.71                   | 17.79                       |
|      | 29.59                      | 44.00               | 254.93           | 241.90               | 18.75                   | 17.79                       |
|      | 28.93                      | 44.00               | 255.65           | 241.90               | 18.80                   | 17.79                       |

In Table 6-5,  $T_{pvcells\_cooled}$  and  $T_{npvcells}$  stand for the temperature of the PV cell layer of the cooled and non-cooled PV module.  $P_{cooled}$ ,  $P_{non-cooled}$ ,  $\eta_{pv\_cooled}$  and  $\eta_{pv\_non-cooled}$  are the power outputs and electrical conversion efficiencies of the cooled and non-cooled PV modules, respectively. Cases maintained the average temperature of the PV cell layer under 25 °C, leading to the PV module's maximum electrical conversion efficiency and power output.

The maximum electrical efficiency improvement was 7.48% in the cases where the PV cell layer temperature was maintained under 25 °C.

A grid independence analysis was conducted to find the optimal number of elements used to discretize the domain. The analysis was realized for the outlet temperature in the first case when the inlet mass flow rate was 0.03 kg/s with the inlet temperature of 15 °C. The optimal number of elements was used in the rest of the analysis. The grid independence analysis result is shown in Figure 6-5.

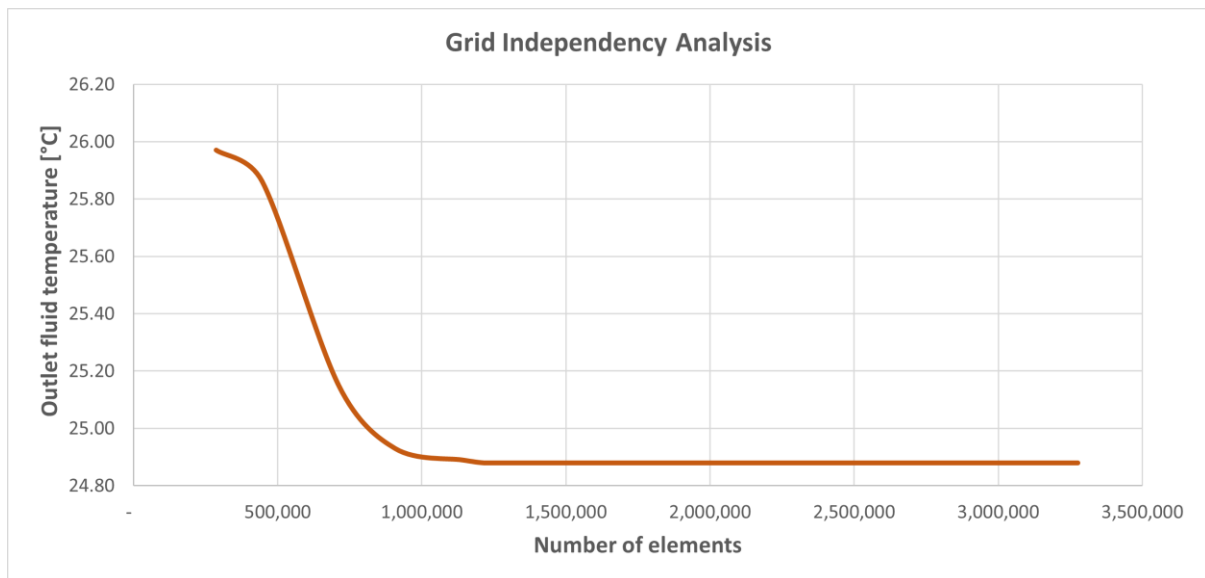


**Figure 6-5. The grid independence analysis**

## 6.2 The enhanced design of the cooling system

When the numerical study was completed, the ways of improving the system's thermal efficiency and cooling effect were investigated. The initial design allowed for maintaining low temperatures at the PV cell layer and accomplishing maximum electrical conversion efficiency. However, the maximum thermal efficiency of the cooling system was reached up to 80.26%.

The extensive heat transfer area contributed significantly to the thermal energy gain of the cooling system. Therefore, the interior design of the cooling system was considered to be enhanced to achieve higher thermal efficiency. The heat rejection to the environment was increased by employing the dorsal-shaped design after the first half of the initial design. The

dorsal-shaped design was removed and changed to a flat plate in the enhanced cooling system design.

Cylindrical turbulator notches were added to the second half of the cooling system to increase the heat transfer, thus improving thermal efficiency and overall performance. The 34 turbulator notches were employed in the second half of the cooling system to enhance the heat transfer and avoid overheating issues below the opening channels to perform uniform cooling. Each turbulator notch has a length of 961 mm with a 6 mm diameter. The cylindrical turbulator notches created in the software and added to the cooling system are shown in Figure 6-6.

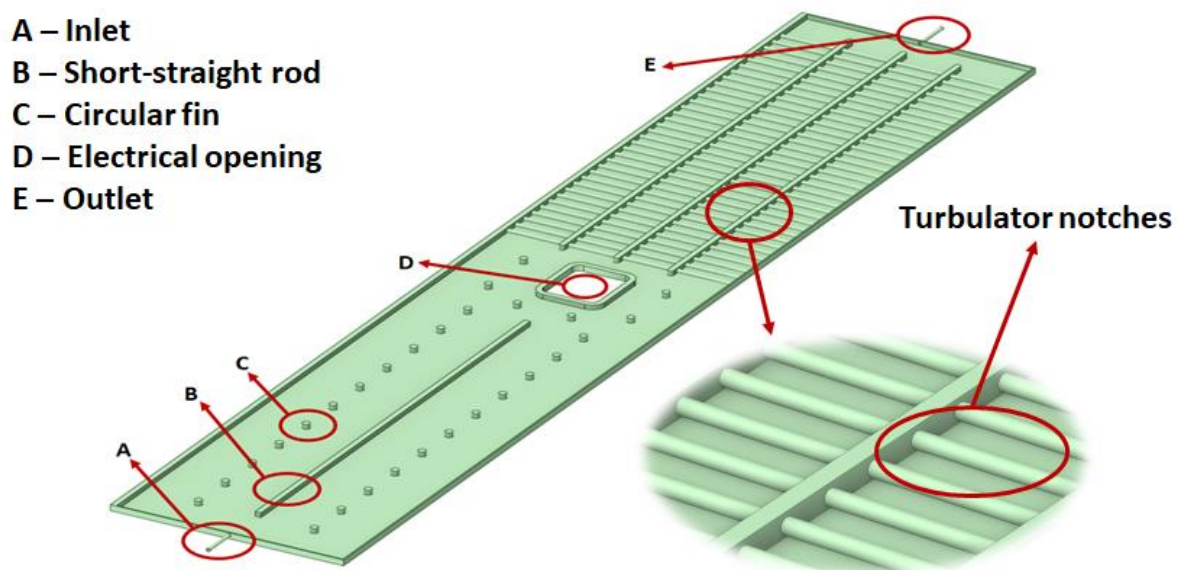


**Figure 6-6. The cylindrical turbulator notches**

In addition to turbulator notches, the thickness of the cooling system was modified. The thickness of the working fluid flow section was 6 mm in the initial design. The thickness of the fluid flow section was extended to 8 mm within the enhanced design to provide a higher amount of working fluid and achieve higher thermal efficiency.

The designed cooling system had 1,670 x 965 x 12 mm dimensions with 7.014 m<sup>2</sup> of total surface area and a surface area of 1.59 m<sup>2</sup> in contact with the rear side of the PV module. The thermal collector allows 0.0109 m<sup>3</sup> working fluid to operate while cooling the PV module and harvesting waste heat.

### **6.3 Numerical analysis of the final PV/T design**

The same procedure explained in section 6.1 was employed for the final design of the cooling system. A 3-D CFD model of the final geometry design was developed in Ansys SpaceClaim 3-D CAD modeling. The middle section was chosen to be studied to obtain a high-resolution mesh to achieve accurate results and reduce computational time as in the numerical analysis

of the initial design. The fluid domain was extracted from the solid domain to be analyzed. The developed fluid domain was discretized using Fluent meshing.

The boundary conditions for the inlet given in Table 6-3 were defined for the numerical analysis. The average PV cell layer temperature and outlet temperature were investigated. The final design's thermal output, efficiency, and cooling effect were analyzed.

The average temperature of the PV cell layer, outlet temperature, thermal energy generated, and thermal efficiency for each case are given in Table 6-6.

**Table 6-6. Numerical model results of final cooling system design under NOCT conditions**

| Case | $\dot{m}_f$ (kg/s) | $T_{f,in}$ (°C) | $T_{f,out}$ (°C) | $T_{pvcells}$ (°C) | Qu (W)   | $\eta_{thermal}$ (%) |
|------|--------------------|-----------------|------------------|--------------------|----------|----------------------|
| 1    | 0.03               | 15              | 25.78            | 26.97              | 1,030.36 | 79.92                |
|      | 0.05               |                 | 20.65            | 21.81              | 1,079.87 | 83.76                |
|      | 0.08               |                 | 18.84            | 20.50              | 1,100.58 | 85.37                |
|      | 0.10               |                 | 17.92            | 19.85              | 1,115.28 | 86.51                |
|      | 0.13               |                 | 17.33            | 19.39              | 1,113.15 | 86.34                |
| 2    | 0.03               | 20              | 29.96            | 30.58              | 951.68   | 73.82                |
|      | 0.05               |                 | 25.23            | 26.65              | 1,000.20 | 77.58                |
|      | 0.08               |                 | 23.55            | 25.45              | 1,018.57 | 79.01                |
|      | 0.10               |                 | 22.69            | 24.77              | 1,026.95 | 79.66                |
|      | 0.13               |                 | 22.14            | 24.32              | 1,023.80 | 79.41                |
| 3    | 0.03               | 25              | 34.13            | 34.22              | 873.18   | 67.73                |
|      | 0.05               |                 | 29.79            | 31.49              | 916.58   | 71.09                |
|      | 0.08               |                 | 28.25            | 30.35              | 931.76   | 72.27                |
|      | 0.10               |                 | 27.46            | 29.70              | 938.93   | 72.83                |
|      | 0.13               |                 | 26.96            | 29.26              | 935.62   | 72.57                |

The average temperature of each PV cell layer decreased when the inlet flow rate increased up to 0.13 kg/s or the inlet temperature decreased as in the initial design. Increasing the mass flow rate from 0.03 kg/s to 0.10 kg/s and decreasing the inlet temperature from 25 °C to 15 °C led to an 18.78% improvement in thermal efficiency and keeping the PV cell layer temperature at 19.85 °C. The final design of the cooling system was able to reduce the temperature of the PV cell layer by 24.61 °C when the inlet mass flow rate and temperature were 0.13 kg/s and 15 °C, respectively. The maximum thermal efficiency of 86.51% was achieved with the inlet mass flow rate of 0.10 kg/s and the inlet temperature of 15 °C. The increase in inlet temperature led to a drop in the thermal efficiency of the cooling system. The maximum thermal efficiency improvement was observed in all cases when the mass flow rate was increased from 0.03 kg/s to 0.05 kg/s. In cases 1, 2, and 3, the improvements were 4.80%, 5.10%, and 4.97%, respectively.

The maximum thermal efficiency of 80.26% was achieved with the initial design of the cooling system. The geometrically enhanced final design was able to achieve the maximum thermal

efficiency of 86.51% under the same conditions, showing a 7.79% improvement. In both cases, the PV cell layer temperature was maintained under 25 °C, optimal for maximum electrical conversion efficiency. In the initial design, the average PV cell layer temperature was 19.53 °C, whereas the final design was able to maintain the PV cell layer temperature at 19.85 °C. A difference of 0.32 °C was observed. The post-processing procedure was carried out to visualize the temperature distribution of the PV cell layer in cases where the maximum thermal efficiency was observed, as shown in Figure 6-7.

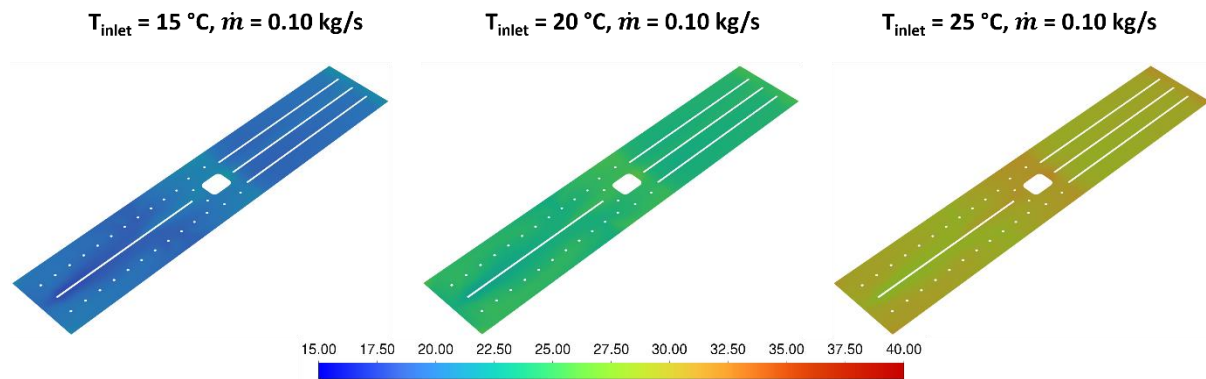


**Figure 6-7. The PV cell layer temperature distribution of cases for the final design**

The maximum thermal efficiency of 86.51%, 79.66%, and 72.83% was achieved with the inlet temperature of 15 °C, 20 °C, and 25 °C at a constant flow rate of 0.10 kg/s, respectively. The post-processing results showed that the average PV cell layer temperature was 19.85 °C, 24.77 °C, and 29.70 °C for the cases studied.

The final design was also able to maintain a uniform temperature distribution for all cases, as seen in Figure 6-7. The increase in the inlet temperature from 15 °C to 20 °C and 25 °C led to an increase in PV cell layer temperature by 4.92 °C and 9.85 °C, respectively.

A grid independence study was conducted similarly as in the case of numerical analysis of the initial design. The convergence criteria were set for  $10^{-10}$  for the monitored residuals, namely, continuity, x-velocity, y-velocity, and z-velocity. In contrast, the monitored residual for the energy equation was set to  $10^{-16}$ . The residual taken from the numerical solver is shown in Figure 6-8.



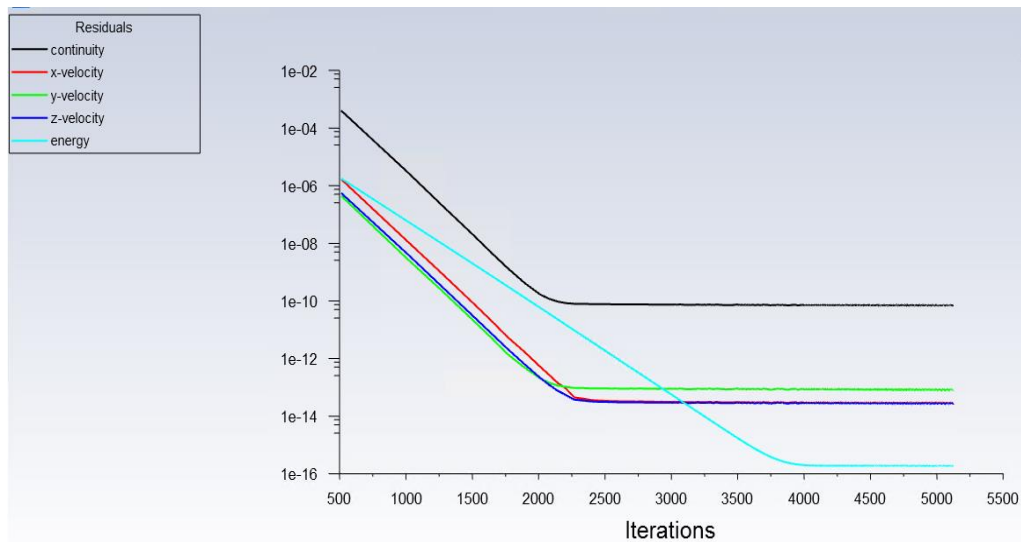


**Figure 6-8. The residual taken from the numerical solver**

The 1-D numerical thermal model was used to estimate the electrical conversion efficiency and power output of the PV module, as given in Table 6-7.

**Table 6-7. The electrical conversion efficiency and power output of the final design at NOCT conditions**

| Case | $T_{pvcells\_cooled}$ (°C) | $T_{npvcells}$ (°C) | $P_{cooled}$ (W) | $P_{non-cooled}$ (W) | $\eta_{pv\_cooled}$ (%) | $\eta_{pv\_non-cooled}$ (%) |
|------|----------------------------|---------------------|------------------|----------------------|-------------------------|-----------------------------|
| 1    | 26.97                      | 44.00               | 257.79           | 241.90               | 18.96                   | 17.79                       |
|      | 21.81                      | 44.00               | 259.94           | 241.90               | 19.12                   | 17.79                       |
|      | 20.50                      | 44.00               | 259.94           | 241.90               | 19.12                   | 17.79                       |
|      | 19.85                      | 44.00               | 259.94           | 241.90               | 19.12                   | 17.79                       |
|      | 19.39                      | 44.00               | 259.94           | 241.90               | 19.12                   | 17.79                       |
| 2    | 30.58                      | 44.00               | 253.85           | 241.90               | 18.67                   | 17.79                       |
|      | 26.65                      | 44.00               | 258.14           | 241.90               | 18.99                   | 17.79                       |
|      | 25.45                      | 44.00               | 259.44           | 241.90               | 19.08                   | 17.79                       |
|      | 24.77                      | 44.00               | 259.94           | 241.90               | 19.12                   | 17.79                       |
|      | 24.32                      | 44.00               | 259.94           | 241.90               | 19.12                   | 17.79                       |
| 3    | 34.22                      | 44.00               | 249.87           | 241.90               | 18.38                   | 17.79                       |
|      | 31.49                      | 44.00               | 252.85           | 241.90               | 18.60                   | 17.79                       |
|      | 30.35                      | 44.00               | 254.10           | 241.90               | 18.69                   | 17.79                       |
|      | 29.70                      | 44.00               | 254.81           | 241.90               | 18.74                   | 17.79                       |
|      | 29.26                      | 44.00               | 255.29           | 241.90               | 18.78                   | 17.79                       |

Cases maintained the average temperature of the PV cell layer under 25 °C, leading to the PV module's maximum electrical conversion efficiency and power output. The electrical efficiency improvement was 7.5% in the cases where the PV cell layer temperature was maintained at 25 °C or lower. The PV cell layer temperature was increased by 9.87 °C when the inlet temperature was increased from 15 °C to 25 °C at a constant inlet mass flow rate of 0.13 kg/s.



In Figure 6-11, the interior of the cooling system before the completion of the manufacturing process is shown.

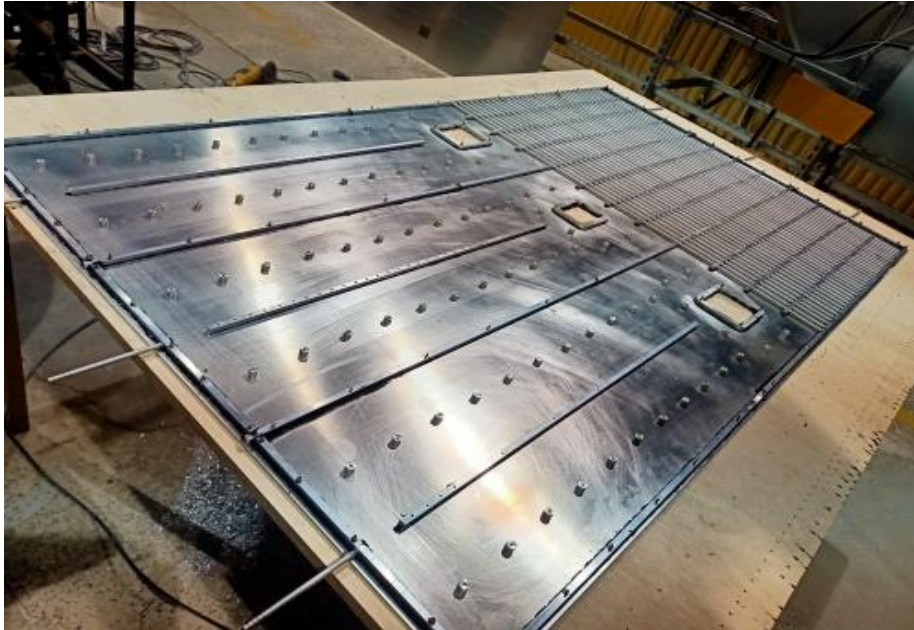


**Figure 6-11. The interior of the cooling system**

When the cooling system prototype was manufactured, the laboratory was prepared for the initial thermal tests of the design.

## **6.5 Summary**

In this chapter, based on the summary drawn from the thermal modeling of the PV module and the extensive literature review, the initial design of the cooling system was prepared. A 3-D CAD model of the design was developed and studied numerically. The initial design was able to achieve 80.26% thermal efficiency while maintaining the maximum electrical efficiency of the PV module. The maximum temperature reduction of 25.21 °C occurred when the inlet mass flow rate and temperature were 0.13 kg/s and 15 °C, respectively.

The first design was further developed for the enhanced cooling system to allow higher thermal efficiency by changing the geometrical properties of the initial design. The enhanced cooling system design achieved a maximum thermal efficiency of 86.51% under the same conditions while maintaining the maximum electrical efficiency of the PV module. The maximum temperature reduction of 24.61 °C occurred when the inlet mass flow rate and temperature were 0.13 kg/s and 15 °C, respectively. Both designs were able to maintain the temperature of the PV cell layer under 25 °C. However, the modified and enhanced system design led to an improvement of 7.79% in thermal efficiency compared to the initial design. The enhanced system design was then manufactured and prepared for the laboratory tests.

## **Chapter 7 - The laboratory tests of the designed cooling system**

The performance of the PV/T systems needs to be characterized in terms of their steady-state and dynamic performance to accurately predict thermal and electrical energy production. Conventional solar collectors have well-established testing standards such as EN 12975-2:2006. The standard specifies test methods for validating the durability, reliability, and safety requirements for liquid heating collectors. However, there is no precise agreed testing standard for PV/T systems, as the PV/T market is newly developed, and the performance data available is scarce.

This chapter presents the experiments conducted with the designed and manufactured cooling system. The cooling system coupled with and without a PV module is investigated thermally in the Cracow University of Technology laboratory, and results are presented. The numerical model of the enhanced cooling system coupled with and without the PV module was validated using the experimental test results.

### **Laboratory thermal test of the designed cooling system**

The laboratory thermal tests were conducted on the manufactured cooling system to analyze the thermal efficiency and heat transfer characteristics under various conditions using water as a working fluid. The initial tests were conducted on the cooling system without coupling with the PV module in the laboratory. The collected data was used to validate the numerical model of the cooling system.

The validation of the numerical model of the cooling system led to coupling the cooling system with the PV module using thermal interface material. The use of thermal grease prevents the air, which is an excellent thermal insulator. The inhibition of air on heat transfer from the PV module to the cooling system was minimized using the liquid properties of thermal grease. Various inlet mass flow rates were tested in the laboratory under different heat flux conditions.

The data obtained during the experiments of the PV/T system were used to validate the numerical model of the PV/T system.

### **7.1 Thermal tests of the cooling system**

The test rig was prepared using three heating radiators, each with three modes of heating powers, P1-800 W, P2-1,600 W, and P3-2,500 W, placed 0.5 m above the cooling system. The test rig was equipped with a flow meter, pump, water storage tank, and K-type sheathed thermocouples in the inlet and outlet sections, as illustrated in the schematic shown in Figure 7-1. A self-calibrating digital heat flux sensor was used to measure the heat flux on the surface of the cooling system.

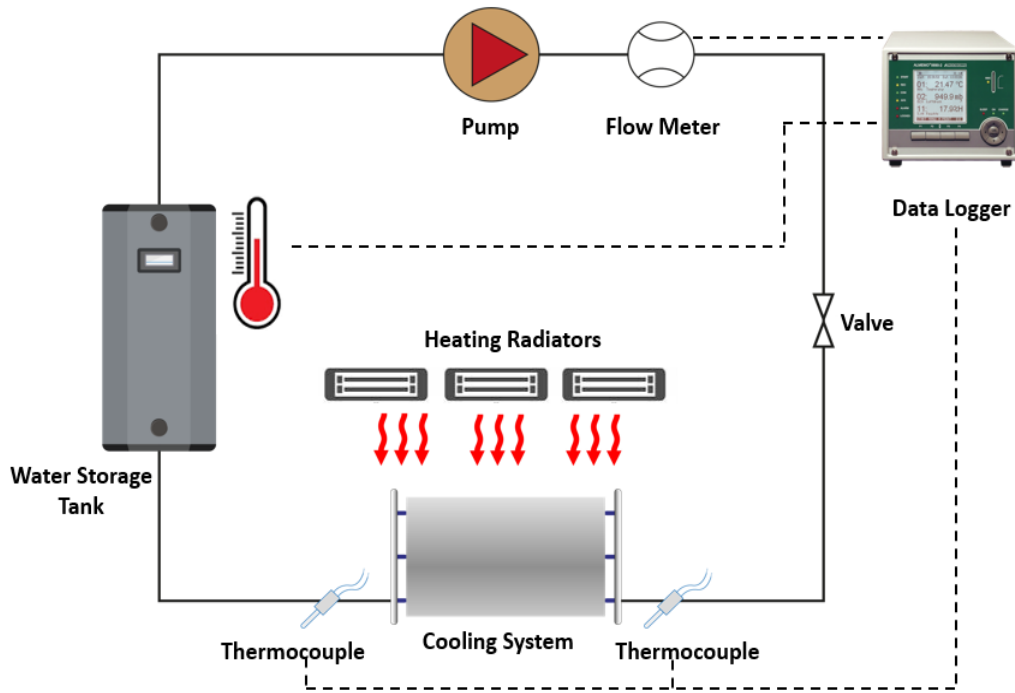


**Figure 7-1. A schematic of the test rig**

The specifications of sensors and equipment used in the experiments are as follows:

- Three heating radiators (source of heat 2-halogen lamp) with three modes of heating power, P1-800 W, P2-1,600 W, and P3-2,500 W, were used to reject heat to the thermal collector.
- A water storage tank without a coil with a 500 L storage capacity was connected to store the working fluid.
- A flow meter was used to measure the flow rate at the inlet, with a measurement range between 0 and 25 L/min powered by a 5V DC battery and with a 1% flow rate uncertainty.
- A water pump, 12 V, to circulate water with a maximum flow rate and max water head of 800 L/h and 5 m, respectively. The maximum power consumption of the pump was 22 W.
- K-type sheathed thermocouples with the capability of measuring temperatures up to 900 °C. The uncertainty of the thermocouples was  $\pm 0.5^{\circ}\text{C}$ .
- A self-calibrating digital heat flux sensor with a nominal sensitivity of  $60 \times 10^{-3} \text{ mV}/(\text{W}/\text{m}^2)$ . The sensor was also able to determine the temperature up to 150 °C. The uncertainty of the measured heat flux was  $\pm 5 \text{ W}/\text{m}^2$ .
- A data logger was used for data acquisition.

As the designed cooling system consists of three inlets and outlets, two collectors were produced and connected to inlet and outlet sections to simplify the control of the flow in the

stand. The cooling system was divided into 18 areas to measure the heat and obtain accurate data. The areas were named from A1 to A18, starting from the left corner of the outlet section to the right corner of the inlet section, as shown in Figure 7-2. A self-calibrating digital heat flux sensor with a nominal sensitivity of  $60 \times 10^{-3} \text{ mV}/(\text{W}/\text{m}^2)$  and with dimensions of  $100 \times 30 \times 1.5 \text{ mm}$  was used to measure the heat flux on each surface area.

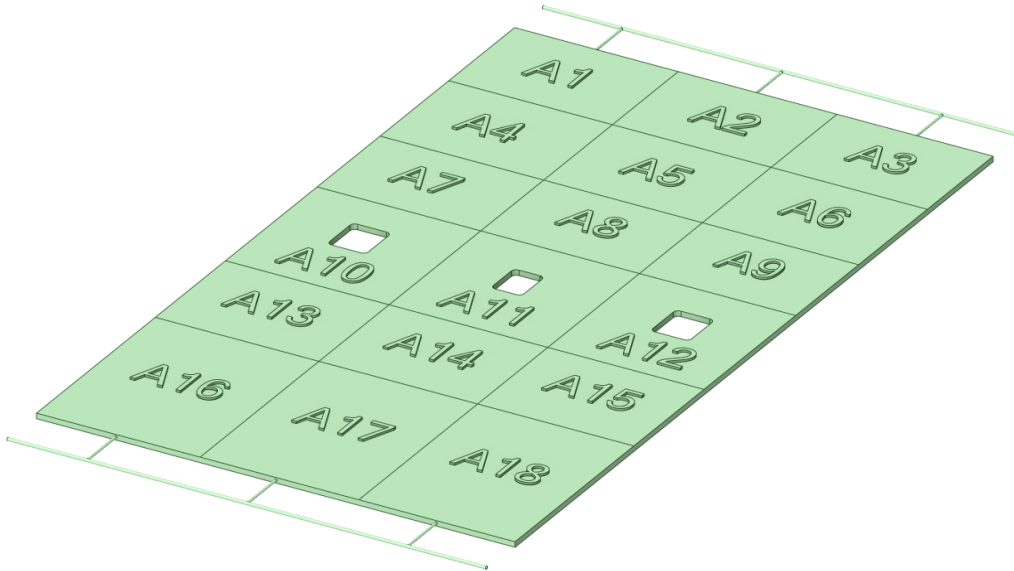


**Figure 7-2. Heat flux measurements on the surface of the cooling system**

The dimensions of the areas, along with measured heat flux on each surface area for the case of a mass flow rate of  $0.0325 \text{ kg/s}$ , are given in Table 7-1.

**Table 7-1. Dimensions of the divided surface areas**

| Area Number | Length (m) | Width (m) | Area ( $\text{m}^2$ ) | Heat flux ( $\text{W}/\text{m}^2$ ) |
|-------------|------------|-----------|-----------------------|-------------------------------------|
| A1          | 0.23       | 0.321     | 0.07383               | 555.3                               |
| A2          | 0.23       | 0.323     | 0.07429               | 755.2                               |
| A3          | 0.23       | 0.321     | 0.07383               | 532.2                               |
| A4          | 0.24       | 0.321     | 0.07704               | 1,118.6                             |
| A5          | 0.24       | 0.323     | 0.07752               | 1,742.5                             |
| A6          | 0.24       | 0.321     | 0.07704               | 1,220.9                             |
| A7          | 0.22       | 0.321     | 0.07062               | 1,027.6                             |
| A8          | 0.22       | 0.323     | 0.07106               | 1,478.3                             |
| A9          | 0.22       | 0.321     | 0.07062               | 979.8                               |
| A10         | 0.32       | 0.321     | 0.10272               | 1,425.7                             |
| A11         | 0.32       | 0.323     | 0.10336               | 1,995.5                             |
| A12         | 0.32       | 0.321     | 0.10272               | 1,358.6                             |
| A13         | 0.25       | 0.321     | 0.08025               | 1,043.5                             |
| A14         | 0.25       | 0.323     | 0.08075               | 1,713.2                             |
| A15         | 0.25       | 0.321     | 0.08025               | 1,012.5                             |
| A16         | 0.41       | 0.321     | 0.13161               | 913.1                               |
| A17         | 0.41       | 0.323     | 0.13243               | 1,292.1                             |
| A18         | 0.41       | 0.321     | 0.13161               | 865.6                               |

The cooling system was tested while the heating radiators worked at the maximum P3-2,500 W heating mode. The cooling system was only tested at maximum to determine the thermal behavior and validate the developed CFD model before coupling with the PV module. The average heat flux on the total surface of the cooling system was found to be 1,178.58 W/m<sup>2</sup> for case 1, given in Table 3. The inlet and outlet temperatures are 22.40 °C and 35.20 °C, respectively, for the tested mass flow rate, 0.0325 kg/s. Similar experiments were conducted for various flow rates, and a summary of the tests is included in Table 7-2.

**Table 7-2. Preliminary experimental test results**

| Case | Heat flux (W/m <sup>2</sup> ) | Flow rate (kg/s) | T <sub>inlet</sub> (°C) | T <sub>outlet</sub> (°C) |
|------|-------------------------------|------------------|-------------------------|--------------------------|
| 1    | 1,178.6                       | 0.0325           | 22.40                   | 35.20                    |
| 2    | 1,184.5                       | 0.0367           | 18.20                   | 29.90                    |
| 3    | 1,184.4                       | 0.0542           | 21.70                   | 29.75                    |
| 4    | 1,244.4                       | 0.0683           | 21.10                   | 27.63                    |
| 5    | 1,281.6                       | 0.0958           | 20.90                   | 25.35                    |
| 6    | 1,300.2                       | 0.1417           | 15.90                   | 18.81                    |

The inlet mass flow rate and temperature were varied to analyze the performance of the cooling system. The temperature difference between the inlet and outlet of the system, total heat transferred to the fluid, and thermal efficiency of the system for each case are given in Table 7-3.

**Table 7-3. Useful thermal energy gain and thermal efficiency of the system**

| Case | Flow rate (kg/s) | T <sub>inlet</sub> (°C) | T <sub>outlet</sub> (°C) | ΔT (°C) | Q <sub>u</sub> (W) | η <sub>th</sub> (%) |
|------|------------------|-------------------------|--------------------------|---------|--------------------|---------------------|
| 1    | 0.0325           | 22.40                   | 35.20                    | 12.80   | 1,739.71           | 91.60%              |
| 2    | 0.0367           | 18.20                   | 29.90                    | 11.70   | 1,794.08           | 93.99%              |
| 3    | 0.0542           | 21.70                   | 29.75                    | 8.05    | 1,823.53           | 95.54%              |
| 4    | 0.0683           | 21.10                   | 27.63                    | 6.53    | 1,866.08           | 93.05%              |
| 5    | 0.0958           | 20.90                   | 25.35                    | 4.45    | 1,783.45           | 86.35%              |
| 6    | 0.1417           | 15.90                   | 18.81                    | 2.91    | 1,724.03           | 82.28%              |

The maximum thermal efficiency of 95.54% was achieved with the inlet flow rate of 0.0542 kg/s and inlet temperature of 21.70 °C under 1,184.4 W/m<sup>2</sup>. The water temperature was increased by 8.05 °C, leading to a thermal output of 1.82 kW. The further increase in the flow rate caused a drop in the thermal efficiency despite the decrease in the inlet temperature.

## 7.2 CFD model validation of the cooling system

The CFD model of the cooling system was prepared using Ansys SpaceClaim 3D CAD modeling software during the design procedure. The model consisted of fluid and solid domains. The inner side of the solid domain, along with the fluid domain, is shown in Figure 7-3. The solid domain dimensions were 1,670 x 965 x 12 mm, excluding the collectors at the inlet and outlet, whereas the dimensions of the fluid domain were 1,666 x 945 x 8 mm.

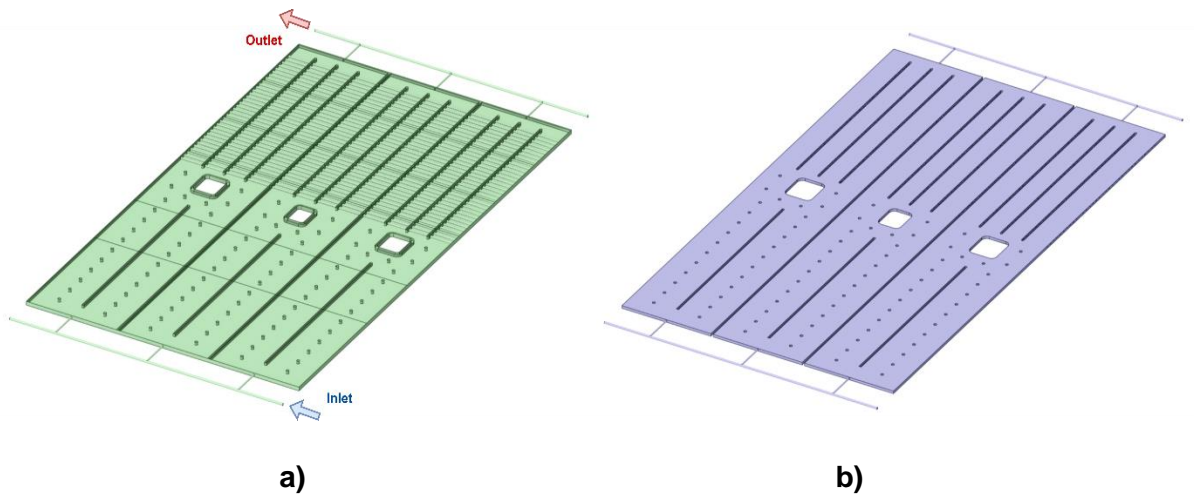


**Figure 7-3. The cooling system, a) interior of the solid domain, b) fluid domain**

The cooling system consisted of three divided sections, each with an inlet and outlet. In order to reduce the computational time and prepare a very high-resolution mesh to achieve accurate results, each divided section of the cooling system was investigated separately. Three channels of the cooling system; two of the channels (left and right) had the dimensions 1,670 x 321 x 12 mm in the solid domain, and the channel in the middle had the dimensions 1,670 x 323 x 12 mm in the solid domain. Each fluid domain inside the solid domains had the same dimensions of 1,666 x 315 x 8 mm. The six faces for heat flux boundary conditions shown in Figure 7-2 were created on the surface of each solid domain. The completed geometry preparation in SpaceClaim led to mesh generation using Ansys Fluent Meshing in the pre-processing phase. In the meshing process, two boundary layers were implemented in the geometries. The first boundary layer consisted of two layers and took place at the solid-fluid interface to adequately capture the conjugate heat transfer. The second boundary layer with three layers was inserted at fluid-region walls to observe the gradients efficiently. The Poly-Hexcore elements were used to generate high-quality and efficient meshes. When the meshing process was completed, the solver settings were inserted into the commercial software. A 3-D, steady, laminar, and incompressible flow was modeled using Ansys Fluent. The gravity was defined as  $9.81 \text{ m/s}^2$  in the  $-y$  direction. The energy equation was activated in order to perform conjugate heat transfer in domains, and the laminar flow type was chosen as the velocity of the fluid is relatively slow, indicating a low Reynolds Number (ranging between 67 and 292). The working fluid was chosen to be water, and a user-defined function (UDF) was prepared for temperature-dependent viscosity, whereas aluminum was selected and modified with the parameters given in Table 6-1 for the solid domain. The boundary conditions were defined in the software. At the inlet, the velocity and the temperature of the working fluid taken from the experimental data were used. At the outlet, the pressure-outlet boundary condition was set. On the surfaces where the measurements were taken, fixed heat



flux condition from wall boundary conditions was set. The convective heat transfer was defined on the side walls of the cooling system with a constant air temperature of 20 °C with the convective heat transfer coefficient calculated using Eq. 12. The comparison of the outlet temperature results of the experiments and the CFD model, along with percentage error, is given in Table 7-4.

**Table 7-4. Comparison of outlet temperature between measurements and CFD model**

| Case | T <sub>outlet_exp</sub> (°C) | T <sub>outlet_cfd</sub> (°C) | Error (%) |
|------|------------------------------|------------------------------|-----------|
| 1    | 34.85                        | 35.89                        | 1.96      |
| 2    | 29.49                        | 30.32                        | 1.40      |
| 3    | 29.75                        | 30.49                        | 2.51      |
| 4    | 27.00                        | 27.86                        | 0.83      |
| 5    | 25.00                        | 25.62                        | 1.07      |
| 6    | 18.50                        | 19.05                        | 1.28      |

T<sub>outlet\_exp</sub> and T<sub>outlet\_cfd</sub> stand for the measured and CFD model outlet temperatures, respectively, in Table 7-4. The average error for outlet temperature between the measurements and the CFD model was 1.51%.

The same boundary conditions were applied to the previous design to compare the outlet temperature and the thermal efficiency of the cooling system. The outlet temperature and the thermal efficiency of the previous design are given in Table 7-5.

**Table 7-5. Outlet temperature and thermal efficiency of the initial design**

| Case | Flow rate (kg/s) | T <sub>inlet</sub> (°C) | T <sub>outlet_cfd_previous</sub> (°C) | ΔT (°C) | Q <sub>u</sub> (W) | η <sub>th</sub> (%) |
|------|------------------|-------------------------|---------------------------------------|---------|--------------------|---------------------|
| 1    | 0.0325           | 22.40                   | 33.59                                 | 11.19   | 1,521.41           | 80.10%              |
| 2    | 0.0367           | 18.20                   | 28.43                                 | 10.23   | 1,569.11           | 82.20%              |
| 3    | 0.0542           | 21.70                   | 28.95                                 | 7.25    | 1,642.31           | 86.04%              |
| 4    | 0.0683           | 21.10                   | 26.84                                 | 5.74    | 1,639.17           | 81.74%              |
| 5    | 0.0958           | 20.90                   | 25.04                                 | 4.14    | 1,659.21           | 80.33%              |
| 6    | 0.1417           | 15.90                   | 18.51                                 | 2.61    | 1,546.29           | 73.80%              |

In Table 7-5, T<sub>outlet\_cfd\_previous</sub> is the outlet temperature obtained from the initial design. The difference of 7.25 °C between the inlet and the outlet temperature led to the generation of 1.64 kW of thermal energy for the initial design in case 3. As in the enhanced cooling system results, the initial design also achieved maximum thermal efficiency, 86.04%, with the inlet mass flow rate of 0.0542 kg/s and the inlet temperature of 21.70 °C whereas the enhanced cooling system design was able to reach up to 95.54% of maximum thermal efficiency under the same conditions. The results showed that the final and manufactured design of the cooling system led to an 11.04% thermal efficiency improvement. The enhanced cooling system was able to generate 0.18 kW more thermal energy than the initial cooling system design. The enhanced cooling system design increased the outlet temperature by 0.91 °C on average.

A post-processing of the results was realized to analyze the temperature distribution of the solid domain, as shown in Figure 7-4.

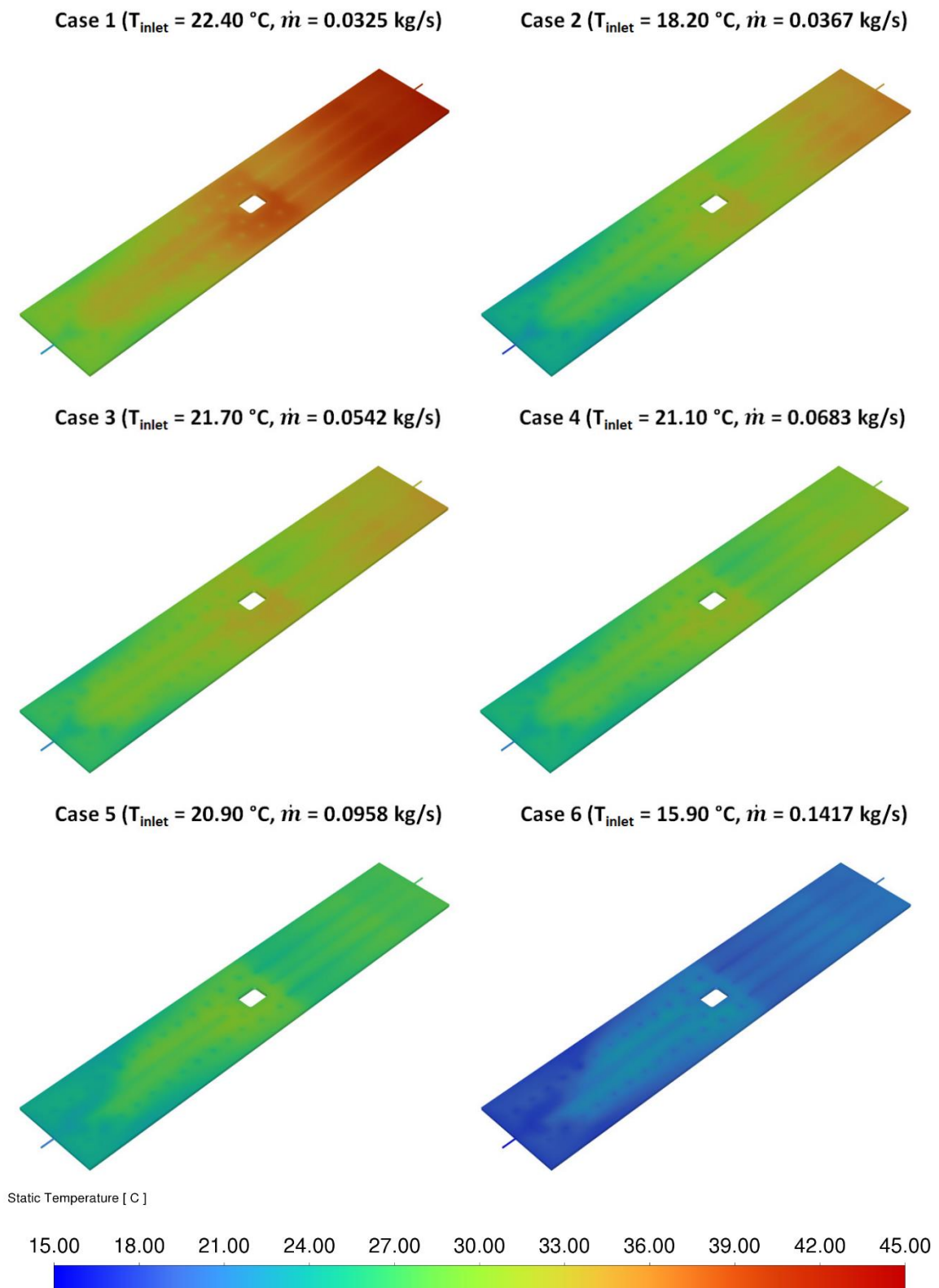
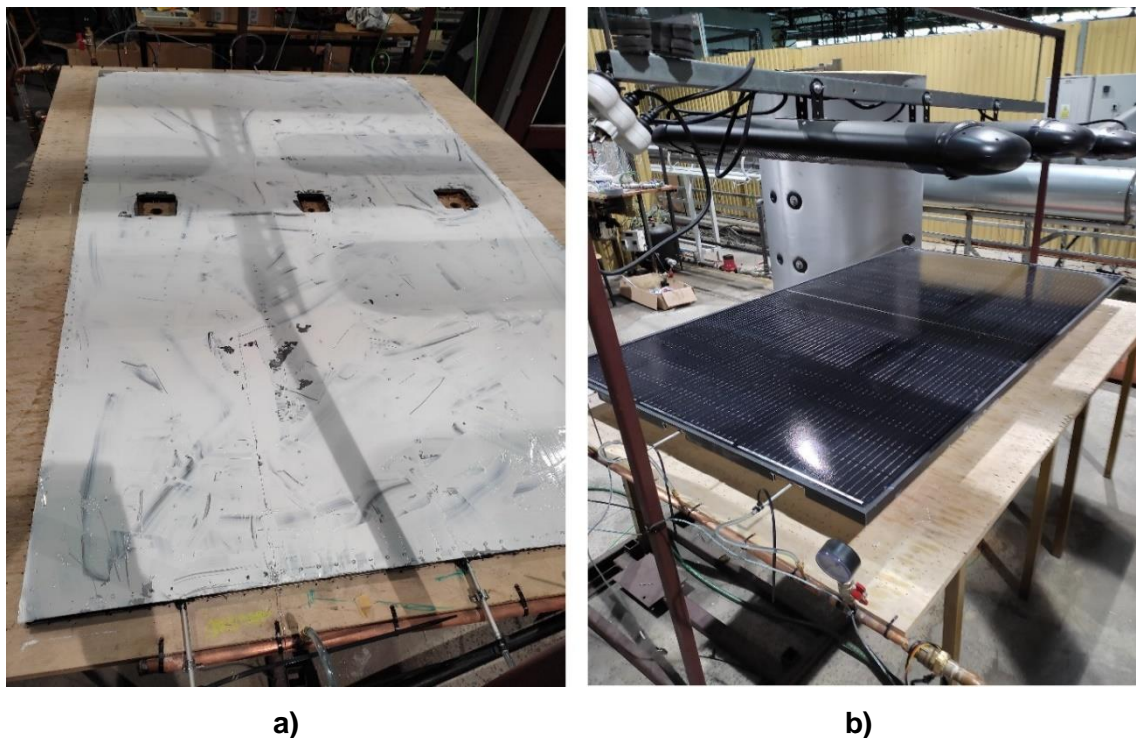


Figure 7-4. The temperature distribution of the solid domains

The temperature distribution results showed that the increase in the mass flow rate and decrease in the inlet temperature led to more uniform cooling, as seen in cases 1 to 6. Despite the non-uniform heat flux on the surface of the cooling system, the design was able to provide uniform temperature distribution on the solid domain. From case 1 to case 3, the increase in mass flow rate led to minimizing the over-heated regions. In case 4, reaching the inlet mass flow rate of 0.0683 kg/s exhibited uniform cooling of the solid domain. The further increase in inlet mass flow rate and decrease in the inlet temperature allowed for uniform cooling.

### 7.3 Thermal tests of the cooling system coupled with the PV module

The experimentally analyzed cooling system coupled with the PV module to conduct thermal tests. The commercial PV module given in Table 5-2 was used to couple with the cooling system. Thermal grease was used between the cooling system and the rear side of the PV module to avoid air bubbles forming and prevent less effective heat transfer. Three K-type sheathed thermocouples were inserted between the cooling system and the rear side of the PV module to compare the average rear side temperature of the PV module with and without an active cooling system. The procedure of the thermal greasing and assembling of the PV/T system is shown in Figure 7-5.



**Figure 7-5. The procedure of assembling the PV/T system, a) thermal greasing of the cooling system, b) complete PV/T system and test rig**

Various inlet mass flow rates and temperatures were investigated under different heat flux conditions, P1-800 W, P2-1,600 W, and P3-2,500 W, as given in Table 7-6. A similar approach shown in Figure 7-2 was used to achieve accurate heat flux data from the PV module surface.

**Table 7-6. Experimental data of the cooling system coupled with the PV module**

| Case | Heating mode | Heat flux (W/m <sup>2</sup> ) | Flow rate (kg/s) | T <sub>inlet</sub> (°C) | T <sub>outlet</sub> (°C) |
|------|--------------|-------------------------------|------------------|-------------------------|--------------------------|
| 1    | P1           | 189.76                        | 0.0042           | 17.70                   | 32.80                    |
| 2    | P1           | 184.71                        | 0.0062           | 20.10                   | 30.66                    |
| 3    | P1           | 266.48                        | 0.0225           | 12.30                   | 16.80                    |
| 4    | P1           | 280.55                        | 0.0375           | 11.40                   | 14.30                    |
| 5    | P2           | 401.98                        | 0.0175           | 20.20                   | 28.80                    |
| 6    | P2           | 469.04                        | 0.0458           | 11.50                   | 15.60                    |
| 7    | P3           | 472.35                        | 0.0083           | 19.50                   | 41.00                    |
| 8    | P3           | 592.89                        | 0.0458           | 11.90                   | 17.30                    |

The inlet and outlet temperatures of the PV/T system, total heat transferred to the fluid, and thermal efficiency of the system for each case are given in Table 7-7.

**Table 7-7. The thermal energy generation and thermal efficiency of the cooling system coupled with the PV module**

| Case | Flow Rate (kg/s) | T <sub>inlet</sub> (°C) | T <sub>outlet</sub> (°C) | ΔT (°C) | Q <sub>u</sub> (W) | η <sub>th</sub> |
|------|------------------|-------------------------|--------------------------|---------|--------------------|-----------------|
| 1    | 0.0042           | 17.70                   | 32.80                    | 15.10   | 263.62             | 81.75%          |
| 2    | 0.0062           | 20.10                   | 31.00                    | 10.56   | 272.85             | 86.92%          |
| 3    | 0.0225           | 12.30                   | 16.80                    | 4.50    | 424.24             | 93.68%          |
| 4    | 0.0375           | 11.40                   | 14.30                    | 2.90    | 455.66             | 95.57%          |
| 5    | 0.0175           | 20.20                   | 28.80                    | 8.60    | 630.60             | 92.31%          |
| 6    | 0.0458           | 11.50                   | 15.60                    | 4.10    | 747.37             | 93.76%          |
| 7    | 0.0083           | 19.50                   | 41.00                    | 21.50   | 750.71             | 93.52%          |
| 8    | 0.0458           | 11.90                   | 17.30                    | 5.40    | 972.03             | 96.47%          |

The maximum thermal efficiency of 96.47% was achieved with the inlet flow rate of 0.0458 kg/s and inlet temperature of 11.90 °C under 592.89 W/m<sup>2</sup>. The water temperature was increased by 5.40 °C, leading to a maximum thermal output of 972.03 W. The comparison between the rear side temperature of the cooled and non-cooled PV module is given in Table 7-8.

**Table 7-8. The rear side temperature of the cooled and non-cooled PV module**

| Case | Heating mode | Heat flux (W/m <sup>2</sup> ) | T <sub>rear_non-cooled</sub> (°C) | T <sub>rear_cooled</sub> (°C) |
|------|--------------|-------------------------------|-----------------------------------|-------------------------------|
| 1    | P1           | 189.76                        | 34.69                             | 28.53                         |
| 2    | P1           | 184.71                        | 34.32                             | 27.54                         |
| 3    | P1           | 266.48                        | 40.14                             | 17.57                         |
| 4    | P1           | 280.55                        | 41.12                             | 15.89                         |
| 5    | P2           | 401.98                        | 49.21                             | 28.94                         |
| 6    | P2           | 469.04                        | 53.46                             | 17.95                         |
| 7    | P3           | 472.35                        | 53.67                             | 37.07                         |
| 8    | P3           | 592.89                        | 60.62                             | 20.88                         |

In Table 7-8,  $T_{\text{rear\_non-cooled}}$  and  $T_{\text{rear\_cooled}}$  stand for the rear side temperature of the non-cooled and cooled PV module, respectively. The rear side temperature of the PV module was used to estimate the PV cell layer temperature using the 1-D transient numerical thermal model explained in section 5. The temperature of the PV cell layer, along with the power output and electrical conversion efficiency of the PV module, are given in Table 7-9.

**Table 7-9. The power output and the electrical conversion efficiency comparison of the cooled and non-cooled PV module**

| Case | $T_{\text{pvcells\_cooled}} (^{\circ}\text{C})$ | $T_{\text{npvcells}} (^{\circ}\text{C})$ | $P_{\text{cooled}} (\text{W})$ | $P_{\text{non-cooled}} (\text{W})$ | $\eta_{\text{pv\_cooled}}$ | $\eta_{\text{pv\_non-cooled}}$ |
|------|---|--|--------------------------------|------------------------------------|----------------------------|--------------------------------|
| 1    | 29.15   | 35.58                                    | 319.34                         | 310.56                             | 18.79%                     | 18.27%                         |
| 2    | 28.29   | 35.22                                    | 320.51                         | 311.05                             | 18.86%                     | 18.30%                         |
| 3    | 18.09   | 40.99                                    | 325.00                         | 303.17                             | 19.12%                     | 17.84%                         |
| 4    | 16.48   | 41.97                                    | 325.00                         | 301.84                             | 19.12%                     | 17.76%                         |
| 5    | 29.28   | 49.95                                    | 319.16                         | 290.94                             | 18.78%                     | 17.12%                         |
| 6    | 18.17   | 54.23                                    | 325.00                         | 285.10                             | 19.12%                     | 16.78%                         |
| 7    | 37.74   | 54.44                                    | 307.61                         | 284.81                             | 18.10%                     | 16.76%                         |
| 8    | 21.20   | 61.92                                    | 325.00                         | 274.60                             | 19.12%                     | 16.16%                         |

The results showed that in case 8, the PV cell layer temperature was reduced by 40.72 °C, leading to an improvement of 18.32% in electrical efficiency. In the last case, the estimated power output increase was 50.4 W compared to the PV module without active cooling.

#### 7.4 CFD model validation of the cooling system coupled with the PV module

A 3-D, steady, laminar, and incompressible flow CFD study of the PV/T system was performed, similar to the work carried out in chapter six. The developed geometry of the PV/T system was meshed by taking the same approach. The boundary conditions, such as heat flux, inlet mass flow rate, and temperature, were defined using Table 7-6. The outlet temperature of the CFD model was compared to the data obtained in experiments, as shown in Table 7-10.

**Table 7-10. Comparison of outlet temperature between measurements and PV/T system CFD model**

| Case | $T_{\text{outlet\_exp}} (^{\circ}\text{C})$ | $T_{\text{outlet\_cfd}} (^{\circ}\text{C})$ | Error (%) |
|------|---|---|-----------|
| 1    | 32.80                                       | 33.61                                       | 2.47      |
| 2    | 30.66                                       | 31.52                                       | 2.80      |
| 3    | 16.80                                       | 17.13                                       | 1.96      |
| 4    | 14.30                                       | 14.79                                       | 3.43      |
| 5    | 28.80                                       | 29.22                                       | 1.46      |
| 6    | 15.60                                       | 16.13                                       | 3.40      |
| 7    | 41.00                                       | 41.96                                       | 2.34      |
| 8    | 17.30                                       | 17.68                                       | 2.20      |

The average error between the results of the temperature of the outlet in the experiments and the outlet temperature of the CFD model is found to be 2.51%.

The same boundary conditions were applied to the initial design to compare the outlet temperature and the thermal efficiency of the cooling system. The outlet temperature and the thermal efficiency of the previous design are given in Table 7-11.

**Table 7-11. Outlet temperature and thermal efficiency of the initial PV/T system**

| Case | Flow Rate (kg/s) | T <sub>inlet</sub> (°C) | T <sub>outlet_cfd_previous</sub> (°C) | ΔT (°C) | Q <sub>u</sub> (W) | η <sub>th</sub> |
|------|------------------|-------------------------|---------------------------------------|---------|--------------------|-----------------|
| 1    | 0.0042           | 17.70                   | 30.31                                 | 12.61   | 220.15             | 68.27%          |
| 2    | 0.0062           | 20.10                   | 28.76                                 | 8.66    | 223.76             | 71.28%          |
| 3    | 0.0225           | 12.30                   | 15.98                                 | 3.68    | 346.93             | 76.61%          |
| 4    | 0.0375           | 11.40                   | 13.69                                 | 2.29    | 359.82             | 75.47%          |
| 5    | 0.0175           | 20.20                   | 27.32                                 | 7.12    | 522.07             | 76.42%          |
| 6    | 0.0458           | 11.50                   | 15.11                                 | 3.61    | 653.27             | 81.96%          |
| 7    | 0.0083           | 19.50                   | 37.33                                 | 17.83   | 622.60             | 77.56%          |
| 8    | 0.0458           | 11.90                   | 16.91                                 | 5.01    | 898.02             | 89.13%          |

When the initial design and the enhanced design of the PV/T systems were compared, the maximum thermal efficiency was reached with the inlet mass flow rate of 0.0458 kg/s and the inlet temperature of 11.90 °C. The initial design reached 89.13% thermal efficiency, whereas the enhanced cooling system reached 96.47%, showing 8.24% improved thermal efficiency. Figure 7-6 shows an outlet temperature comparison between the experimental test results of the PV/T system with the enhanced cooling system and the CFD results of the initial PV/T design under test conditions employed in the laboratory.

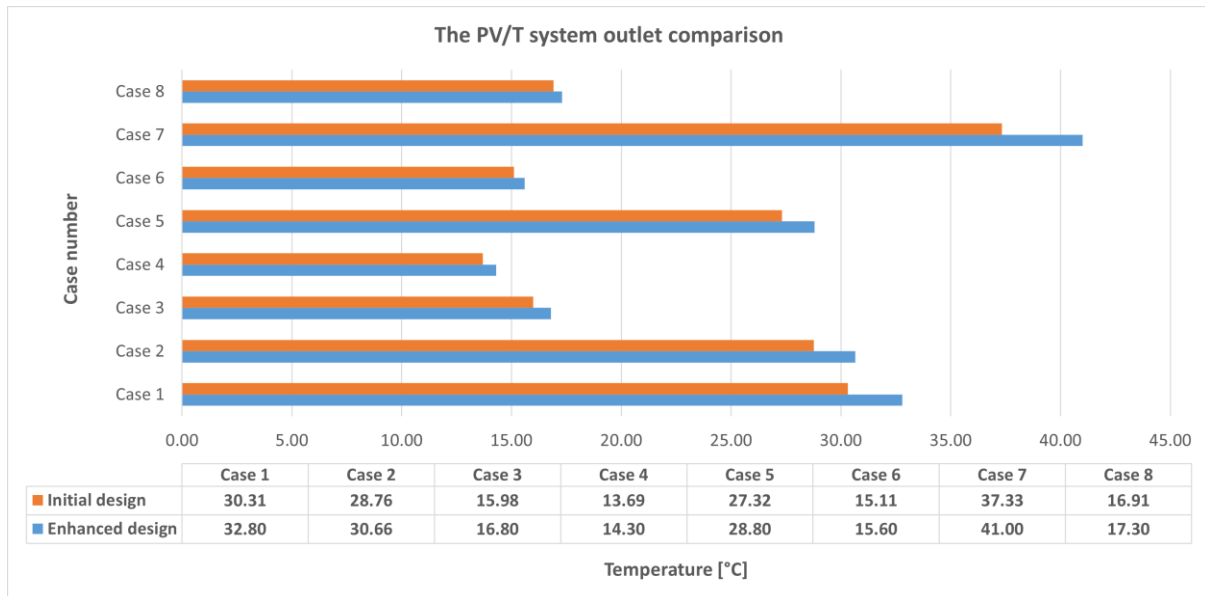


**Figure 7-6. The outlet temperature comparison of the initial design and manufactured final design**

Figure 7-6 shows that the difference between the outlet temperature of the initial design and the final design varies from 0.39 °C to 3.67 °C. The average increase in outlet temperature of the novel design was 1.48 °C.




## 7.5 Uncertainty analysis

An uncertainty analysis was conducted for the measured quantities to determine the reliability of the experiments. The accuracy of each measuring device used in experiments is given in Table 7-12. The analysis was carried out for thermal efficiency ( $\eta_{th}$ ), and the uncertainty in thermal efficiency was calculated using Eq. 48.

$$\frac{U_{n_{th}}}{n_{th}} = \left[ \left( \frac{U_{T_{inlet}}}{T_{inlet}} \right)^2 + \left( \frac{U_{T_{outlet}}}{T_{outlet}} \right)^2 + \left( \frac{U_H}{H} \right)^2 + \left( \frac{U_{\dot{m}}}{\dot{m}} \right)^2 \right]^{1/2} \quad (48)$$

where  $U_{n_{th}}$  is the uncertainty in the results of thermal efficiency.  $U_{T_{inlet}}$ ,  $U_{T_{outlet}}$ ,  $U_H$ , and  $U_{\dot{m}}$  are the uncertainties associated with the independent variables.

**Table 7-12. Uncertainties in measuring instruments**

| Instrument           | Parameter       | Unit             | Uncertainty | Pictures  |
|----------------------|-----------------|------------------|-------------|---|
| Heat flux sensor     | Heat flux       | W/m <sup>2</sup> | ±5          |   |
| K-type thermocouples | Temperature     | °C               | ±0.5        |  |
| Flow meter           | Water flow rate | L/min            | ±1%         |  |

The uncertainty of thermal efficiency varied between 1.12% and 1.15% in the stand-alone cooling system experiments from case 1 to case 6, with an average uncertainty of 1.13%. In contrast, the uncertainty of thermal efficiency varied between 1.40% and 2.90% for the measurements conducted from case 1 to case 8, with an average uncertainty of 2.20%.

## 7.6 Summary

The laboratory thermal test of the enhanced cooling system design was realized in this chapter. The stand-alone cooling system was first tested to the limits thermally to assess the design's capabilities. A 3-D CFD model of the cooling system was developed and validated using experimental data. An average error of 1.51% occurred between the experimental data and the CFD model output. The same boundary conditions were applied to the initial design

to compare thermal efficiency. The initial design reached up to 86.04% thermal efficiency, whereas the enhanced cooling system reached  $95.54 \pm 1.12\%$ , showing 11.04% improved thermal efficiency.

The experimental tests were extended by coupling the cooling system with a PV module. Various flow rates and inlet temperatures were investigated under different heat flux conditions. Maximum thermal efficiency of  $96.47 \pm 1.40\%$  was achieved during the experiments with the inlet mass flow rate of 0.0458 kg/s and inlet temperature of 11.90 °C under 592.89 W/m<sup>2</sup>. In the same case, the rear side temperature of the PV module was reduced by around 40.72 °C, maintaining the maximum electrical conversion efficiency of the module under consideration. The numerical model estimated that the designed cooling system can improve the electrical power output of the PV module by 18.32%.

The 3-D model of the stand-alone cooling system was coupled with the 3-D model of the PV module. The model was validated using experimental data. A maximum error of 3.40% occurred between the complete CFD model of the proposed PV/T system and experimental data. The boundary conditions applied to the proposed PV/T system model were employed in the initial design. The initial PV/T design reached up to 89.13% thermal efficiency, whereas the enhanced cooling system reached  $96.47 \pm 1.40\%$ , showing 8.24% improved thermal efficiency.

The uncertainty of thermal efficiency varied between 1.12% and 1.15% in the stand-alone cooling system experiments from case 1 to case 6, with an average uncertainty of 1.13%. In contrast, the uncertainty of thermal efficiency varied between 1.40% and 2.90% for the measurements conducted from case 1 to case 8, with an average uncertainty of 2.20%.



## Chapter 8 - Outdoor experiments of the designed PV/T module

This chapter presents the preparation of the outdoor test rig and conducting experiments outdoors. The test rig consisted of a single-axis sun-tracking system with two PV modules; one was coupled with the designed cooling system, and the other was non-cooled to compare the cooling system's effectiveness. The thermal energy generation of the PV/T system was investigated along with the electricity generation of the cooled and non-cooled PV modules. The tests were conducted for two months to analyze the performance of the PV/T system in September and October. The cooling uniformity analysis was performed to determine the effect of the designed cooling system on the PV module. The pressure drop tests were conducted with various flow rates in the test rig, and an equation was derived to estimate the pressure drop. TRNSYS software [55] was used to model the PV/T module to estimate the yearly energy generation of the designed system. An uncertainty analysis was performed for the collected data during experiments. The reliability of the measured quantities obtained during the experiments was determined.

### 8.1 The test rig preparation

The test rig preparation was started by placing four PT-1000 temperature sensors on the rear side of the non-cooled PV module, and three PT-1000 temperature sensors were put on the rear side of the cooling system, as shown in Figure 8-1.

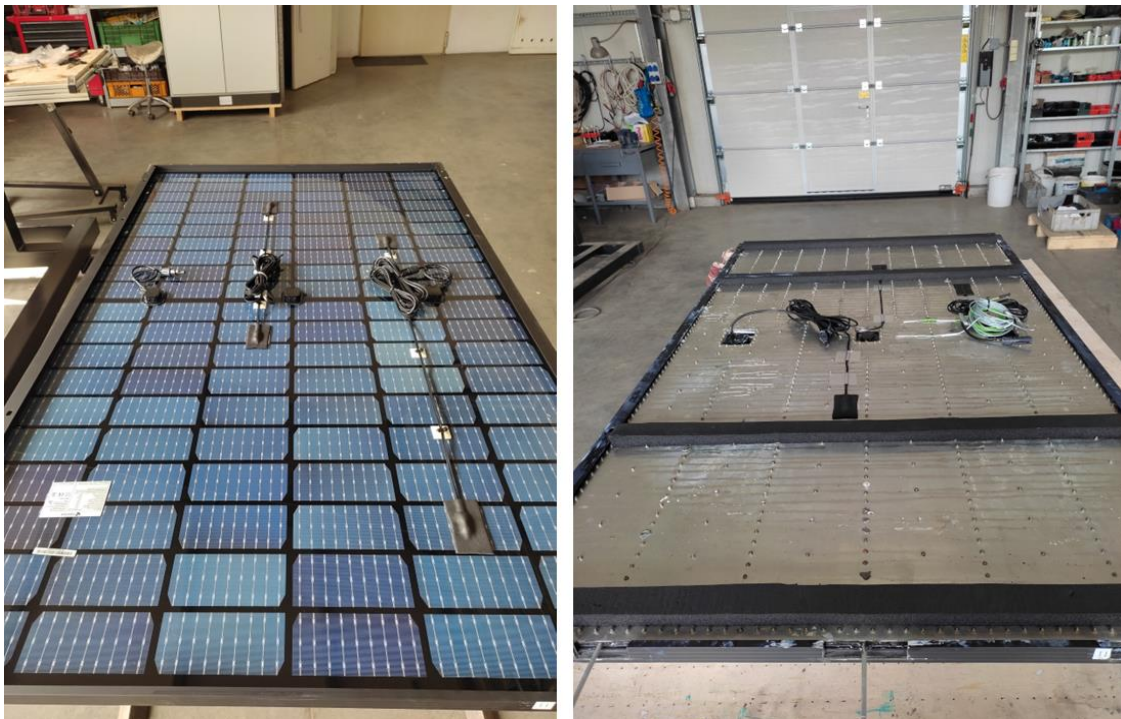


**Figure 8-1. The PT-1000 temperature sensor placement on the rear side of the non-cooled PV module and cooling system**

Three K-type sheathed thermocouples were inserted between the cooling system and the PV module to measure the rear side temperature of the PV module during the laboratory tests. The thermocouples were kept in the same place to measure the temperature in the outdoor tests. The test rig preparation was continued with the construction of the single-axis sun-tracking system. Aluminum frames, bracket sets, and center and edge clamps were used to design the rack for holding the PV modules shown on the left side of Figure 8-2.



**Figure 8-2. The single-axis sun-tracking system with cooled and non-cooled PV modules**

Upon completion of the frame, the non-cooled PV module and PV/T system were placed on the sun-tracking system with a tilt angle of 30°, as shown on the right side of Figure 8-2.

The sun-tracking system, coupled with PV/T module and non-cooled PV module, was placed near the roof of the building where solar irradiation was not interrupted by any disturbance. The system was donated with a sun-tracking solar irradiation sensor, pyranometer, control system, and grid-tie microinverters, as shown in Figure 8-3. The sun-tracking system solar irradiation sensor senses the intensity of the solar irradiation and allows the control of the system to rotate in the correct direction. The pyranometer was used to measure the solar irradiation falling on the PV modules and placed between the non-cooled and cooled PV modules. High-performance PLC controllers and analog input modules were used to control and monitor the system and collect data from the sensors. Two 400W grid-tie microinverters were connected to the PV modules to convert generated DC electricity to AC electricity and

maintain the PV modules to generate the maximum electrical energy available. The inverters had a built-in maximum power point tracking charge controller, which had an effectiveness of 99.5% in maintaining the maximum power output. The maximum energy conversion efficiency from DC to AC of grid-tie microinverters was 92.5%.

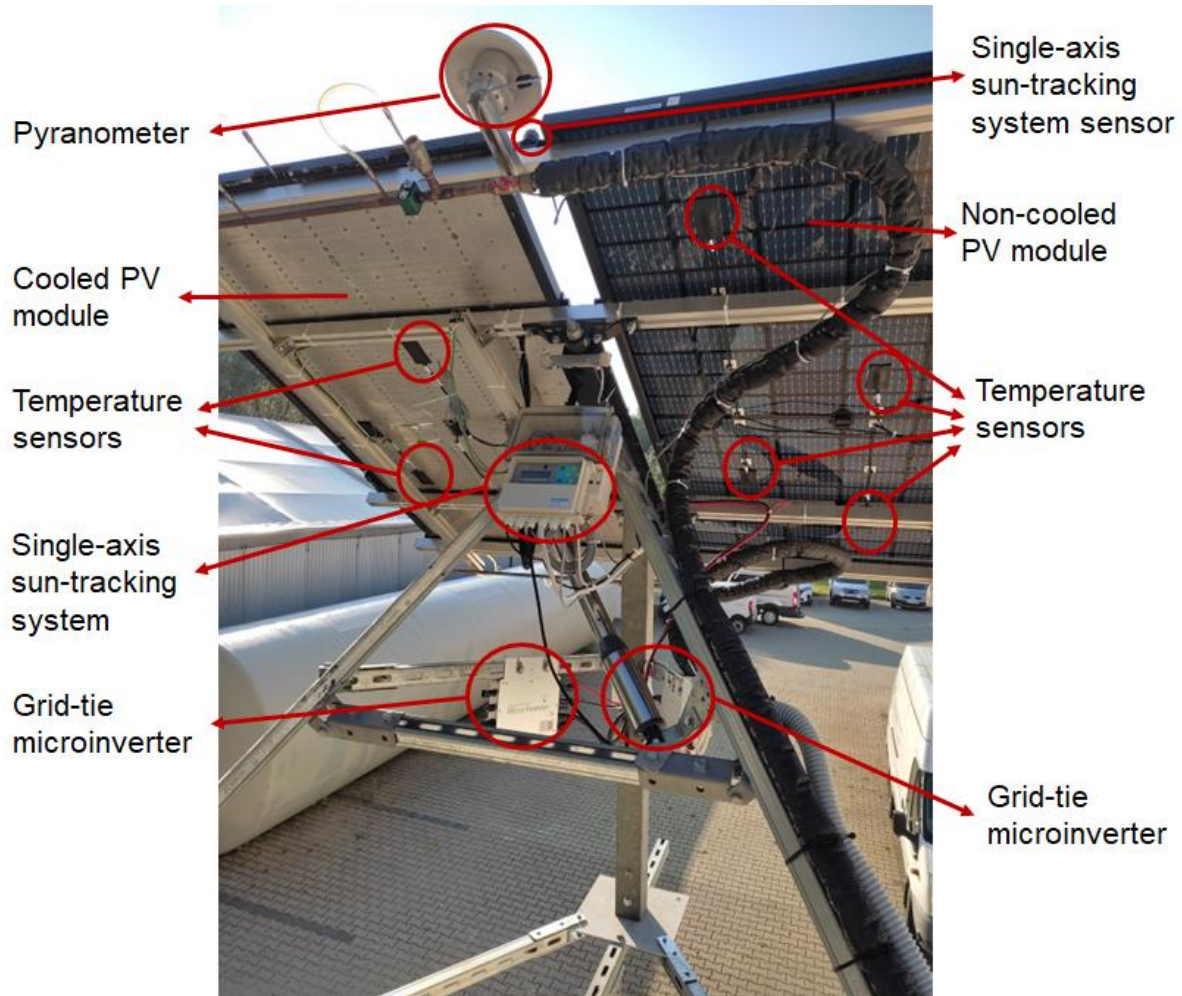


**Figure 8-3. The placement of the pyranometer on the test rig**

The designed test rig consisted of two loops where water was used in the PV/T cooling loop, and water/glycol mixture was used in the chiller loop. The PV/T loop comprised a pump, expansion vessel, heat meter, and hydraulic elements.

The buffer tank contained an immersed coil heat exchanger. The tank was filled with water and used in the PV/T cooling loop. The water/glycol mixture was circulated through the heat exchanger coils inside the buffer tank. The coil of the immersed heat exchanger was connected to a heat exchanger, which was placed between the chiller and the buffer tank. The evaporator side of the chiller was connected to the heat exchanger to cool down the water inside the buffer tank. The condenser side was connected to another heat exchanger, which was connected to an underground heat storage unit to reject the heat. Another heat meter

was placed between the buffer tank and the heat exchanger to measure how much heat was rejected from the buffer tank. The buffer tank, chiller, pumps, pressure transmitters, heat exchangers, and other parts of the test rig are shown in Figure 8-4.

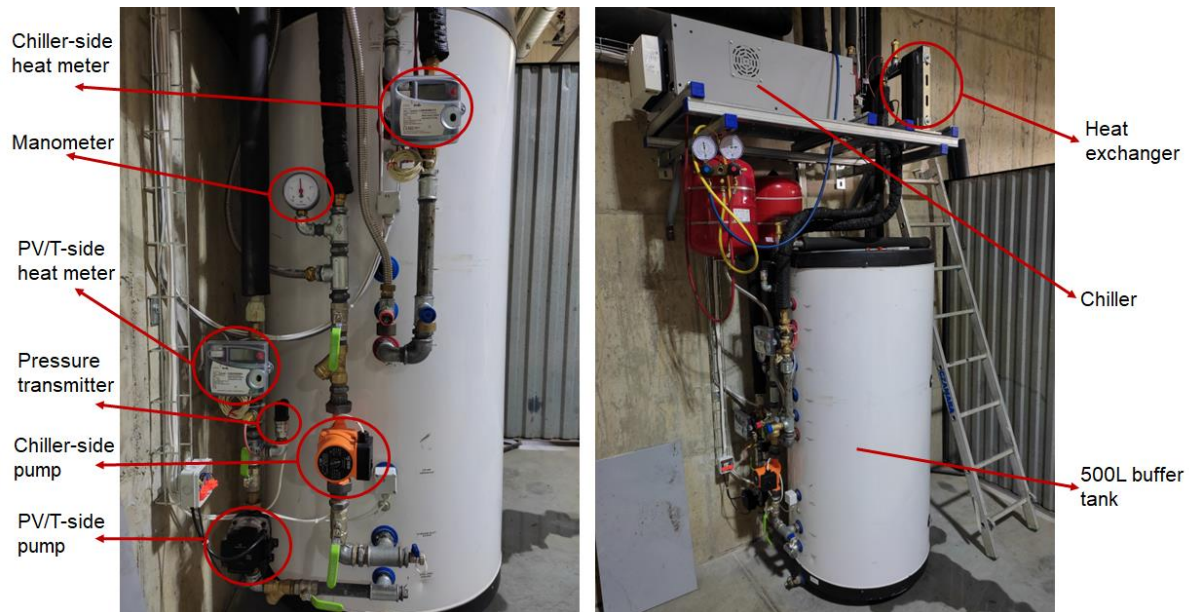


**Figure 8-4. The components of the test rig**

An operational panel was prepared to monitor the temperature, flow rate, and thermal energy exchange in the system. The developed panel allowed for control of the tracking system, pump for the PV/T system, and chiller, as shown in Figure 8-5.

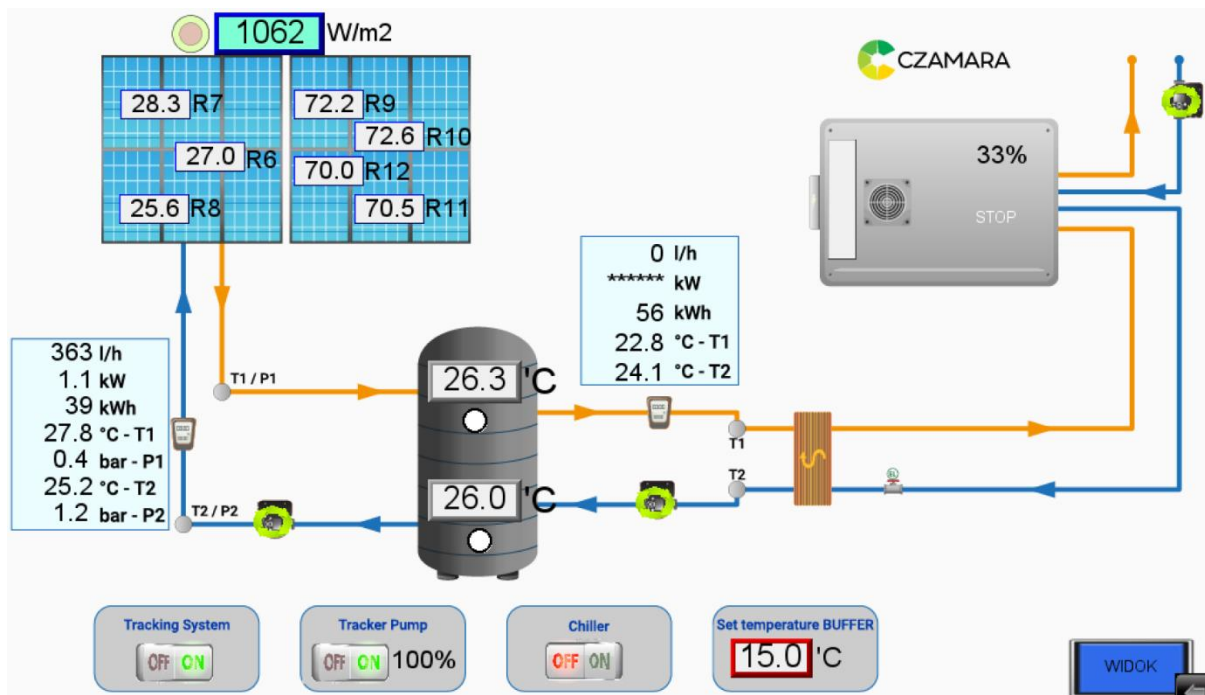


**Figure 8-5. The operational panel**

The tests started once all parts of the test rig were connected. A summary of the components used in the test rig was as follows:

- Two PV modules, each with a maximum power output of 325 W and an electrical conversion efficiency of 19.12% under STC, a maximum power output of 241.9 W, and an electrical conversion efficiency of 17.79% under NOCT, were used.
- A single-axis sun-tracking system for two PV modules; one is cooled, and the other is non-cooled, placed with a tilt angle of 30° facing south. The system consisted of a sun-tracking solar irradiation sensor, controller, and 24 V DC weatherproof actuator with 2,000 N force for automatic change of direction.
- PT-1000 temperature sensors were used for temperature measurements and logging on monitoring. The measurement range of the sensors was between -40 °C and 100 °C. The uncertainty in temperature sensors used in the tests was  $\pm 0.04$  °C.
- Two stand-alone ultrasonic heat meters with a temperature range of 0 to 180 °C were used in the test rig. The heat meters were donated with a MODBUS module for data collection. The DN15 heat meter was used on the PV/T side, and the DN20 heat meter was placed between the buffer tank and the heat exchanger. The heat meters had the EN1434 class 2 rating with  $\pm 1\%$  uncertainty with the flow rate and thermal energy calculations. PT100 temperature sensors were used within the heat meters with an uncertainty of  $\pm 0.05$  °C.
- LP PYRA 02 AC pyranometer was used to measure the irradiance on the plane surface in  $W/m^2$ . The used pyranometer was a First Class pyranometer in accordance with ISO 9060 standards and with the criteria of the WMO 'Guide to Meteorological Instruments and Methods of Observation.' The sensitivity of the LP PYRA 02 AC was 4..20 mA (0-2,000  $W/m^2$  with an uncertainty of  $\pm 10$   $W/m^2$ .
- A chiller with a cooling capacity of 8 kW was used to reject the heat accumulated within the 500 L buffer tank, which had an immersed heat exchanger. A water/glycol mixture was used as a working fluid.
- Two plate heat exchangers, each with a 5 kW capacity, were used in the test rig. One of the heat exchangers was placed between the chiller and buffer tank, and the other was installed between the underground heat storage unit and the chiller.
- K-type sheathed thermocouples with the capability of measuring temperatures up to 900 °C and uncertainty of  $\pm 0.5$  °C were used.
- Two pumps were used in the main test rig. A pump with a nominal diameter of suction and discharge port of 15 mm and a maximum head of 7.5 m was used to circulate the water through the designed cooling system. The maximum power consumption of the pump was 60 W while providing a flow rate of 1  $m^3/h$ . The second pump, with a nominal

diameter of 25 mm, was placed between the buffer tank and the heat exchanger to circulate the water-glycol mixture. The chosen pump had an operating range between 0.2 and 3.5 m<sup>3</sup>/h with a maximum head of 3.8 m. The maximum power of the pump was 65 W.

## **8.2 Outdoor experiments**

The outdoor experiments were conducted for 19 days in September 2023 between the 12<sup>th</sup> and 30<sup>th</sup> of September using the test rig prepared. The tests were continued in October for 31 days between the 1<sup>st</sup> of October and the 31<sup>st</sup> of October 2023. The electrical conversion efficiency of the cooled and non-cooled PV modules was compared to assess the energy yield. The thermal energy generation of the designed PV/T system was investigated during the outdoor tests.

The chiller was used in the experiments to control the inlet temperature of the cooling system in September and October. The chiller was not activated during a part of the experiments to analyze the maximum achievable temperature in the buffer tank. Daily electrical and thermal energy generation of the PV/T system was studied, and the yearly energy yield of the system was estimated.

### **8.2.1 Outdoor experiments with active chiller**

The chiller-active experiments were conducted by controlling the inlet temperature and back surface temperature of the PV module to maintain the maximum electrical conversion efficiency in the PV/T system. The back surface temperature of the cooled and non-cooled PV modules was investigated along with the power output, thermal energy generation, and electrical and thermal efficiency of the system. In this section, the results of outdoor tests conducted on the 12<sup>th</sup> of September, 13<sup>th</sup> of September, and 14<sup>th</sup> of October are presented. The rest of the results obtained from the tests are provided in Appendix B.

#### **Experiment – 12/09/2023**

An experiment was conducted on the 12<sup>th</sup> of September, 2023. During the day, the average solar irradiation was 490.07 W/m<sup>2</sup>, and the average ambient temperature was 24.05 °C. The maximum solar irradiation falling onto the PV modules was recorded as 998 W/m<sup>2</sup>, while the maximum ambient temperature was 29.20 °C. The weather data is presented in Figure 8-6. The data was collected every five minutes and saved in a file. The fall in solar irradiation occurred due to the cloud cover on the clear sky rarely, as seen in Figure 8-6.

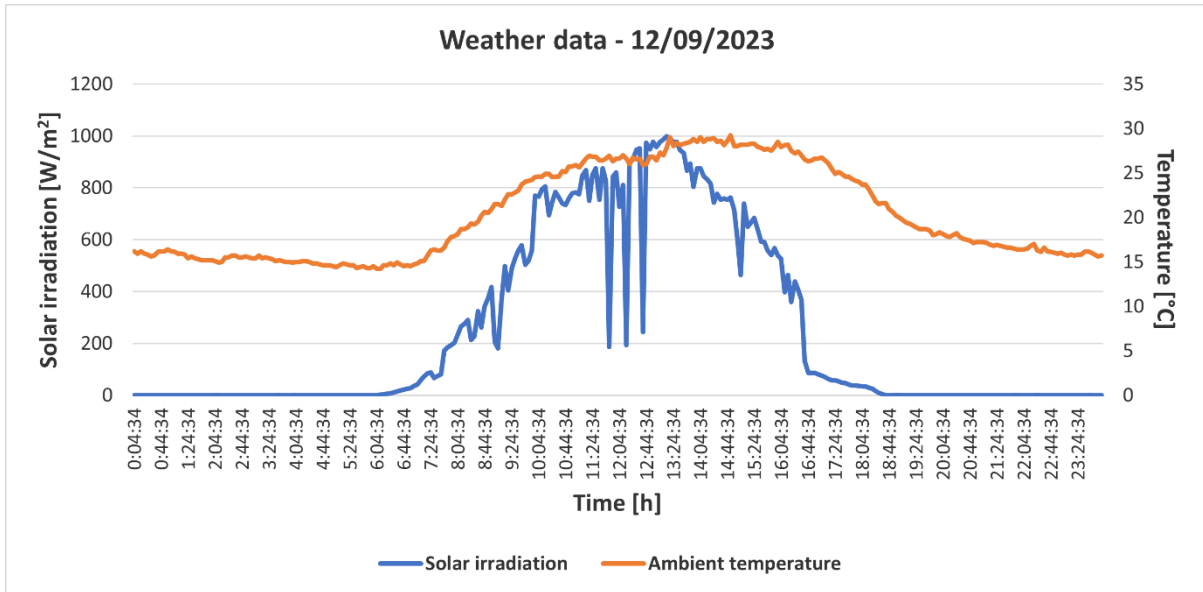


**Figure 8-6. The weather data – 12/09/2023**

The circulation pump worked between 9 a.m. and 5 p.m. to cool the PV module to maintain the maximum power output and harvest the waste heat from the PV module, whereas the chiller was active between 10 a.m. and 5 p.m. The hourly average back surface temperature of the PV modules, solar irradiation, ambient temperature, and buffer tank temperature are given in Table 8-1.

**Table 8-1. The temperatures in the test rig – 12/09/2023**

| Time     | $G_{sur}$ (W/m <sup>2</sup> ) | $T_{amb}$ (°C) | $T_{bcooled}$ (°C) | $T_{bncooled}$ (°C) | $T_{buffertop}$ (°C) | $T_{bufferbot}$ (°C) |
|----------|-------------------------------|----------------|--------------------|---------------------|----------------------|----------------------|
| 6:04:34  | 14.25                         | 14.57          | 13.68              | 12.87               | 24.43                | 23.80                |
| 7:04:22  | 109.67                        | 16.30          | 15.64              | 17.46               | 24.41                | 23.80                |
| 8:04:10  | 285.67                        | 19.67          | 22.61              | 31.00               | 24.40                | 23.80                |
| 9:03:58  | 496.67                        | 23.02          | 24.33              | 52.22               | 24.61                | 23.82                |
| 10:03:46 | 761.75                        | 25.02          | 22.82              | 59.80               | 24.64                | 23.09                |
| 11:03:34 | 775.33                        | 26.50          | 20.82              | 61.58               | 22.47                | 21.11                |
| 12:03:22 | 794.17                        | 26.49          | 22.91              | 60.26               | 20.77                | 18.35                |
| 13:03:10 | 934.67                        | 28.17          | 18.39              | 68.12               | 20.33                | 18.93                |
| 14:02:58 | 769.08                        | 28.58          | 17.89              | 62.06               | 19.30                | 18.23                |
| 15:02:46 | 602.08                        | 28.01          | 16.63              | 54.02               | 18.00                | 17.15                |
| 16:02:34 | 285.67                        | 27.14          | 15.28              | 38.79               | 16.54                | 15.80                |
| 17:02:22 | 51.83                         | 25.09          | 20.33              | 24.76               | 15.66                | 14.25                |

In Table 8-1,  $G_{sur}$  and  $T_{amb}$  are the solar irradiation falling onto the surface of PV modules and ambient temperature.  $T_{bcooled}$  and  $T_{bncooled}$  are the rear side temperatures of the cooled and non-cooled PV modules, respectively.  $T_{buffertop}$  and  $T_{bufferbot}$  stand for the top side and bottom side temperatures of the buffer tank. A graphical representation of the hourly average back surface of the PV modules is illustrated in Figure 8-7.

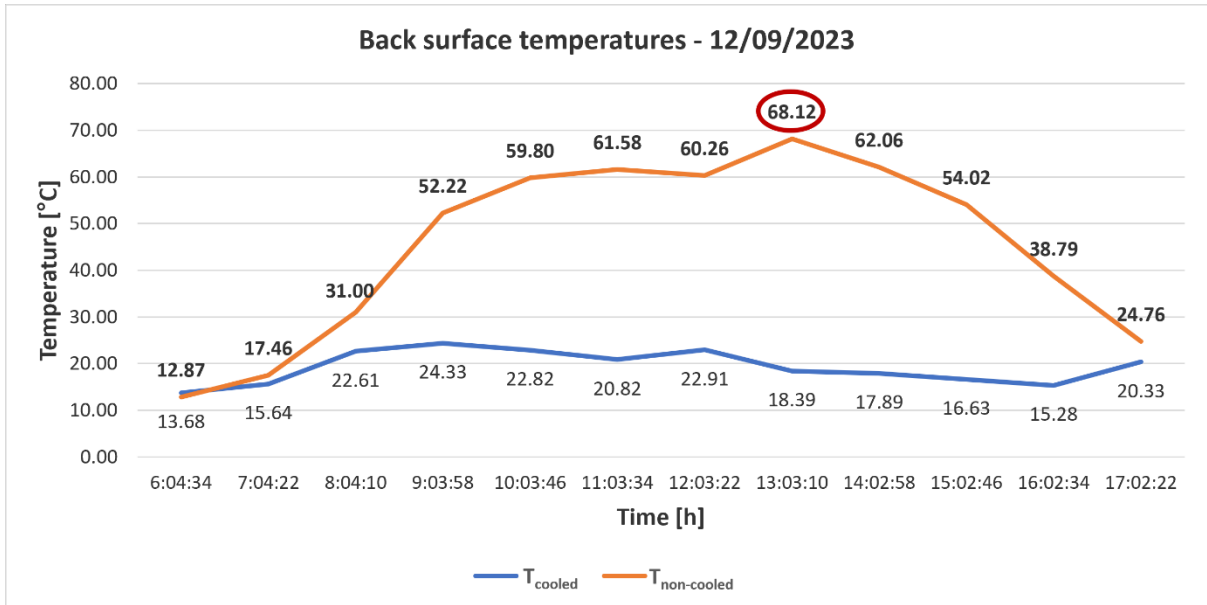


**Figure 8-7. The hourly average back surface temperature of the PV modules – 12/09/2023**

The average back surface temperature of the non-cooled PV module reached 68.12 °C, highlighted with a red oval in Figure 8-7, while the average back surface temperature of the cooled PV module reached 24.33 °C.

The maximum back surface temperature of 70.98 °C occurred at 1.20 p.m. when the solar irradiation was 990 W/m<sup>2</sup>, and the ambient temperature was 29 °C for the non-cooled PV module. The hourly average flow rate of the PV/T system, along with inlet and outlet temperatures, are shown in Figure 8-8.

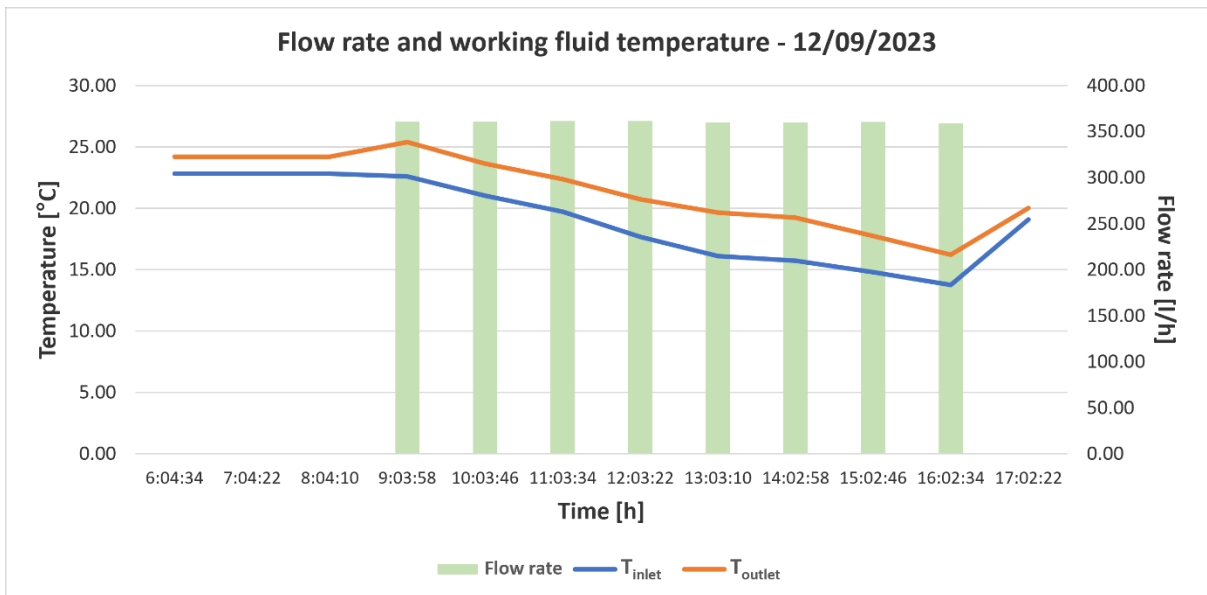


**Figure 8-8. The flow rate and temperatures in the PV/T system – 12/09/2023**



The electrical energy generated by the PV modules was compared using the data acquired from the grid-tie microinverters. The total electrical energy generated by the cooled PV module was 1.71 kWh (AC), whereas the total electrical energy generated by the non-cooled PV module was 1.23 kWh (AC). The implemented cooling system allowed for generating 38.86% more electrical energy at the end of the test day.

The maximum improvement in electrical efficiency was observed around 1:20 p.m., where the back surface temperatures of cooled and non-cooled PV modules were 16.56 °C and 70.98 °C. The maximum thermal efficiency occurred at 2:05 p.m. with a value of 98.03%. During the maximum thermal efficiency observation, the volumetric flow rate was 6.02 L/min, and inlet and outlet temperatures were 16.25 °C and 19.70 °C with a thermal power output of 1.45 kW. The solar irradiation level and the ambient temperature were 875 W/m<sup>2</sup> and 29 °C, respectively, at 2.05 p.m. The 12h (6 a.m. – 6 p.m.) total thermal energy generated by the PV/T system was 7.74 kWh. An energy analysis was performed to assess the available solar energy, thermal energy generated by the PV/T system, and electrical energy generated by the cooled and non-cooled PV module. The analysis is presented in Figure 8-9.

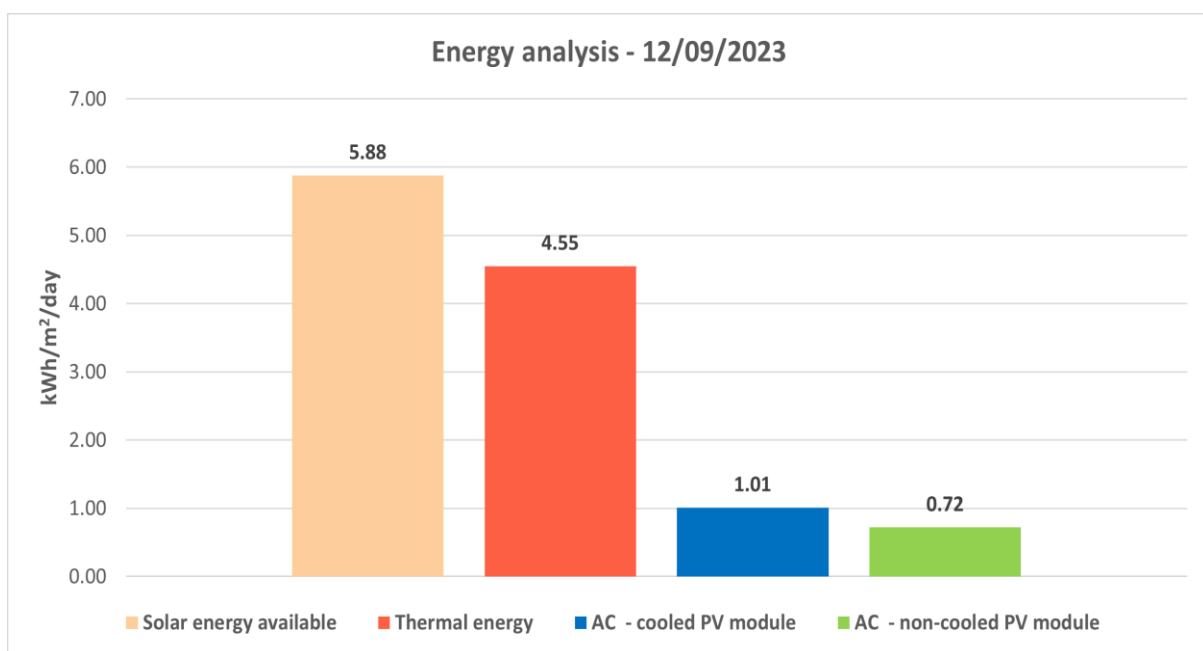


**Figure 8-9. The energy analysis – 12/09/2023**

The analysis showed that the available solar energy was 5.88 kWh/m<sup>2</sup>/day on the 12<sup>th</sup> of September, 2023. The thermal energy generation of the PV/T system was 4.55 kWh/m<sup>2</sup>/day. The electrical energy yield kWh/m<sup>2</sup>/day was 1.01 and 0.72 for cooled and non-cooled PV modules, respectively. The non-cooled PV module converted 13.68% of available solar energy into electrical energy, whereas the PV/T module converted 19.00% during 12 hours of operation.

## Experiment – 13/09/2023

Another experiment was conducted on the 13<sup>th</sup> of September, 2023, where the average solar irradiation was 484.95 W/m<sup>2</sup>, and the average ambient temperature was 24.06 °C. The maximum solar irradiation falling onto the PV modules was recorded as 942 W/m<sup>2</sup>, while the maximum ambient temperature was 29.80 °C. The weather data is shown in Figure 8-10.

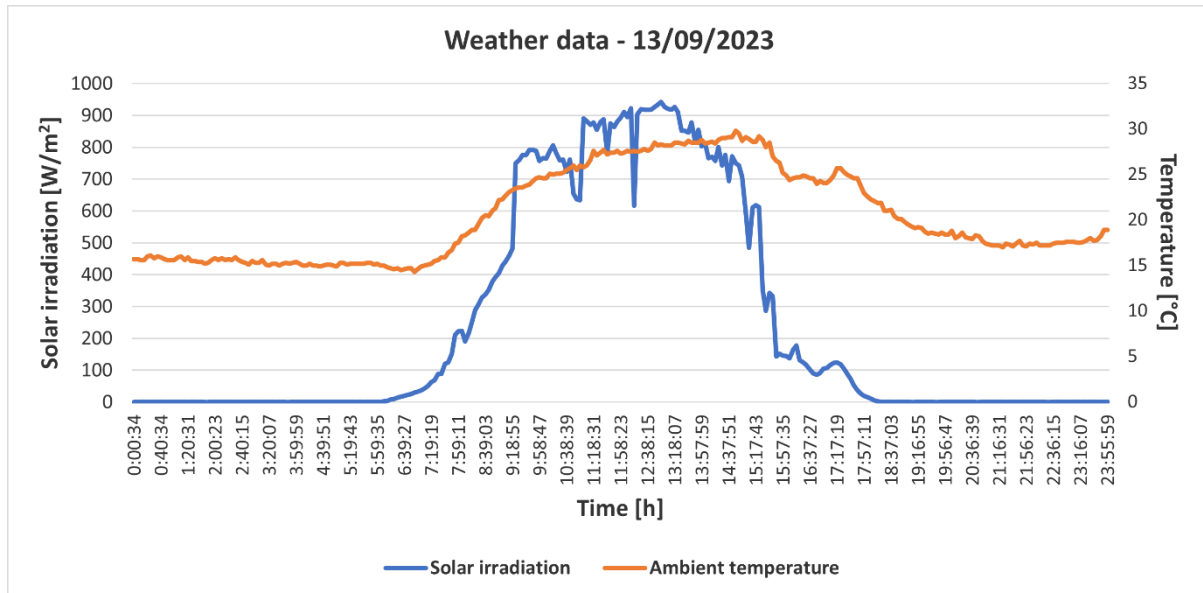


**Figure 8-10. The weather data – 13/09/2023**

The circulation pump worked between 9 a.m. and 4 p.m. to cool the PV module, whereas the chiller was active between noon and 3 p.m. The hourly average back surface temperature of the PV modules, solar irradiation, ambient temperature, and buffer tank temperature are given in Table 8-2.

**Table 8-2. The temperatures in the test rig – 13/09/2023**

| Time     | $G_{sur}$ (W/m <sup>2</sup> ) | $T_{amb}$ (°C) | $T_{bcooled}$ (°C) | $T_{bncooled}$ (°C) | $T_{buffertop}$ (°C) | $T_{bufferbot}$ (°C) |
|----------|-------------------------------|----------------|--------------------|---------------------|----------------------|----------------------|
| 6:04:34  | 15.33                         | 14.68          | 13.90              | 12.97               | 16.53                | 15.52                |
| 7:04:22  | 105.58                        | 15.92          | 15.08              | 16.09               | 16.52                | 15.50                |
| 8:04:10  | 305.75                        | 19.84          | 21.46              | 29.24               | 16.53                | 15.56                |
| 9:03:58  | 666.75                        | 23.62          | 18.55              | 57.30               | 19.27                | 18.03                |
| 10:03:46 | 736.17                        | 25.28          | 21.68              | 58.82               | 21.07                | 20.86                |
| 11:03:34 | 869.42                        | 27.09          | 24.90              | 63.24               | 24.31                | 24.08                |
| 12:03:22 | 893.58                        | 27.78          | 27.86              | 62.42               | 27.62                | 27.25                |
| 13:03:10 | 875.00                        | 28.44          | 25.32              | 63.16               | 27.52                | 25.79                |
| 14:02:58 | 757.25                        | 28.91          | 22.48              | 59.89               | 24.58                | 22.92                |
| 15:02:46 | 389.58                        | 27.89          | 19.86              | 47.04               | 21.86                | 20.68                |
| 16:02:34 | 122.25                        | 24.55          | 18.59              | 29.31               | 19.10                | 18.88                |
| 17:02:22 | 82.75                         | 24.66          | 22.51              | 26.97               | 19.31                | 19.36                |

A graphical representation of the hourly average back surface of the PV modules is illustrated in Figure 8-11.

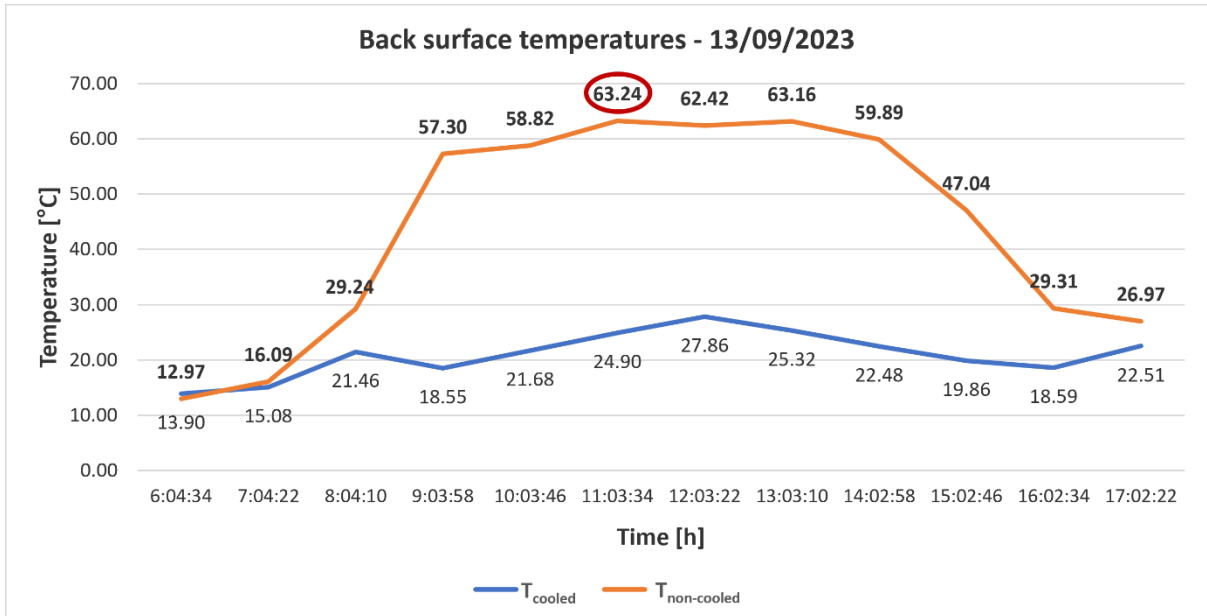


**Figure 8-11. The hourly average back surface temperature of the PV modules – 13/09/2023**

The average back surface temperature of the non-cooled PV module reached 63.24 °C, highlighted with a red oval in Figure 8-11, whereas the average back surface temperature of the cooled PV module reached 27.86 °C. The maximum back surface temperature of 66.45 °C occurred at 11.30 a.m. when the solar irradiation was 879 W/m<sup>2</sup>, and the ambient temperature was 27.7 °C. The hourly average flow rate of the PV/T system, along with inlet and outlet temperatures, are shown in Figure 8-12.

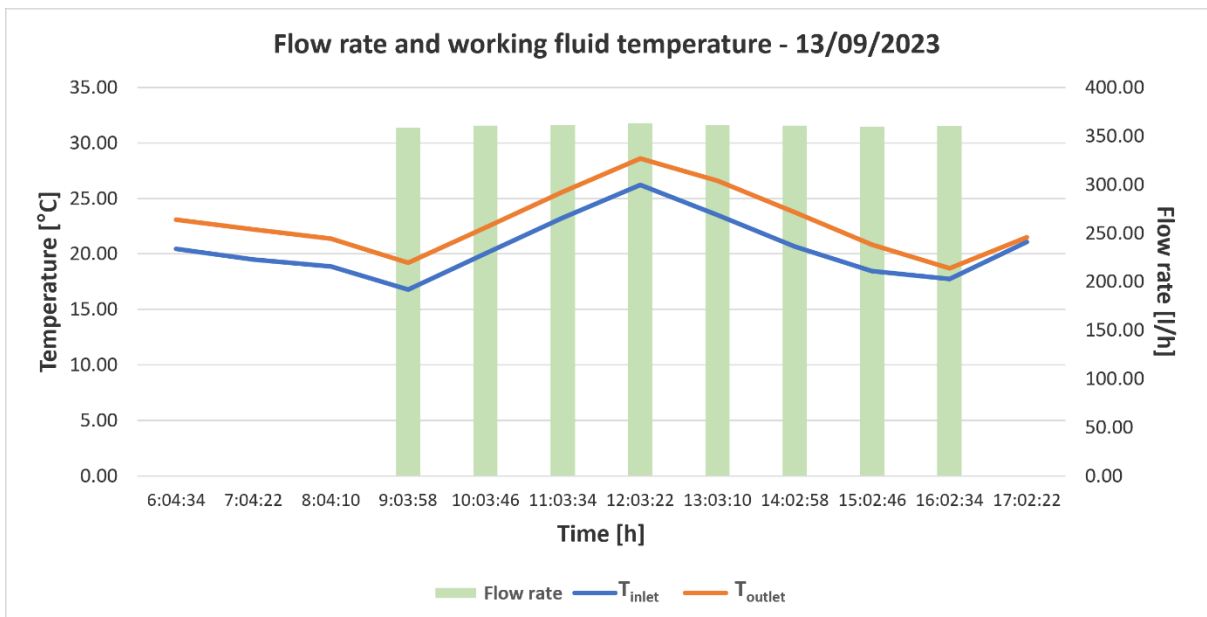


**Figure 8-12. The flow rate and temperatures in the PV/T system – 13/09/2023**

The total electrical energy generated by the cooled PV module was 1.69 kWh (AC), whereas the total electrical energy generated by the non-cooled PV module was 1.28 kWh (AC). The implemented cooling system allowed for generating the maximum electrical energy by increasing the production by 32.57% at the end of the test day.

The maximum electrical power output improvement was observed around 11:30 a.m., where the back surface temperatures of cooled and non-cooled PV modules were 24.93 °C and 66.45 °C.

The maximum thermal efficiency occurred at 12:58 p.m. with a value of 95.07%. During the maximum thermal efficiency observation, the volumetric flow rate was 6.02 L/min, and inlet and outlet temperatures were 25.6 °C and 29.2 °C with a maximum thermal power output of 1.52 kW under 942 W/m<sup>2</sup> with the ambient temperature of 28.3 °C.

The 12h (6 a.m. – 6 p.m.) total thermal energy generated by the PV/T system was 7.49 kWh. Similarly, an energy analysis was performed to assess the available solar energy, thermal energy generated by the PV/T system, and electrical energy generated by the cooled and non-cooled PV module, as shown in Figure 8-13.

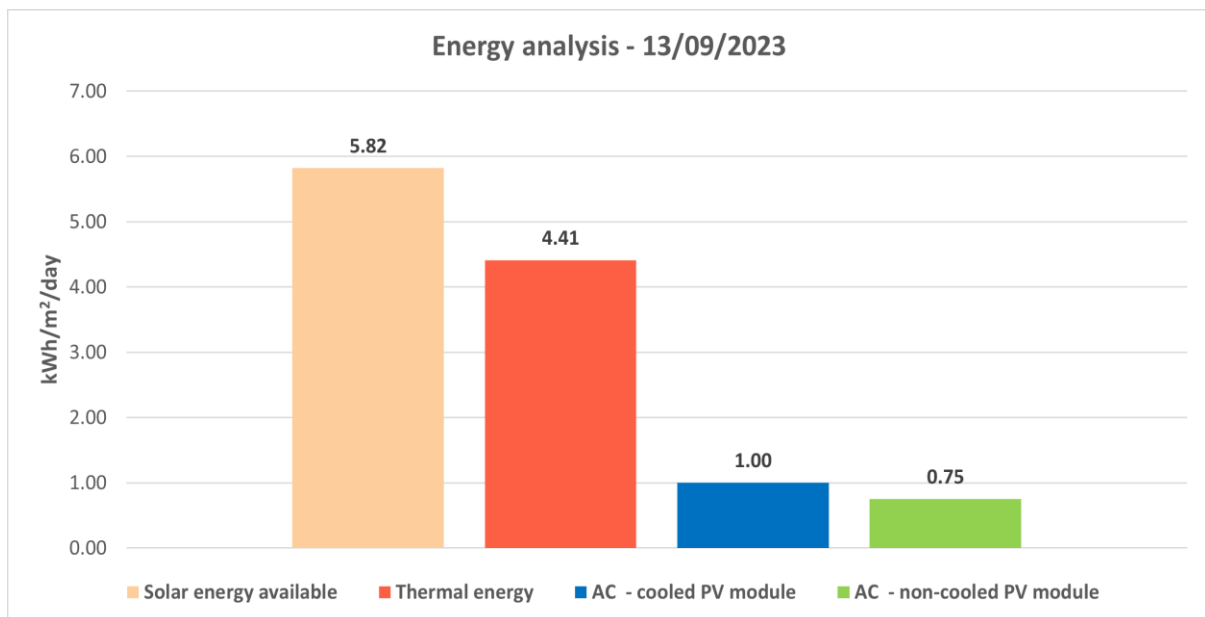


**Figure 8-13. The energy analysis – 13/09/2023**

The analysis showed that the available solar energy was 5.82 kWh/m<sup>2</sup>/day on the 13<sup>th</sup> of September, 2023. The thermal energy generation of the PV/T system was 4.41 kWh/m<sup>2</sup>/day. The electrical energy yield kWh/m<sup>2</sup>/day was 1.00 and 0.75 for cooled and non-cooled PV modules, respectively. The non-cooled PV module converted 14.34% of available solar energy into electrical energy, whereas the PV/T module converted 19.01% during 12 hours of operation.

## Experiment – 14/10/2023

An experiment was conducted on the 14<sup>th</sup> of October, 2023. During the day, the average solar irradiation was 471.67 W/m<sup>2</sup>, and the average ambient temperature was 21.18 °C. The maximum solar irradiation falling onto the PV modules was recorded as 852 W/m<sup>2</sup> while the maximum ambient temperature was 24.70 °C. The weather data is presented in Figure 8-14.

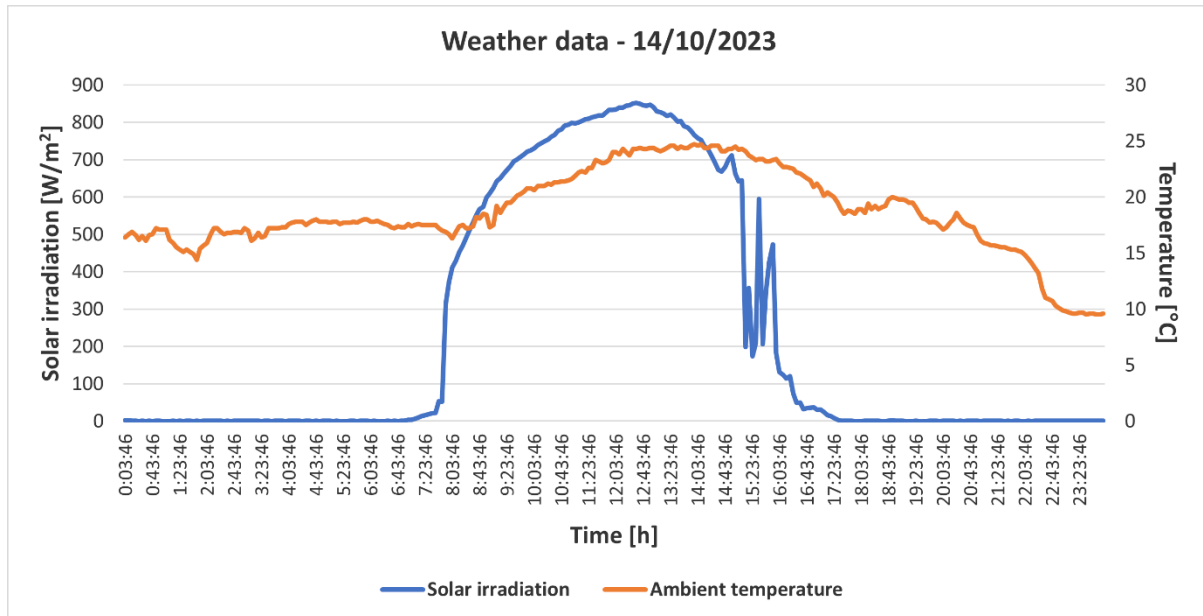


**Figure 8-14. The weather data – 14/10/2023**

The circulation pump worked between 8 a.m. and 4 p.m. to cool the PV module, whereas the chiller was active between 9 a.m. and 1 p.m. The hourly average back surface temperature of the PV modules, solar irradiation, ambient temperature, and buffer tank temperature are given in Table 8-3.

**Table 8-3. The temperatures in the test rig – 14/10/2023**

| Time     | $G_{sur}$ (W/m <sup>2</sup> ) | $T_{amb}$ (°C) | $T_{bcooled}$ (°C) | $T_{bncooled}$ (°C) | $T_{buffertop}$ (°C) | $T_{bufferbot}$ (°C) |
|----------|-------------------------------|----------------|--------------------|---------------------|----------------------|----------------------|
| 6:03:46  | 0.75                          | 17.53          | 15.57              | 14.33               | 15.56                | 15.69                |
| 7:03:46  | 75.08                         | 17.32          | 15.50              | 14.98               | 15.60                | 15.70                |
| 8:03:46  | 516.33                        | 17.53          | 19.18              | 32.32               | 15.92                | 15.73                |
| 9:03:46  | 683.42                        | 19.64          | 16.41              | 44.20               | 17.36                | 16.28                |
| 10:03:46 | 765.42                        | 21.20          | 15.83              | 46.02               | 16.52                | 15.57                |
| 11:03:46 | 814.92                        | 22.81          | 17.18              | 49.04               | 17.94                | 16.65                |
| 12:03:46 | 844.58                        | 24.18          | 15.54              | 50.19               | 17.47                | 15.54                |
| 13:03:46 | 804.75                        | 24.42          | 16.60              | 48.84               | 16.96                | 16.11                |
| 14:03:46 | 706.00                        | 24.43          | 19.47              | 47.83               | 19.07                | 18.87                |
| 15:03:46 | 371.17                        | 23.58          | 21.27              | 35.62               | 20.89                | 20.93                |
| 16:03:46 | 69.25                         | 22.08          | 20.97              | 25.43               | 21.61                | 20.85                |
| 17:03:46 | 8.33                          | 19.44          | 19.77              | 18.32               | 21.40                | 19.30                |

A graphical representation of the hourly average back surface of the PV modules is illustrated in Figure 8-15.

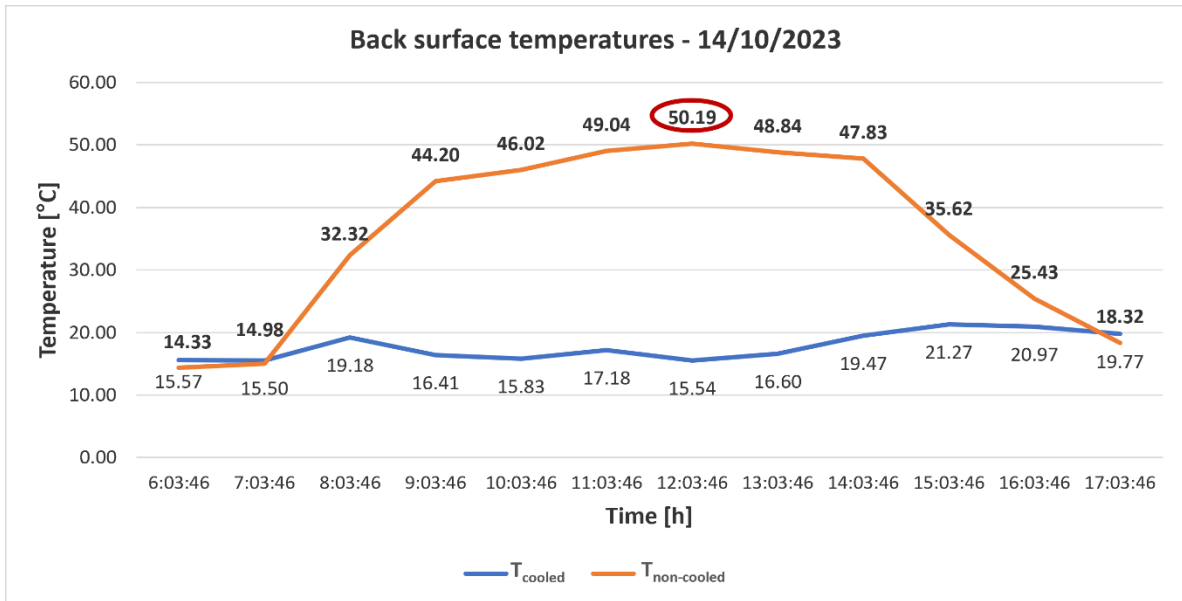


**Figure 8-15. The hourly average back surface temperature of the PV modules – 14/10/2023**

The average back surface temperature of the non-cooled PV module reached 50.19 °C, highlighted with a red oval in Figure 8-15. In comparison, the average back surface temperature of the cooled PV module reached 21.27 °C. The maximum back surface temperature of 52.75 °C occurred at 11.55 a.m. when the solar irradiation was 833 W/m<sup>2</sup>, and the ambient temperature was 24 °C. The hourly average flow rate of the PV/T system, along with inlet and outlet temperatures, are shown in Figure 8-16.

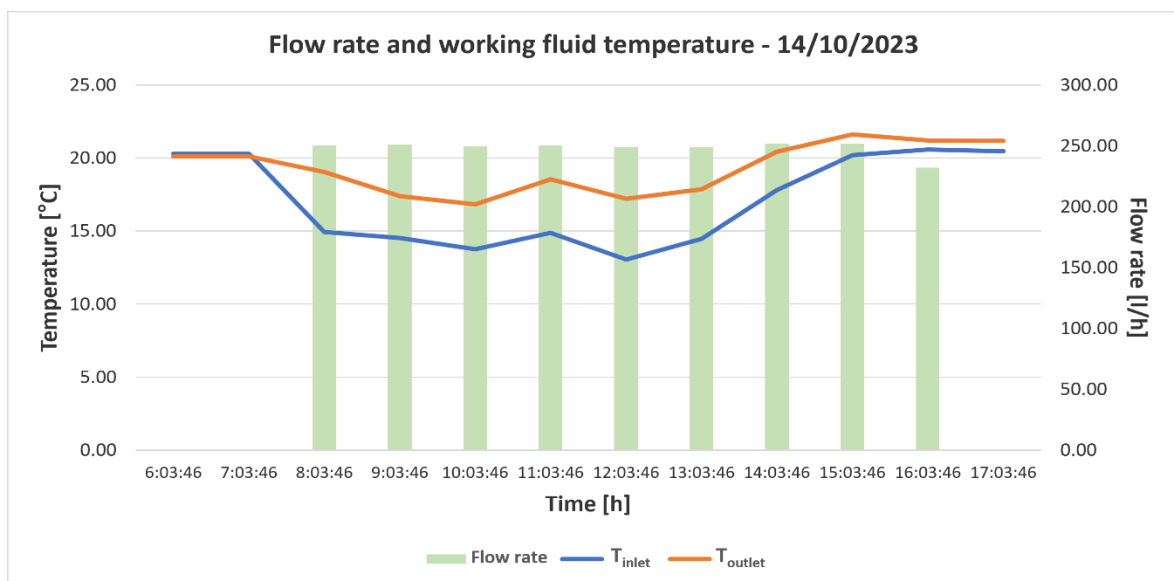


**Figure 8-16. The flow rate and temperatures in the PV/T system – 14/10/2023**

The total electrical energy generated by the cooled PV module was 1.66 kWh (AC), whereas the total electrical energy generated by the non-cooled PV module was 1.33 kWh (AC). The implemented cooling system allowed for generating the maximum electrical energy by increasing the production by 24.09% at the end of the test day.

The maximum electrical power output improvement was observed around 11:55 a.m., where the back surface temperatures of cooled and non-cooled PV modules were 15.90 °C and 52.75 °C.

The maximum thermal efficiency occurred at 11:33 a.m. with a value of 88.97%. During the maximum thermal efficiency observation, the volumetric flow rate was 4.20 L/min, and inlet and outlet temperatures were 14.7 °C and 18.9 °C with a maximum thermal power output of 1.23 kW under 816 W/m<sup>2</sup> with the ambient temperature of 23.3 °C.

The 12h (6 a.m. – 6 p.m.) total thermal output of the PV/T system was 6.78 kWh. Similarly, an energy analysis was performed to assess the available solar energy, thermal energy generated by the PV/T system, and electrical energy generated by the cooled and non-cooled PV module, as shown in Figure 8-17.

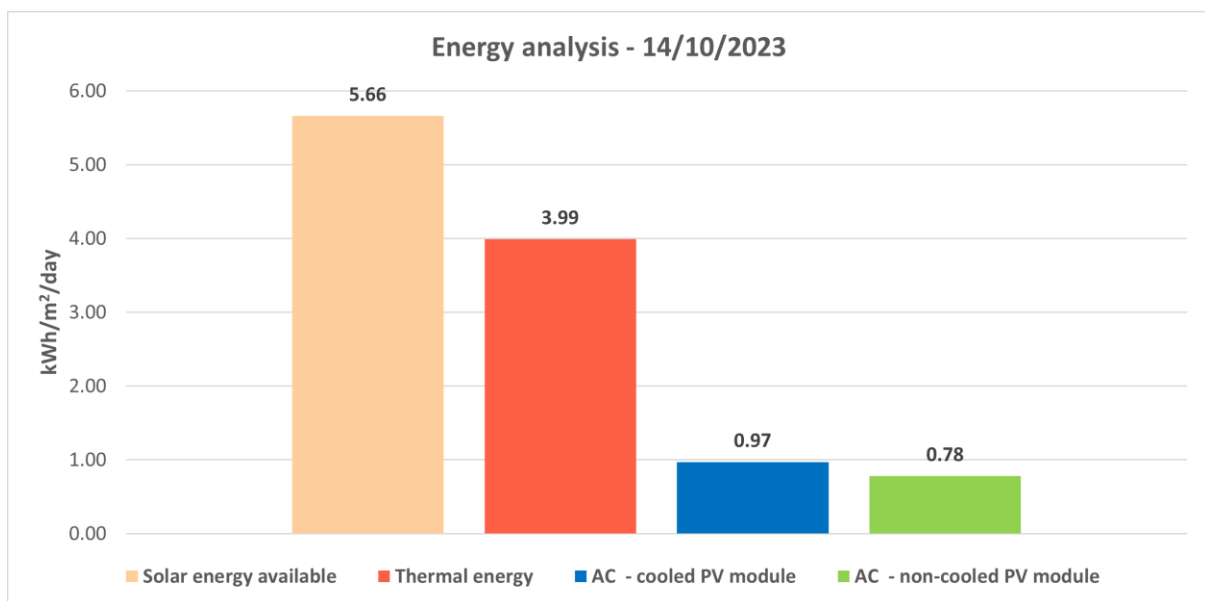


**Figure 8-17. The energy analysis – 14/10/2023**

The analysis showed that the available solar energy was 5.66 kWh/m<sup>2</sup>/day on the 14<sup>th</sup> of October, 2023. The thermal energy generation of the PV/T system was 3.99 kWh/m<sup>2</sup>/day. The electrical energy yield kWh/m<sup>2</sup>/day was 0.97 and 0.78 for cooled and non-cooled PV modules, respectively. The non-cooled PV module converted 15.41% of available solar energy into electrical energy, whereas the PV/T module converted 19.12% during 12 hours of operation.

## 8.2.2 Outdoor experiments without an active chiller

The outdoor experiments were performed without an active chiller for most of the tests to charge and observe the temperature in the buffer tank. The water in the buffer tank was circulated through the cooling system on the rear side of the PV module. The electrical conversion efficiency, power output, and thermal energy generation of the PV/T system were analyzed along with the non-cooled PV module to compare the results. In this part, the real-life tests conducted on the 26<sup>th</sup> and 29<sup>th</sup> of September and the 18<sup>th</sup> of October are presented. The rest of the results of the outdoor experiments are presented in Appendix B.

### Experiment – 26/09/2023

An outdoor experiment was conducted on the 26<sup>th</sup> of September, 2023, where the average outdoor temperature was 21.05 °C, and the average solar irradiation falling onto PV modules was 543.88 W/m<sup>2</sup> between 6 a.m. and 6 p.m. The maximum ambient temperature of 25.20 °C and solar irradiation of 904 W/m<sup>2</sup> were observed during the tests. The weather data, recorded every five minutes during the day, is shown in Figure 8-18.

The circulation pump was activated at 8:30 a.m. to start cooling the PV module, and the temperature on the bottom and top sides of the buffer tank was 16.4 °C and 21.3 °C, respectively. The pump worked until 3:30 p.m. to harvest the waste heat from the PV module and charge the 500 L buffer tank.

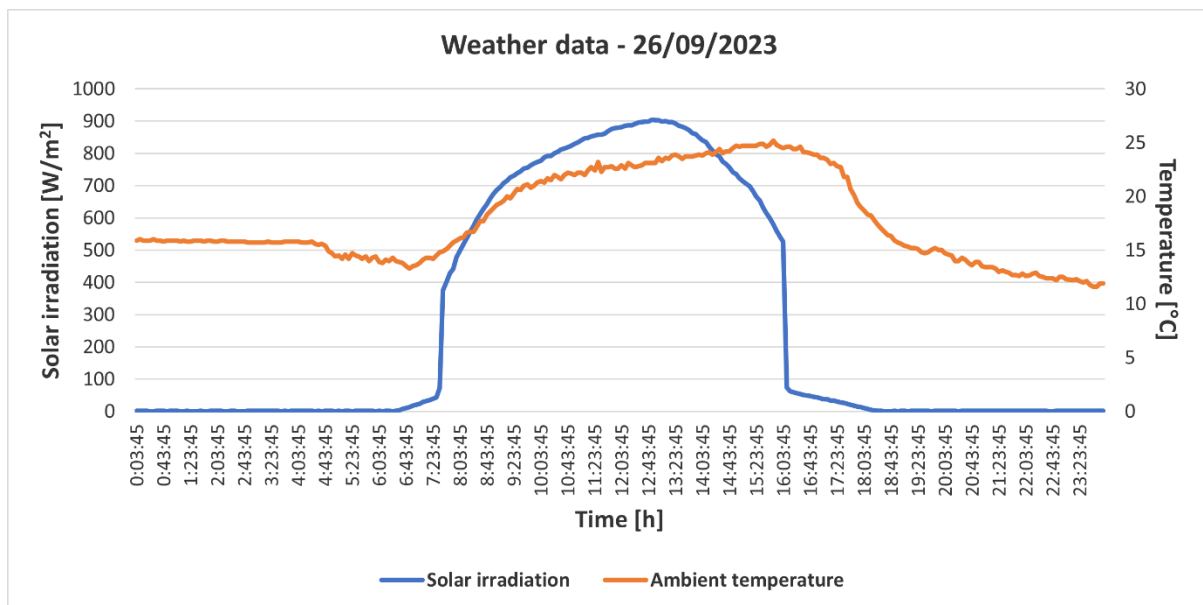


Figure 8-18. The weather data – 26/09/2023

The hourly average solar irradiation, outdoor temperature, the back surface temperature of PV modules, and buffer tank temperatures are given in Table 8-4.



**Table 8-4. The hourly weather data and temperature in the test rig – 26/09/2023**

| Time     | G <sub>sur</sub> (W/m <sup>2</sup> ) | T <sub>amb</sub> (°C) | T <sub>bcooled</sub> (°C) | T <sub>bncooled</sub> (°C) | T <sub>buffertop</sub> (°C) | T <sub>bufferbot</sub> (°C) |
|----------|--------------------------------------|-----------------------|---------------------------|----------------------------|-----------------------------|-----------------------------|
| 6:03:45  | 6.17                                 | 13.81                 | 12.42                     | 11.09                      | 21.40                       | 16.22                       |
| 7:03:45  | 200.08                               | 14.75                 | 13.53                     | 15.93                      | 21.37                       | 16.30                       |
| 8:03:45  | 598.92                               | 17.49                 | 20.28                     | 37.95                      | 21.52                       | 17.03                       |
| 9:03:45  | 739.58                               | 20.47                 | 21.66                     | 47.59                      | 22.15                       | 21.37                       |
| 10:03:45 | 807.33                               | 21.82                 | 23.94                     | 49.98                      | 25.37                       | 22.74                       |
| 11:03:45 | 860.42                               | 22.55                 | 26.66                     | 51.42                      | 27.34                       | 25.82                       |
| 12:03:45 | 894.17                               | 22.99                 | 28.69                     | 51.29                      | 30.25                       | 27.38                       |
| 13:03:45 | 881.25                               | 23.67                 | 30.54                     | 51.02                      | 32.02                       | 29.97                       |
| 14:03:45 | 782.67                               | 24.21                 | 32.38                     | 49.60                      | 32.96                       | 32.20                       |
| 15:03:45 | 637.42                               | 24.77                 | 32.85                     | 44.42                      | 34.62                       | 32.94                       |
| 16:03:45 | 92.25                                | 24.22                 | 33.29                     | 30.74                      | 34.81                       | 33.30                       |
| 17:03:45 | 26.33                                | 21.78                 | 25.81                     | 18.77                      | 34.62                       | 33.27                       |

A graphical representation of the back surface temperature of PV modules is shown in Figure 8-19 to present the cooling effect precisely.

The average back surface temperature of the non-cooled PV module reached 51.42 °C, highlighted with a red oval in Figure 8-19. In comparison, the average back surface temperature of the cooled PV module reached 33.29 °C.

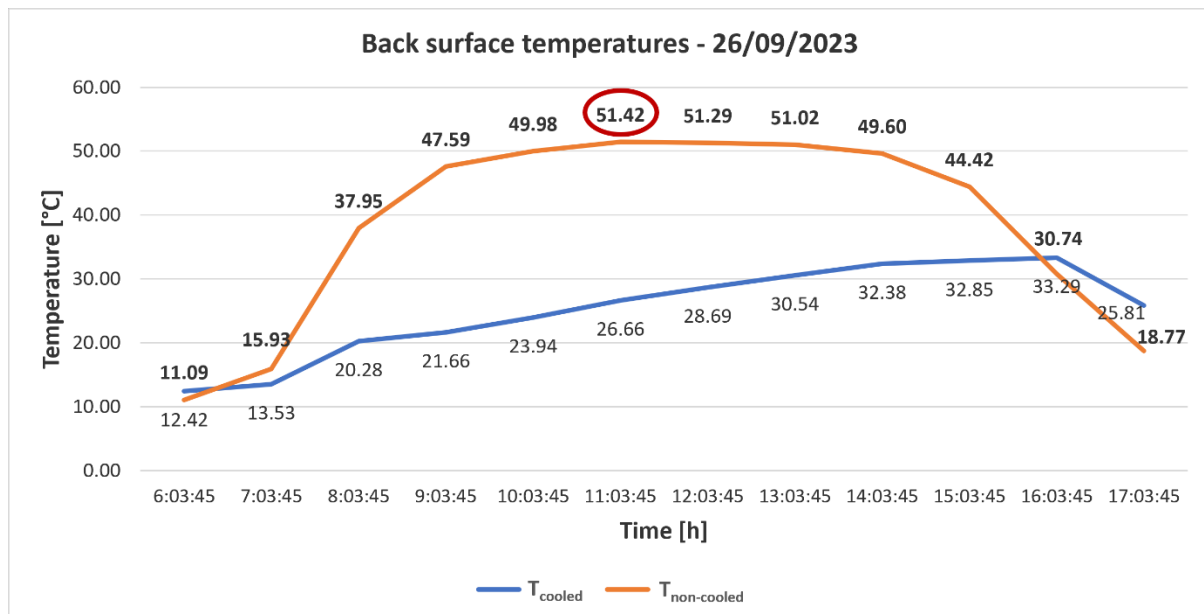


**Figure 8-19. The hourly average back surface temperature of the PV modules – 26/09/2023**

The maximum back surface temperature of 52.3 °C occurred at 11.30 a.m. when the solar irradiation was 858 W/m<sup>2</sup>, and the ambient temperature was 22.3 °C. The change in temperature of the bottom and top sides of the buffer tank during operation hours of the circulation pump is shown in Figure 8-20. The temperature at the bottom and top sides of the buffer tank reached 33.2 °C and 35.2 °C. The seven hours of operation between 8:30 a.m.

and 3:30 p.m. led to a 16.8 °C and 13.9 °C increase at the bottom and top sides of the buffer tank, respectively.

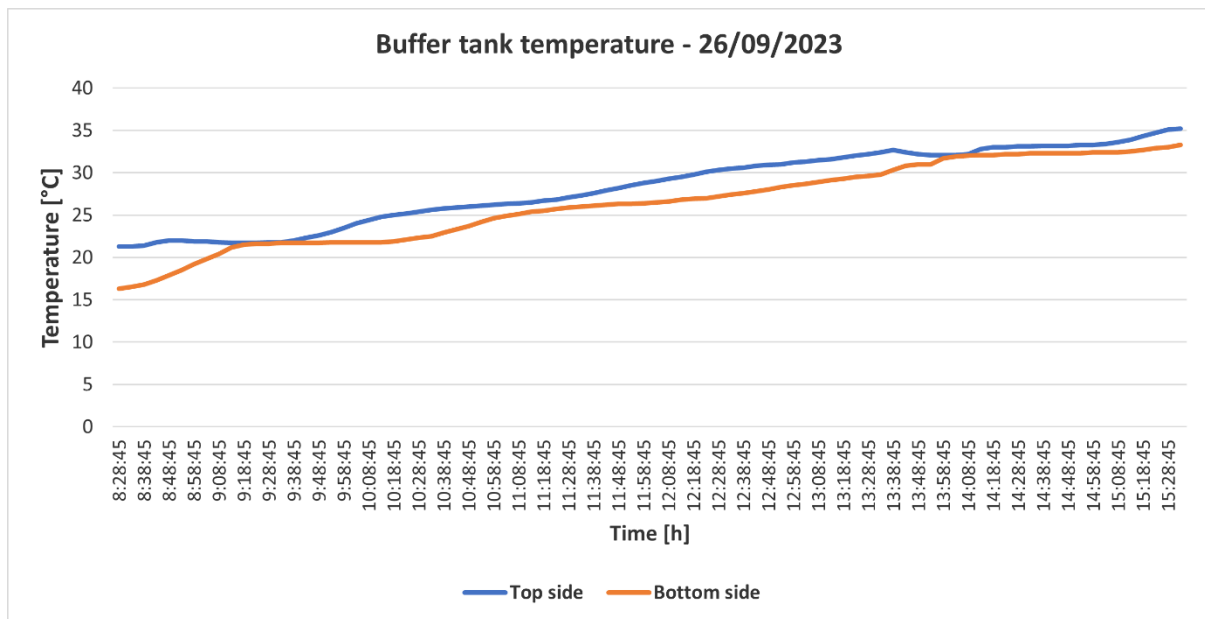


**Figure 8-20. The temperature change in the buffer tank – 26/09/2023**

On average, the buffer tank temperature was increased by 15.35 °C, meaning 8.93 kWh of thermal energy was generated using the waste heat from a single PV module during seven hours of operation.

A graphical representation of the hourly average flow rate of the PV/T system, along with inlet and outlet temperatures, is shown in Figure 8-21.

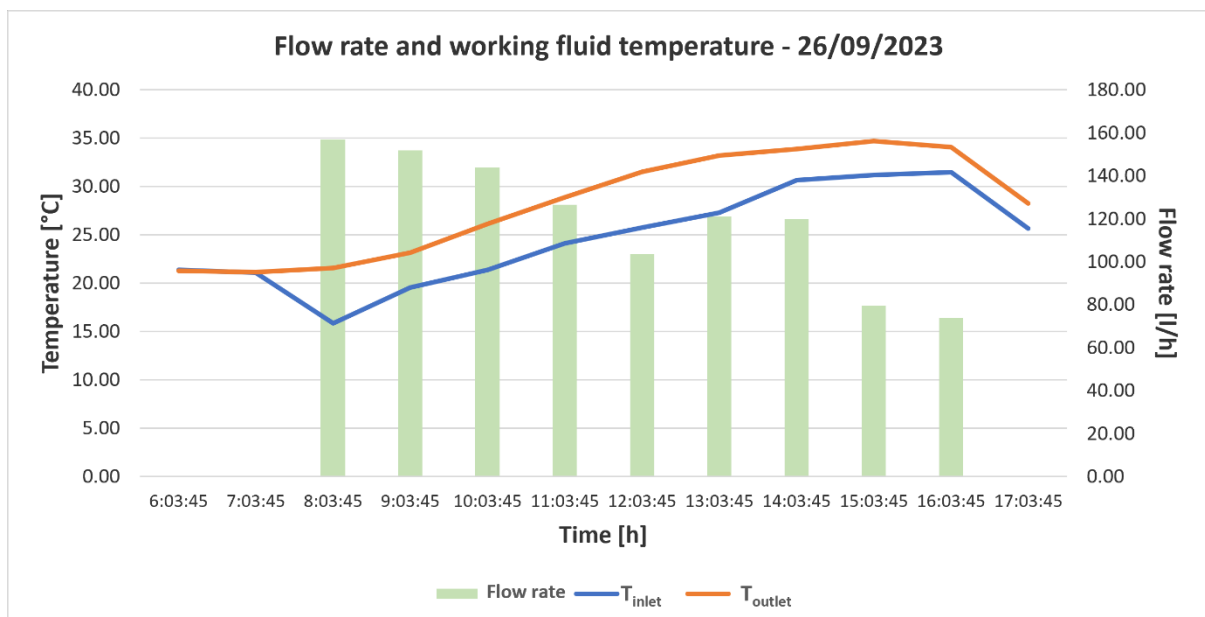


**Figure 8-21. The flow rate and temperatures in the PV/T system – 26/09/2023**

The total electrical energy generated by the PV modules was compared using the data acquired from the grid-tie microinverters. The total electrical energy generated by the cooled PV module was 1.86 kWh (AC), whereas the total electrical energy generated by the non-cooled PV module was 1.57 kWh (AC). The implemented cooling system allowed for generating the maximum electrical energy by increasing the production by 18.42% at the end of the test day.

The maximum electrical power output improvement was observed around 11:13 a.m., where the back surface temperatures of cooled and non-cooled PV modules were 25.73 °C and 51.05 °C. The maximum thermal efficiency occurred at 10:13 a.m. with a value of 61.77%. During the maximum thermal efficiency observation, the volumetric flow rate was 2.48 L/min, and inlet and outlet temperatures were 21.1 °C and 25.9 °C with a maximum thermal power output of 0.83 kW under 792 W/m<sup>2</sup> with the ambient temperature of 21.7 °C. The 12h (6 a.m. – 6 p.m.) total thermal energy generated by the PV/T system was 8.93 kWh. Similarly, an energy analysis was performed to assess the available solar energy, thermal energy generated by the PV/T system, and electrical energy generated by the cooled and non-cooled PV module, as shown in Figure 8-22.

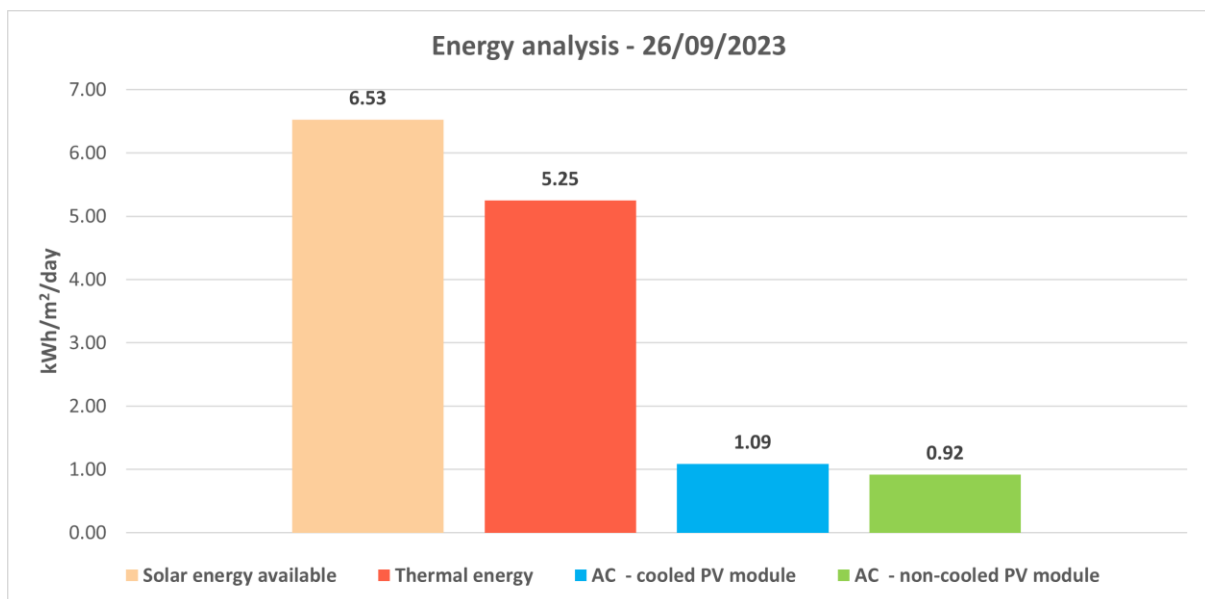


**Figure 8-22. The energy analysis – 26/09/2023**

The analysis showed that the available solar energy was 6.53 kWh/m<sup>2</sup>/day on the 26<sup>th</sup> of September, 2023. The thermal energy generation of the PV/T system was 5.25 kWh/m<sup>2</sup>/day. The electrical energy yield kWh/m<sup>2</sup>/day was 1.09 and 0.92 for cooled and non-cooled PV modules, respectively. The non-cooled PV module converted 15.73% of available solar energy into electrical energy, whereas the PV/T module converted 18.62% during 12 hours of operation.

## Experiment – 29/09/2023

On the 29<sup>th</sup> of September, 2023, another experiment was conducted, and the weather data is shown in Figure 8-23. The average outdoor temperature was 19.51 °C, and the average solar irradiation falling onto PV modules was 539.12 W/m<sup>2</sup> between 6 a.m. and 6 p.m. The maximum ambient temperature of 25.20 °C and solar irradiation of 922 W/m<sup>2</sup> were observed during the tests.

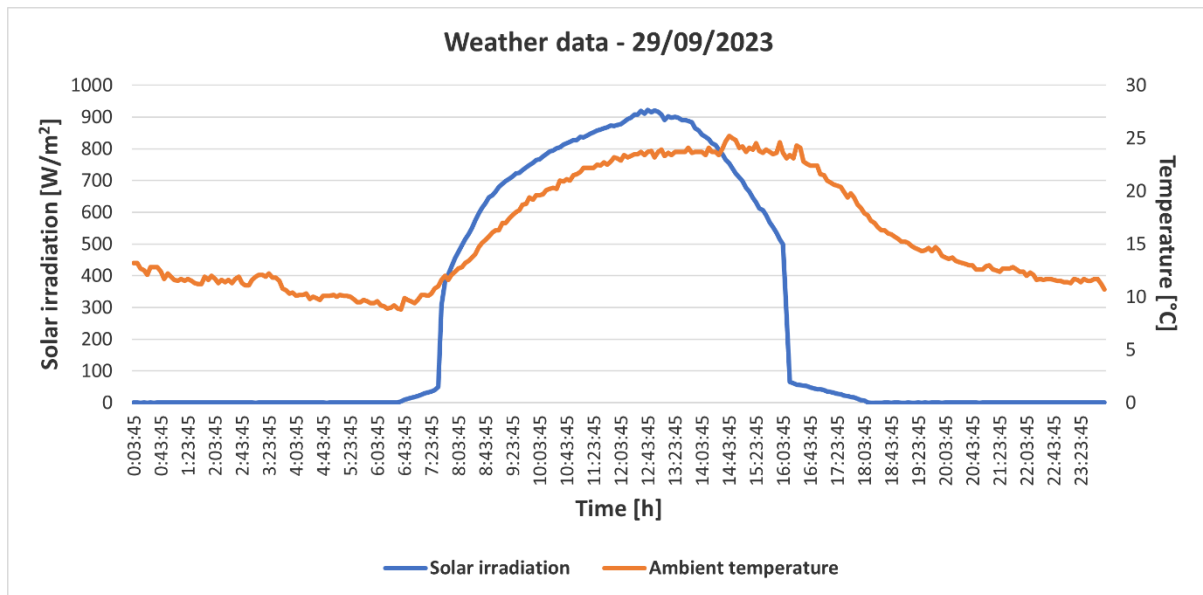


**Figure 8-23. The weather data – 29/09/2023**

The hourly average solar irradiation, outdoor temperature, back surface temperature of PV modules, and buffer tank temperatures are given in Table 8-5.

**Table 8-5. The hourly weather data and temperature in the test rig – 29/09/2023**

| Time     | $G_{sur}$ (W/m <sup>2</sup> ) | $T_{amb}$ (°C) | $T_{bcooled}$ (°C) | $T_{bncooled}$ (°C) | $T_{buffertop}$ (°C) | $T_{bufferbot}$ (°C) |
|----------|-------------------------------|----------------|--------------------|---------------------|----------------------|----------------------|
| 6:03:45  | 5.42                          | 9.27           | 8.25               | 6.89                | 15.20                | 15.36                |
| 7:03:45  | 184.25                        | 11.00          | 9.60               | 11.87               | 15.26                | 15.37                |
| 8:03:45  | 578.67                        | 14.42          | 20.35              | 33.46               | 15.29                | 15.43                |
| 9:03:45  | 722.67                        | 18.11          | 19.71              | 45.30               | 17.03                | 16.27                |
| 10:03:45 | 802.00                        | 20.60          | 19.71              | 47.95               | 19.32                | 18.89                |
| 11:03:45 | 857.25                        | 22.48          | 22.18              | 51.84               | 21.77                | 21.32                |
| 12:03:45 | 905.92                        | 23.44          | 24.54              | 52.90               | 24.27                | 23.84                |
| 13:03:45 | 888.92                        | 23.67          | 26.67              | 51.81               | 26.49                | 26.21                |
| 14:03:45 | 784.25                        | 24.15          | 28.49              | 51.73               | 28.31                | 28.16                |
| 15:03:45 | 607.83                        | 23.92          | 29.25              | 45.93               | 30.02                | 29.30                |
| 16:03:45 | 107.75                        | 22.98          | 30.01              | 30.11               | 29.97                | 30.09                |
| 17:03:45 | 24.50                         | 20.03          | 24.09              | 17.90               | 29.90                | 30.00                |

The back surface temperature of PV modules during the day is shown in Figure 8-24.

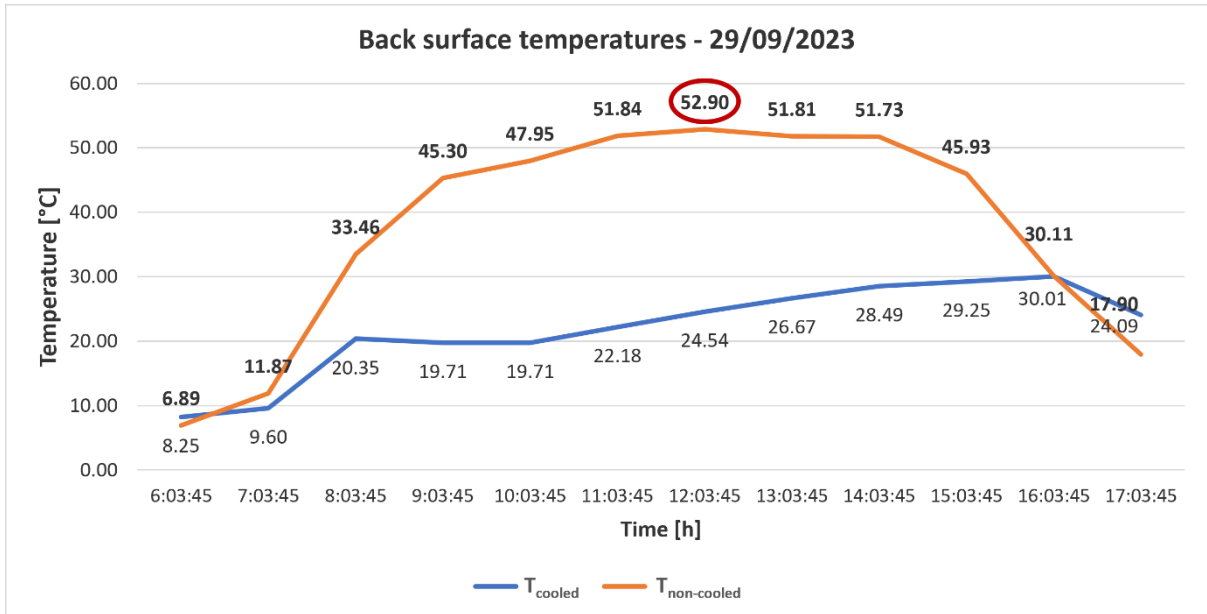


**Figure 8-24. The hourly average back surface temperature of the PV modules – 29/09/2023**

The average back surface temperature of the non-cooled PV module reached 52.90 °C, highlighted with a red oval in Figure 8-24. In comparison, the average back surface temperature of the cooled PV module reached 30.01 °C. The maximum back surface temperature of 54.3 °C occurred at 12.13 p.m. when the solar irradiation was 893 W/m<sup>2</sup>, and the ambient temperature was 23.2 °C. The hourly average flow rate of the PV/T system, along with inlet and outlet temperatures, are shown in Figure 8-25.

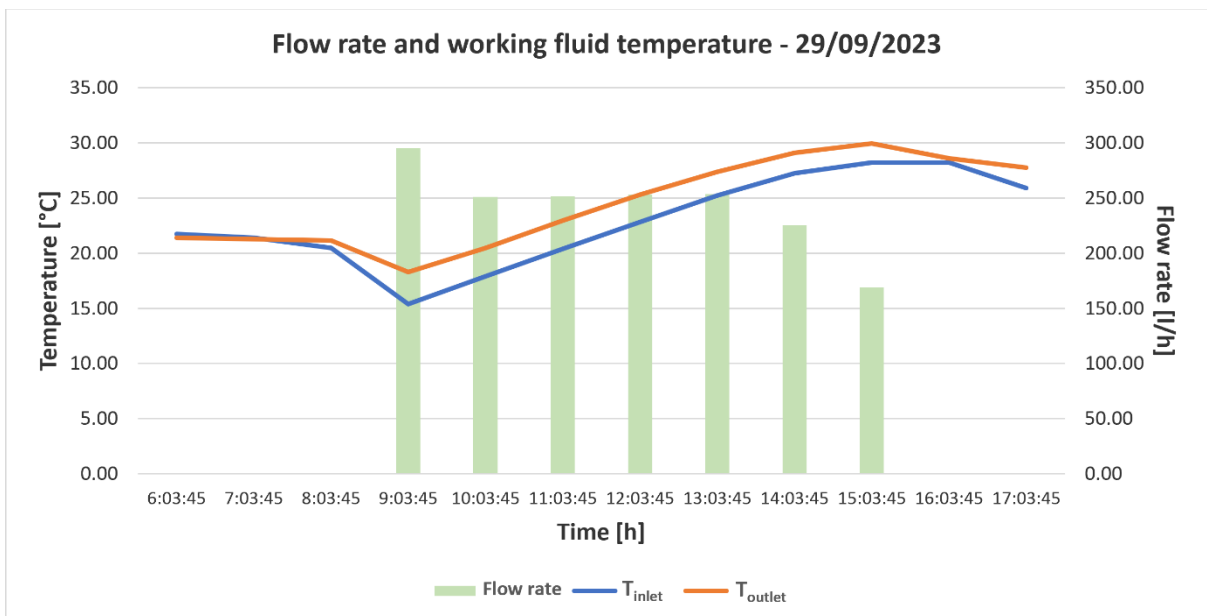


**Figure 8-25. The flow rate and temperatures in the PV/T system – 29/09/2023**

The circulation pump was activated at 8:50 a.m. to start cooling the PV module, and the temperature on the bottom and top sides of the buffer tank was 15.3 °C and 15.2 °C, respectively. The pump worked until 4:10 p.m. to harvest the waste heat from the PV module and charge the 500 L buffer tank. The change in temperature of the bottom and top sides of the buffer tank during operation hours of the circulation pump is shown in Figure 8-26.

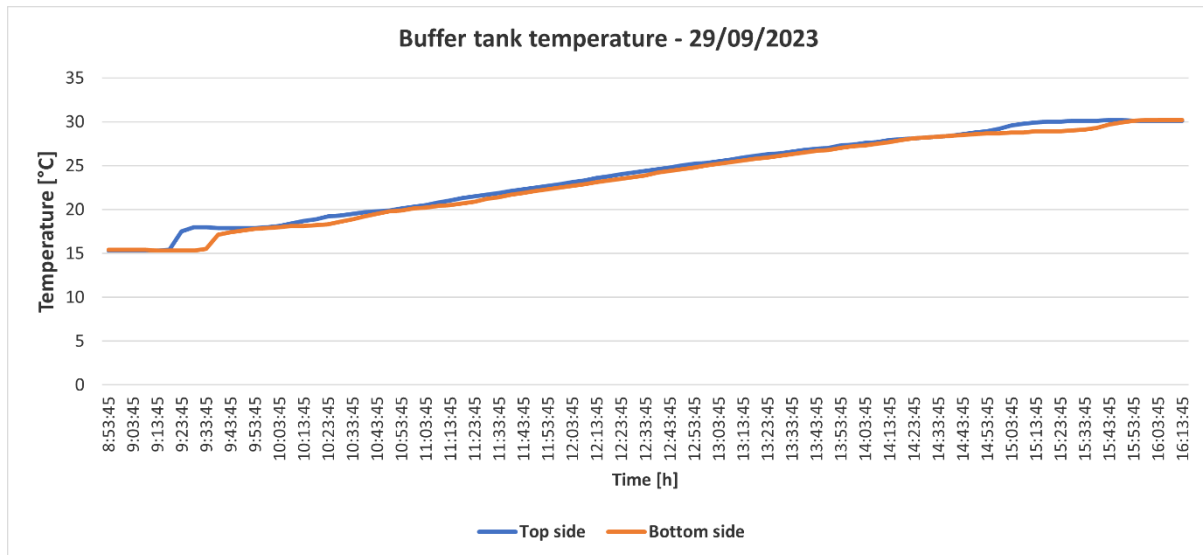


**Figure 8-26. The temperature change in the buffer tank – 29/09/2023**

The temperature at the bottom and top sides of the buffer tank reached 30.2 °C and 30.1 °C. The seven hours and twenty minutes of operation between 8:50 a.m. and 4:10 p.m. led to a 14.9 °C increase at the bottom and top sides of the buffer tank.

On average, the buffer tank temperature was increased by 14.9 °C, meaning 8.67 kWh of thermal energy was generated using the waste heat from a single PV module.

The electrical energy generated by the PV modules was compared using the data acquired from the grid-tie microinverters. The total electrical energy generated by the cooled PV module was 1.87 kWh (AC), whereas the total electrical energy generated by the non-cooled PV module was 1.55 kWh (AC).

The implemented cooling system allows for generating the maximum electrical energy by increasing the production by 20.70% at the end of the test day.

The maximum electrical power output improvement was observed around 12:13 a.m., where the back surface temperatures of cooled and non-cooled PV modules were 23.9 °C and 54.3 °C.

The maximum thermal efficiency occurred at 10:23 a.m. with a value of 60.64%. During the maximum thermal efficiency observation, the volumetric flow rate was 4.17 L/min, and inlet

and outlet temperatures were 17.4 °C and 20.2 °C with a maximum thermal power output of 0.81 kW under 795 W/m<sup>2</sup> with the ambient temperature of 20.3 °C. The 12h (6 a.m. – 6 p.m.) total thermal output of the PV/T system was 8.67 kWh.

Similarly, an energy analysis was performed to assess the available solar energy, thermal energy generated by the PV/T system, and electrical energy generated by the cooled and non-cooled PV module, as shown in Figure 8-27.

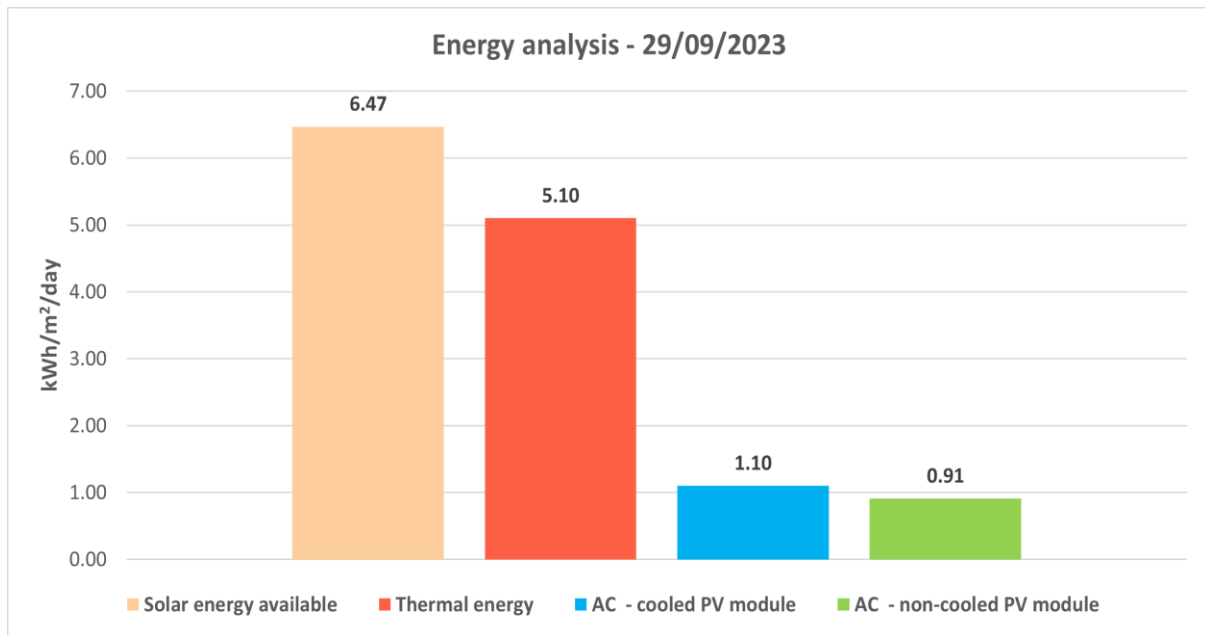


**Figure 8-27. The energy analysis – 29/09/2023**

The analysis showed that the available solar energy was 6.47 kWh/m<sup>2</sup>/day on the 29<sup>th</sup> of September, 2023. The thermal energy generated by the PV/T system was 5.10 kWh/m<sup>2</sup>/day. The electrical energy yield kWh/m<sup>2</sup>/day was 1.10 and 0.91 for cooled and non-cooled PV modules, respectively. The non-cooled PV module converted 15.68% of available solar energy into electrical energy, whereas the PV/T module converted 18.93% during 12 hours of operation.

### **Experiment – 18/10/2023**

On the 18<sup>th</sup> of October, 2023, another experiment was conducted. The average outdoor temperature was 7.64 °C, and the average solar irradiation falling onto PV modules was 503.35 W/m<sup>2</sup> between 6 a.m. and 6 p.m. The maximum ambient temperature of 13.20 °C and solar irradiation of 911 W/m<sup>2</sup> were observed during the tests. The weather data is shown in Figure 8-28.

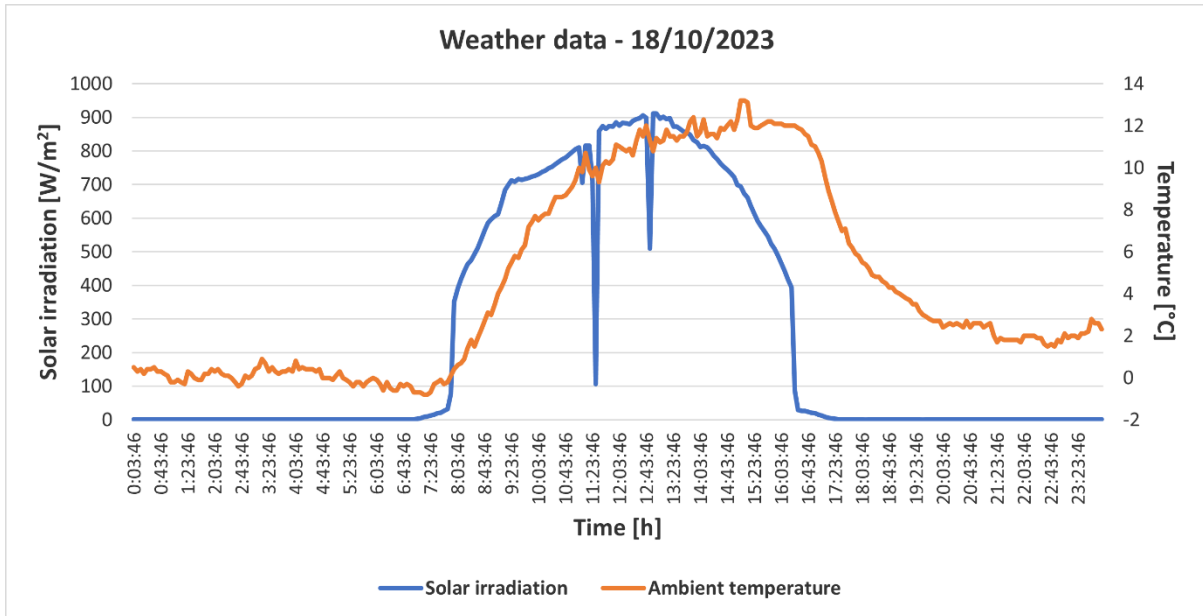


**Figure 8-28. The weather data – 18/10/2023**

The hourly average solar irradiation, outdoor temperature, the back surface temperature of PV modules, and buffer tank temperatures are given in Table 8-6.

**Table 8-6. The hourly weather data and temperature in the test rig – 18/10/2023**

| Time     | $G_{sur}$ (W/m <sup>2</sup> ) | $T_{amb}$ (°C) | $T_{bcooled}$ (°C) | $T_{bncooled}$ (°C) | $T_{buffertop}$ (°C) | $T_{bufferbot}$ (°C) |
|----------|-------------------------------|----------------|--------------------|---------------------|----------------------|----------------------|
| 6:03:45  | 1.25                          | -0.42          | 10.26              | -3.44               | 11.20                | 11.50                |
| 7:03:45  | 48.58                         | -0.36          | 9.73               | -2.67               | 10.62                | 10.89                |
| 8:03:45  | 506.67                        | 1.95           | 12.94              | 15.62               | 10.54                | 10.68                |
| 9:03:45  | 697.58                        | 5.82           | 11.80              | 33.47               | 11.46                | 11.37                |
| 10:03:45 | 765.33                        | 8.41           | 13.75              | 37.04               | 12.97                | 13.12                |
| 11:03:45 | 766.58                        | 10.12          | 15.33              | 37.78               | 14.61                | 14.66                |
| 12:03:45 | 861.50                        | 11.19          | 17.09              | 40.83               | 16.28                | 16.36                |
| 13:03:45 | 868.33                        | 11.62          | 18.33              | 41.50               | 18.28                | 18.00                |
| 14:03:45 | 767.50                        | 11.84          | 19.57              | 41.13               | 19.63                | 19.49                |
| 15:03:45 | 589.17                        | 12.33          | 20.22              | 33.03               | 20.41                | 20.53                |
| 16:03:45 | 164.17                        | 11.64          | 20.54              | 25.39               | 20.67                | 20.83                |
| 17:03:45 | 3.50                          | 7.57           | 18.31              | 4.60                | 20.22                | 20.26                |

A graphical representation of the back surface temperature of PV modules is shown in Figure 8-29 to present the cooling effect precisely. The average back surface temperature of the non-cooled PV module reached 41.50 °C, highlighted with a red oval in Figure 8-29. In comparison, the average back surface temperature of the cooled PV module reached 20.54 °C. The maximum back surface temperature of 44.22 °C occurred at 1.48 p.m. for the non-cooled PV module when the solar irradiation was 848 W/m<sup>2</sup>, and the ambient temperature was 12.2 °C.



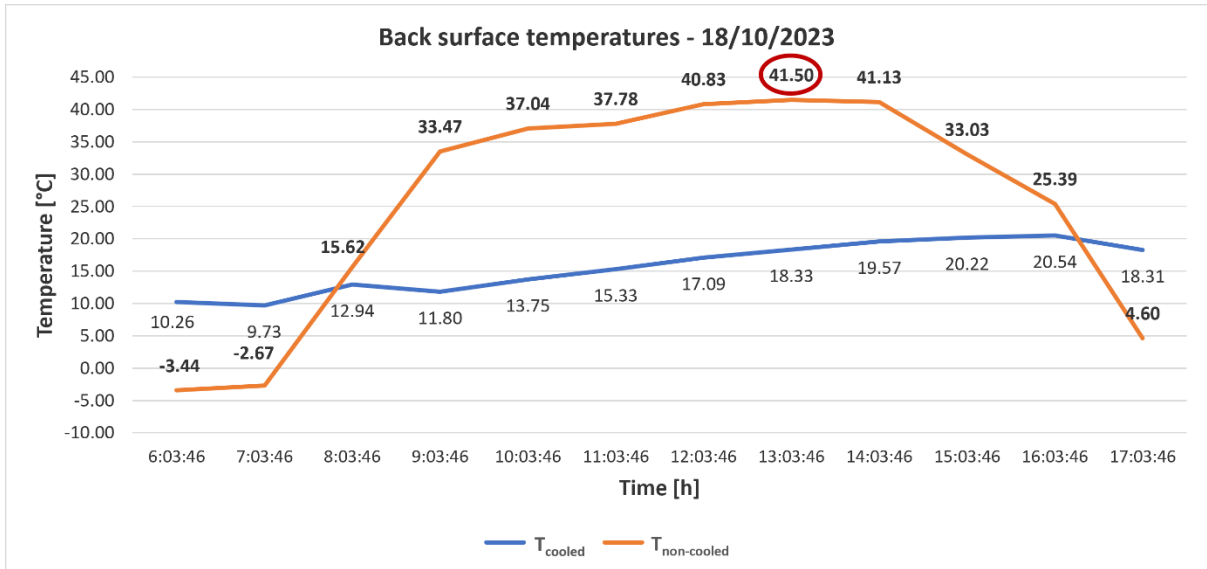


**Figure 8-29. The hourly average back surface temperature of the PV modules – 18/10/2023**

A graphical representation of the hourly average flow rate of the PV/T system, along with inlet and outlet temperatures, is shown in Figure 8-30.

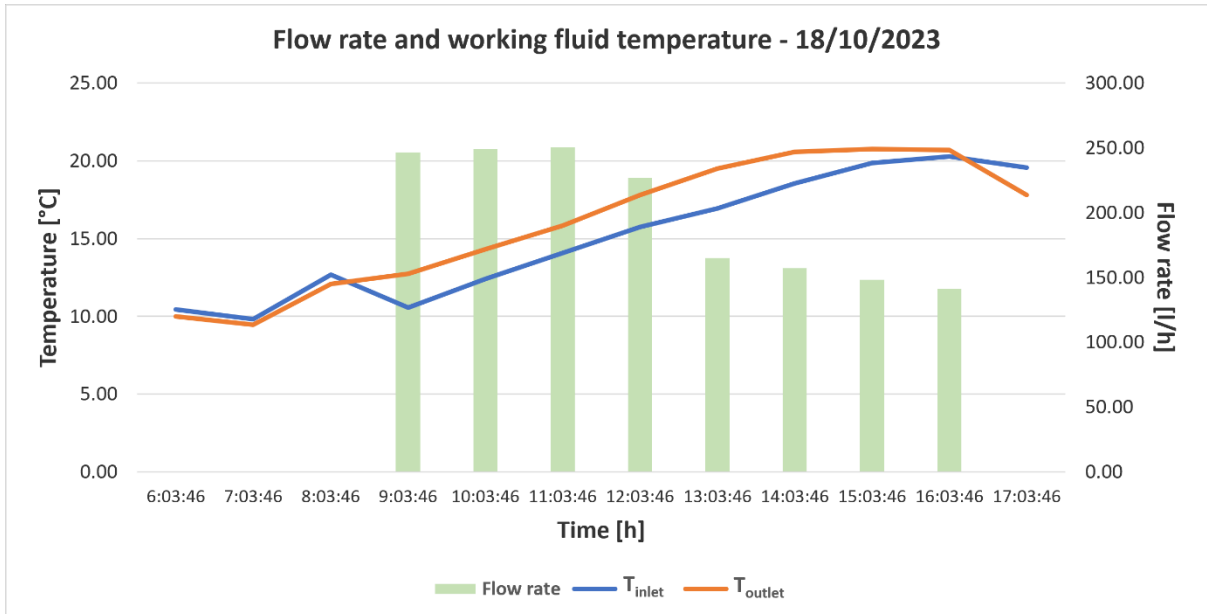


**Figure 8-30. The flow rate and temperatures in the PV/T system – 18/10/2023**

The circulation pump was activated at 9:03 a.m. to start cooling the PV module, and the temperature on the bottom and top sides of the buffer tank was 10.7 °C and 10.6 °C, respectively. The pump worked until 4:28 p.m. to harvest the waste heat from the PV module and charge the 500 L buffer tank. The temperature at the bottom and top sides of the buffer

tank reached 20.9 °C and 20.7 °C. The change in temperature of the bottom and top sides of the buffer tank during operation hours of the circulation pump is shown in Figure 8-31.

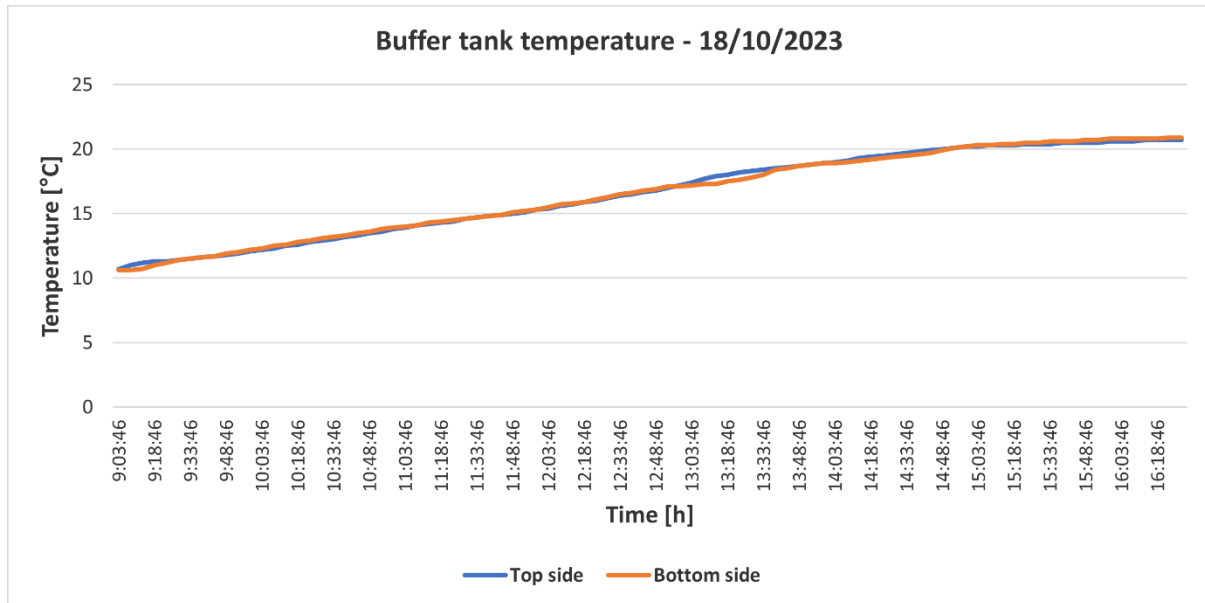


**Figure 8-31. The temperature change in the buffer tank – 18/10/2023**

The seven hours and thirty minutes of operation between 9:03 a.m. and 4:28 p.m. led to a 10.3 °C and 10.0 °C increase at the bottom and top sides of the buffer tank, respectively. On average, the buffer tank temperature was increased by 10.15 °C, meaning 5.91 kWh of thermal energy is generated using the waste heat from a single PV module.

The electrical energy generated by the PV modules was compared. The total electrical energy generated by the cooled PV module was 1.77 kWh (AC), whereas the total electrical energy generated by the non-cooled PV module was 1.60 kWh (AC). The implemented cooling system allowed for generating the maximum electrical energy by increasing the production by 10.66% at the end of the test day.

The maximum electrical power output improvement was observed around 1:48 p.m., where the back surface temperatures of cooled and non-cooled PV modules were 18.71 °C and 44.22 °C.

The maximum thermal efficiency occurred at 11:08 a.m. with a value of 49.16%. During the maximum thermal efficiency observation, the volumetric flow rate was 4.2 L/min, and inlet and outlet temperatures were 13.4 °C and 15.4 °C with a maximum thermal power output of 0.59 kW under 706 W/m<sup>2</sup> with the ambient temperature of 9.8 °C. The 12h (6 a.m. – 6 p.m.) total thermal output of the PV/T system was 5.91 kWh. Similarly, an energy analysis was performed to assess the available solar energy, thermal energy generated by the PV/T system, and

electrical energy generated by the cooled and non-cooled PV modules, as shown in Figure 8-32.

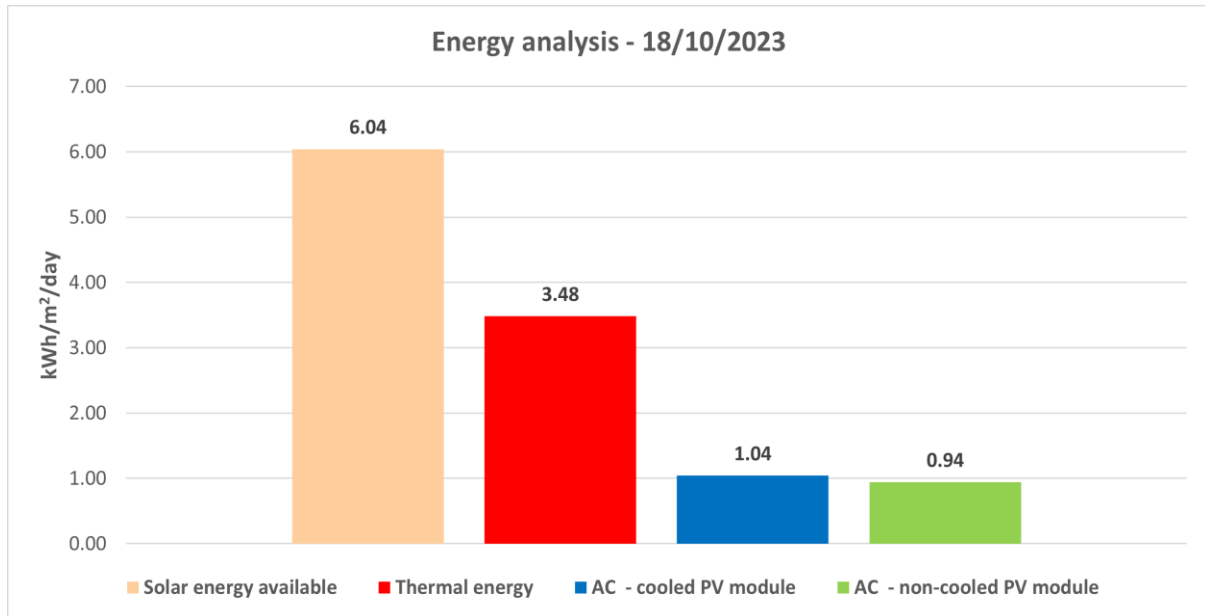


**Figure 8-32. The energy analysis – 18/10/2023**

The analysis showed that the available solar energy was 6.04 kWh/m<sup>2</sup>/day on the 18<sup>th</sup> of October, 2023. The thermal energy generation of the PV/T system was 3.48 kWh/m<sup>2</sup>/day. The electrical energy yield kWh/m<sup>2</sup>/day was 1.04 and 0.94 for cooled and non-cooled PV modules, respectively. The non-cooled PV module converted 17.28% of available solar energy into electrical energy, whereas the PV/T module converted 19.12% during 12 hours of operation.

### 8.3 Cooling uniformity

The uniformity of the cooling is one of the essential features of the cooling system on the PV/T systems. Cooling uniformity enhances efficiency by maintaining consistent temperature across the PV cells, as in the cases of non-uniform cooling, some areas of the PV cells can be cooler than others, leading to variations in electrical energy generation. The uniform cooling also eliminates the hot spots that can cause damage and reduce the lifetime of the PV cells.

Thermal stress due to temperature variation is another effect of non-uniform cooling and can lead to material degradation. The uniform cooling contributes to the predictability of the electrical and thermal energy output of the PV/T system. In order to investigate the uniformity of the cooling system, a thermographic camera was used to take thermal images from the PV/T system on the 18<sup>th</sup> of September, 2023.

The thermal image taken from the test rig is shown in Figure 8-33.

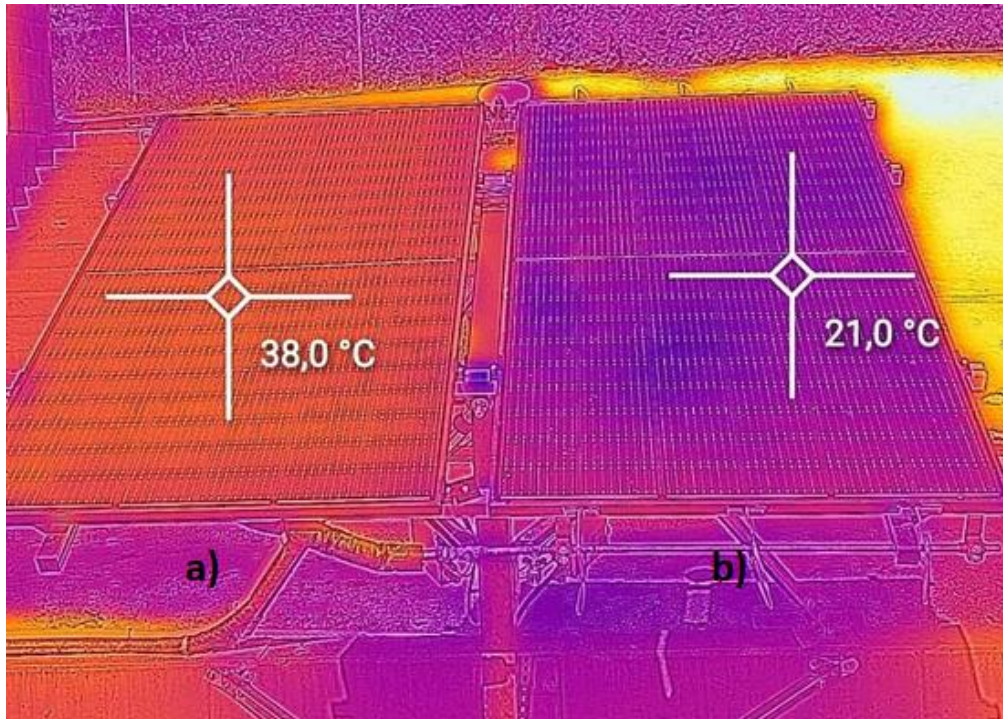


**Figure 8-33. The thermal image of a) the non-cooled PV module and b) the PV/T system**

As seen in Figure 8-33, the PV module was uniformly cooled and maintained the temperature as low as possible to produce maximum electrical power output. The optimal temperature for PV cells is 25 °C or lower to generate maximum electrical power output and maintain the maximum electrical conversion efficiency. During the measurements at 2.30 p.m., the back surface temperature of the non-cooled PV module was 37.05 °C, showing a good agreement with the surface temperature measured by the thermal camera. In contrast, the back surface temperature of the cooled PV module was 20.12 °C. The designed cooling system was able to ensure uniform cooling for the PV module while harvesting the waste heat.

#### **8.4 Pressure drop in the test rig**

Two pressure transmitters with a pressure range of 6 bar were placed in the test rig during the preparation. The minimum and maximum working temperatures of the transmitters were -40 °C and 85 °C.

One of the transmitters was placed directly after the circulation pump, which circulates the water through the inlet collector, PV/T module, outlet collector, and buffer tank. The second pressure transmitter was placed before the buffer tank. The placement of the pressure transmitters allowed for measuring the pressure in the inlet and outlet collectors of the PV/T module.

The pressure drop in the system with respect to flow rate was analyzed, and the results are shown in Figure 8-34.

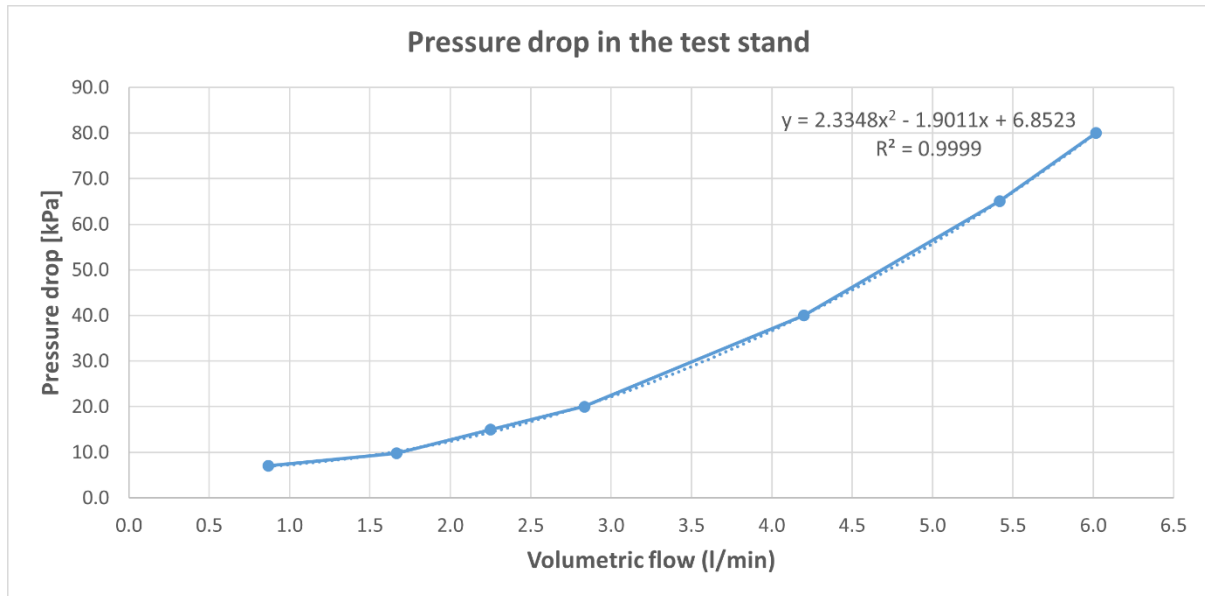


**Figure 8-34. The pressure drop in the test rig with respect to the flow rate**

The volumetric flow rate dependent pressure drop equation was defined as:

$$P_{drop} = 2.3348q^2 - 1.9011q + 6.8523 \quad (49)$$

In Eq. 49,  $P_{drop}$  is the pressure drop with a unit of  $kPa$  in the system, and  $q$  is the volumetric flow rate in  $l/min$ .

## 8.5 The energy analysis

An energy analysis was performed using the collected data from the outdoor experiments to estimate the yearly energy yield of the designed PV/T system. The PV/T and non-cooled PV modules integrated with a single-axis sun-tracking system were tested outdoors 19 days in September and 31 days in October 2023. During the experiments, thermal and electrical energy generated with the designed PV/T system and electrical energy generated with the stand-alone PV module were collected.

Two identical grid-tie microinverters were used to measure the electrical energy generation. An ultra-sonic heat meter with high accuracy was used to measure the inlet volumetric flow rate and inlet and outlet temperatures of the PV/T system.

The collected data was then used to validate the PV/T model developed in TRNSYS software to conduct yearly energy analysis and further used for the economic analysis of the designed system.

The daily available solar energy, average ambient temperature, electrical energy, and thermal energy generation for September are presented in Table 8-7.

**Table 8-7. The energy analysis on collected data for September 2023**

| Date       | $G_{\text{available}}$<br>(kWh/m <sup>2</sup> ) | $T_{\text{amb}}$<br>(°C) | $P_{\text{cooled}}$<br>(kWh/m <sup>2</sup> ) | $P_{\text{non-cooled}}$<br>(kWh/m <sup>2</sup> ) | $Q_{\text{thermal}}$<br>(kWh/m <sup>2</sup> ) |
|------------|---|--------------------------|--|--|---|
| 12/09/2023 | 5.88  | 24.05                    | 1.01   | 0.72   | 4.55  |
| 13/09/2023 | 5.82  | 24.06                    | 1.00   | 0.75   | 4.41  |
| 14/09/2023 | 0.63  | 16.56                    | 0.11   | 0.11   | 0.00  |
| 15/09/2023 | 5.98  | 17.31                    | 0.99   | 0.82   | 2.02  |
| 16/09/2023 | 6.22  | 17.66                    | 1.05   | 0.84   | 2.04  |
| 17/09/2023 | 5.36  | 20.85                    | 0.91   | 0.71   | 2.77  |
| 18/09/2023 | 6.33  | 21.70                    | 1.09   | 0.92   | 4.51  |
| 19/09/2023 | 0.75  | 17.06                    | 0.13   | 0.13   | 0.00  |
| 20/09/2023 | 6.84  | 19.12                    | 1.18   | 0.97   | 4.04  |
| 21/09/2023 | 7.04  | 20.63                    | 1.21   | 1.02   | 4.22  |
| 22/09/2023 | 5.34  | 21.87                    | 0.92   | 0.79   | 2.97  |
| 23/09/2023 | 0.69  | 15.82                    | 0.12   | 0.12   | 0.00  |
| 24/09/2023 | 0.53  | 11.85                    | 0.09   | 0.09   | 0.00  |
| 25/09/2023 | 1.02  | 16.00                    | 0.18   | 0.18   | 0.00  |
| 26/09/2023 | 6.53  | 21.05                    | 1.09   | 0.92   | 5.25  |
| 27/09/2023 | 6.13  | 20.21                    | 0.98   | 0.87   | 1.41  |
| 28/09/2023 | 5.73  | 20.14                    | 0.98   | 0.84   | 2.85  |
| 29/09/2023 | 6.47  | 19.51                    | 1.10   | 0.91   | 5.10  |
| 30/09/2023 | 0.70  | 14.70                    | 0.12   | 0.12   | 0.00  |

In Table 8-7,  $G_{\text{available}}$  is the available solar energy, and  $Q_{\text{thermal}}$  stands for the thermal energy generation of the PV/T module. The power output of the PV/T module and non-cooled PV module is given AC form.

The measurement results showed that the total electrical energy generated by the PV/T module and stand-alone PV module were 24.21 kWh/month and 20.11 kWh/month, respectively. The average improvement in electrical energy generation was 20.40% compared to the stand-alone PV module.

The total thermal energy yield of the PV/T module was 78.39 kWh/month during the 19 days of the experiments.

The monthly available solar energy was 83.98 kWh/m<sup>2</sup>/month, the thermal energy generated was 46.13 kWh/m<sup>2</sup>, and the electrical energy generated by the PV/T module was 14.25 kWh/m<sup>2</sup> (AC). The PV/T module was able to convert 54.93% and 18.85% of the available solar energy into thermal and electrical energy (DC), respectively. The non-cooled PV module converted 15.65% of the available solar energy into electrical energy (DC).

The outdoor experiments were continued in October 2023 to assess the performance of the PV/T module and compare it to the stand-alone PV module, as given in Table 8-8. The daily

available solar energy, average ambient temperature, electrical energy, and thermal energy generation for October were investigated.

**Table 8-8. The energy analysis on collected data for October 2023**

| Date       | G <sub>available</sub><br>(kWh/m <sup>2</sup> ) | T <sub>amb</sub><br>(°C) | P <sub>cooled</sub><br>(kWh/m <sup>2</sup> ) | P <sub>non-cooled</sub><br>(kWh/m <sup>2</sup> ) | Q <sub>thermal</sub><br>(kWh/m <sup>2</sup> ) |
|------------|---|--------------------------|--|--|---|
| 01/10/2023 | 2.95  | 13.09                    | 0.50   | 0.48   | 0.38  |
| 02/10/2023 | 3.20  | 16.46                    | 0.54   | 0.51   | 1.18  |
| 03/10/2023 | 6.36  | 19.29                    | 1.09   | 0.91   | 3.47  |
| 04/10/2023 | 3.85  | 14.39                    | 0.66   | 0.60   | 1.42  |
| 05/10/2023 | 4.56  | 13.72                    | 0.78   | 0.73   | 1.73  |
| 06/10/2023 | 4.91  | 14.02                    | 0.85   | 0.76   | 2.00  |
| 07/10/2023 | 3.35  | 17.43                    | 0.58   | 0.53   | 1.29  |
| 08/10/2023 | 2.76  | 9.31                     | 0.48   | 0.45   | 0.49  |
| 09/10/2023 | 0.59  | 4.58                     | 0.10   | 0.10   | 0.00  |
| 10/10/2023 | 2.30  | 9.20                     | 0.40   | 0.39   | 0.28  |
| 11/10/2023 | 4.65  | 17.85                    | 0.80   | 0.71   | 2.35  |
| 12/10/2023 | 4.49  | 18.73                    | 0.77   | 0.69   | 2.88  |
| 13/10/2023 | 3.35  | 17.19                    | 0.58   | 0.51   | 2.52  |
| 14/10/2023 | 5.66  | 21.18                    | 0.97   | 0.78   | 3.99  |
| 15/10/2023 | 1.59  | 8.76                     | 0.27   | 0.27   | 0.00  |
| 16/10/2023 | 1.56  | 6.11                     | 0.27   | 0.27   | 0.00  |
| 17/10/2023 | 2.38  | 6.73                     | 0.41   | 0.40   | 0.24  |
| 18/10/2023 | 6.04  | 7.64                     | 1.04   | 0.94   | 3.48  |
| 19/10/2023 | 2.68  | 10.29                    | 0.46   | 0.45   | 0.87  |
| 20/10/2023 | 1.64  | 15.93                    | 0.28   | 0.28   | 0.43  |
| 21/10/2023 | 1.52  | 18.62                    | 0.26   | 0.25   | 0.33  |
| 22/10/2023 | 1.16  | 13.22                    | 0.19   | 0.19   | 0.00  |
| 23/10/2023 | 2.15  | 9.84                     | 0.36   | 0.32   | 0.00  |
| 24/10/2023 | 3.49  | 13.32                    | 0.60   | 0.56   | 1.26  |
| 25/10/2023 | 0.65  | 11.81                    | 0.11   | 0.11   | 0.00  |
| 26/10/2023 | 1.47  | 11.88                    | 0.25   | 0.25   | 0.00  |
| 27/10/2023 | 0.28  | 9.66                     | 0.05   | 0.05   | 0.00  |
| 28/10/2023 | 3.47  | 12.01                    | 0.60   | 0.58   | 0.70  |
| 29/10/2023 | 4.60  | 13.93                    | 0.79   | 0.73   | 1.73  |
| 30/10/2023 | 3.76  | 16.21                    | 0.65   | 0.60   | 1.33  |
| 31/10/2023 | 1.16  | 16.30                    | 0.20   | 0.19   | 0.46  |

The total electrical energy generated by the PV/T module and non-cooled PV module were 27.01 kWh/month and 24.83 kWh/month, respectively. The overall electrical energy generation was enhanced by 8.78% compared to the non-cooled PV module during October 2023. The total thermal energy generation of the PV/T module was 59.17 kWh/month.

During the active cooling period of the PV module, the electrical energy generation was improved by 9.71% on average in October 2023. The monthly available solar energy was 92.61 kWh/m<sup>2</sup>, the thermal energy generation was 34.82 kWh/m<sup>2</sup>, and the electrical energy generation of the PV/T module was 15.89 kWh/m<sup>2</sup> (AC). The PV/T module was able to convert 37.60% and 19.07% of the available solar energy into thermal and electrical energy (DC),

respectively. The non-cooled PV module converted 17.53% (DC) of the available solar energy into electrical energy.

### 8.5.1 Numerical model of the PV/T module

The numerical model of the designed PV/T module was developed in TRNSYS software. TRNSYS is a dynamic simulation software developed by "Thermal Energy System Specialists, LLC" in collaboration with Solar Energy Laboratory, University of Wisconsin, Madison (USA) [55].

TRNSYS has an open and modular structure. The modular structure is constructed by connecting individual component models (Types) into a complete model. Each of these Types represents a piece of equipment, such as pumps, chillers, solar collectors, buildings, weather, schedule, and many more. These are then linked together in the TRNSYS environment, similar to how they would be connected in real life. The program comprises energy system component models grouped around a simulation engine (solver). Each component Type is described by a mathematical model in the TRNSYS simulation engine and has a set of matching proforma in the simulation studio. The proforma has a black-box description of a component: inputs, outputs, and parameters. The other main part of TRNSYS is an engine (the kernel), which reads and processes the input file and iteratively solves the equation system that describes the behavior of the simulated system.

In TRNSYS software, Type 50 (photovoltaic-thermal collector) was used to develop the numerical model of the PV/T module. Type 50 comprises parameters, inputs, and outputs. In the parameters section, mode 2 was chosen as it states that the losses occur as a function of temperature, windspeed, and geometry. The parameters defined in the numerical model of the PV/T module are given in Table 8-9.

**Table 8-9. Numerical model parameters**

| <b>Parameters</b>                             | <b>Value</b> | <b>Units</b>   |
|---|--------------|----------------|
| Collector gross area                          | 1.70         | m <sup>2</sup> |
| Collector fin efficiency factor               | 0.96         | -              |
| Fluid thermal capacitance                     | 4.19         | kJ/kg.K        |
| Collector plate absorptance                   | 0.85         | -              |
| Number of glass covers                        | 1            | -              |
| Collector plate emittance                     | 0.09         | -              |
| Collector slope                               | 30           | degrees        |
| Temperature coefficient of PV cell efficiency | 0.0042       | 1/K            |
| Temperature for cell reference efficiency     | 25           | °C             |
| Packing factor                                | 0.8898       | -              |

Upon definition of the parameters in Type 50, inputs, inlet fluid temperature, fluid mass flow rate, ambient temperature, incident radiation, windspeed, and cell efficiency were defined



using the experimental data to validate the numerical model. The cell efficiency was defined as 0.1912.

The experimental data collected on the 17<sup>th</sup>, 28<sup>th</sup> of September, and 7<sup>th</sup>, 11<sup>th</sup>, and 24<sup>th</sup> of October was used to validate the numerical model of the PV/T module in TRNSYS software. Different days with various input conditions were selected to analyze the reliability of the numerical model. The inputs of the model were the inlet flow rate and temperature, ambient temperature, solar irradiation falling onto the PV/T module, and the wind speed. Inputs used for the numerical model, Type 50, are given in Table 8-10.

**Table 8-10. The experimental data collected for the validation of Type 50**

| Time              | T <sub>inlet</sub> (°C) | q (L/h) | T <sub>amb</sub> (°C) | G (W/m <sup>2</sup> ) | v <sub>w</sub> (m/s) |
|-------------------|-------------------------|---------|-----------------------|-----------------------|----------------------|
| <b>17/09/2023</b> |                         |         |                       |                       |                      |
| 10:00:34          | 19.23                   | 359.00  | 23.17                 | 932.00                | 0.88                 |
| 11:00:34          | 22.47                   | 360.75  | 24.02                 | 923.67                | 0.89                 |
| 12:00:34          | 25.27                   | 335.63  | 23.65                 | 787.83                | 0.91                 |
| 13:00:34          | 27.08                   | 361.58  | 23.32                 | 722.00                | 1.16                 |
| 14:00:34          | 28.88                   | 363.83  | 23.70                 | 635.75                | 0.87                 |
| <b>28/09/2023</b> |                         |         |                       |                       |                      |
| 9:03:45           | 14.75                   | 149.64  | 18.72                 | 693.27                | 0.43                 |
| 10:03:45          | 17.15                   | 147.83  | 20.87                 | 810.00                | 1.49                 |
| 11:03:45          | 19.72                   | 144.58  | 21.77                 | 874.17                | 1.76                 |
| 12:03:45          | 22.70                   | 140.75  | 23.37                 | 846.67                | 1.34                 |
| 13:03:45          | 25.12                   | 134.83  | 23.91                 | 647.50                | 2.02                 |
| 14:03:45          | 27.38                   | 128.25  | 24.58                 | 303.08                | 1.69                 |
| 15:03:45          | 28.36                   | 123.80  | 25.09                 | 270.92                | 1.29                 |
| <b>07/10/2023</b> |                         |         |                       |                       |                      |
| 12:03:22          | 17.78                   | 249.75  | 18.75                 | 448.75                | 2.34                 |
| 13:03:10          | 19.30                   | 249.00  | 19.77                 | 602.50                | 2.90                 |
| 14:02:58          | 20.99                   | 248.17  | 20.20                 | 505.83                | 2.02                 |
| 15:02:46          | 22.59                   | 246.67  | 20.42                 | 382.50                | 2.06                 |
| <b>11/10/2023</b> |                         |         |                       |                       |                      |
| 10:03:46          | 14.80                   | 248.75  | 18.30                 | 659.58                | 1.43                 |
| 11:03:46          | 17.22                   | 249.75  | 19.88                 | 744.08                | 2.99                 |
| 12:03:46          | 19.47                   | 249.75  | 20.66                 | 678.33                | 2.72                 |
| 13:03:46          | 21.43                   | 250.00  | 21.53                 | 565.50                | 2.43                 |
| <b>24/10/2023</b> |                         |         |                       |                       |                      |
| 10:03:46          | 14.78                   | 249.20  | 14.36                 | 434.22                | 1.71                 |
| 11:03:51          | 16.10                   | 185.75  | 15.47                 | 557.25                | 2.22                 |
| 12:03:39          | 17.26                   | 161.58  | 16.14                 | 332.83                | 1.63                 |
| 13:03:27          | 18.07                   | 153.92  | 17.00                 | 483.75                | 1.69                 |
| 14:03:15          | 19.63                   | 146.36  | 17.08                 | 187.64                | 1.06                 |

The outlet temperature, thermal energy generation, and electrical power output of the Type 50 were compared to the measured data. The average percentage error between the model output and the measured data was investigated. The comparison of the results is given in Table 8-11.

**Table 8-11. The measured data and Type 50 model output**

| Time                 | T <sub>outlet</sub> (°C) | Q <sub>u</sub> (W) | P (W)  | T <sub>outlet</sub> (°C) | Q <sub>u</sub> (W) | P (W)  |
|----------------------|--------------------------|--------------------|--------|--------------------------|--------------------|--------|
| <b>Measured data</b> |                          |                    |        | <b>Model output</b>      |                    |        |
| <b>17/09/2023</b>    |                          |                    |        | <b>17/09/2023</b>        |                    |        |
| 10:00:34             | 21.71                    | 1035.31            | 296.77 | 21.51                    | 953.20             | 303.20 |
| 11:00:34             | 24.83                    | 993.70             | 294.12 | 24.67                    | 925.00             | 296.60 |
| 12:00:34             | 27.17                    | 742.20             | 248.01 | 27.22                    | 760.90             | 251.20 |
| 13:00:34             | 28.58                    | 631.26             | 225.82 | 28.68                    | 674.60             | 229.00 |
| 14:00:34             | 30.37                    | 628.13             | 202.38 | 30.24                    | 575.10             | 200.60 |
| <b>28/09/2023</b>    |                          |                    |        | <b>28/09/2023</b>        |                    |        |
| 9:03:45              | 18.95                    | 733.06             | 220.76 | 18.80                    | 704.80             | 230.10 |
| 10:03:45             | 22.12                    | 854.57             | 257.92 | 21.90                    | 817.00             | 265.20 |
| 11:03:45             | 24.86                    | 863.83             | 278.36 | 24.86                    | 865.00             | 282.50 |
| 12:03:45             | 27.38                    | 767.21             | 268.22 | 27.74                    | 826.40             | 270.70 |
| 13:03:45             | 28.71                    | 563.64             | 203.52 | 29.04                    | 614.40             | 206.30 |
| 14:03:45             | 29.37                    | 296.05             | 94.62  | 29.15                    | 264.70             | 96.69  |
| 15:03:45             | 29.82                    | 210.37             | 84.35  | 29.95                    | 228.70             | 86.16  |
| <b>07/10/2023</b>    |                          |                    |        | <b>07/10/2023</b>        |                    |        |
| 12:03:22             | 19.27                    | 431.18             | 142.89 | 19.32                    | 446.9              | 148.60 |
| 13:03:10             | 21.26                    | 567.54             | 191.85 | 21.33                    | 588.30             | 197.50 |
| 14:02:58             | 22.55                    | 450.11             | 161.07 | 22.68                    | 486.70             | 165.10 |
| 15:02:46             | 23.73                    | 327.76             | 121.80 | 23.82                    | 352.20             | 124.50 |
| <b>11/10/2023</b>    |                          |                    |        | <b>11/10/2023</b>        |                    |        |
| 10:03:46             | 17.00                    | 636.94             | 210.03 | 17.13                    | 675.00             | 219.80 |
| 11:03:46             | 19.67                    | 712.17             | 236.93 | 19.80                    | 751.20             | 245.00 |
| 12:03:46             | 21.61                    | 620.12             | 216.00 | 21.79                    | 674.30             | 221.70 |
| 13:03:46             | 23.22                    | 521.33             | 180.07 | 23.34                    | 554.50             | 183.90 |
| <b>24/10/2023</b>    |                          |                    |        | <b>24/10/2023</b>        |                    |        |
| 10:03:46             | 16.12                    | 388.66             | 138.27 | 16.22                    | 417.8              | 145.7  |
| 11:03:51             | 18.33                    | 482.83             | 177.44 | 18.56                    | 532.8              | 185.2  |
| 12:03:39             | 18.80                    | 289.93             | 105.98 | 18.91                    | 310.1              | 110.7  |
| 13:03:27             | 20.43                    | 423.97             | 154.04 | 20.62                    | 455.9              | 159.7  |
| 14:03:15             | 20.46                    | 142.48             | 59.75  | 20.54                    | 155.4              | 62.07  |

The average percentage errors of 0.64%, 6.72%, and 2.72% were observed for the outlet temperature, thermal energy generation, and electrical power output between the measured data and the TRNSYS model output.

### 8.5.2 Yearly energy generation

The validation of the TRNSYS model led to an analysis of the yearly energy generation of the PV/T module. In order to develop the simulation, Type 15-3 – weather component, Type 24 – integrator, Type 25 – printer, Type 50 – validated PV/T module, Type 113 – basic aquastat (cooling mode), and Type 114 – constant-speed pump were used. The location for the weather component was chosen Cracow, Poland. The typical meteorological year (TMY) data collected between 2004 and 2018 was used for the simulation. A summary of the monthly global solar irradiation level and average outdoor temperature is given in Table 8-12.

**Table 8-12. Monthly weather data for Cracow, Poland**

| Months    | G <sub>available</sub> (kWh/m <sup>2</sup> ) | T <sub>amb</sub> (°C) |
|-----------|--|-----------------------|
| January   | 28.63  | -1.22                 |
| February  | 45.27  | 0.13                  |
| March     | 87.35  | 3.71                  |
| April     | 141.26                                       | 9.39                  |
| May       | 176.25                                       | 14.28                 |
| June      | 184.76                                       | 17.47                 |
| July      | 197.77                                       | 19.87                 |
| August    | 163.67                                       | 18.43                 |
| September | 108.41                                       | 14.68                 |
| October   | 66.63  | 9.61                  |
| November  | 32.49  | 4.92                  |
| December  | 21.81  | 0.87                  |

Type 24 and Type 25 were used to integrate monthly energy generation and print the results to a text file, respectively. Type 113 was used to control the cooling of the PV/T module. The average cell temperature of the PV/T module was monitored by Type 113, and cooling was activated where the PV cell temperature was above 25 °C with a temperature deadband of 2 °C. Type 114 provides a constant flow rate for cooling the PV module and harvesting waste heat. The constant flow rate of 60 L/h with a constant inlet temperature of 20 °C was set as the parameters of the pump. The working fluid of the PV/T module was chosen as a water-glycol mixture whose properties are given in Table 6-2. The monthly electrical and thermal energy generated by the PV/T module and the pump's monthly power consumption used to circulate the working fluid were investigated. A summary of the monthly energy analysis in stationary mode is given in Table 8-13.

**Table 8-13. The summary of monthly energy analysis**

| Months    | Q <sub>u</sub> (kWh) | P <sub>PV/T</sub> (kWh) | P <sub>pump</sub> (kWh) | T <sub>avg-outlet</sub> (°C) |
|-----------|----------------------|-------------------------|-------------------------|------------------------------|
| January   | 5.13                 | 14.43                   | 0.51                    | 10.77                        |
| February  | 19.80                | 21.12                   | 1.19                    | 15.07                        |
| March     | 44.56                | 35.11                   | 2.42                    | 22.80                        |
| April     | 103.41               | 51.83                   | 4.20                    | 28.92                        |
| May       | 133.30               | 59.04                   | 5.10                    | 30.31                        |
| June      | 147.40               | 59.58                   | 5.74                    | 30.79                        |
| July      | 180.95               | 66.13                   | 6.39                    | 30.71                        |
| August    | 156.06               | 58.92                   | 5.60                    | 30.15                        |
| September | 94.77                | 42.64                   | 4.12                    | 28.99                        |
| October   | 50.29                | 29.78                   | 2.73                    | 24.01                        |
| November  | 11.84                | 15.35                   | 0.91                    | 16.57                        |
| December  | 3.61                 | 10.85                   | 0.39                    | 10.15                        |

In Table 8-13, P<sub>PV/T</sub> and P<sub>pump</sub> are the electrical energy generated by the PV/T module and the electricity consumption of the pump. T<sub>avg-outlet</sub> stands for the monthly average outlet temperature of the PV/T module between 8 a.m. and 6 p.m. The yearly electrical and thermal

energy generated by the designed PV/T module was 418.31 kWh (AC) and 951.11 kWh, respectively. The yearly power consumption of the pump was 39.30 kWh/y, leading to a net electricity production of 379.01 kWh/y for the PV/T module.

## 8.6 The uncertainty analysis

An uncertainty analysis was conducted for the measured quantities to determine the reliability of the outdoor experiments. The precision of each measuring device used in experiments is given in Table 8-14.

**Table 8-14. Uncertainties in measuring instruments**

| Instrument             | Parameter         | Unit             | Uncertainty |
|------------------------|-------------------|------------------|-------------|
| PT-1000 sensors        | Temperature       | °C               | ±0.3        |
| Ultrasonic heat meters | Flow rate         | %                | ±1          |
|                        | Temperature       | °C               | ±0.05       |
| Pyranometer            | Solar irradiation | W/m <sup>2</sup> | ±10         |
| K-type thermocouples   | Temperature       | °C               | ±0.5        |
| Digital multi-meters   | Voltage           | %                | ±0.05       |
|                        | Current           | %                | ±0.04       |

The analysis was carried out for thermal efficiency ( $n_{th}$ ), and the uncertainty in thermal efficiency is calculated using Eq. 48. The uncertainty varied between 1.48% and 1.80% for the experiments shown in section 8.2, with an average uncertainty of 1.63%. Eq. 50 is used to calculate the uncertainty in the measured electrical power output of the PV modules.

$$\frac{U_{n_{el}}}{n_{el}} = \left[ \left( \frac{U_V}{V} \right)^2 + \left( \frac{U_I}{I} \right)^2 + \left( \frac{U_G}{G} \right)^2 \right]^{1/2} \quad (50)$$

where  $U_{n_{el}}$  is the uncertainty in the results of electrical conversion efficiency,  $n_{el}$  is a given function of the independent variables, voltage,  $V$ , current,  $I$ , and solar irradiation,  $G$ , whereas  $U_V$ ,  $U_I$ , and  $U_G$  are the uncertainties associated with the independent variables. The uncertainty for the electrical conversion efficiency varied between 1.06% and 1.42% for the experiments, with an average uncertainty of 1.23%.

## 8.7 Summary

The outdoor test rig preparation was presented in this chapter, along with the details of the components used to assess the performance of the designed PV/T module. The tests started on the 12<sup>th</sup> of September, 2023, and continued until the end of October, 2023. The experiments were conducted with and without active chiller to analyze the performance of the PV/T module. The maximum improvement in electrical efficiency was observed on the 12<sup>th</sup> of September, where the back surface temperatures of cooled and non-cooled PV modules were 16.56 °C and 70.98 °C, respectively. The maximum thermal efficiency of 98.03±1.57% was achieved at

1.20 p.m. when the volume flow rate was 6.02 L/min, and inlet and outlet temperatures were 16.25 °C and 19.70 °C with a maximum thermal power output of 1.45 kW. The maximum electrical efficiency of  $19.12 \pm 1.14\%$  was observed at the time of achieving the highest thermal efficiency.

The cooling uniformity of the designed system was investigated along with the pressure drop in the test rig. A volumetric flow rate dependent pressure drop equation was formed.

An energy analysis was conducted on the real-life tests to assess the performance of the PV/T module and estimate the yearly thermal and electrical energy yield. TRNSYS software was used to develop the numerical model of the PV/T module to conduct energy analysis. The developed numerical model was validated using experimental data. The yearly expected net electrical and thermal energy generation of the PV/T module was found to be 379.01 kWh and 951.11 kWh, respectively.

An uncertainty analysis was conducted to determine the reliability of the outdoor experiments. The uncertainty varied between 1.48% and 1.80% for the thermal efficiency, with an average uncertainty of 1.63%. The uncertainty for the electrical conversion efficiency varied between 1.06% and 1.42% for the experiments, with an average uncertainty of 1.23%.

## Chapter 9 - Discussion

In order to assess the effectiveness of the designed PV/T system, a comparative study of existing literature with the proposed PV/T system was imperative. This chapter implies a comparative framework to highlight the key performance metrics. The comparative analysis encompasses the electrical conversion efficiency and thermal efficiency.

The comparison of the designed PV/T system with the existing systems allows for objective evaluation and contribution to the PV/T technology. The identification of the strengths and weaknesses of the system, potential limitations, and insights from the analysis can guide the future development of PV/T systems. The designed PV/T system contributes valuable insights into the renewable energy sector and the scientific community by conducting a rigorous comparative analysis.

### 9.1 Comparison between the proposed PV/T systems in the literature and the designed PV/T system

Abdullah et al. [32] designed a PV/T system with an absorber plate, a dual-oscillating copper absorber tube, and a 100 W PV module with a maximum electrical conversion efficiency of 15.50%. The copper water tubes were attached to the copper plate, and the cooling system was insulated to prevent heat loss from the bottom and edges. The designed PV/T system was investigated theoretically and experimentally. Indoor tests were conducted to analyze the performance of the system by varying the solar irradiation between 500 and 1,000 W/m<sup>2</sup> and the volumetric flow rate between 2 L/min and 6 L/min. The wind speed was assumed to be constant, along with the occurrence of heat loss only from the top. The maximum PV cell temperature of 63.22 °C was observed for the conventional PV module during the indoor experiments, whereas the maximum temperature of PV cells was found to be 57.32 °C using the water-based PV/T system. Maximum electrical conversion efficiency of 8.23% and thermal efficiency of 58.64% were achieved with a volumetric flow rate of 5 L/min under 1,000 W/m<sup>2</sup>.

Dubey and Tay [70] investigated two different types of commercially available PV/T modules - tube-and-sheet type and parallel-plate type thermal collectors integrated with PV modules under the tropical climatic conditions of Singapore. The tube-and-sheet PV/T system consisted of copper/aluminum tubes, a copper/aluminum absorber plate, a 190 W PV module with a maximum electrical conversion efficiency of 15.00%, and thermal insulation. The parallel-plate type of thermal collector consisted of rectangular microchannels, a 200 W PV module with a maximum electrical conversion efficiency of 13.60%, and thermal insulation. The water was used as a working fluid for both PV/T systems, and a pump was used to circulate the water from a storage tank to the thermal collectors. During the outdoor test, the

mass flow rate varied between 0.03 kg/s and 0.06 kg/s. The maximum thermal and electrical conversion efficiency of 40.70% and 11.80% were achieved using tube-and-sheet PV/T system, whereas these values are found to be 39.40% and 11.50% for the parallel-plate type PV/T system in a tropical climate.

Boumaaraf et al. [71] designed a special heat exchanger as a thermal collector and combined with a PV module. A spiral-shaped tube made of copper with a 14-mm diameter was used as a thermal collector on the rear side of the square-shaped 50 W PV module with a maximum electrical conversion efficiency of 12%. Thermal insulation of glass wool was used, and the whole design was encapsulated with an aluminum casing. The water was used as the working fluid in the PV/T system. During the outdoor tests, a maximum solar irradiation of 880 W/m<sup>2</sup> and a maximum ambient temperature of 30 °C were observed. The results showed that the proposed PV/T system reduced the temperature of the PV module by 20.1 °C while enhancing the electrical conversion efficiency by 1.73%. The system achieved a maximum thermal efficiency of 74.30% while generating a 282.6 W thermal energy peak. A maximum electrical conversion efficiency of 9.65% was obtained during the tests.

Kianifard et al. [72] proposed a PV/T system design by modifying a sheet-and-tube type collector. The thermal resistance of the conventional sheet-and-tube type PV/T system was reduced by eliminating several layers. In the designed system, solar cells were placed on an anodized metal plate, and the full pipe shape design was changed to half pipe to increase the fluid contact with the absorber plate. The half-pipe design was bonded to the absorber plate using adhesives. The serpentine-shaped half-pipe design thermal collector was placed at the rear side of a PV module, with a maximum power output of 90 W and maximum electrical conversion efficiency of 12.50%. The outdoor tests were conducted with the PV/T system by varying the inlet volumetric flow rate between 0.5 L/min and 4 L/min. The results concluded that the optimum volumetric flow rate for the proposed system was 2 L/min, achieving a maximum thermal efficiency of 70% and an electrical conversion efficiency of 11.50%. The designed PV/T system exhibited greater efficiency, such as higher thermal efficiency by 10% to 13% and higher electrical conversion efficiency by 0.40% to 0.60% compared to conventional sheet-and-tube PV/T system.

Abdallah et al. [73] conducted outdoor experiments on a nanofluid-based PV/T system and compared the results to the water-based PV/T system and stand-alone PV system. A 0.3 mm copper sheet was attached as a heat absorber on the rear side of a PV module with a maximum power output of 10 W. A commercially available serpentine-shaped copper tube with a 6.4 mm diameter was used for the water-nanofluid mixture circulation. Multi-walled carbon nanotubes with 5-12 μm length, 30-50 nm outer diameter, 5-12 nm inner diameter, and

thermal conductivity of 3,000 W/m.K were used as heat absorption agents. Five different concentrations of nanofluid varying between 0% and 0.3% at a constant volumetric flow rate of 1.2 L/min were tested. The experimental results showed that using a 0.075% volume concentration of the nanoparticles in water-based working fluid achieved a maximum thermal efficiency of 69.26% and a maximum electrical conversion efficiency of 14.00%. The module temperature was reduced by 12 °C.

Venkatesh et al. [74] investigated a hybrid solar PV/T system with graphene-based nanofluids. Graphene nanoparticles with a volume concentration of 0.3% were used in water-based working fluid to enhance heat transfer. The thermal conductivity of the nanofluid-water mixture increased with the concentration of the nanoparticles and increased with the nanofluid's temperature. The circular pipeline with a 2 m length and 10 mm diameter and an absorber plate was placed on the rear side of a PV module with a maximum power output of 13 W. An annulus tank was used to control the inlet temperature of the nanofluid and the temperature was kept constant at 20 °C while the volume of nanoparticle concentration was varied between 0.1% and 0.3%. The outdoor tests were carried out between 9 a.m. and 4 p.m., and the mass flow rate of the nanofluid ranged between 0.065 kg/s and 0.085 kg/s. A maximum thermal and electrical conversion efficiency of 64.80% and 16.20% were achieved, respectively, when the mass flow rate of the system was 0.085 kg/s. The nanoparticle volume concentration was 0.3%. The use of nanofluid in the PV/T system led to a reduction in panel temperature by 20 °C. The results showed that the investigated PV/T system enhances the efficiency by 13% compared to the water-based PV/T system.

Bassam et al. [75] conducted an experimental analysis of a water-based nanofluid-enhanced PV/T system with nano-PCM, counterclockwise twisted tape, and micro-fin tubes. The pipe used in the PV/T system was designed with a sheet and micro-fin tube (inner grooved) twisted tape with a 12.7 outer diameter. 3-mm copper tapes were used for soldering the pipe. The paraffin PCM was enhanced with 1% silicon carbide nanoparticles and placed in a PCM container. The nanofluid was prepared using water as the base fluid and 0.3% and 0.6% volume fraction of SiC nanomaterial. A PV module with a maximum power output of 30 W was used in the PV/T system design. The mass flow rate ranged from 0.008 kg/s to 0.058 kg/s in an indoor controlled environment. The experiments were performed using a solar simulator consisting of 35 halogen lamps, each with 500 W power to provide 600, 800, and 1,000 W/m<sup>2</sup> of solar irradiation. During the indoor tests, the room temperature and the nanofluid temperature were 27 °C and 18 °C, respectively; thus, a water-cooler chiller was used to regulate the temperature. The indoor test results showed that the stand-alone PV module temperature reached 86.4 °C, whereas the designed PV/T system with a volume fraction of 0.3% SiC nanofluid was able to reduce the temperature of the PV module to 41.6 °C. The



thermal and electrical conversion efficiency of 80.8% and 10.51% was achieved using this configuration. In contrast, the PV/T system with a 0.6% volume fraction of SiC nanofluid reduced the temperature of the PV module by 44.5 °C, achieving 83.8% thermal efficiency and 10.59% electrical conversion efficiency.

Hassan et al. [76] experimentally studied nanofluid and PCM-enhanced water-based PV/T system. Graphene nanoparticles were used to prepare the nanofluid with three concentrations: 0.05%, 0.1%, and 0.15%. A network of 10 mm diameter and 0.6 mm thick 24 copper pipes in parallel connected with U bends was used to circulate the nanofluid. RT35-HC organic paraffin PCM was filled in a container on the rear side of the PV module, with a maximum power output of 30 W, for thermal regulation. The copper tube network was immersed in the PCM container. Six different cases were considered during the outdoor test: conventional PV system, PV system integrated with PCM, PV system integrated with PCM and water cooling, and PV system integrated with PCM and nanofluid cooling with three different concentrations. The volumetric flow rate during the tests varied between 20 L/min and 40 L/min. Maximum solar irradiation of 1,101 W/m<sup>2</sup> and maximum ambient temperature of 40 °C were recorded during the outdoor tests. The best performance of the PV/T system was achieved with the configuration where the system was enhanced with PCM, 0.1% volume nanoparticle concentration was added to the base fluid, and the volumetric flow rate was 40 L/min. A maximum electrical and thermal efficiency of 14% and 47% were achieved using the designed PV/T system.

Al-Aasam et al. [77] proposed a PV/T system by combining nanofluids and nano-PCM with twisted absorber tubes. The water was combined with 0.3% and 0.6% volume fractions of SiC nanoparticles to prepare the nanofluid; a 1% volume fraction of SiC nanoparticles was combined with paraffin wax to develop the nano-PCM. The twisted 11 copper tubes were surrounded by the nano-PCM and placed underneath the PV module with a maximum power output of 30 W. The designed system was investigated in a controlled environment: indoor experiments with a room temperature of 25 °C and solar irradiation level of 800 W/m<sup>2</sup>. A cooling unit was used to regulate and maintain at 20 °C the inlet temperature of the PV/T system. The mass flow rate of the system ranged from 0.008 kg/s to 0.04 kg/s. The test results showed that the temperature of the non-cooled PV module reached 77.59 °C, and electrical conversion efficiency dropped to approximately 7% under 800 W/m<sup>2</sup> and at room temperature of 25 °C. The proposed cooling system design reduced the temperature of the PV module by 38.31 °C and achieved a maximum thermal efficiency of 84.74% and a maximum electrical conversion efficiency of 9.61%.

Das et al. [78] proposed a rectangular spiral copper tube equipped water-based PV/T system with the rear side embedded in a form-stable composite consisting of OM35 PCM and biochar obtained from the water hyacinth. After placing the rectangular spiral tubing, a 10 mm thick layer of PCM-biochar composite was filled on the rear side of the PV module. Aluminum powder was added to the composite to increase thermal conductivity. An insulation layer of polyethylene foam sheet with 13 mm thickness was applied to the system. The outdoor tests were conducted with the inlet mass flow rate of 0.015 kg/s in Guwahati, India. The maximum thermal and electrical efficiency of 84.71% and 14.02% were reached under 928 W/m<sup>2</sup> solar irradiation and 32 °C of ambient temperature.

In Table 9-1, a summary of thermal and electrical conversion efficiency comparison between the designed PV/T system and proposed PV/T systems in the literature is given. In addition to comparing the electrical and thermal efficiency, a more detailed summary of the comparison was provided, including the solar irradiation level, ambient temperature, type of material, flow rate, the maximum power output of PV modules, and reduction in PV temperature in Table 9-1.

**Table 9-1. A comparison between the designed PV/T system and proposed PV/T systems in the literature**

| Ref.            | System type   | Working fluid  | Type          | G (W/m <sup>2</sup> ) | T <sub>amb</sub> (°C) | ṁ (kg/s) | T <sub>in</sub> (°C) | P <sub>max</sub> (W) | T <sub>red</sub> (°C) | η <sub>el</sub> (%) | η <sub>th</sub> (%) |
|-----------------|---|--|---------------|-----------------------|-----------------------|-----------|----------------------|----------------------|-----------------------|---------------------|---------------------|
| [32]            | A dual-oscillating copper absorber tube integrated PV/T system with back insulation                                   | Water  | Exp. and num. | 1,000                 | -                     | 0.0833    | -                    | 100                  | 8.90                  | 8.23                | 58.64               |
| [48]            | Hybrid nanofluid based PV/T system with copper tube collector with insulation   | Hybrid nanofluid (SiO <sub>2</sub> -Al <sub>2</sub> O <sub>3</sub> -water) | Exp.          | 1,000                 | 26                    | 0.0500    | 42                   | 35                   | -                     | 13.17               | 65.05               |
| [70]            | Sheet-and-tube (Cu) type PV/T system with thermal insulation  | Water  | Exp.          | 1,000                 | 30.0                  | 0.0600    | -                    | 190                  | -                     | 11.80               | 40.70               |
| [71]            | A spiral-shaped CU tube and sheet based PV/T system with thermal insulation   | Water  | Exp.          | 880                   | 30.0                  | 0.0065    | 25                   | 50                   | 20.10                 | 9.65                | 74.30               |
| [72]            | Water-based PV/T system with serpentine half-pipe design and thermal insulation                                       | Water  | Exp. and num. | 1,000                 | 25.0                  | 0.0333    | 25                   | 90                   | -                     | 11.50               | 70.00               |
| [73]            | Nanofluid-based PV/T system with copper sheet and serpentine-shaped copper tube                                       | MWCNT-water nanofluid  | Exp.          | 1,000                 | 30.0                  | 0.0200    | -                    | 10                   | 12.00                 | 14.00               | 69.26               |
| [74]            | Nanofluid-based PV/T system with sheet and serpentine-shaped tube   | Graphene-water nanofluid   | Exp.          | 750                   | 30.0                  | 0.0850    | 20                   | 13                   | 20.00                 | 16.20               | 64.80               |
| [75]            | PV/T system with nano PCM and copper micro-fins tube counterclockwise twisted tape nanofluid                          | SiC-water nanofluid  | Exp.          | 800                   | 27.0                  | 0.0410    | 18                   | 30                   | 44.50                 | 10.59               | 83.80               |
| [76]            | PCM and nano-fluid based PV/T system with serpentine-shaped copper tube   | Graphene-water nanofluid   | Exp.          | 1,050                 | 40.0                  | 0.6667    | -                    | 30                   | 29.30                 | 14.00               | 47.00               |
| [77]            | Nano-PCM and nanofluid based PV/T system with twisted copper tubes  | SiC-water nanofluid  | Exp.          | 800                   | 25.0                  | 0.0400    | -                    | 30                   | 38.31                 | 9.61                | 84.74               |
| [78]            | Rectangular spiral (copper tubes) flow PV/T system with PCM (enhanced with composite material) and thermal insulation | Water  | Exp.          | 928                   | 32.0                  | 0.015     | 32.10                | 100                  | -                     | 14.02               | 84.71               |
| [present study] | Water-based PV/T system with a highly efficient cooling design  | Water  | Exp. And num. | 875                   | 29.0                  | 0.1003    | 16.25                | 325                  | 54.40                 | 19.12               | 98.03               |

In Table 9-1,  $T_{red}$  stands for the temperature reduction on the back surface of the PV module. As seen from Table 9-1, copper tubes were used to circulate the working fluid in most of the systems, and the PV/T systems were insulated on the rear side. Various configurations, such as serpentine-shaped tubing, rectangular tubing, spiral tubing, and conventional sheet-and-tube, were investigated to maximize the thermal efficiency and electrical conversion efficiency of PV/T systems. Different nanoparticles were studied to improve the thermal properties of the working fluid.

The designed PV/T system in this dissertation took advantage of the extensive heat transfer area and enhanced the heat transfer with its unique interior design. The designed cooling system achieved the maximum temperature reduction on the rear side of the PV module. Despite the sophisticated design of the systems and working fluids used, the electrical and thermal efficiency of the proposed PV/T systems in the literature was lower than the designed PV/T system in this dissertation.

## **9.2 Summary**

The comprehensive comparative analysis results showed that the proposed PV/T system exhibits better performance compared to the proposed solutions in the literature. Most of the research focused either on the shape of the pipes in the cooling design of the PV/T system or on improving the thermal properties of the working fluid. The conventional PV/T system designs were modified by changing the shape of the pipes or adding PCM materials to regulate the temperature.

The investigations on increasing the efficiency of PV/T systems also targeted the working fluid by adding nanomaterials to enhance thermal conductivity and heat-carrying capacity. Despite the sophisticated design of the systems, the electrical and thermal efficiency of the proposed PV/T system was lower than the designed PV/T system.

The thermal efficiency of the state-of-the-art water-based active cooling PV/T systems proposed in the literature ranged between 40% and 85%, whereas the electrical efficiency of the systems varied between 7% and 16%. The designed PV/T system achieved  $19.12 \pm 1.14\%$  electrical efficiency and  $98.03 \pm 1.57\%$  thermal efficiency in this dissertation, exceeding its rivals.

## Chapter 10 - The economic analysis of the designed PV/T system

The space available in urban areas suitable for new energy conversion systems is limited. The scarcity of the limited space led to maximization of the efficiency of the systems, both electrical and thermal. PV/T modules present a unique advantage by generating heat and electricity simultaneously using the same area. However, PV/T modules have not yet been adopted extensively due to the lack of reliable data on the operation of PV/T modules that establish a benchmark for engineers, designers, and energy planners. Another aspect is the high capital costs of the PV/T systems.

The cost of solar-thermal systems for hot water generation ranges between 0.2 €/kWh and 0.35 €/kWh in Europe, depending on the location [79]. The capital costs of solar-thermal water heating systems (small scale – from 2 m<sup>2</sup> to 8 m<sup>2</sup> collector array), including installations, vary between 500 €/m<sup>2</sup> and 1,300 €/m<sup>2</sup> depending on the maturity (Austria is one of the most mature markets) of the solar-thermal market in the European country. A typical 5 m<sup>2</sup> solar-thermal collector with a 250 L storage system, including installation, has an average capital cost of 1,000 €/m<sup>2</sup>. In Poland, an average 6 m<sup>2</sup> solar-thermal collector with a 200 L storage tank, including installation costs, is 750 €/m<sup>2</sup>.

The cost of electrical energy generated by the PV systems was 0.046 €/kWh on average globally in 2022 [11]. In Poland, the capital costs of residential small-scale (1 to 10 kW) PV systems ranged between 940 €/kW and 1,300 €/kW, whereas the large-scale (100 kW to 5 MW) PV system's capital cost varied between 500 €/kW and 800 €/kW. The highest learning rate in PV technology compared to other renewable energy sources and a downward trend in solar PV module costs, which account for 40% of the total price, led to a continuous declining trend in capital costs of PV systems.

In Poland, a few cost data were available for PV/T modules. The price of the PV/T systems ranged from 500 € to 2,000 € per PV/T module, according to the market search conducted.

### 10.1 The cost analysis of the designed PV/T module

The proposed PV/T module comprises a PV module and the designed cooling system. The global solar market hit record highs in the volume of installations, leading to lower prices for PV modules in August 2023. The module prices were as low as 0.16 €/W and were expected to fall until the end of 2023 [80]. Based on the information, the cost of the PV module used in the PV/T system was calculated as 52 € as the PV module had a peak power output of 325 W.

The cooling system was made of aluminum alloy 6061. The designed cooling system had 1,670 x 965 x 12 mm dimensions with 7.0138 m<sup>2</sup> of total surface area and 0.0082 m<sup>3</sup> volume. The thermal collector allows 0.0109 m<sup>3</sup> working fluid to operate while cooling the PV module and harvesting waste heat. The cost of the materials used for the thermal collector was 215 €. The cooling system was expected to be produced with CNC machining. In CNC machining, stainless steel and aluminum are some of the easiest materials for machining. CNC machining of aluminum is relatively inexpensive due to the softer material feature, corrosion resistance, strength-to-weight ratio, recyclability, and less complexity. The non-complex geometry of the cooling system allows for the use of 3-axis CNC machining that is cheaper to operate compared to 4-axis and 5-axis CNC machining. The CNC machining and person-hours for manufacturing the cooling system were estimated to be 3 hours [81]. The 3-axis CNC machine costs range from 30 € to 35 € per hour in Europe. The total cost of CNC machining and person-hours was estimated to be 213 €. In Table 10-1, a summary of the unit cost of the designed PV/T system is presented.

**Table 10-1. The summary of the unit cost**

| <b>Components</b>      | <b>Unit cost (€)</b>  |
|------------------------|-----------------------|
| PV module              | 52.00                 |
| Material               | 215.00                |
| CNC machining          | 105.00                |
| Person-hour            | 108.00                |
| Profit margin [81]     | 20% of the total cost |
| <b>Total unit cost</b> | <b>576.00 €</b>       |

The total unit cost of the PV/T module was calculated as 576.00 €.

## 10.2 Economic analysis

In this section, an economic analysis of the designed PV/T was conducted by comparing the cost of the designed PV/T module to PV/T modules available in the Polish market. Most of the PV/T modules available in the market did not provide yearly thermal and electrical energy yield. In the majority of the PV/T modules, the manufacturer data did not state under which conditions the thermal power output values were obtained or provide any certification. Only one of the manufacturers provided detailed information on their PV/T module. The PV/T module consisted of a modular heat sink, connecting in a parallel-serial manner, and a 310 W PV module with a 1.67 m<sup>2</sup> surface area. Each heat sink consists of two aluminum sheets of different thicknesses, 0.5 mm, and 0.2 mm, respectively, and two U-tubes through which the cooling medium flows. The yearly net electrical and thermal energy generation of the PV/T module is 269.34 kWh and 339.48 kWh, respectively. The PV/T module with detailed information will be called PV/T–A in the rest of the dissertation. A summary of the market analysis with yearly energy yields and power outputs is given in Table 10-2.

**Table 10-2. A summary of the market analysis**

| <b>PV/T modules</b> | <b>P<sub>annual</sub> (kWh/y)</b> | <b>Q<sub>annual</sub> (kWh/y)</b> | <b>P<sub>max</sub> (W)</b> | <b>Q<sub>max</sub> (kW)</b> | <b>Cost (€)</b> |
|---------------------|-----------------------------------|-----------------------------------|----------------------------|-----------------------------|-----------------|
| Designed PV/T       | 379.01                            | 951.11                            | 325                        | 1.52                        | 576             |
| PV/T–A              | 269.34                            | 339.48                            | 310                        | -                           | 650             |
| PV/T–B              | -                                 | -                                 | 300                        | 1.04                        | 852             |
| PV/T–C              | -                                 | -                                 | 330                        | 0.91                        | -               |

In Table 10-2,  $P_{\text{annual}}$  and  $Q_{\text{annual}}$  are the yearly electrical and thermal energy production in kWh, respectively.  $Q_{\text{max}}$  stands for the maximum thermal power output of PV/T modules.

The PV/T–B was designed using an aluminum roll-bond heat exchanger with an area of 1.86 m<sup>2</sup>. The working fluid capacity of the PV/T module was 1.2 L. The manufacturer provided information regarding the thermal power output obtained. The maximum thermal power output of 1.04 kW was observed under 1,000 W/m<sup>2</sup>. However, no information was available on the ambient temperature, wind speed, and tilt angle of the PV/T module.

The PV/T–C was designed using copper pipes as a thermal absorber and wool insulation with 35 mm thickness on the rear side of the PV/T module. The total area of the PV/T module was 1.62 m<sup>2</sup>. The maximum thermal power output of the PV/T module was 0.91 kW. However, the manufacturer did not provide any information regarding the test conditions.

The designed PV/T in this dissertation achieved a maximum thermal power output of 1.52 kW when the volumetric flow rate was 6.02 L/min, and inlet and outlet temperatures were 25.6 °C and 29.2 °C under 942 W/m<sup>2</sup> with the ambient temperature of 28.3 °C.

Based on the limited data available in the PV/T market, the designed PV/T module was compared to PV/T–A.

### **Levelized cost of energy (LEC)**

The designed PV/T module and PV/T–A were compared in terms of their levelized energy cost of electrical and thermal energy on an assumed 25-year system lifetime in this section. The lifetime of PV modules is generally estimated based on manufacturer warranty guarantees. The warranty often guarantees at least 80% power output after 25 years of operation [82]. In the literature, the research conducted on the life cycle and economic analysis of PV systems assumed a 25-year lifetime [83, 84, 85]. A yearly degradation [86] in electrical energy production analysis was conducted for the designed PV/T module and PV/T–A to analyze the 25-year system lifetime energy analysis. The analysis results for the designed PV/T are given in Table 10-3.

**Table 10-3. The yearly degradation in energy production analysis for designed PV/T**

| Year | Degradation (%) | P (kWh) | Q (kWh) | Year | Degradation (%) | P (kWh) | Q (kWh) |
|------|-----------------|---------|---------|------|-----------------|---------|---------|
| 1    | 3.00            | 379.01  | 951.11  | 14   | 0.71            | 335.12  | 951.11  |
| 2    | 0.71            | 367.64  | 951.11  | 15   | 0.71            | 332.74  | 951.11  |
| 3    | 0.71            | 365.03  | 951.11  | 16   | 0.71            | 330.37  | 951.11  |
| 4    | 0.71            | 362.44  | 951.11  | 17   | 0.71            | 328.03  | 951.11  |
| 5    | 0.71            | 359.86  | 951.11  | 18   | 0.71            | 325.70  | 951.11  |
| 6    | 0.71            | 357.31  | 951.11  | 19   | 0.71            | 323.39  | 951.11  |
| 7    | 0.71            | 354.77  | 951.11  | 20   | 0.71            | 321.09  | 951.11  |
| 8    | 0.71            | 352.25  | 951.11  | 21   | 0.71            | 318.81  | 951.11  |
| 9    | 0.71            | 349.75  | 951.11  | 22   | 0.71            | 316.55  | 951.11  |
| 10   | 0.71            | 347.27  | 951.11  | 23   | 0.71            | 314.30  | 951.11  |
| 11   | 0.71            | 344.80  | 951.11  | 24   | 0.71            | 312.07  | 951.11  |
| 12   | 0.71            | 342.36  | 951.11  | 25   | 0.71            | 335.12  | 951.11  |
| 13   | 0.71            | 339.92  | 951.11  |      |                 |         |         |

The total electrical and thermal energy generation of the designed PV/T module was 8.52 MWh and 23.78 MWh, respectively, over a 25-year lifetime. The total electrical and thermal energy generation of the PV/T–A was 6.05 MWh and 8.49 MWh, respectively, over a 25-year lifetime. The 25-year lifetime energy analysis estimation showed that the proposed PV/T module produces 1.41 times and 2.80 times more electrical and thermal energy than PV/T–A. The energy results of the PV/T modules over a 25-year lifetime are shown in Figure 10-1.

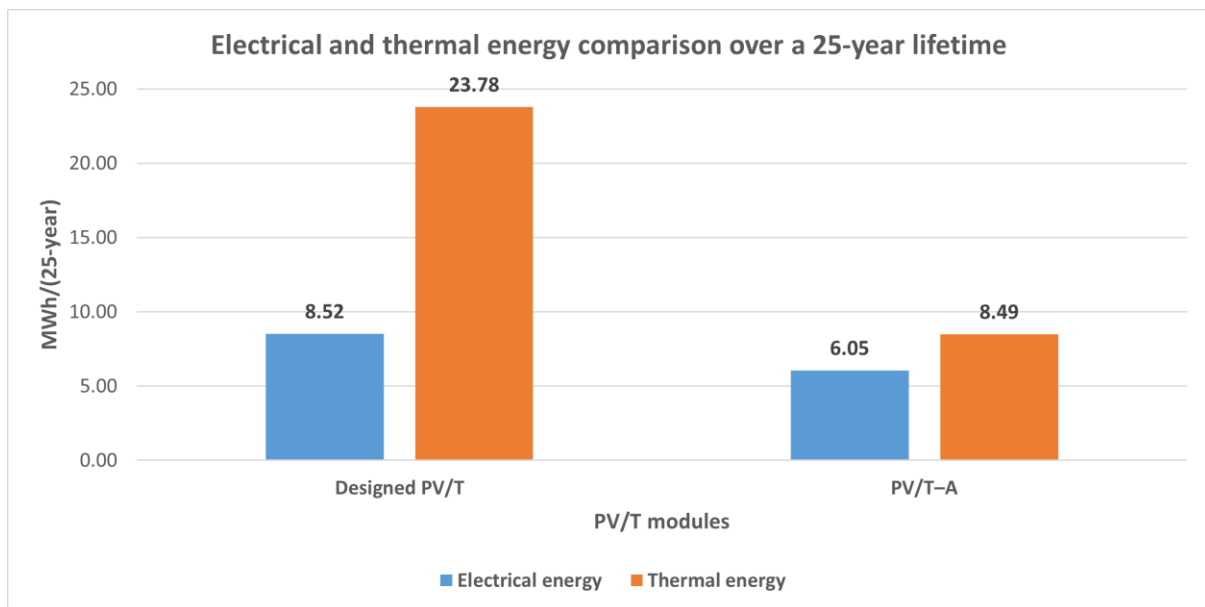


**Figure 10-1. The energy results of the PV/T modules over a 25-year lifetime**

The electrical and thermal energy generation analysis of a 25-year lifetime led to the calculation of the LEC for the PV/T modules. The PV/T module system costs comprised capital costs and annual incurring running costs. The annual incurring running costs were assumed to be only operation and maintenance (OM) costs. In solar PV/T systems, the annual and



recurring costs are almost negligible as the input fuel is sunlight. Therefore, the OM costs were assumed to be 1% of the capital cost of each system [87]. As the PV/T–A has a similar construction to the designed PV/T module, the installation costs of the systems were assumed to be equal to 425 € [81], including pump, piping, and electrical installation. The capital and OM costs of the PV/T modules are given in Table 10-4.

**Table 10-4. The capital costs and OM costs of the PV/T modules**

| PV/T modules  | Capital costs (€) | OM costs (€) |
|---------------|-------------------|--------------|
| Designed PV/T | 1,001             | 10.01        |
| PV/T–A        | 1,075             | 10.75        |

The LEC is calculated using Eq. 51.

$$LEC = \frac{NPV_Y}{\sum_{Y=1}^Y (E_T / (1+r)^Y)}, \quad (51)$$

where  $NPV_Y$  is the net present value that represents the system's total cost over its lifetime. The subscript  $Y$  stands for the years. The  $NPV_Y$  comprises the sum of the capital cost  $K_C$  and the present value of the annualized costs of OMs,  $K_{OM}$ . The  $NPV_Y$  can be calculated by applying Eq. 52.

$$NPV_Y = K_C + \sum_{Y=1}^Y \frac{K_{OM}(1+i)^{Y-1}}{(1+r)^Y}, \quad (52)$$

In Eq. 51,  $E_T$  indicates either the annual electrical or thermal energy or the sum of the electrical and thermal energy. The  $E_T$  was assumed as the sum of electrical and thermal energy generation for all PV/T systems.  $r$  is the discount rate for renewable energy systems. The predominant practice applies a priori fixed 5% discount rate,  $r$  [88]. However, the study indicated that the discount rate can be reduced to 4.39% due to long-term planning horizons for energy policies. Therefore, in Eq. 51, the discount rate was assumed to be 4.39%. In Eq. 52,  $i$  stands for the inflation rate, which was taken as the average of the last 13 years between 2010 and 2023. The value of the inflation rate was found to be 3.26% [89]. The data provided in Table 10-4 were applied in Eqs. 51 and 52. The LEC values calculated for PV/T modules are presented in Table 10-5.

**Table 10-5. LEC values of PV/T modules**

| PV/T modules  | LEC (€/kWh) |
|---------------|-------------|
| Designed PV/T | 0.0624      |
| PV/T–A        | 0.1485      |

The LEC analysis showed that the designed PV/T module can produce 2.38 times cheaper per kWh energy than the PV/T–A.

### 10.3 Case study system definition

In this section, a case study on domestic hot water (DHW) demand coverage analysis of a single-family house using the designed PV/T module was conducted. The designed DHW system was compared to a conventional combined condensing gas boiler system. Ratajczak et al. [90] investigated the annual gas and water consumption for three single-family houses between 2016 and 2019 to estimate the monthly gas consumption for DHW. In this case study, the B3 single-family house, which had an area of 100 m<sup>2</sup> and was occupied by three people, was chosen. The list of domestic hot water intake points was as follows: kitchen sink, two sinks, two toilet bowls, bath, shower, dishwasher, and washing machine. According to the analysis, the monthly gas consumption and the final energy per year were 23.66 m<sup>3</sup> and 2,437 kWh, respectively. The calorific value of the natural gas was taken as 31 MJ/m<sup>3</sup> [91]. The useful energy for the DHW was calculated by multiplying the final energy required with the efficiency of the heat source, such as the combined condensing gas boiler. According to the methodology applied in Poland [92], a 90% efficiency of the gas boiler was assumed for a heating installation and a 60% efficiency for the DHW preparation. The usable energy for DHW,  $Q_{DHW,yearly}$ , was found to be 1,462 kWh/y.

The water consumption per person was calculated using Eq. 53 [90].

$$Q_{DHW,monthly} = \frac{V_{DHW} N_p (T_{DHW} - T_C) \rho c_w D_m c_R}{3600} \quad (53)$$

where  $Q_{DHW,monthly}$  is the monthly usable energy for DHW with a unit of *kWh/month*.  $V_{DHW}$  indicates the daily demand for DHW related to the number of people,  $N_p$ , with a unit of *dm<sup>3</sup>/person/day*.  $T_{DHW}$  and  $T_C$  are the designated temperature of DHW in the tap, 55 °C, and the temperature before heating, 10 °C, respectively.  $D_m$  and  $c_R$  are the number of days in the month and the correction factor for the assumption of the time of presence of occupants. The value for  $c_R$  was taken as 0.9, indicating that the residents are present 90% of the time [93]. When the parameters were applied in Eq. 53, the daily water consumption per person was found to be 28.3 dm<sup>3</sup>/person/day. The domestic hot water demand of the single-family house studied was 76.50 L/day, at an initial temperature of 10 °C to be heated to 55 °C.

In this case study, an external auxiliary heater was used to increase the water temperature to the required temperature for the designed system with the PV/T module. Auxiliary heating can be provided in different ways, such as heat pumps, biomass boilers, electric resistance heaters, and gas/coal boilers. An electric resistance heater has been considered in this analysis due to its inexpensive cost and ability to convert electrical energy into thermal energy

with an efficiency of 100%. Two different cases were considered for comparison in this study as follows:

- the domestic hot water system designed with the proposed PV/T module;
- the conventional gas boiler and power system.

The system components for the PV/T-based energy systems are listed in Table 10-6. The cost data of the components to construct the systems were taken from the retailers in the EU during 2022-2023.

**Table 10-6. Cost of the electrical and hydraulic components of PV/T systems**

| Component                             | Range (€/unit) | Source    |
|---------------------------------------|----------------|-----------|
| Designed PV/T module                  | 576            | [81]      |
| Inverter and solar controller         | 150-350        | [94, 95]  |
| Cables and mounting brackets          | 10-20          | [96, 97]  |
| Circulation pump                      | 70-120         | [97, 98]  |
| Tank integrated with auxiliary heater | 250-350        | [97, 99]  |
| Pipes                                 | 50-100         | [97]      |
| Expansion vessel                      | 20-50          | [99, 100] |
| Installation cost                     | 80-100         | [81]      |

The objective of sizing the PV/T system was first to cover the demand by thermal energy and utilize the electrical energy generated. An electric resistance heater was considered immersed in a buffer tank to meet the required temperature during the seasons where there is insufficient thermal energy. The optimal number of PV/T modules was found to be two. The system cost breakdown for PV/T-based DHW is shown in Figure 10-2.

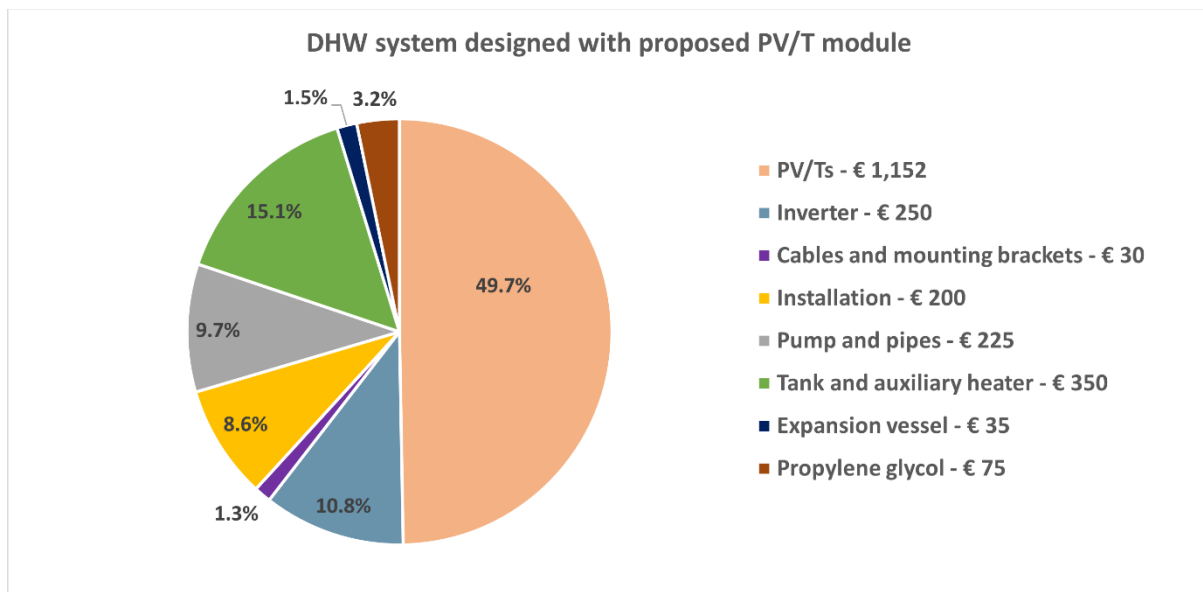


**Figure 10-2. The cost breakdown of the DHW system designed with PV/T modules**

The capital cost of the DHW system designed with the proposed PV/T module was € 2,317.

### 10.3.1 DHW system developed in TRNSYS

The design of the solar domestic hot water (SDHW) system was started by identifying the DHW profile. DHWcalc [101] tool for the generation of DHW profiles on a statistical basis was used. The daily DHW profile generated using the software is shown in Figure 10-3.

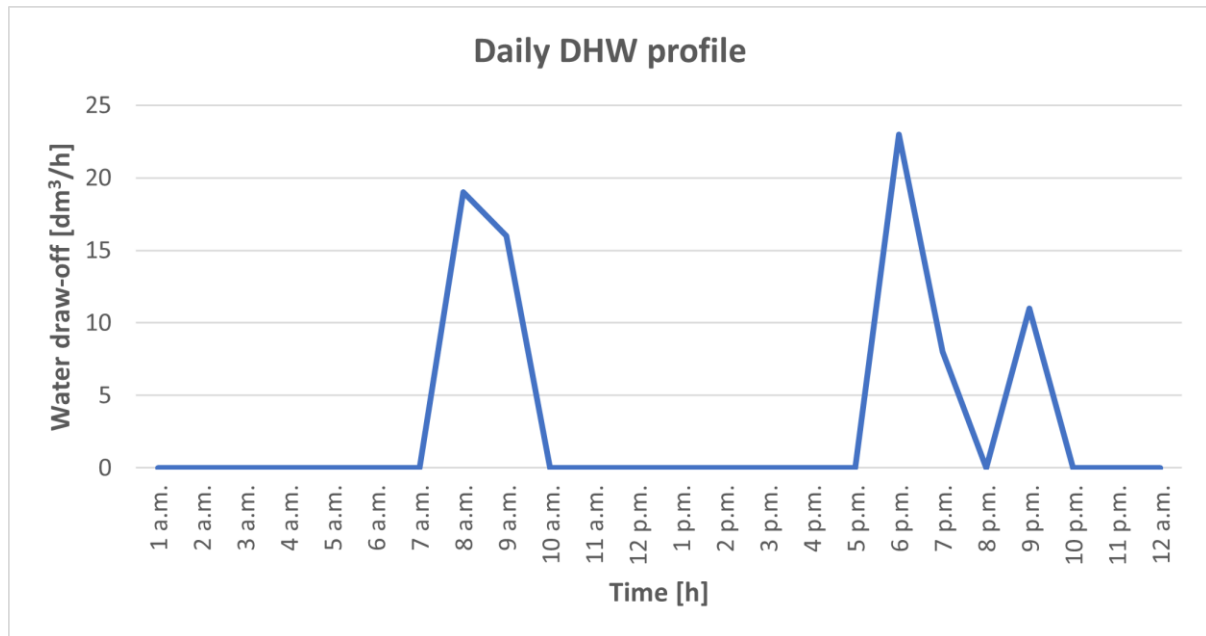


Figure 10-3. The daily DHW profile

In TRNSYS software, Type 14b was used to develop the water draw-off profile for the simulation. In order to prepare the DHW loop, the Type 11f – flow diverter, Type 11h – flow mixer, and Type 31 – pipe components were used and connected. In the flow diverter, the setpoint temperature was set up to be 55 °C as the designated temperature. The first inlet of the flow diverter was connected to the inlet-1 of the Type 156 – DHW tank (300 L). The outlet-1 of the DHW tank and the flow diverter outlet were connected to the flow mixer to meet the required temperature and deliver to the load. The graphical representation of the DHW system loop is shown in Figure 10-4.

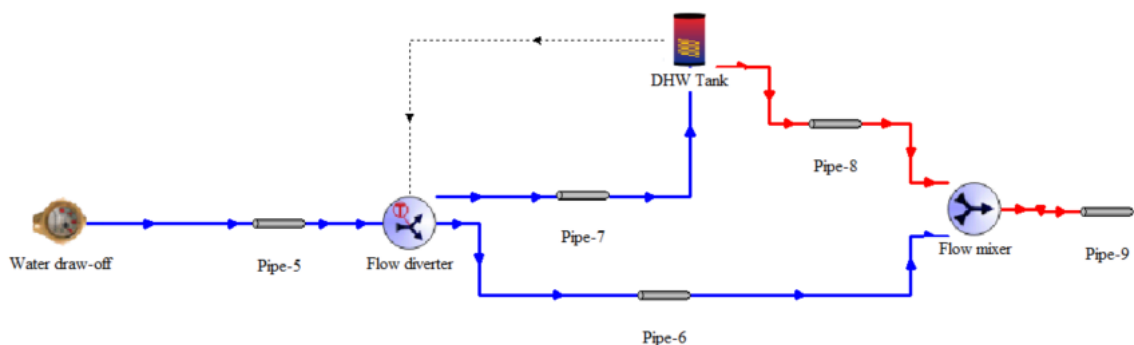
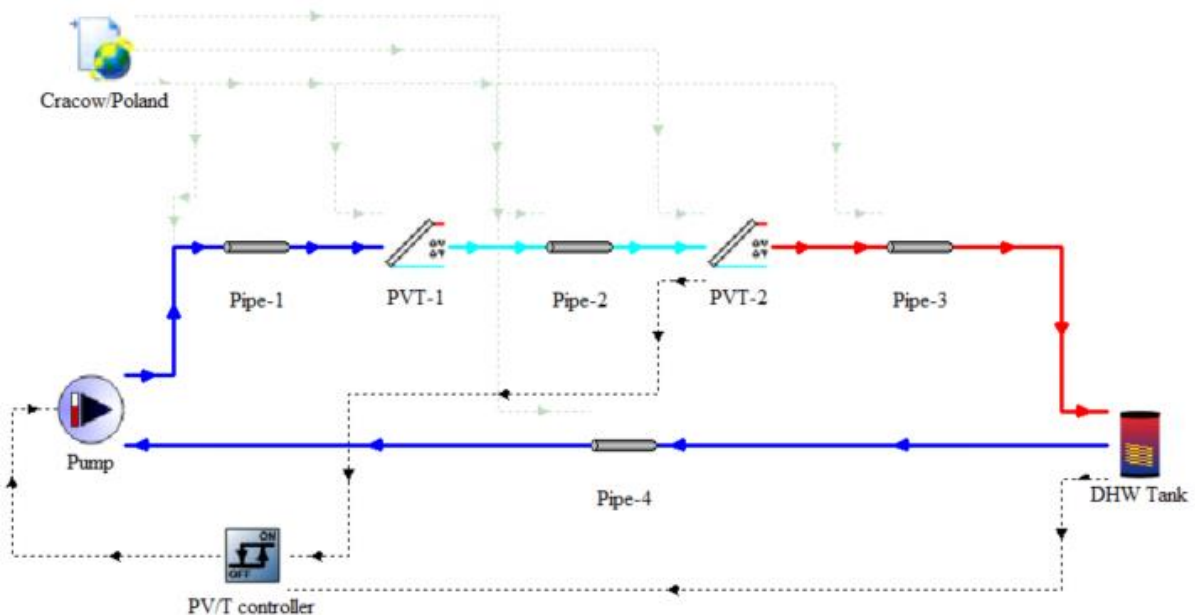


Figure 10-4. The DHW preparation loop

The PV/T loop of the DHW system consisted of the Type 15-3 – weather component, two Type 50 – PV/T modules, a Type 110 – variable-speed pump, a Type 165 – differential controller with hysteresis, and the DHW tank. The initial water temperature in the DHW tank was assumed to be 20 °C. The differential controller with hysteresis was used to control the cooling of the PV/T module based on the temperature in the DHW tank and the outlet temperature of the PV/T module. The water-glycol mixture, whose properties are given in Table 6-2, was used as a working fluid. The mixture was circulated through the immersed heat exchanger of the DHW tank and the PV/T modules. A constant flow rate of 60 L/h was set throughout the year. The system developed in TRNSYS software is shown in Figure 10-5.



**Figure 10-5. The PV/T loop developed in TRNSYS**

The auxiliary heating loop of the DHW system comprised a Type 110 – variable-speed pump, a Type 138 – auxiliary fluid heater, a Type 106 – simple aquastat (heating mode), a Type 14 – time-dependent forcing function, and the DHW tank. A constant flow of 80 L/h was set for water circulation from the DHW tank to the auxiliary heater. The outlet-2 of the DHW tank was connected to the pump for circulating through the heater. The auxiliary heater was connected to the inlet-2 of the DHW tank. The efficiency of the auxiliary heater was set to 100% as it was assumed to be an electric heater. The monitoring temperature in the simple aquastat was set to be the temperature reading from the thermostat of the DHW tank. The heating setpoint was 60 °C with a deadband temperature of 5 °C. The time-dependent forcing function was used to generate a control signal to turn on the auxiliary heater before the DHW demand occurred. The control signal produced by the simple aquastat and time-dependent forcing function was

delivered to an equation to generate the final control signal for the pump and the auxiliary heater. The auxiliary heating loop of the DHW system is shown in Figure 10-6.

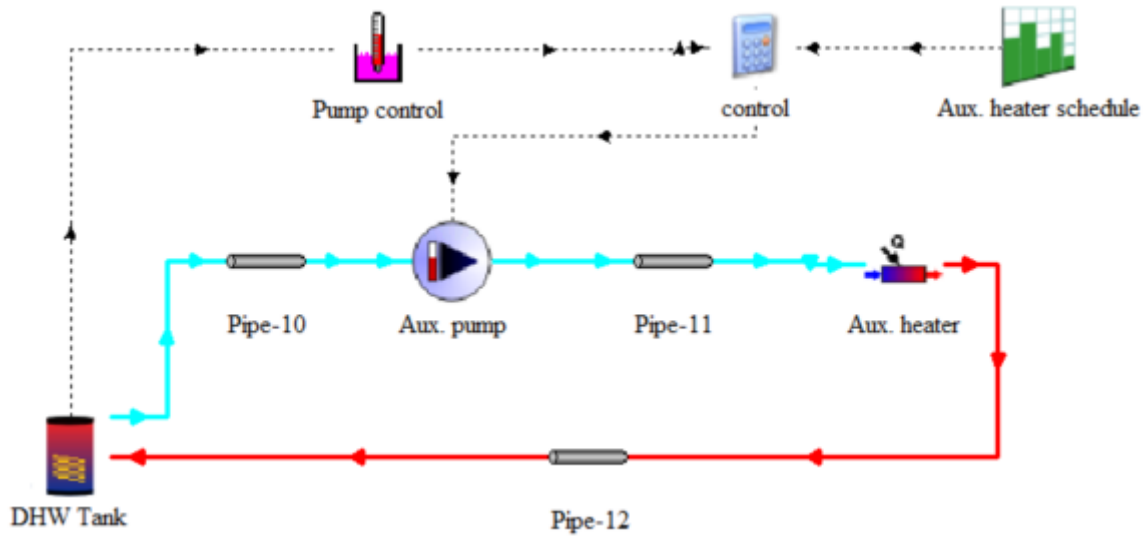


**Figure 10-6. The auxiliary heating loop of the DHW system**

Developing and preparing the DHW loop, PV/T loop, and auxiliary heating loop led to finalizing the complete DHW system setup. The complete DHW system prepared in TRNSYS software is shown in Figure 10-7.

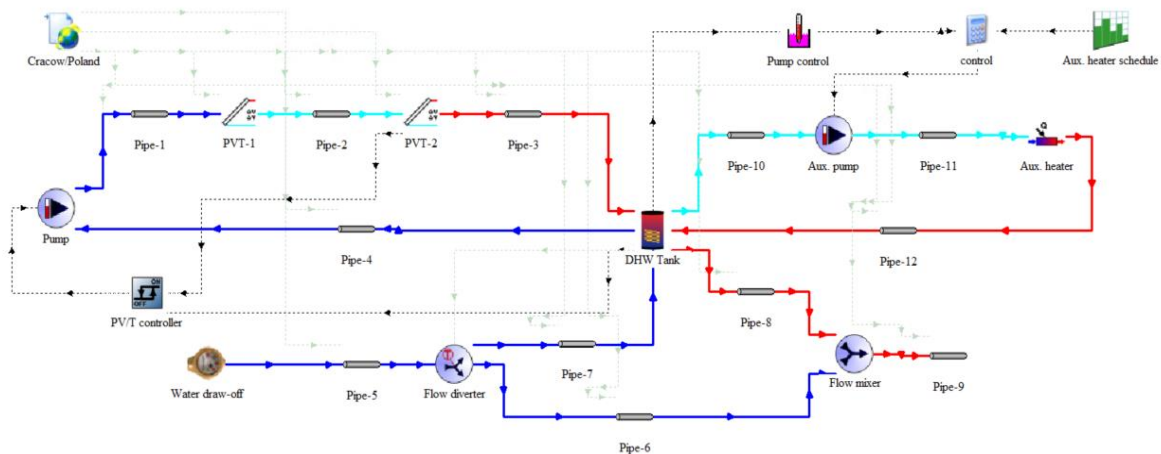


**Figure 10-7. The complete DHW system**

A yearly energy analysis of the DHW system based on the designed PV/T module was simulated. The monthly DHW demand coverage, thermal and electrical energy generated by the PV/T modules, power consumption of the pumps, electrical energy consumption of the auxiliary heater, and thermal energy provided by the auxiliary heater were monitored during the simulation.

The monthly thermal energy generated by two PV/T modules, DHW demand, and coverage of the DHW demand are shown in Figure 10-8.

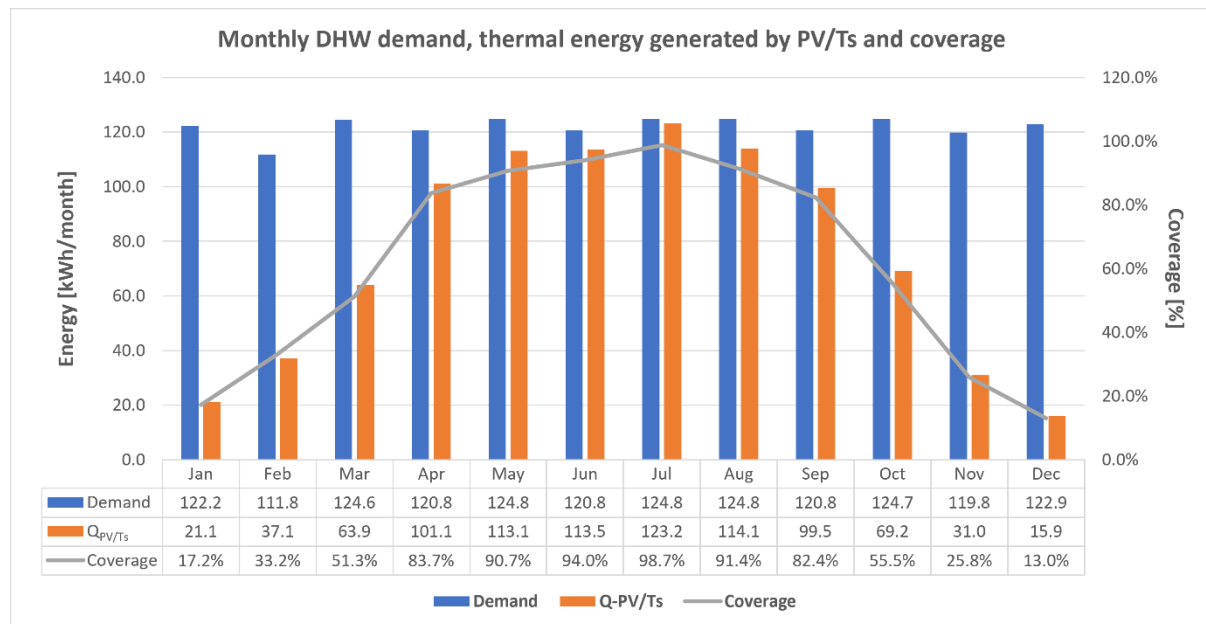


**Figure 10-8. The monthly thermal energy generation of the PV/Ts and coverage of the DHW demand**

In Figure 10-8,  $Q_{PV/Ts}$  represents the monthly total thermal energy generated by the PV/T modules. The analysis showed that the thermal energy generated by two PV/T modules was able to cover 61.4% of the DHW demand yearly. The maximum coverage occurred in July, with 98.73%. In July, the DHW demand was 124.78 kWh, and the thermal energy generated by the PV/T modules was 123.20 kWh. The average coverage was 94.73% during the summer months. The lowest coverage occurred in December, with 12.97%. In December, the DHW demand was 122.89 kWh, and the thermal energy generated by the PV/T modules was 15.94 kWh. The average DHW coverage was 21.12% during the winter months. In the Autumn months, the average DHW coverage was 54.56%, whereas in the Spring months, the average DHW coverage was 75.21%.

The total thermal energy generated by the PV/T modules was 902.6 kWh/y, whereas the DHW demand was 1462.7 kWh/y, as defined in section 10.3. The auxiliary heater covered the remaining DHW demand, 560.1 kWh/y. As the auxiliary heater was chosen to be electrical resistance, the energy consumption of the auxiliary heater was covered by the electrical energy generated by the PV/T modules.

The total monthly electrical energy generated by the PV/T modules, the total power consumption of the pumps, and the electricity consumption of the auxiliary heater are given in Table 10-7.

**Table 10-7. The monthly electrical energy generation and consumption**

| Months    | $P_{PV/T}$ (kWh) | $P_{pump}$ (kWh) | $P_{aux}$ (kWh) | $P_{net}$ (kWh) |
|-----------|------------------|------------------|-----------------|-----------------|
| January   | 26.31            | 3.35             | 101.15          | -78.19          |
| February  | 37.59            | 3.86             | 74.75           | -41.02          |
| March     | 61.24            | 5.69             | 60.72           | -5.17           |
| April     | 86.72            | 6.22             | 19.70           | 60.80           |
| May       | 96.68            | 6.38             | 11.63           | 78.66           |
| June      | 96.32            | 6.34             | 7.21            | 82.77           |
| July      | 103.79           | 6.04             | 1.58            | 96.17           |
| August    | 93.08            | 5.37             | 10.71           | 77.00           |
| September | 71.27            | 6.62             | 21.28           | 43.37           |
| October   | 51.63            | 5.86             | 55.52           | -9.76           |
| November  | 27.73            | 3.87             | 88.87           | -65.02          |
| December  | 19.76            | 2.94             | 106.94          | -90.12          |

In Table 10-7, the  $P_{aux}$  and  $P_{net}$  are the electrical energy consumption of the auxiliary heater and net electrical energy balance for the DHW system. The yearly total electrical energy generated was 772.10 kWh, and the total energy consumption of the pumps was 62.54 kWh. The yearly electrical energy consumption of the auxiliary heater was 560.07 kWh. The thermal and electrical energy generated by the PV/T modules during January, February, March, October, November, and December were insufficient to cover the DHW demand. The total required electrical energy during those months was 289.29 kWh. The excess electricity produced during the rest of the months, 438.78 kWh, was utilized to cover the DHW demand.

According to regulations implied in Poland, the net-billing system came into force by the 1<sup>st</sup> of April 2022 [102]. The current net-billing system states that the excess electrical energy produced is sold at wholesale price and is repurchased at retail price when the electricity demand occurs [103]. The 368.70 kWh of electrical energy needed to be sold at wholesale price and repurchased at retail price when the demand occurred to cover 289.29 kWh [104].

The utilization of 368.70 kWh to cover the electrical energy consumption of the auxiliary heating led to yearly net excess electricity of 70.08 kWh.

The accuracy of the simulation was checked by analyzing the energy balance as suggested by the TRNSYS manual. The manual states that the total energy balance error should be under 2%. The monthly total thermal gains and losses in the system were analyzed. The monthly total thermal gains are calculated using Eq. 54.

$$Q_{monthly\_gains} = Q_{PV/T} + Q_{pump} + Q_{aux} \quad (54)$$

In Eq. 54,  $Q_{monthly\_gains}$  is the total monthly thermal gains in the system.  $Q_{PV/T}$ ,  $Q_{pump}$  and  $Q_{aux}$  are the thermal energy gains from PV/T modules, heat transferred to the fluid by the



pump operation (due to motor inefficiency), and thermal energy generated by the auxiliary heater. The thermal losses in the DHW system are calculated using Eq. 55.

$$Q_{monthly\_losses} = Q_{DHW} + Q_{pump\_loss} + Q_{pipe} \quad (55)$$

In Eq. 55,  $Q_{monthly\_losses}$  stands for the monthly thermal losses from the DHW system.  $Q_{DHW}$ ,  $Q_{pump\_loss}$  and  $Q_{pipe}$  are the thermal energy losses of the pumps and pipes to the environment. The difference between the monthly gains and losses,  $Q_{check}$ , is calculated using Eq. 56.

$$Q_{check} = Q_{monthly\_gains} - Q_{monthly\_losses} \quad (56)$$

The monthly energy balance is calculated based on Eq. 57.

$$E_b = \frac{Q_{check}}{(Q_{monthly\_gains} + Q_{monthly\_losses})/2} \times 100 \quad (57)$$

In Eq. 57,  $E_b$  is the monthly energy balance error in percentages. A summary of the monthly energy balance is given in Table 10-8.

**Table 10-8. The monthly energy balance of the DHW system**

| Months    | $Q_{monthly\_gains}$ (kJ) | $Q_{monthly\_losses}$ (kJ) | $Q_{check}$ (kJ) | $E_b$ (%) |
|-----------|---------------------------|----------------------------|------------------|-----------|
| January   | 455,213.8                 | 455,296.3                  | -82.5            | -0.02%    |
| February  | 414,475.9                 | 414,179.0                  | 296.9            | 0.07%     |
| March     | 454,663.9                 | 454,656.2                  | 7.7              | 0.00%     |
| April     | 443,422.5                 | 443,841.8                  | -419.3           | -0.09%    |
| May       | 460,132.2                 | 460,839.6                  | -707.4           | -0.15%    |
| June      | 435,440.0                 | 436,301.1                  | -861.2           | -0.20%    |
| July      | 456,400.5                 | 457,527.6                  | -1127.2          | -0.25%    |
| August    | 420,308.6                 | 421,362.9                  | -1054.3          | -0.25%    |
| September | 445,417.9                 | 445,705.9                  | -287.9           | -0.06%    |
| October   | 449,247.5                 | 449,208.5                  | 39.0             | 0.01%     |
| November  | 423,409.6                 | 422,983.2                  | 426.4            | 0.10%     |
| December  | 439,092.6                 | 438,382.7                  | 709.9            | 0.16%     |

The total energy balance error of the DHW system simulation was -0.68%. The calculated value was under 2% as 2% is the maximum value for energy balance error for an accurate simulation indicated by the software manual.

### 10.3.2 Payback period analysis

A payback period analysis was performed to determine the time to recover the investment cost. The designed DHW system with PV/T modules to cover DHW and electrical energy demands allows for savings in gas and electricity bills compared to the conventional gas boiler.

In order to compare the results of the DHW system based on the designed PV/T module to the existing energy systems, a conventional combined condensing gas boiler was chosen to

be studied. The cost of the gas boiler, installation cost, yearly gas and electricity consumption cost of the gas boiler, and annual OM costs of the system were considered. The cost breakdown of the conventional gas boiler system is shown in Figure 10-9.

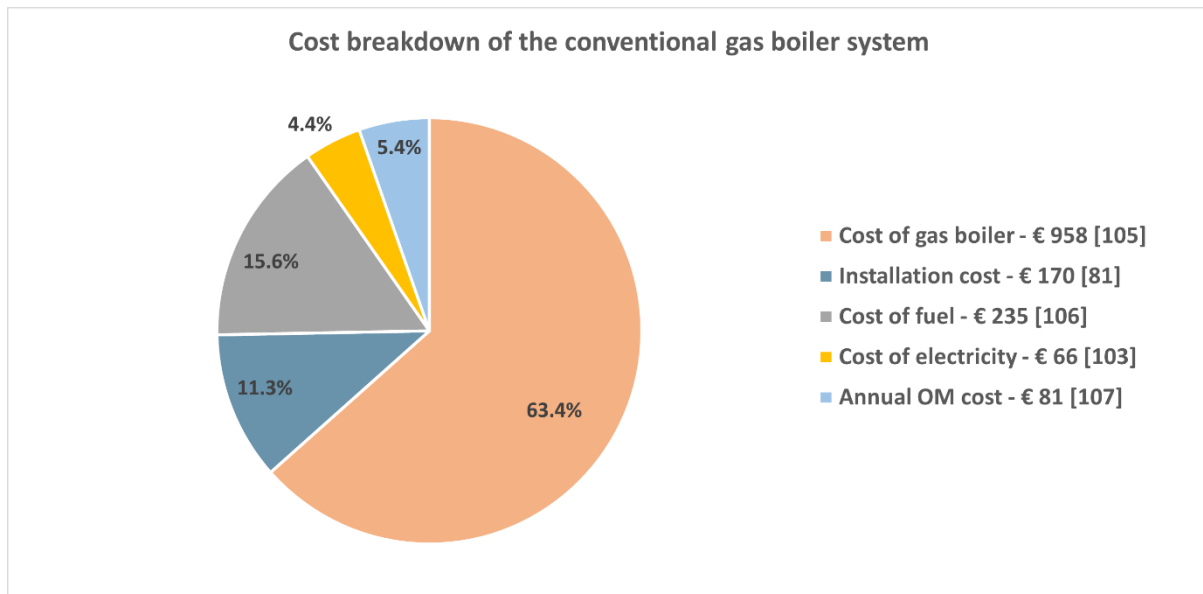


**Figure 10-9. The cost breakdown of the conventional gas boiler system for DHW**

In section 10.3, the yearly gas consumption of the building was given as 283 m<sup>3</sup>. The capital cost of the conventional gas boiler system was 1,128 €, along with annual gas, electricity, and OM costs (annual maintenance and gas line inspection) of 234.88 €, 66.16 €, and 81 €.

The total yearly savings from the bills were calculated as 382.05 €, including gas and electricity. In addition to the savings from the bills, the yearly excess electricity generated by the PV/T modules, 70.08 kWh, was also considered to be sold at wholesale price and added to the savings, 9.73 €. A summary of the total costs of the systems, OM costs, and bill savings is given in Table 10-9.

**Table 10-9. The summary of costs and bill savings**

| PV/T modules                   | Capital costs (€) | OM costs (€) | Yearly savings (€) |
|--------------------------------|-------------------|--------------|--------------------|
| Proposed PV/T module           | 2,317             | 23.17        | 368.60             |
| Conventional gas boiler system | 1,128             | 81.00        | -                  |

The yearly savings for the system were calculated by summing up the total bill savings (382.05 €) and excess electricity (9.73 €) produced by the PV/T modules and subtracting the OM costs (23.17 €) from the total savings.

Based on Table 10-9, the 25 years of operation costs were estimated for each system. The total cost of 25 years of operation was 2,653.07 € and 10,679.13 € for the DHW system with proposed PV/T modules and the gas boiler. The cost analysis showed that the designed DHW

system with the proposed PV/T module was four times cheaper than the conventional gas boiler system.

A payback period analysis was performed, and the result is shown in Figure 10-10.

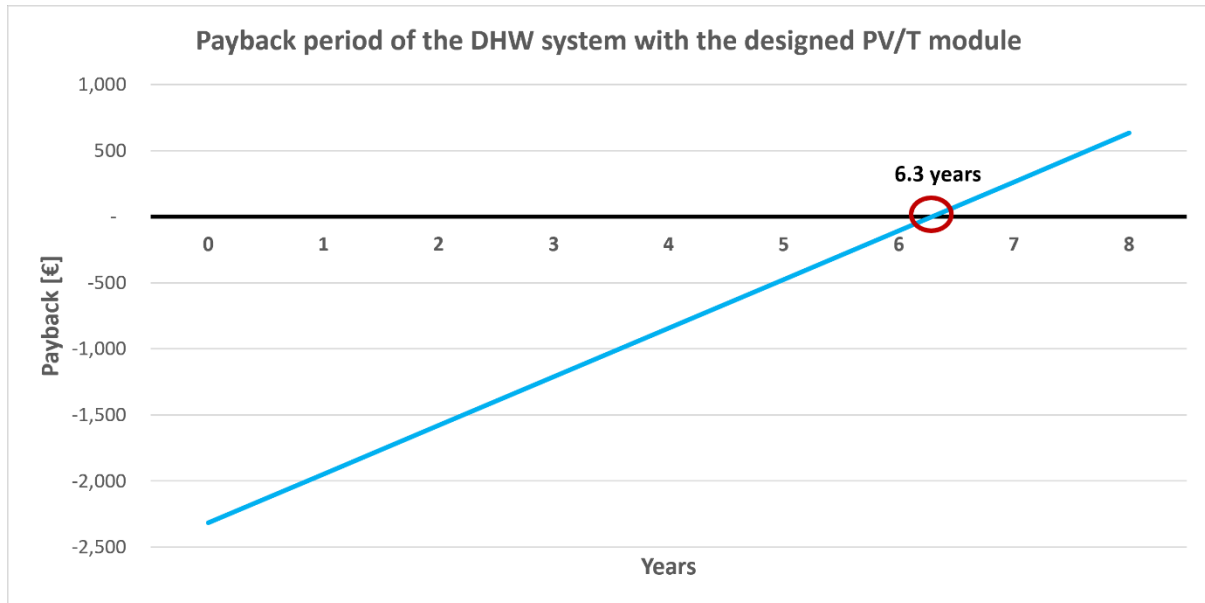


**Figure 10-10. The payback period of the PV/T system**

The results showed that the payback period of the system designed with the proposed PV/T module was 6.3 years. The yearly savings from the bills were assumed to stay stable over the course of the years.

The levelized cost of heat (LCOH) and levelized cost of electricity were calculated for the system based on Eqs. 51 and 52, and the results are given in Table 10-10.

**Table 10-10. The levelized cost of heat and electricity**

| PV/T modules         | LCOH (€/kWh) | LCOE (€/kWh) | LEC (€/kWh) |
|----------------------|--------------|--------------|-------------|
| Proposed PV/T module | 0.21         | 0.27         | 0.12        |

The LCOH, LCOE, and LEC were obtained by taking into account the total capital costs and annual incurring costs of the PV/T system without splitting the costs between electrical and hydraulic components.

The analysis showed that the cost of the thermal energy generated per kWh was 0.21 €, and the cost of the electrical energy generated per kWh was 0.27 €. In contrast, the cost of combined energy generated (electrical and thermal energy combined) per kWh was 0.12 €.

## 10.4 Summary

In this chapter, an economic analysis of the designed PV/T module was conducted. The unit cost of the designed PV/T module was calculated and found to be 576 €.

A levelized energy cost analysis was conducted for over a 25-year lifetime. The total electrical and thermal energy generation of the designed PV/T module was 8.52 MWh and 23.78 MWh, respectively, over a 25-year lifetime. The total electrical and thermal energy generation of the PV/T–A was 6.05 MWh and 8.49 MWh, respectively, over a 25-year lifetime. The 25-year lifetime energy analysis estimation showed that the proposed PV/T module produces 1.41 times and 2.80 times more electrical and thermal energy than PV/T–A. When the maximum thermal output of the designed PV/T module is compared to PV/T modules available in the Polish market, the designed PV/T modules produce 1.46 times and 1.67 times more thermal energy than the PV/T – B and PV/T – C.

A case study on domestic hot water (DHW) demand coverage analysis of a single-family house using the designed PV/T module and the conventional gas boiler was conducted. The 25 years of operation costs were estimated for each system. The total cost of 25 years of operation was 2,653.07 € and 10,679.13 € for the DHW system with proposed PV/T modules and the gas boiler. The cost analysis showed that the designed DHW system with the proposed PV/T module was four times cheaper than the conventional gas boiler system.

A payback period analysis was conducted for the PV/T module-based DHW system. The results showed that the payback period of the system designed with the proposed PV/T modules was 6.3 years.

The LCOH and LCOE analyses were performed for the case study to investigate the energy costs. The thermal energy cost per kWh was 0.21 €, and the electrical energy cost per kWh was 0.27 €, whereas the levelized energy cost (combined electricity and thermal energy) per kWh was 0.12 €.

## Chapter 11 - Conclusions

In the last decades, hybrid energy generation has drawn greater attention due to its advantages compared to ST and PV systems. The PV/T systems brought an innovative approach to utilizing solar energy by generating electrical and thermal energy simultaneously from a single PV module. The development of the PV/T system continuously advances as PV/T systems are one of the key components of sustainable energy goals, reducing the environmental impact of energy generation and encouraging the responsible management of energy resources.

The aim of this dissertation was to invent a highly efficient, easy-to-produce, and compact cooling system for PV modules. The comprehensively studied effects of temperature on power output and efficiency of PV modules and the extensive literature review led to the design of a novel cooling system. The energy performance of the designed PV/T module was investigated in laboratory and outdoor environments. The economic viability study was conducted for the designed PV/T system.

This doctoral thesis hypothesized that the designed cooling system for photovoltaic modules needs to maintain the maximum electrical conversion efficiency while achieving thermal efficiency higher than 90%. The outdoor experiments showed that the designed system can achieve a maximum thermal efficiency of  $98.03 \pm 1.57\%$ , far exceeding the initial expectations. The superior thermal management allowed for maintaining the maximum electrical conversion efficiency of  $19.12 \pm 1.14\%$ . The use of working fluid as water makes the system preferable due to its availability, non-toxic characteristics, environmentally friendly behavior, high specific heat capacity, and thermal stability. The achieved results present significant improvements in energy conversion and utilization.

The designed system can contribute substantially by simultaneously providing electrical and thermal energy to de-carbonization and green energy transition for commercial and residential buildings where available space is scarce. The previous studies and PV/T modules available on the market showed that substantial improvement was needed in the efficiency of the PV/T modules to make the technology cost-competitive and easily adaptable. The achieved results not only exceed the established benchmarks but also endeavor a promising path for more effective energy solutions. The techno-economic analysis results showed that the designed PV/T module is able to produce more energy than PV/T modules available in the Polish market. In addition to energy comparison, the cost analysis concluded that the proposed PV/T module is a cost-effective solution. The case study based on DHW demand coverage shows the scalability, adaptability, effectiveness, and compactness of the designed PV/T module.

## Summary of the dissertation findings

The adverse effects of the temperature on PV modules were investigated delicately to understand the thermal behavior of the PV modules. A numerical thermal model of the PV module was developed and validated using various approaches. A critical review of relevant research work on PV/T systems was conducted and provided an in-depth understanding of the various proposed systems in the literature. The performance of the various PV/T systems was reviewed to determine and highlight key points in designing a cooling system for PV modules. The state-of-the-art PV/T systems, such as air-based, water-based, heat pipe integrated, TEG combined, PCM-based, and nanofluid-based PV/T systems, were reviewed, and the advantages of each system were highlighted.

Based on the critical literature review and the thermal behavior of the PV modules, a design guideline for PV/T systems was prepared. During the design process, the following considerations were taken: selection of cooling method, geometry and heat transfer of the design, material selection, coolant selection, thermal efficiency, and cooling effect of the design. While designing the cooling system, the prepared guideline was taken into account, and each step was detailed. The initial design was created, and a numerical study was conducted. Based on the numerical study results of the initial design, improvements were made to enhance the effectiveness of the cooling system. The final design of the cooling system was manufactured for the laboratory and outdoor experiments.

The designed PV/T module was first tested in the laboratory. The thermal efficiency and heat transfer characteristics under various conditions were investigated. Maximum thermal efficiency of  $96.47 \pm 1.40\%$  was achieved during the experiments with the inlet mass flow rate of  $0.0458 \text{ kg/s}$  and inlet temperature of  $11.90 \text{ }^\circ\text{C}$  under  $592.89 \text{ W/m}^2$ . The boundary conditions applied to the final design of the cooling system were applied to the previous design to compare performance. The previous design was able to reach up to  $89.13\%$  thermal efficiency. The final PV/T design showed  $8.24\%$  improved thermal efficiency.

The outdoor experiments were conducted for two months, in September and October, to analyze the performance of the designed PV/T module. The maximum cooling of the PV module was observed on the 12<sup>th</sup> of September, 2023, where the back surface temperatures of cooled and non-cooled PV modules were  $16.56 \text{ }^\circ\text{C}$  and  $70.98 \text{ }^\circ\text{C}$ , respectively. The maximum thermal efficiency of  $98.03 \pm 1.57\%$  achieved during the day was the highest thermal efficiency observed during the experiment period of two months. During the day, achieved thermal efficiency surpassed the projected  $90\%$  thermal efficiency target and maintained the maximum electrical conversion efficiency. The electrical conversion efficiency of the PV module was  $19.12 \pm 1.14\%$ . The implemented cooling system allowed for generating  $38.86\%$

more electrical energy at the end of the test day. The measurement results showed that in September, the total electrical energy generated by the PV/T module and stand-alone PV module were 24.21 kWh/month and 20.11 kWh/month, respectively. The average improvement in electrical energy generation was 20.40% compared to the stand-alone PV module. The monthly available solar energy was 83.98 kWh/m<sup>2</sup>/month, the thermal energy generated was 46.13 kWh/m<sup>2</sup>, and the electrical energy generated by the PV/T module was 14.25 kWh/m<sup>2</sup> (AC). The PV/T module was able to convert 54.93% and 18.85% of the available solar energy into thermal and electrical energy (DC), respectively. The non-cooled PV module converted 15.65% of the available solar energy into electrical energy (DC). In October, The total electrical energy generated by the PV/T module and non-cooled PV module were 27.01 kWh/month and 24.83 kWh/month, respectively. The overall electrical energy generation was enhanced by 8.78% compared to the non-cooled PV module. The monthly available solar energy was 92.61 kWh/m<sup>2</sup>, the thermal energy generation was 34.82 kWh/m<sup>2</sup>, and the electrical energy generation of the PV/T module was 15.89 kWh/m<sup>2</sup> (AC). The PV/T module was able to convert 37.60% and 19.07% of the available solar energy into thermal and electrical energy (DC), respectively. The non-cooled PV module converted 17.53% (DC) of the available solar energy into electrical energy. Yearly energy analysis was conducted on a validated numerical model. The yearly electrical and thermal energy generated by the designed PV/T module was 418.31 kWh (AC) and 951.11 kWh, respectively. The yearly power consumption of the pump was 39.30 kWh/y, leading to a net electricity production of 379.01 kWh/y for the PV/T module.

The effectiveness of the designed PV/T system was analyzed by conducting a comparative study of existing literature with the proposed PV/T design. The comparative framework was employed to highlight the key performance metrics. The comparative analysis encompassed the electrical energy conversion efficiency and thermal efficiency. The designed PV/T system was compared to ten different state-of-the-art PV/T systems proposed in the literature. The comprehensive comparative analysis results showed that the proposed PV/T system exhibits better performance compared to the proposed solutions in the literature. Most of the research conducted focused either on the shape of the pipes in the cooling design of the PV/T system or on the improvement of the thermal properties of the working fluid. The conventional PV/T system designs were modified by changing the shape of the pipes or adding PCM materials to regulate the temperature. The investigations on increasing the efficiency of PV/T systems also targeted the working fluid by adding nanomaterials to enhance thermal conductivity and heat-carrying capacity. The main drawbacks of the proposed solutions were the complex nature of designs, lack of economic analysis, low electrical and thermal efficiencies, and not utilizing the available heat transfer area effectively. The thermal efficiency of the state-of-the-

art water-based active cooling PV/T systems proposed in the literature ranged between 40% and 85%, whereas the electrical efficiency of the systems varied between 7% and 16%. The designed PV/T system achieved  $19.12 \pm 1.14\%$  electrical efficiency and  $98.03 \pm 1.57\%$  thermal efficiency in this dissertation, exceeding its rivals.

An economic analysis of the proposed PV/T module was conducted. The unit cost of the designed PV/T module was calculated and found to be 576 €. A levelized energy cost analysis was conducted for over a 25-year lifetime. The total electrical and thermal energy generation of the designed PV/T module was 8.52 MWh and 23.78 MWh, respectively, over a 25-year lifetime. The total electrical and thermal energy generation of the PV/T–A was 6.05 MWh and 8.49 MWh, respectively, over a 25-year lifetime. The 25-year lifetime energy analysis estimation showed that the proposed PV/T module produces 1.41 times and 2.80 times more electrical and thermal energy than PV/T–A. When the maximum thermal output of the designed PV/T module is compared to PV/T modules available in the Polish market, the designed PV/T modules produce 1.46 times and 1.67 times more thermal energy than the PV/T – B and PV/T – C. A case study on domestic hot water (DHW) demand coverage analysis of a single-family house using the designed PV/T module and the conventional gas boiler was conducted. The 25 years of operation costs were estimated for each system. The total cost of 25 years of operation was 2,653.07 € and 10,679.13 € for the DHW system with proposed PV/T modules and the gas boiler. The cost analysis showed that the designed DHW system with the proposed PV/T module was four times cheaper than the conventional gas boiler system. A payback period analysis was conducted for the PV/T module-based DHW system. The results showed that the payback period of the system designed with the proposed PV/T modules was 6.3 years. The LCOH and LCOE analyses were performed for the case study to investigate the energy costs. The thermal energy cost per kWh was 0.21 €, and the electrical energy cost per kWh was 0.27 €, whereas the levelized energy cost (combined electricity and thermal energy) per kWh was 0.12 €.



## Bibliography

1. Eurostat. Renewable energy statistics. URL [https://ec.europa.eu/eurostat/statistics-explained/index.php?title=Renewable\\_energy\\_statistics](https://ec.europa.eu/eurostat/statistics-explained/index.php?title=Renewable_energy_statistics). Accessed on 5 August 2023.
2. European Parliament, Council of the European Union. Directive 2010/31/EU of the European Parliament and of the Council of 19 May 2010 on the energy performance of buildings (recast). **2010**. (URL: <http://data.europa.eu/eli/dir/2010/31/oj>)
3. Commission Recommendation (EU) 2016/1318 of 29 July 2016 on guidelines for the promotion of nearly zero-energy buildings and best practices to ensure that, by 2020, all new buildings are nearly zero-energy buildings. *Official Journal*, **2016**, 46-57. (Link: <http://data.europa.eu/eli/reco/2016/1318/oj>)
4. Yuan X.; Heikari L.; Hirvonen, J.; Liang Y.; Virtanen M.; Kosonen R.; Pan Y. System modelling and optimization of a low temperature local hybrid energy system based on solar energy for a residential district. *Energy Conversion and Management*, **2022**, 267. (DOI: <https://doi.org/10.1016/j.enconman.2022.115918>)
5. Rohde D.; Andresen T.; Nord N. Analysis of an integrated heating and cooling system for a building complex with focus on long-term thermal storage. *Applied Thermal Engineering*, **2018**, 145. (DOI: <https://doi.org/10.1016/j.applthermaleng.2018.09.044>)
6. European Commission, Directorate-General for Energy, Clean energy for all Europeans. *Publications Office*, **2019**. (Link: <https://data.europa.eu/doi/10.2833/9937>)
7. Eurostat. Energy statistics – an overview. URL [https://ec.europa.eu/eurostat/statistics-explained/index.php?title=Energy\\_statistics\\_-\\_an\\_overview](https://ec.europa.eu/eurostat/statistics-explained/index.php?title=Energy_statistics_-_an_overview). Accessed on 1 June 2023.
8. Energy consumption by source **2023**. URL <https://ourworldindata.org/grapher/energy-consumption-by-source-and-country?tab=table&time=2021>. Accessed on 1 February 2023.
9. Telsnig T.; Vazquez H.C. Wind Energy Technology Market Report, EUR 29922 EN, *European Commission, Luxembourg*, **2019**. (DOI: <http://doi.org/10.2760/223306>)
10. BP. Installed solar PV capacity. URL <https://ourworldindata.org/grapher/installed-solar-pv-capacity>. Accessed on 15 August 2023.
11. Renewable Power Generation Costs in **2022**. (Data retrieved from <https://www.irena.org/publications/2022/Jul/Renewable-Power-Generation-Costs-in-2021> on 01/10/2023)
12. Malko J. Polityka energetyczna państwa do 2030 roku. *Prz. Elektrotechniczny*, **2009**, 85, 261–267. (DOI: <http://yadda.icm.edu.pl/baztech/element/bwmeta1.element.baztech-article-BPOC-0054-0047>)
13. Łukasz M.; Mikołaj Ś. Polish Energy Policy until 2040 – prospects and challenges. *Zeszyty Naukowe Instytutu Gospodarki Surowcami Mineralnymi i Energią PAN*, **2022**, 110. (DOI: <https://doi.org/10.24425/140525>)
14. Ministry of Climate and Environment, Poland. Energy Policy of Poland until 2040 (EPP2040). URL <https://www.gov.pl/web/climate/energy-policy-of-poland-until-2040-epp2040>. Accessed on 10 September **2022**.
15. Dubey S.; Sarvaiya J.N.I Seshadri B. Temperature Dependent Photovoltaic (PV) Efficiency and Its Effect on PV Production in the World – A Review. *Energy Procedia*, **2013**, 33, 311-321. (DOI: <https://doi.org/10.1016/j.egypro.2013.05.072>)

16. Koehl M.; Hoffmann S.; Wiesmeier S. Evaluation of damp-heat testing of photovoltaic modules. *Progress in Photovoltaics*, **2016**, 25. (DOI: <https://doi.org/10.1002/pij.2842>)
17. Baljit S.S.S.; Hoy-Yen C.; Kamaruzzaman S. Review of building integrated applications of photovoltaic and solar thermal systems. *Journal of Cleaner Production*, **2016**, 137, 677-689. (DOI: <https://doi.org/10.1016/j.jclepro.2016.07.150>)
18. Cetina-Quiñones A.J.; Polanco-Ortiz I.; Alonzo P.M.; Hernandez-Perez J.G.; Bassam A. Innovative heat dissipation design incorporated into a solar photovoltaic thermal (PV/T) air collector: An optimization approach based on 9E analysis. *Thermal Science and Engineering Progress*, **2023**, 38. (DOI: <https://doi.org/10.1016/j.tsep.2022.101635>)
19. Saygin H.; Nowzari R.; Mirzaei N.; Aldabbagh L.B.Y. Performance evaluation of a modified PV/T solar collector: A case study in design and analysis of experiment. *Solar Energy*, **2017**, 141, 210-221. (DOI: <https://doi.org/10.1016/j.solener.2016.11.048>)
20. Sarhaddi F.; Farahat S.; Ajam H.; Behzadmehr A.; Mahdavi A.M. An improved thermal and electrical model for a solar photovoltaic thermal (PV/T) air collector. *Applied Energy*, **2010**, 87, 2328-2339. (DOI: <https://doi.org/10.1016/j.apenergy.2010.01.001>)
21. Ozakin A.N.; Kaya F. Effect on the exergy of the PVT system of fins added to an air-cooled channel: A study on temperature and air velocity with ANSYS Fluent. *Solar Energy*, **2019**, 184, 561-569. (DOI: <https://doi.org/10.1016/j.solener.2019.03.100>)
22. Teo H.G.; Lee P.S.; Hawlader M.N.A. An active cooling system for photovoltaic modules. *Applied Energy*, **2012**, 90. (DOI: <https://doi.org/10.1016/j.apenergy.2011.01.017>)
23. Hussein A.K. Evaluation and analysis of water-based photovoltaic/thermal (PV/T) system. *Case Studies in Thermal Engineering*, **2019**, 13. (DOI: <https://doi.org/10.1016/j.csite.2019.100401>)
24. Shalaby S.M.; Elfakharany M.K.; Moharram B.M.; Abosheisha H.F. Experimental study on the performance of PV with water cooling. *Energy Reports*, **2022**, 8, 957-961. (DOI: <https://doi.org/10.1016/j.egyr.2021.11.155>)
25. Gomaa M.R.; Ahmed M.; Rezk H. Temperature distribution modeling of PV and cooling water PV/T collectors through thin and thick cooling cross-fined channel box. *Energy Reports*, **2022**, 8, 1144-1153. (DOI: <https://doi.org/10.1016/j.egyr.2021.11.061>)
26. Ocioń P.; Cisek P.; Kozak-Jagiela E.; Taler J.; Taler D.; Skrzyniowska D.; Fedorczyk-Cisak M. Modeling and experimental validation and thermal performance assessment of a sun-tracked and cooled PVT system under low solar irradiation. *Energy Conversion and Management*, **2020**, 222. (DOI: <https://doi.org/10.1016/j.enconman.2020.113289>)
27. Zhang Q.; He S.; Song T.; Wang M.; Liu Z.; Zhao J.; Gao Q.; Huang X.; Han K.; Qi J.; Gao M.; Shi Y. Modeling of a PV system by a back-mounted spray cooling section for performance improvement. *Applied Energy*, **2023**. (DOI: <https://doi.org/10.1016/j.apenergy.2022.120532>)
28. Salman A.H.A.; Hilal K.H.; Ghadhban S.A. Enhancing performance of PV module using water flow through porous media. *Case Studies in Thermal Engineering*, **2022**, 34. (DOI: <https://doi.org/10.1016/j.csite.2022.102000>)
29. Erdogan I.; Bilen K.; Kivrak S. Experimental Investigation of The Efficiency of Solar Panel Over Which Water Film Flows. *Journal of Polytechnic*, **2023**, 26. (DOI: <https://doi.org/10.2339/politeknik.1163785>)
30. Nižetić S.; D.; Yadav A.; Grubišić-Čabo F. Water spray cooling technique applied on a photovoltaic panel: The performance response. *Energy Conversion and Management*, **2016**, 108, 287-296. (DOI: <https://doi.org/10.1016/j.enconman.2015.10.079>)

31. Herrando M.; Fantoni G.; Cubero A.; Simón-Allué R.; Guedea I.; Fueyo N. Numerical analysis of the fluid flow and heat transfer of a hybrid PV-thermal collector and performance assessment. *Renewable Energy*, **2023**, 209, 122-132. (DOI: <https://doi.org/10.1016/j.renene.2023.03.125>)
32. Abdullah A.L.; Misha S.; Tamaldin N.; Rosli M.A.M.; Sachit F.A. Theoretical study and indoor experimental validation of performance of the new photovoltaic thermal solar collector (PVT) based water system. *Case Studies in Thermal Engineering*, **2020**. (DOI: <https://doi.org/10.1016/j.csite.2020.100595>)
33. Gang P.; Huide F.; Huijuan Z.; Jie J. Performance study and parametric analysis of a novel heat pipe PV/T system. *Energy*, **2012**, 384-395. (DOI: <https://doi.org/10.1016/j.energy.2011.11.017>)
34. Zhang T.; Yan Z.W.; Xiao L.; Fu H.D.; Pei G.; Ji J. Experimental, study and design sensitivity analysis of a heat pipe photovoltaic/thermal system. *Applied Thermal Engineering*, **2019**, 162. (DOI: <https://doi.org/10.1016/j.applthermaleng.2019.114318>)
35. Hou L.; Quan Z.; Zhao Y.; Wang L.; Wang G. An experimental and simulative study on a novel photovoltaic-thermal collector with micro heat pipe array (MHPA-PV/T). *Energy and Buildings*, **2016**, 124, 60-69. (DOI: <https://doi.org/10.1016/j.enbuild.2016.03.056>)
36. Moradgholi M.; Nowee S.M.; Abrishamchi I. Application of heat pipe in an experimental investigation on a novel photovoltaic/thermal (PV/T) system. *Solar Energy*, **2014**, 107, 82-88. (DOI: <https://doi.org/10.1016/j.solener.2014.05.018>)
37. Modjinou M.; Ji J.; Li J.; Yuan W.; Zhou F. A numerical and experimental study of micro-channel heat pipe solar photovoltaics thermal system. *Applied Energy*, **2017**, 206, 708-722. (DOI: <https://doi.org/10.1016/j.apenergy.2017.08.221>)
38. Lin J.; Liao T.; Lin B. Performance analysis and load matching of a photovoltaic–thermoelectric hybrid system. *Energy Conversion and Management*, **2015**, 105, 891-899. (DOI: <https://doi.org/10.1016/j.enconman.2015.08.054>)
39. Babu C.; Ponnambalam P. The theoretical performance evaluation of hybrid PV-TEG system. *Energy Conversion and Management*, **2018**, 173, 450-460. (DOI: <https://doi.org/10.1016/j.enconman.2018.07.104>)
40. Fini M.A.; Gharapetian D.; Masoud Asgari. Efficiency improvement of hybrid PV-TEG system based on an energy, exergy, energy-economic and environmental analysis; experimental, mathematical and numerical approaches. *Energy Conversion and Management*, **2022**, 265. (DOI: <https://doi.org/10.1016/j.enconman.2022.115767>)
41. Maleki Y.; Pourfayaz F.; Mehrpooya. Experimental study of a novel hybrid photovoltaic/thermal and thermoelectric generators system with dual phase change materials. *Renewable Energy*, **2022**, 201, 202-215. (DOI: <https://doi.org/10.1016/j.renene.2022.11.037>)
42. Gopinath M.; Marimuthu R. PV-TEG output: Comparison with heat sink and graphite sheet as heat dissipators. *Case Studies in Thermal Engineering*, **2023**, 45. (DOI: <https://doi.org/10.1016/j.csite.2023.102935>)
43. Nižetić, S.; Jurčević, M.; Čoko, D.; Arıcı, M.; Hoang, A.T. Implementation of phase change materials for thermal regulation of photovoltaic thermal systems: Comprehensive analysis of design approaches. *Energy*, **2021**, 228. (DOI: <https://doi.org/10.1016/j.energy.2021.120546>)
44. Zheng X.; Zhou Y. A three-dimensional unsteady numerical model on a novel aerogel-based PV/T-PCM system with dynamic heat-transfer mechanism and solar energy

- harvesting analysis. *Applied Energy*, **2023**, 338. (DOI: <https://doi.org/10.1016/j.apenergy.2023.120899>)
45. Xu H.; Wang N.; Zhang C.; Qu Z.; Karimi F. Energy conversion performance of a PV/T-PCM system under different thermal regulation strategies. *Energy Conversion and Management*, **2021**, 229. (DOI: <https://doi.org/10.1016/j.enconman.2020.113660>)
  46. Zohra M.B.; Riad A.; Alhamany A. Optimising the conception of hybrid PV/PCM by optimizing the heat transfer at the contact interface and by integrating two types of PCM. *Results in Engineering*, **2022**, 16. (DOI: <https://doi.org/10.1016/j.rineng.2022.100614>)
  47. Hossain M.S.; Pandey A.K.; Selvaraj J.; Rahim N.A.; Islam M.M.; Tyagi V.V. Two side serpentine flow based photovoltaic-thermal-phase change materials (PVT-PCM) system: Energy, exergy and economic analysis. *Renewable Energy*, **2019**, 136, 1320-1336. (DOI: <https://doi.org/10.1016/j.renene.2018.10.097>)
  48. Hooshmandzade N.; Motevali A.; Seyedi S.R.M.; Biparva P. Influence of single and hybrid water-based nanofluids on performance of microgrid photovoltaic/thermal system. *Applied Energy*, **2021**, 304. (DOI: <https://doi.org/10.1016/j.apenergy.2021.117769>)
  49. Karaaslan I.; Menlik T. Numerical study of a photovoltaic thermal (PV/T) system using mono and hybrid nanofluid. *Solar Energy*, **2021**, 224, 1260-1270. (DOI: <https://doi.org/10.1016/j.solener.2021.06.072>)
  50. Sangeetha M.; Manigandan S.; Ashok B.; Brindhadevi K.; Pugazhendhi A. Experimental investigation of nanofluid based photovoltaic thermal (PV/T) system for superior electrical efficiency and hydrogen production. *Fuel*, **2021**, 286. (DOI: <https://doi.org/10.1016/j.fuel.2020.119422>)
  51. Naghdbishi A.; Yazdi M.E.; Akbari G. Experimental investigation of the effect of multi-wall carbon nanotube – Water/glycol-based nanofluids on a PVT system integrated with PCM-covered collector. *Applied Thermal Engineering*, **2020**, 178. (DOI: <https://doi.org/10.1016/j.applthermaleng.2020.115556>)
  52. Margoum S.; Fouas C.E.; Bekkay H.; Aneli S.; Gagliano A.; Mannino G.; Tina G.M. Study Effect of Nanofluids on the Performance Enhancement of PV/T Collector. *Proceedings of the 3rd International Conference on Electronic Engineering and Renewable Energy Systems – ICEERE*, **2022**, 954. (DOI: [https://doi.org/10.1007/978-981-19-6223-3\\_93](https://doi.org/10.1007/978-981-19-6223-3_93))
  53. The MathWorks Inc. (2021). MATLAB version: 9.13.0 (R2021a), Natick, Massachusetts: The MathWorks Inc. URL <https://www.mathworks.com>
  54. Ansys® Academic Research Fluent, 2020, 2021, 2022, and 2023 R1, R2 Releases. URL <https://www.ansys.com/>
  55. Klein S.A.; Beckman W.A. TRNSYS 18: A Transient System Simulation Program, Solar Energy Laboratory, University of Wisconsin, Madison, USA, **2017**. URL <http://sel.me.wisc.edu/trnsys>
  56. Ilse K.; Pfau C.; Miclea P.T.; Krause S.; Hagendorf C. Quantification of abrasion-induced ARC transmission losses from reflection spectroscopy. *IEEE 46th Photovoltaic Specialists Conference*, **2019**, 2883-2888. (DOI: <https://doi.org/10.1109/PVSC40753.2019.8980700>)
  57. Duffie J.A.; Beckman W.A. Solar engineering of thermal processes 4<sup>th</sup> edition, **2013**.
  58. Erbs D.G.; Klein S.A.; Duffie J.A. Estimation of the diffuse radiation fraction for hourly, daily and monthly-average global radiation. *Solar Energy*, **1982**, 28, 293-302. (DOI: [https://doi.org/10.1016/0038-092X\(82\)90302-4](https://doi.org/10.1016/0038-092X(82)90302-4))

59. Orgill J.F.; Hollands K.G.T. Correlation equation for hourly diffuse radiation on a horizontal surface. *Solar Energy*, **1977**, 19, 357-359. (DOI: [https://doi.org/10.1016/0038-092X\(77\)90006-8](https://doi.org/10.1016/0038-092X(77)90006-8))
60. Fanney A.H.; Dougherty B.P.; Davis M.W. Evaluating Building Integrated Photovoltaic Performance Models. *Proceedings of the Twenty-Ninth IEEE Photovoltaic Specialists Conference (PVSC)* New Orleans, LA, **2002**. (DOI: <https://doi.org/10.1109/PVSC.2002.1190893>)
61. Oliveti G.; Marletta L.; Arcuri N.; De Simone M.; Bruno R.; Evola G. *Solar energy, Green Energy Technology*, **2014** (DOI: [https://doi.org/10.1007/978-3-319-03074-6\\_4](https://doi.org/10.1007/978-3-319-03074-6_4))
62. Armstrong S.; Hurley W.G. A thermal model for photovoltaic panels under varying atmospheric conditions. *Applied Thermal Engineering*, **2010**, 30, 1488-1495. (DOI: <https://doi.org/10.1016/j.applthermaleng.2010.03.012>)
63. Lloyd, J.R.; Moran, W.R. Natural Convection Adjacent to Horizontal Surface of Various Planforms. *J. Heat Transfer*, **1974**, 96, 443-447. (DOI: <https://doi.org/10.1115/1.3450224>)
64. Kaplani E.; Kaplanis S. Thermal modelling and experimental assessment of the dependence of PV module temperature on wind velocity and direction, module orientation and inclination. *Solar Energy*, **2014**, 107, 443-460. (DOI: <https://doi.org/10.1016/j.solener.2014.05.037>)
65. Ernani S. Convection coefficient equations for forced air flow over flat surfaces. *Solar Energy*, **2006**, 80, 1063-1071. (DOI: <https://doi.org/10.1016/j.solener.2005.11.001>)
66. Shahzada P.A.; Said A.; Nicolas B.; Benjamin W.F. Two-dimensional finite difference-based model for coupled irradiation and heat transfer in photovoltaic modules. *Solar Energy Materials and Solar Cells*, **2018**, 180, 289-302. (DOI: <https://doi.org/10.1016/j.solmat.2017.06.055>)
67. Jones A.D.; Underwood C.P. A thermal model for photovoltaic systems. *Solar Energy*, **2001**, 70, 349-359. (DOI: [https://doi.org/10.1016/S0038-092X\(00\)00149-3](https://doi.org/10.1016/S0038-092X(00)00149-3))
68. International Electrotechnical Commission, 2021. IEC 61215-1:2021, Terrestrial photovoltaic (PV) modules - Design qualification and type approval - Part 1: Test requirements, **2023**. URL <https://webstore.iec.ch/publication/61345>. Accessed on 15 August 2023
69. Versteeg HK, Malalasekera W. An introduction to computational fluid dynamics. 2nd ed. Harlow, England: Pearson;207.
70. Dubey S.; Tay A.A.O. Testing of two different types of photovoltaic–thermal (PVT) modules with heat flow pattern under tropical climatic conditions. *Energy for Sustainable Development*, **2013**, 17, 1-12. (DOI: <https://doi.org/10.1016/j.esd.2012.09.001>)
71. Boumaaraf B.; Boumaaraf H.; Ait-cheikh M.S.; Khelifa A. Experimental energy improvement of a special design heat exchanger-based hybrid solar collector for a photovoltaic module square surface. *Environmental Science and Pollution Research*, **2021**, 28. (DOI: <https://doi.org/10.1007/s11356-021-14895-2>)
72. Kianifard S.; Zamen M.; Nejad A.A. Modeling, designing and fabrication of a novel PV/T cooling system using half pipe. *Journal of Cleaner Production*, **2020**, 253. (DOI: <https://doi.org/10.1016/j.jclepro.2020.119972>)
73. Abdallah S.R.; Saidani-Scott H.; Abdellatif O.E. Performance analysis for hybrid PV/T system using low concentration MWCNT (water-based) nanofluid. *Solar Energy*, **2019**, 181, 108-115. (DOI: <https://doi.org/10.1016/j.solener.2019.01.088>)

74. Venkatesh T.; Manikandan S.; Selvam C.; Harish S. Performance enhancement of hybrid solar PV/T system with graphene based nanofluids. *Int. Commun. in Heat and Mass Transfer*, **2022**, 130. (DOI: <https://doi.org/10.1016/j.icheatmasstransfer.2021.105794>)
75. Bassam A.M.; Sopian K.; Ibrahim A.; Al-Aasam A.B.; Daye M. Experimental analysis of photovoltaic thermal collector (PVT) with nano PCM and micro-fins tube counterclockwise twisted tape nanofluid. *Case Studies in Thermal Engineering*, **2023**, 45. (DOI: <https://doi.org/10.1016/j.csite.2023.102883>)
76. Hassan A.; Wahab A.; Qasim M.A.; Janjua M.M.; Ali M.A.; Ali H.M.; Jadoon T.R.; Ali E.; Raza A.; Javaid N. Thermal management and uniform temperature regulation of photovoltaic modules using hybrid phase change materials-nanofluids system. *Renewable Energy*, **2020**, 145. (DOI: <https://doi.org/10.1016/j.renene.2019.05.130>)
77. Al-Aasam A.B.; Ibrahim A.; Sopian K.; Abdulsahib M.B.; Dayer M. Nanofluid-based photovoltaic thermal solar collector with nanoparticle-enhanced phase change material (Nano-PCM) and twisted absorber tubes. *Case Studies in Thermal Engineering*, **2023**, 49. (DOI: <https://doi.org/10.1016/j.csite.2023.103299>)
78. Das D.; Bordoloi U.; Kamble A.D.; Muigai H.H.; Pai R.K.; Kalita P. Performance investigation of a rectangular spiral flow PV/T collector with a novel form-stable composite material. *Applied Thermal Engineering*, **2021**, 182. (DOI: <https://doi.org/10.1016/j.applthermaleng.2020.116035>)
79. Alexandra Sutu. Solar Thermal Markets In Europe – Trends And Market Statistics 2021 Technical report, *Solar Heat Europe*, **2022**.
80. Pvxchange. Solar price index and solar module price development, 2023. URL <https://www.pvxchange.com/Price-Index>. Accessed 30 August 2023.
81. Czamara. Czamara Renewable Energy, 2023. URL <https://www.czamara.eu/>. Accessed on 11 September **2023**.
82. Kang D.; White T.; Thomson A. PV Module Recycling: Mining Australian Rooftops. *In Proceedings of the 2015 Asia-Pacific Solar Research Conference*, Brisbane, Australia, 9 December **2015**.
83. Hosseini-Fashami F.; Motevali A.; Nabavi-Pelesaraei A.; Hashemi S.J.; Kwok-Wing C. Energy-Life cycle assessment on applying solar technologies for greenhouse strawberry production. *Renewable and Sustainable Energy Reviews*, **2019**, 116. (DOI: <https://doi.org/10.1016/j.rser.2019.109411>)
84. Ghasemi-Mobtaker H.; Mostashari-Rad F.; Saber Z.; Chau K.; Nabavi-Pelesaraei A. Application of photovoltaic system to modify energy use, environmental damages and cumulative exergy demand of two irrigation systems-A case study: Barley production of Iran. *Renewable Energy*, **2020**, 160. (DOI: <https://doi.org/10.1016/j.renene.2020.07.047>)
85. Nabavi-Pelesaraei A.; Azadi H.; Van Passel S.; Saber Z.; Hosseini-Fashami F.; Mostashari-Rad F.; Ghasemi-Mobtaker H. Prospects of Solar Systems in Production Chain of Sunflower Oil Using Cold Press Method with Concentrating Energy and Life Cycle Assessment. *Energy*, **2021**, 223. (DOI: <https://doi.org/10.1016/j.energy.2021.120117>)
86. The Hybrid Solar Panel produces electricity and heat simultaneously. Abora Advanced Solar Technology. URL <https://abora-solar.com/en/hybrid-solar-panel/>. Accessed 30 August 2023.

87. Kalogirou S.A.; Tripanagnostopoulos Y. Hybrid PV/T solar systems for domestic hot water and electricity production. *Energy Conversion and Management*, **2006**, 47, 3368-3382. (DOI: <https://doi.org/10.1016/j.enconman.2006.01.012>)
88. Foltyn-Zarychta, M.; Buła, R.; Pera, K. Discounting for Energy Transition Policies— Estimation of the Social Discount Rate for Poland. *Energies*, **2021**, 14, 741. (DOI: <https://doi.org/10.3390/en14030741>)
89. Poland Inflation Rate, 2023. URL <https://tradingeconomics.com/poland/inflation-cpi>. Accessed 1 September **2023**.
90. Ratajczak K.; Michalak K.; Narojczyk M.; Amanowicz Ł. Real Domestic Hot Water Consumption in Residential Buildings and Its Impact on Buildings' Energy Performance— Case Study in Poland. *Energies*, **2021**, 14. (DOI: <https://doi.org/10.3390/en14165010>)
91. PGNiG—Polish Oil and Gas Company. What is natural gas? URL <https://pgniq.pl/czym- jest-gaz-ziemny>. Accessed 10 September **2023**.
92. Regulation of the Minister of Infrastructure and Development of July 2014 on the Methodology for Calculating the Energy Performance of a Building and a Dwelling or a Part of a Building. URL <https://isap.sejm.gov.pl/isap.nsf/DocDetails.xsp?id=WDU20140000888>. Accessed 10 September **2023**.
93. Gelažanskas L.; Gamage K.A.A. Forecasting Hot Water Consumption in Residential Houses. *Energies*, **2015**, 8, 12702-12717. (DOI: <https://doi.org/10.3390/en81112336>)
94. Sklep Soltech. Inverters, 2023. URL <https://sklepsoltech.pl/pl/c/Inwertery/14>. Accessed on 11 September **2023**.
95. ASAT. Inverters, 2023. URL <https://sklep.asat.pl/inwertery>. Accessed on 11 September **2023**.
96. Solar Power Supply. Accessories, 2023. URL <https://solarpowersupply.eu/accessories>. Accessed on 11 September **2023**.
97. Onninen. Photovoltaic and energy storage systems, mounting systems, 2023. URL <https://onninen.pl/en/products/Photovoltaic-and-energy-storage-systems/Mounting-systems>. Accessed on 11 September **2023**.
98. Epompa. Pumps, 2023. URL [https://epompa.pl/pol\\_m\\_Dom-i-ogrod\\_POMPY-101.html](https://epompa.pl/pol_m_Dom-i-ogrod_POMPY-101.html). Accessed on 11 September **2023**.
99. Hydromix. Domestic hot water tanks, 2023. URL <https://hydromix.pl/557-zbiorniki-buforowe>. Accessed on 11 September **2023**.
100. Aquatik. Expansion vessels, 2023. <https://aquatik.eu/zbiorniki-hydroforowe-c-2.html>. Accessed on 11 September **2023**.
101. DHW calc. Tool for the Generation of Domestic Hot Water (DHW) Profiles on a Statistical Basis. Version 2.02b, **2017**. URL <https://www.uni-kassel.de/maschinenbau/en/institute/thermische-energietechnik/fachgebiete/solar-und-anlagentechnik/downloads>.
102. Ministry of Climate and Environment, Poland. A new settlement system, the so-called net-billing, 2021. URL <https://www.gov.pl/web/klimat/nowy-system-rozliczania-tzw-net-billing>. Accessed on 12 September **2023**.
103. Eurostat. Electricity price statistics, 2023. URL [https://ec.europa.eu/eurostat/statistics-explained/index.php?title=Electricity\\_price\\_statistics](https://ec.europa.eu/eurostat/statistics-explained/index.php?title=Electricity_price_statistics). Accessed on 12 September **2023**.

104. Statista. Wholesale prices of electricity in Poland from 2018 to 2023. URL <https://www.statista.com/statistics/1066654/poland-wholesale-electricity-prices/>. Accessed on 12 September **2023**.
105. Termet. Gas condensing boilers, 2023. URL <https://www.termet.com.pl/en/products/2>. Accessed on 12 September **2023**.
106. PGNiG. Tariff archive, 2023. URL <https://pgnig.pl/archiwum-taryf>. Accessed on 12 December **2023**.
107. Drozd W.; Kowalik M. Analysis of renewable energy use in single-family housing. *Open Engineering*, **2019**, 9, 269-281. (DOI: <https://doi.org/10.1515/eng-2019-0039>)



## Appendices

### Appendix A

This part provides the technical drawings of the designed cooling system. The technical drawings of the cooling system comprise six parts: top part, left part, right part, inlet part, outlet part, and bottom part.

The general views of each part are provided in Appendix A. Fully detailed technical drawings of each part were provided during the manufacturing process of the cooling system.

#### A.1 Top part

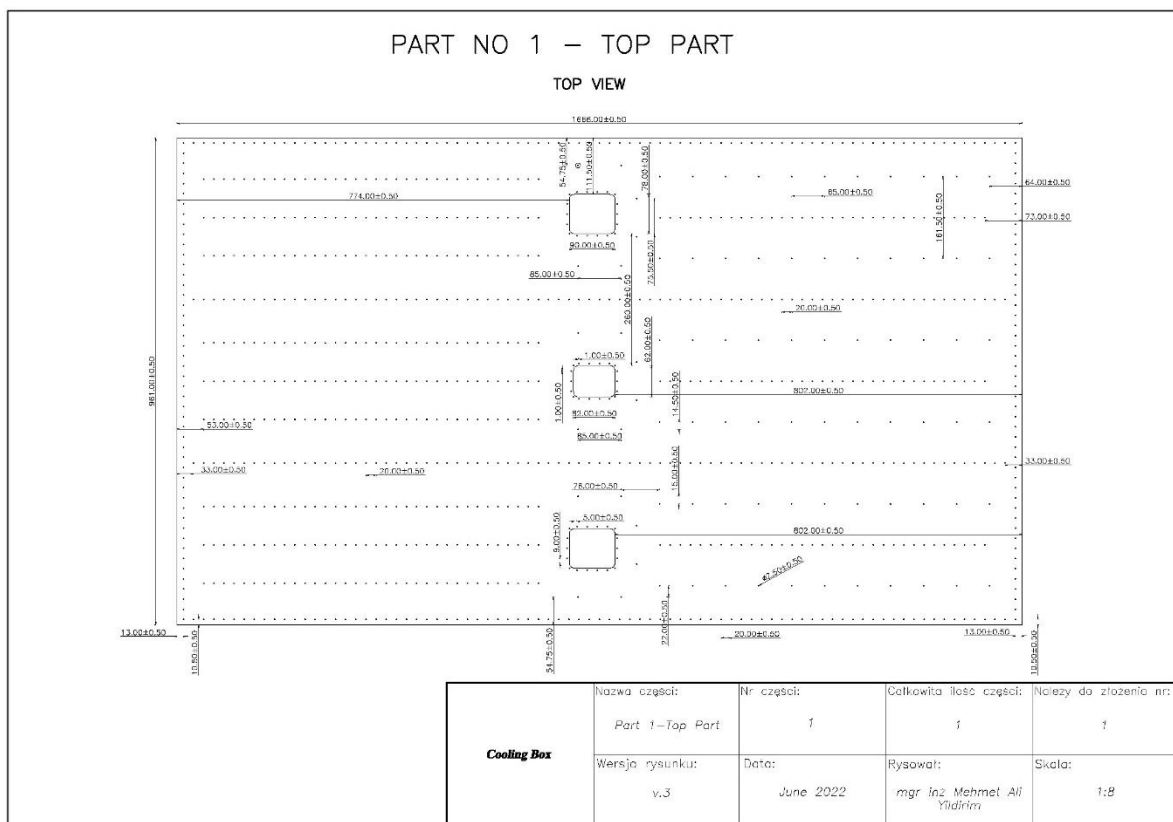


**Figure A. 1. Top part**

## A.2 Left part

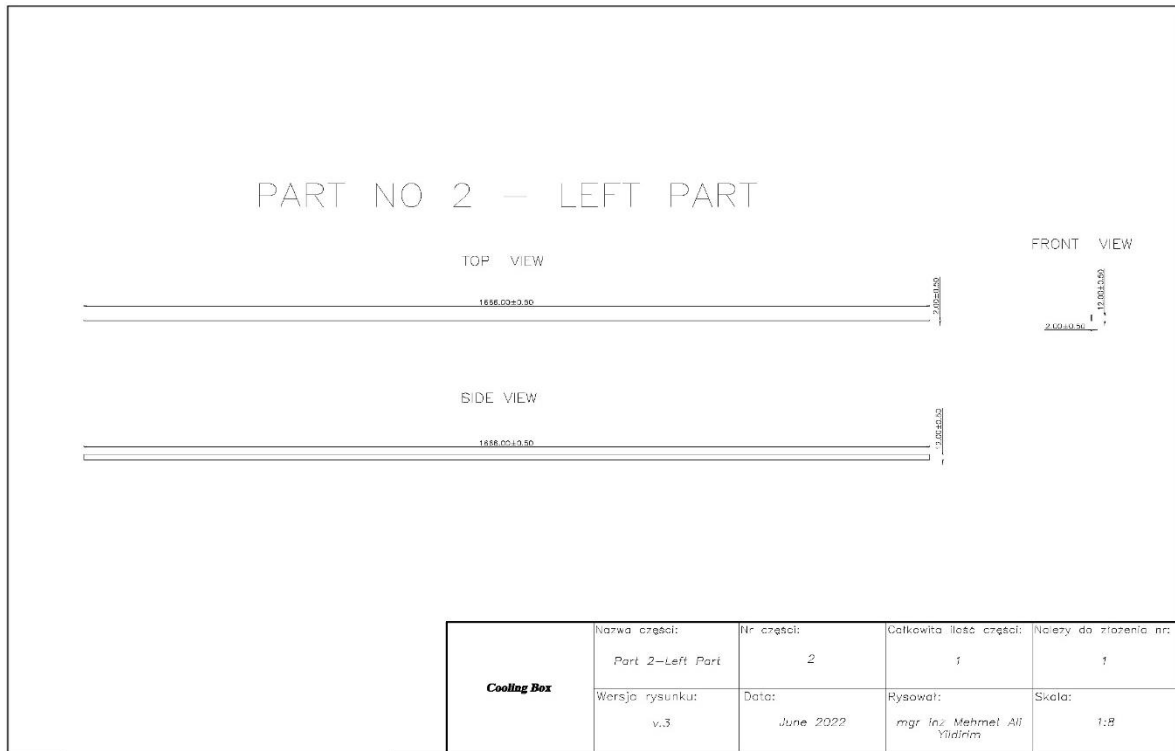


Figure A. 2. Left part

## A.3 Right part

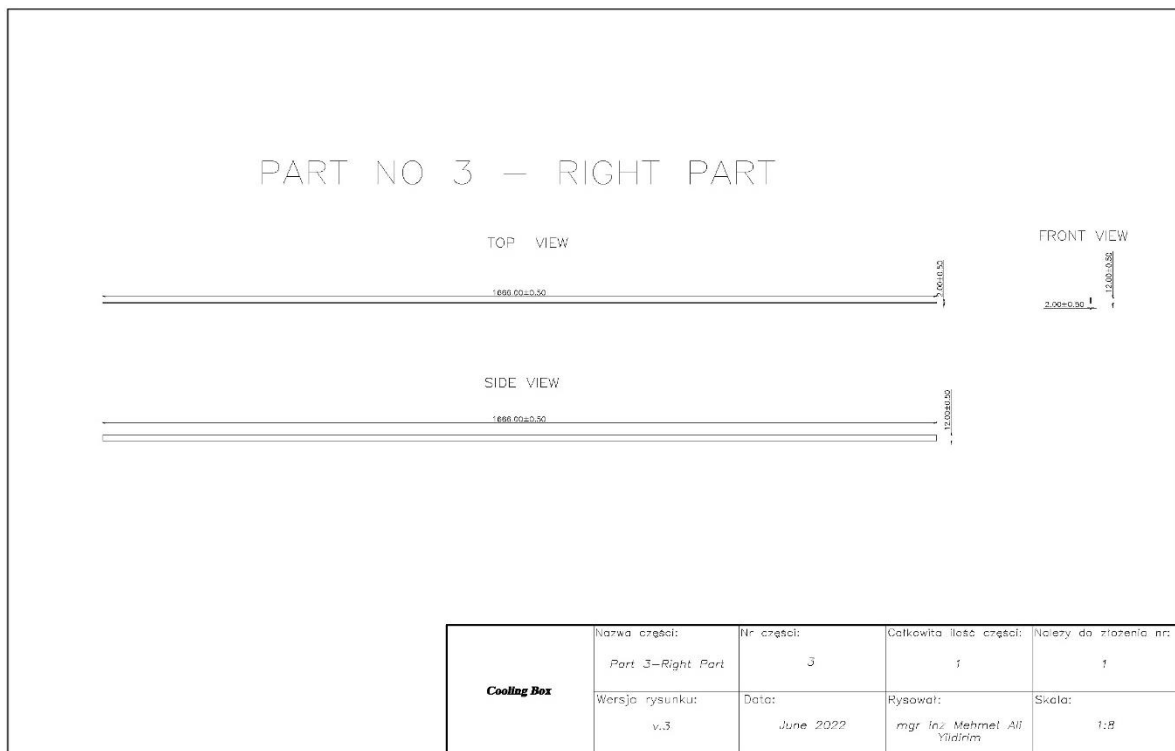


Figure A. 3. Right part

## A.4 Inlet part

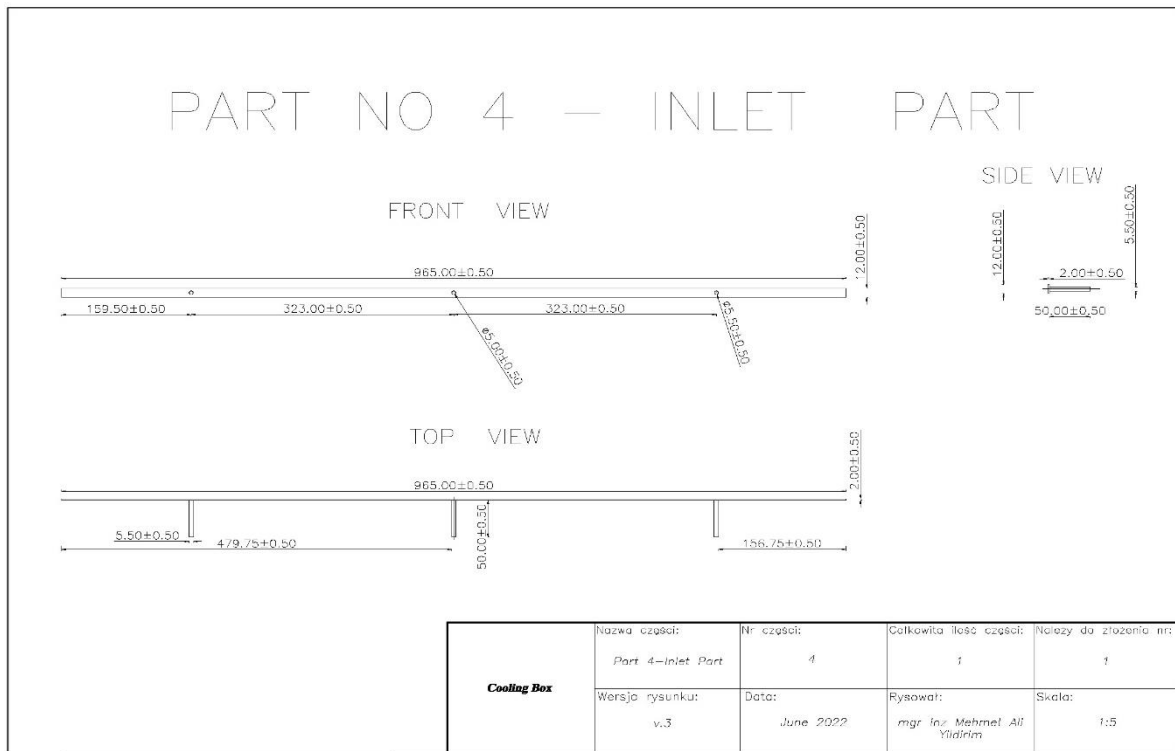


Figure A. 4. Inlet part

## A.5 Outlet part

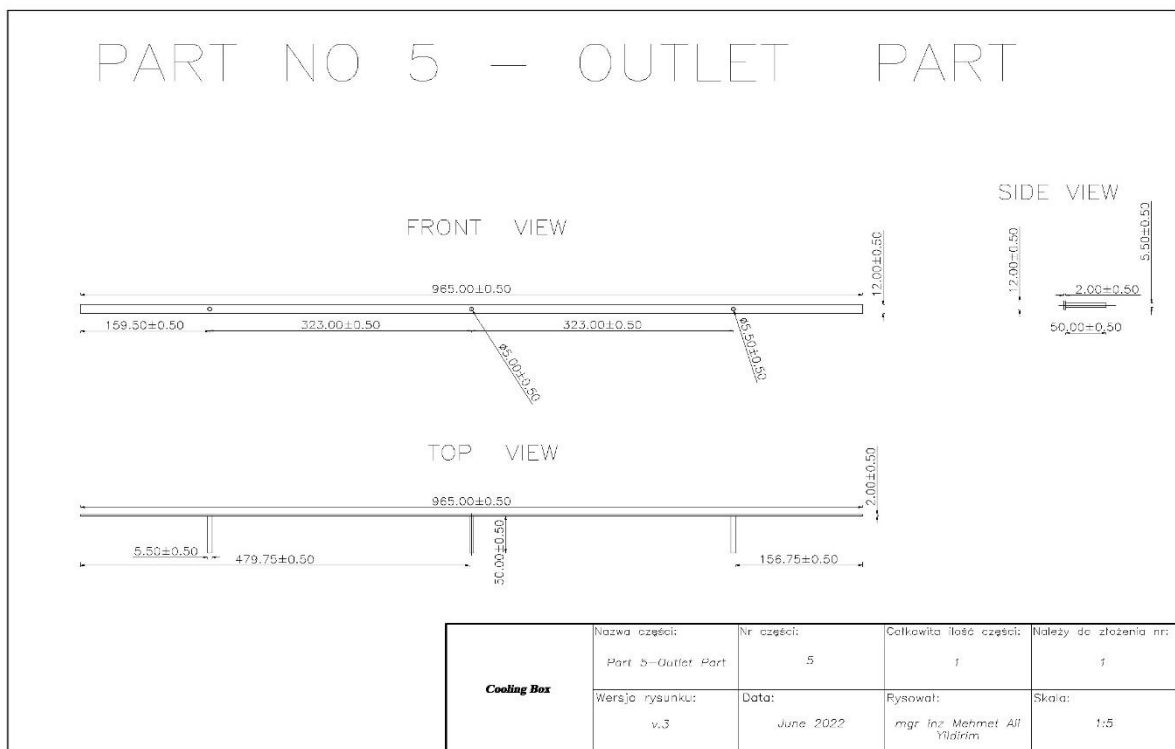


Figure A. 5. Outlet part

## A.6 Bottom part

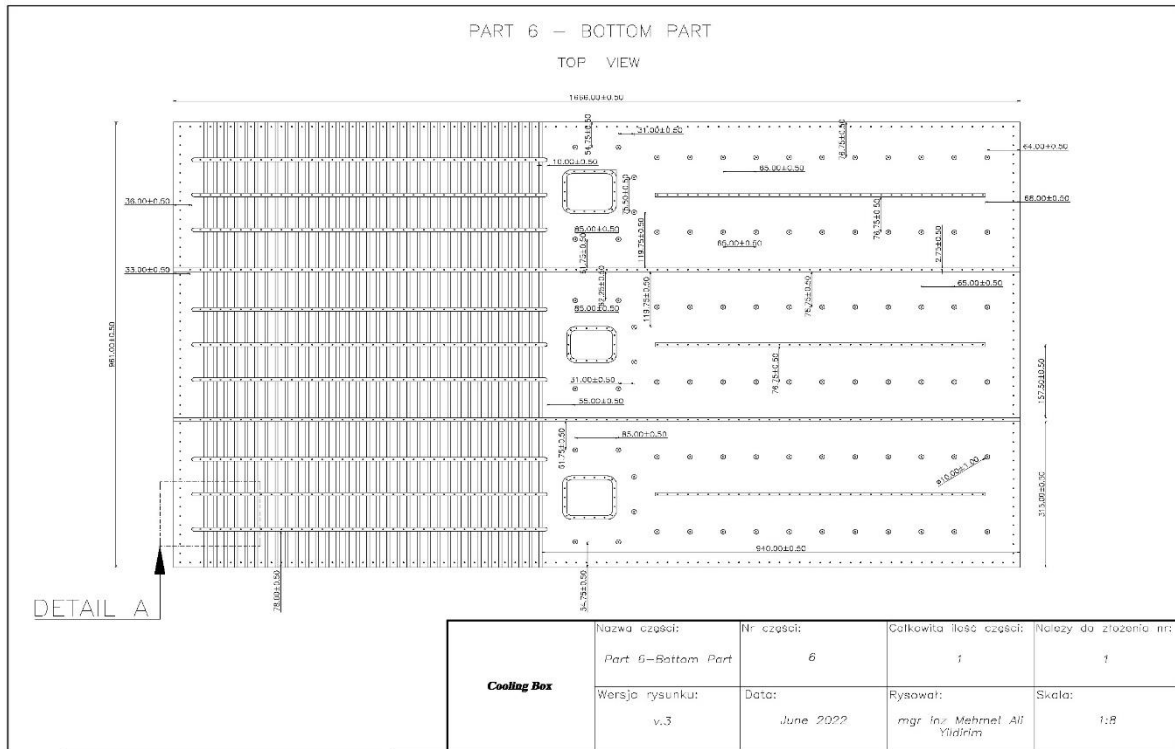


Figure A. 6. Bottom part

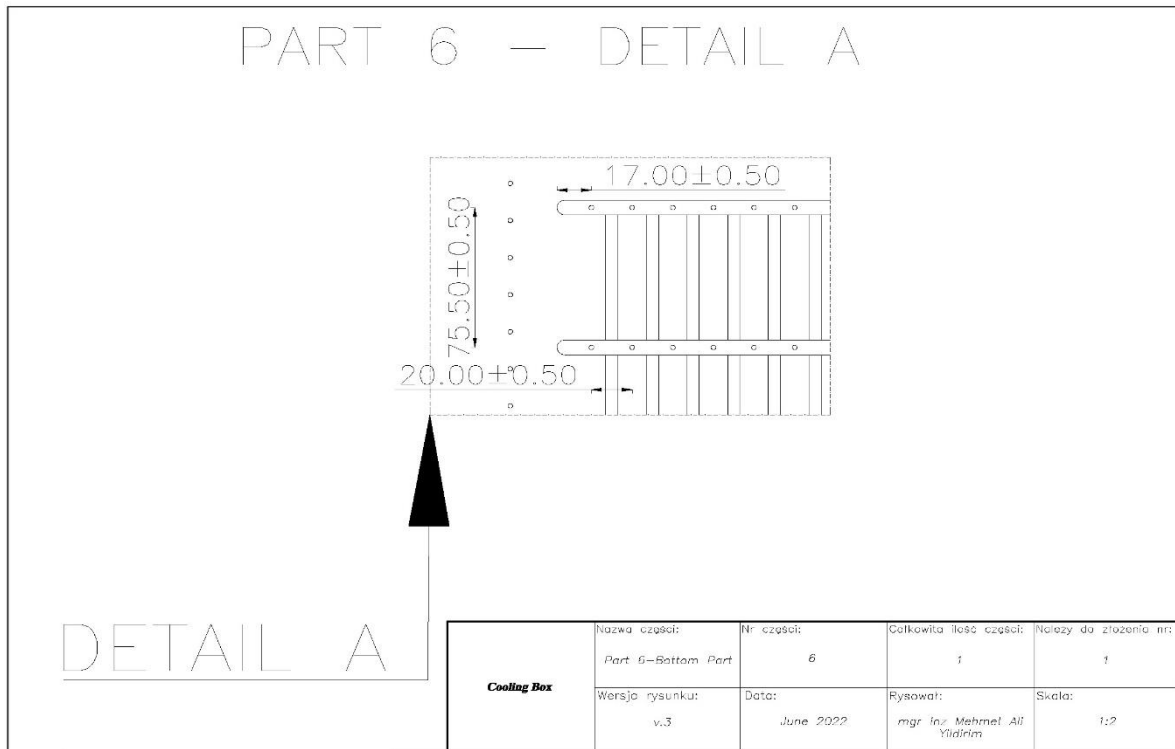


Figure A. 7. Bottom part – detail A

## Appendix B

### B.1 Test results – 15/09/2023 and 16/09/2023



Figure B. 1. Test results obtained on 15/09/2023 (left) and 16/09/2023 (right)

### B.2 Test results – 17/09/2023 and 18/09/2023



Figure B. 2. Test results obtained on 17/09/2023 (left) and 18/09/2023 (right)

### B.3 Test results – 20/09/2023 and 21/09/2023



Figure B. 3. Test results obtained on 20/09/2023 (left) and 21/09/2023 (right)

### B.4 Test results – 22/09/2023 and 02/10/2023

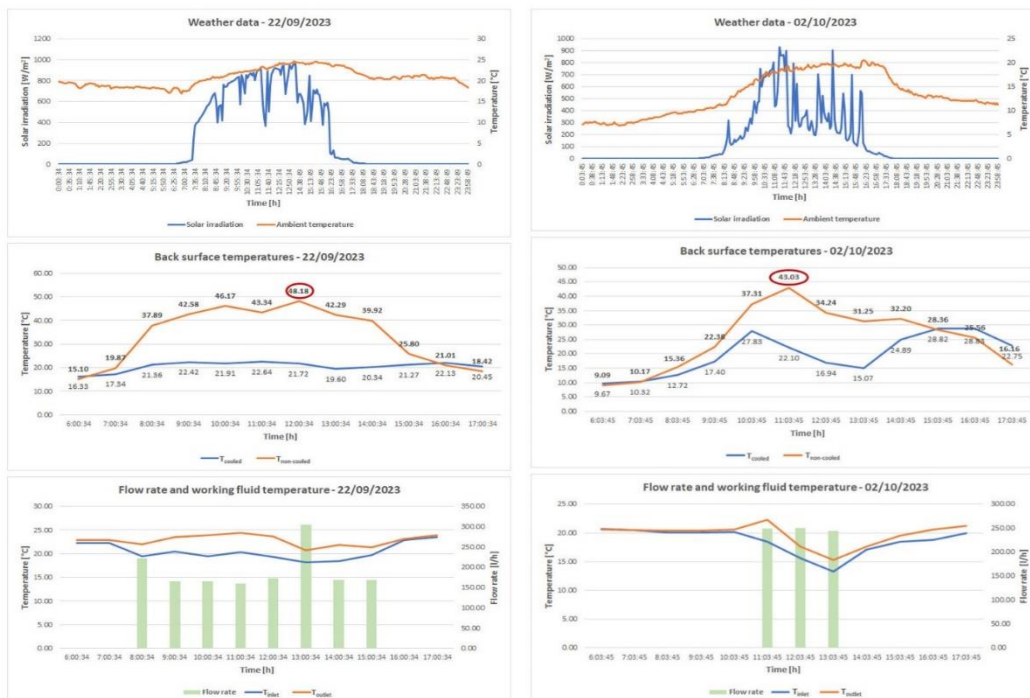


Figure B. 4. Test results obtained on 22/09/2023 (left) and 02/10/2023 (right)

## B.5 Test results – 27/09/2023 and 28/09/2023



Figure B. 5. Test results obtained on 27/09/2023 (left) and 28/09/2023 (right)

## B.6 Test results – 03/10/2023 and 04/10/2023

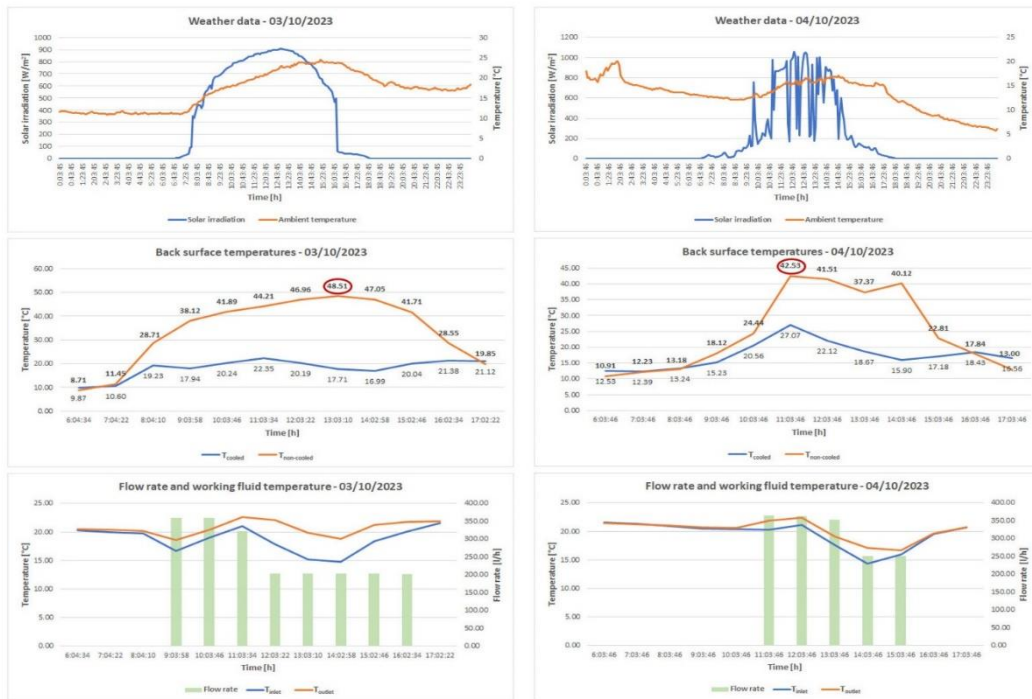


Figure B. 6. Test results obtained on 03/10/2023 (left) and 04/10/2023 (right)

## B.7 Test results – 05/10/2023 and 06/10/2023



Figure B. 7. Test results obtained on 05/10/2023 (left) and 06/10/2023 (right)



## B.8 Test results – 07/10/2023 and 11/10/2023



Figure B. 8. Test results obtained on 07/10/2023 (left) and 11/10/2023 (right)

## B.9 Test results – 12/10/2023 and 13/10/2023

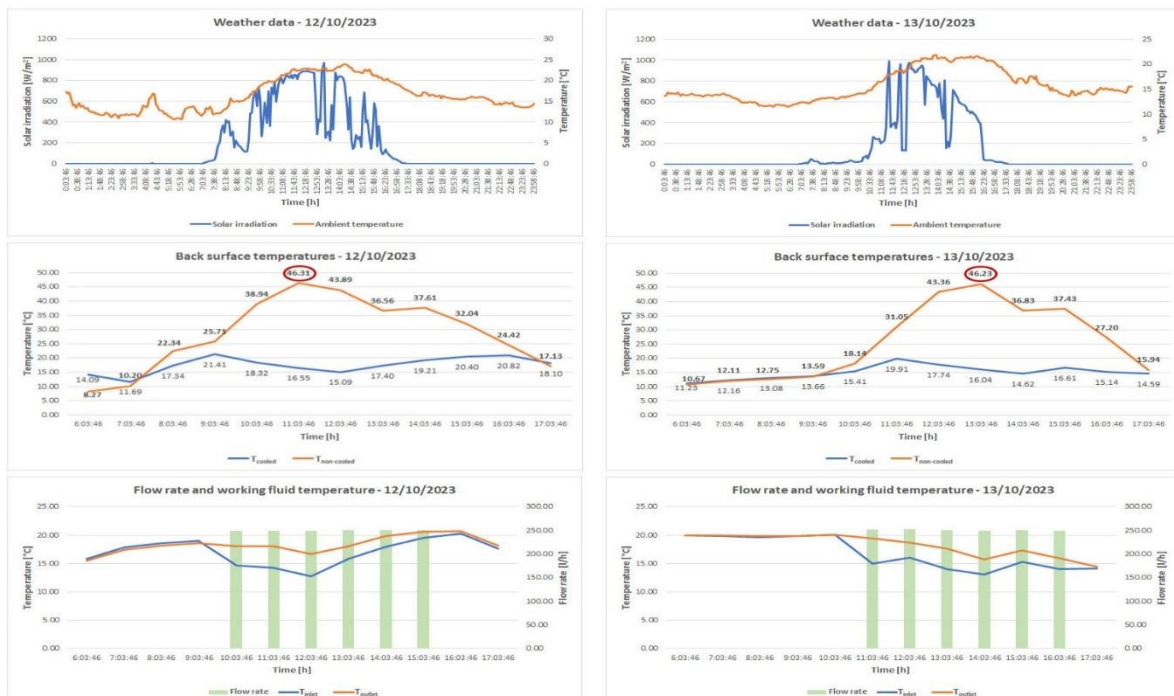


Figure B. 9. Test results obtained on 12/10/2023 (left) and 13/10/2023 (right)

## B.10 Test results – 19/10/2023 and 20/10/2023

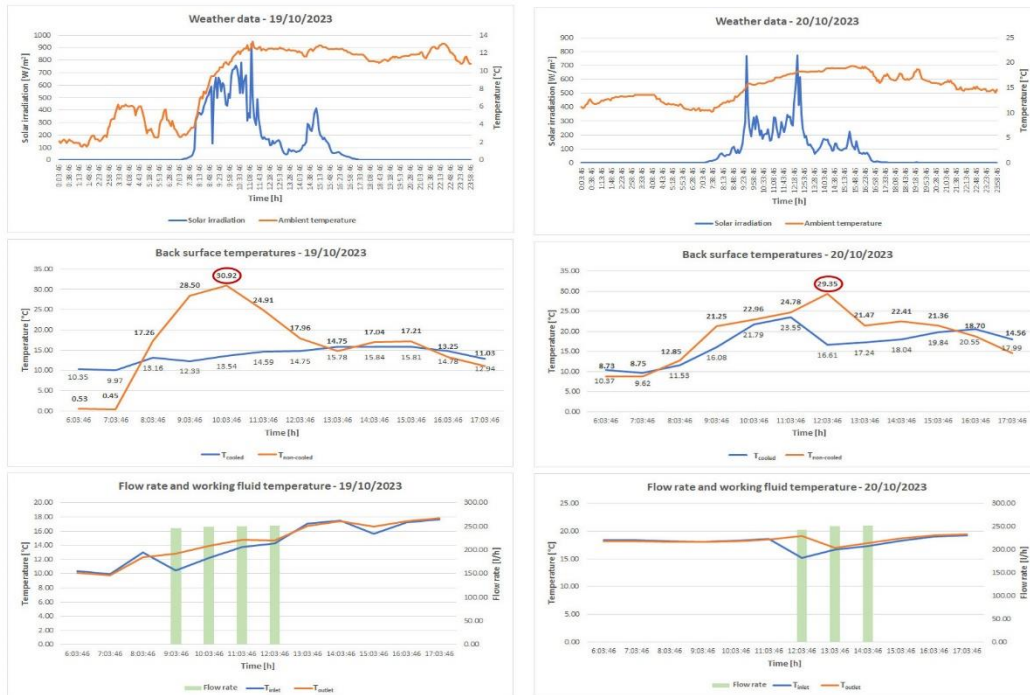


Figure B. 10. Test results obtained on 19/10/2023 (left) and 20/10/2023 (right)

## B.11 Test results – 21/10/2023 and 24/10/2023



Figure B. 11. Test results obtained on 21/10/2023 (left) and 24/10/2023 (right)

## B.12 Test results – 28/10/2023 and 29/10/2023

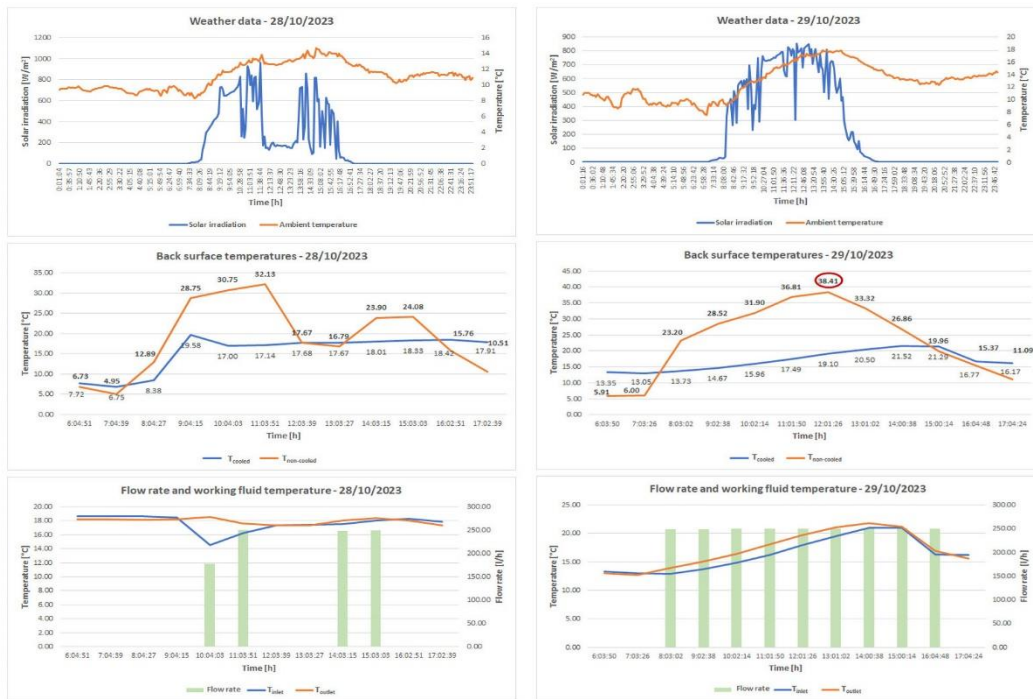


Figure B. 12. Test results obtained on 28/10/2023 (left) and 29/10/2023 (right)

## List of Figures

|   |    |
|---|----|
| Figure 1-1. EU27 energy consumption by source.....  | 3  |
| Figure 1-2 PV installation capacity of Poland during the years [10].....  | 4  |
| Figure 1-3 The global total installed cost of the PV system .....   | 4  |
| Figure 1-4 The global weighted average levelized cost of electricity .....  | 5  |
| Figure 3-1. The temperature effect on open-circuit voltage and short-circuit current .....  | 9  |
| Figure 3-2. Electroluminescence pictures of a PV cell at different times during damp-heat testing at 85 °C [16] .....                             | 9  |
| Figure 3-3. Schematic diagram of an air-based PV/T system [19].....   | 11 |
| Figure 3-4. Water-based PV/T system [30] .....  | 14 |
| Figure 3-5. The front view of the heat pipe employed PV/T system [34].....  | 16 |
| Figure 3-6. TEG combined PV/T system [42] .....   | 18 |
| Figure 3-7. PCM-based PV/T system [45].....   | 19 |
| Figure 5-1. Considered PV panel layers.....   | 27 |
| Figure 5-2. Grid formation .....  | 32 |
| Figure 5-3. The temperature profile of the PV module under NOCT conditions .....  | 36 |
| Figure 5-4. PV cell layer temperature under different solar irradiation levels .....  | 37 |
| Figure 5-5. PV cell layer temperature at different ambient temperatures under 1000 W/m <sup>2</sup> . .....                                       | 37 |
| Figure 6-1. The initial design of the cooling system.....   | 40 |
| Figure 6-2. The dorsal-shaped design.....   | 41 |
| Figure 6-3. Dimensions of the dorsal-shaped geometry .....  | 41 |
| Figure 6-4. The PV cell layer temperature distribution of cases for the initial design .....  | 46 |
| Figure 6-5. The grid independence analysis.....   | 47 |
| Figure 6-6. The cylindrical turbulator notches.....   | 48 |
| Figure 6-7. The PV cell layer temperature distribution of cases for the final design.....   | 50 |
| Figure 6-8. The residual taken from the numerical solver.....   | 51 |
| Figure 6-9. Technical drawing of the bottom part of the cooling system .....  | 52 |
| Figure 6-10. The production process of the cooling system a) the top part of the cooling system, b) the interior parts of the cooling system..... | 52 |
| Figure 6-11. The interior of the cooling system.....  | 53 |

|   |    |
|---|----|
| Figure 7-1. A schematic of the test rig.....  | 55 |
| Figure 7-2. Heat flux measurements on the surface of the cooling system.....  | 56 |
| Figure 7-3. The cooling system, a) interior of the solid domain, b) fluid domain.....   | 58 |
| Figure 7-4. The temperature distribution of the solid domains.....  | 60 |
| Figure 7-5. The procedure of assembling the PV/T system, a) thermal greasing of the cooling system, b) complete PV/T system and test rig..... | 61 |
| Figure 7-6. The outlet temperature comparison of the initial design and manufactured final design.....  | 64 |
| Figure 8-1. The PT-1000 temperature sensor placement on the rear side of the non-cooled PV module and cooling system.....                     | 67 |
| Figure 8-2. The single-axis sun-tracking system with cooled and non-cooled PV modules .   | 68 |
| Figure 8-3. The placement of the pyranometer on the test rig.....   | 69 |
| Figure 8-4. The components of the test rig.....   | 70 |
| Figure 8-5. The operational panel.....  | 70 |
| Figure 8-6. The weather data – 12/09/2023.....  | 73 |
| Figure 8-7. The hourly average back surface temperature of the PV modules – 12/09/2023  | 74 |
| Figure 8-8. The flow rate and temperatures in the PV/T system – 12/09/2023.....   | 74 |
| Figure 8-9. The energy analysis – 12/09/2023.....   | 75 |
| Figure 8-10. The weather data – 13/09/2023.....   | 76 |
| Figure 8-11. The hourly average back surface temperature of the PV modules – 13/09/2023.....  | 77 |
| Figure 8-12. The flow rate and temperatures in the PV/T system – 13/09/2023.....  | 77 |
| Figure 8-13. The energy analysis – 13/09/2023.....  | 78 |
| Figure 8-14. The weather data – 14/10/2023.....   | 79 |
| Figure 8-15. The hourly average back surface temperature of the PV modules – 14/10/2023.....  | 80 |
| Figure 8-16. The flow rate and temperatures in the PV/T system – 14/10/2023.....  | 80 |
| Figure 8-17. The energy analysis – 14/10/2023.....  | 81 |
| Figure 8-18. The weather data – 26/09/2023.....   | 82 |
| Figure 8-19. The hourly average back surface temperature of the PV modules – 26/09/2023.....  | 83 |
| Figure 8-20. The temperature change in the buffer tank – 26/09/2023.....  | 84 |
| Figure 8-21. The flow rate and temperatures in the PV/T system – 26/09/2023.....  | 84 |

|   |     |
|---|-----|
| Figure 8-22. The energy analysis – 26/09/2023 .....   | 85  |
| Figure 8-23. The weather data – 29/09/2023 .....  | 86  |
| Figure 8-24. The hourly average back surface temperature of the PV modules – 29/09/2023 .....       | 87  |
| Figure 8-25. The flow rate and temperatures in the PV/T system – 29/09/2023 .....                   | 87  |
| Figure 8-26. The temperature change in the buffer tank – 29/09/2023 .....                           | 88  |
| Figure 8-27. The energy analysis – 29/09/2023 .....   | 89  |
| Figure 8-28. The weather data – 18/10/2023 .....  | 90  |
| Figure 8-29. The hourly average back surface temperature of the PV modules – 18/10/2023 .....       | 91  |
| Figure 8-30. The flow rate and temperatures in the PV/T system – 18/10/2023 .....                   | 91  |
| Figure 8-31. The temperature change in the buffer tank – 18/10/2023 .....                           | 92  |
| Figure 8-32. The energy analysis – 18/10/2023 .....   | 93  |
| Figure 8-33. The thermal image of a) the non-cooled PV module and b) the PV/T system..              | 94  |
| Figure 8-34. The pressure drop in the test rig with respect to the flow rate.....                   | 95  |
| Figure 10-1. The energy results of the PV/T modules over a 25-year lifetime .....                   | 114 |
| Figure 10-2. The cost breakdown of the DHW system designed with PV/T modules.....                   | 117 |
| Figure 10-3. The daily DHW profile .....  | 118 |
| Figure 10-4. The DHW preparation loop .....   | 118 |
| Figure 10-5. The PV/T loop developed in TRNSYS.....   | 119 |
| Figure 10-6. The auxiliary heating loop of the DHW system.....                                      | 120 |
| Figure 10-7. The complete DHW system.....   | 120 |
| Figure 10-8. The monthly thermal energy generation of the PV/Ts and coverage of the DHW demand..... | 121 |
| Figure 10-9. The cost breakdown of the conventional gas boiler system for DHW .....                 | 124 |
| Figure 10-10. The payback period of the PV/T system.....  | 125 |
| <br>  |     |
| Figure A. 1. Top part .....   | 139 |
| Figure A. 2. Left part .....  | 140 |
| Figure A. 3. Right part.....  | 140 |
| Figure A. 4. Inlet part.....  | 141 |
| Figure A. 5. Outlet part.....   | 141 |

|   |     |
|---|-----|
| Figure A. 6. Bottom part .....  | 142 |
| Figure A. 7. Bottom part – detail A .....   | 142 |
| Figure B. 1. Test results obtained on 15/09/2023 (left) and 16/09/2023 (right) .....  | 143 |
| Figure B. 2. Test results obtained on 17/09/2023 (left) and 18/09/2023 (right) .....  | 143 |
| Figure B. 3. Test results obtained on 20/09/2023 (left) and 21/09/2023 (right) .....  | 144 |
| Figure B. 4. Test results obtained on 22/09/2023 (left) and 02/10/2023 (right) .....  | 144 |
| Figure B. 5. Test results obtained on 27/09/2023 (left) and 28/09/2023 (right) .....  | 145 |
| Figure B. 6. Test results obtained on 03/10/2023 (left) and 04/10/2023 (right) .....  | 146 |
| Figure B. 7. Test results obtained on 05/10/2023 (left) and 06/10/2023 (right) .....  | 146 |
| Figure B. 8. Test results obtained on 07/10/2023 (left) and 11/10/2023 (right) .....  | 147 |
| Figure B. 9. Test results obtained on 12/10/2023 (left) and 13/10/2023 (right) .....  | 147 |
| Figure B. 10. Test results obtained on 19/10/2023 (left) and 20/10/2023 (right) ..... | 148 |
| Figure B. 11. Test results obtained on 21/10/2023 (left) and 24/10/2023 (right) ..... | 148 |
| Figure B. 12. Test results obtained on 28/10/2023 (left) and 29/10/2023 (right) ..... | 149 |

## List of Tables

|  |    |
|--|----|
| Table 5-1. Material properties of the layers .....   | 26 |
| Table 5-2. PV module properties under STC.....   | 27 |
| Table 5-3. PV module datasheet under NOCT conditions .....   | 35 |
| Table 6-1. The material and thermal properties of the base material.....   | 42 |
| Table 6-2. Water/propylene glycol mixture properties.....  | 43 |
| Table 6-3. The boundary conditions .....   | 44 |
| Table 6-4. Numerical model results of initial cooling system design under NOCT conditions .....                              | 45 |
| Table 6-5. The electrical conversion efficiency and power output of initial design at NOCT conditions.....                   | 46 |
| Table 6-6. Numerical model results of final cooling system design under NOCT conditions                                      | 49 |
| Table 6-7. The electrical conversion efficiency and power output of the final design at NOCT conditions.....                 | 51 |
| Table 7-1. Dimensions of the divided surface areas .....   | 56 |
| Table 7-2. Preliminary experimental test results .....   | 57 |
| Table 7-3. Useful thermal energy gain and thermal efficiency of the system .....   | 57 |
| Table 7-4. Comparison of outlet temperature between measurements and CFD model.....  | 59 |
| Table 7-5. Outlet temperature and thermal efficiency of the initial design.....  | 59 |
| Table 7-6. Experimental data of the cooling system coupled with the PV module .....  | 62 |
| Table 7-7. The thermal energy generation and thermal efficiency of the cooling system coupled with the PV module .....       | 62 |
| Table 7-8. The rear side temperature of the cooled and non-cooled PV module .....  | 62 |
| Table 7-9. The power output and the electrical conversion efficiency comparison of the cooled and non-cooled PV module ..... | 63 |
| Table 7-10. Comparison of outlet temperature between measurements and PV/T system CFD model.....                             | 63 |
| Table 7-11. Outlet temperature and thermal efficiency of the initial PV/T system .....                                       | 64 |
| Table 7-12. Uncertainties in measuring instruments.....  | 65 |
| Table 8-1. The temperatures in the test rig – 12/09/2023 .....   | 73 |
| Table 8-2. The temperatures in the test rig – 13/09/2023 .....   | 76 |



|  |     |
|--|-----|
| Table 8-3. The temperatures in the test rig – 14/10/2023 .....   | 79  |
| Table 8-4. The hourly weather data and temperature in the test rig – 26/09/2023 .....                      | 83  |
| Table 8-5. The hourly weather data and temperature in the test rig – 29/09/2023 .....                      | 86  |
| Table 8-6. The hourly weather data and temperature in the test rig – 18/10/2023 .....                      | 90  |
| Table 8-7. The energy analysis on collected data for September 2023 .....                                  | 96  |
| Table 8-8. The energy analysis on collected data for October 2023 .....                                    | 97  |
| Table 8-9. Numerical model parameters .....  | 98  |
| Table 8-10. The experimental data collected for the validation of Type 50 .....                            | 99  |
| Table 8-11. The measured data and Type 50 model output .....   | 100 |
| Table 8-12. Monthly weather data for Cracow, Poland .....  | 101 |
| Table 8-13. The summary of monthly energy analysis .....   | 101 |
| Table 8-14. Uncertainties in measuring instruments .....   | 102 |
| Table 9-1. A comparison between the designed PV/T system and proposed PV/T systems in the literature ..... | 109 |
| Table 10-1. The summary of the unit cost .....   | 112 |
| Table 10-2. A summary of the market analysis .....   | 113 |
| Table 10-3. The yearly degradation in energy production analysis for designed PV/T .....                   | 114 |
| Table 10-4. The capital costs and OM costs of the PV/T modules .....                                       | 115 |
| Table 10-5. LEC values of PV/T modules .....   | 115 |
| Table 10-6. Cost of the electrical and hydraulic components of PV/T systems .....                          | 117 |
| Table 10-7. The monthly electrical energy generation and consumption .....                                 | 122 |
| Table 10-8. The monthly energy balance of the DHW system .....   | 123 |
| Table 10-9. The summary of costs and bill savings .....  | 124 |
| Table 10-10. The levelized cost of heat and electricity .....  | 125 |